JYU DISSERTATIONS 686

Moona Kurttila

Tripping the Light Fantastic

Signal Transduction Pathways in a Bacterial Phytochrome

UNIVERSITY OF JYVÄSKYLÄ
FACULTY OF MATHEMATICS
AND SCIENCE

JYU DISSERTATIONS 686

Moona Kurttila

Tripping the Light Fantastic

Signal Transduction Pathways in a Bacterial Phytochrome

Esitetään Jyväskylän yliopiston matemaattis-luonnontieteellisen tiedekunnan suostumuksella
julkisesti tarkastettavaksi Ambiotica-rakennuksen salissa YAA303
syyskuun 1. päivänä 2023 kello 12.

Academic dissertation to be publicly discussed, by permission of
the Faculty of Mathematics and Science of the University of Jyväskylä,
in building Ambiotica, auditorium YAA303, on September 1, 2023, at 12 o'clock.

JYVÄSKYLÄN YLIOPISTO
UNIVERSITY OF JYVÄSKYLÄ

JYVÄSKYLÄ 2023

Editors
Matti Jalasvuori
Department of Biological and Environmental Science, University of Jyväskylä
Päivi Vuorio
Open Science Centre, University of Jyväskylä

ISBN 978-951-39-9713-7 (PDF)
URN:ISBN:978-951-39-9713-7
ISSN 2489-9003

Permanent link to this publication: http://urn.fi/URN:ISBN:978-951-39-9713-7

ABSTRACT

Kurttila, Moona
Tripping the Light Fantastic: Signal Transduction Pathways in a Bacterial Phytochrome
Jyväskylä: University of Jyväskylä, 2023, 81p.
(JYU Dissertations
ISSN 2489-9003; 686)
ISBN 978-951-39-9713-7 (PDF)
Yhteenveto: Jalalla koreasti valon tahtiin: bakteerifytokromin signaalinvälitysreitit
Diss.

Phytochromes are red and far-red light sensing photoreceptors found in plants, bacteria, algae and fungi. They translate light cues into biochemical signalling cascades and thus allow organisms to adapt to the environment. They control growth and reproduction of nearly all vegetation, and have enormous potential for optogenetic applications to control desired cellular events by light. Light absorption causes isomerization of a bilin chromophore, which triggers structural rearrangements of the protein, ultimately controlling the biochemical activity of the system. In this thesis, spectroscopic, structural and biochemical data were combined to understand the function of a bacterial phytochrome from *Deinococcus radiodurans*. The system consists of a conserved photosensory module (PSM), which has a chromophore binding domain (CBD) and a phytochrome specific (PHY) domain. The PHY domain structurally and functionally connects the chormophore in CBD to the biologically active output module (OPM). Moreover, it includes a structurally flexible hairpin extension, "tongue", that extends to the vicinity of the chromophore and refolds during photoconversion. In the experimental part of the work, a method suitable to study dynamics of the tongue with UV–vis spectroscopy was established. With this method, combined with activity assays and other spectroscopic approaches, the dynamics of the tongue were shown to be dictated by the coupling with the CBD and stabilized in a complete system by the OPM. The tongue dynamics do not virtually affect the chromophore environment in the dark state, but were shown to be necessary for the thermal stability of the full-length system. The tongue is also crucial for controlling the biochemical activity of the system by light. Spectroscopic measurements suggested that in a tongueless systems, light signal becomes trapped within the CBD, which prohibits (de)activation of the OPM. During the photocycle, the tongue was shown to be in action in all intermediate states using site-selective labeling and time-resolved vibrational spectroscopy. The profound characterization of the tongue properties and dynamics with biophysical as well as biochemical approaches in this thesis revealed that the tongue is a key component in phytochrome allostery.

Keywords: Allostery; enzymatic activity; histidine kinase; photosensor; protein modifications; spectroscopy.

Moona Kurttila, Nanoscience Center, University of Jyväskylä, Department of Bio and Environmental Science, P.O. Box 35, 40014, University of Jyväskylä, Finland

TIIVISTELMÄ

Kurttila, Moona

Jalalla koreasti valon tahtiin: bakteerifytokromin signaalinvälitysreitit
Jyväskylä: University of Jyväskylä, 2023, 81 s.
(JYU Dissertations
ISSN 2489-9003; 686)
ISBN 978-951-39-9713-7 (PDF)
Yhteenveto: Jalalla koreasti valon tahtiin: bakteerifytokromin signaalinvälitysreitit
Diss.

Fytokromit ovat punaista ja kaukopunaista valoa aistivia reseptoreja kasveissa, bakteereissa, levissä ja sienissä. Ne säätelevät eliöiden kasvua ja kehitystä ympäröivien valo-olosuhteiden mukaisesti kääntämällä muutoin solulle näkymättömän valosignaalin biokemialliseen muotoon ja auttavat siten eliötä sopeutumaan ympäristöönsä. Valoaktivoituminen alkaa proteiinin sisälle hautautuneesta kromoforista, jossa tapahtuu absorption seurauksena rakenteellinen muutos. Tästä seuraa rakennemuutoksia proteiinin muissa osissa, mitkä lopulta säätelevät biokemiallista aktiivisuutta. Tätä ominaisuutta voidaan hyödyntää myös optogeneettisissä sovelluksissa solun toimintojen keinotekoiseen säätelyyn valon avulla. Tässä väitöskirjatyössä syvennyttiin valoaktivoituvana fosfataasina toimivan *Deinococcus radiodurans* -bakteerin fytokromin toimintaan sekä signaalinvälitykseen. Muiden fytokromien tavoin se koostuu sensori- ja toiminnallisesta yksiköstä. Sensori rakentuu kromoforin sitovasta sekä fytokromi-spesifisestä osasta (PHY), joka yhdistää sensorin biokemiallisesti toiminnalliseen osaan. Lisäksi PHY-osa sisältää tämän työn keskiössä olevan erikoisen ulokkeen, joka kurottautuu lähelle kromoforia ja uudelleen laskostuu valosyklin myötä. Tässä työssä kehitettiin UV–vis spektroskopiaa hyödyntävä menetelmä PHY-ulokkeen dynaamisuuden määrittämiseen. Ulokkeen dynaamisuuteen vaikutti sen kytkeytyminen kromoforiin, ja kokopitkässä systeemissä toiminnallinen osa stabiloi sitä. Liikehdinnän osoitettiin kytkeytyvän lisääntyneeseen toiminnallisen osan aktiivisuuteen johtaen epäspesifiseen signalointiin perustilassa. Toisaalta ilman uloketta systeemin biokemiallista toimintaa ei voitu aktivoida valolla, luultavasti koska ilman sitä signaali ei etene kromoforin sitovasta osasta eteenpäin. Ulokkeen uudelleenlaskostumista valosyklin aikana tutkittiin aikaerotteisella värähdysspektroskopialla yhdistettynä paikkaspesifiseen reportterimolekyyliin. Uloke oli aktiivinen kaikissa valosyklin välitiloissa ja päätti muutoksensa yhtäaikaisesti kromoforin kanssa. Ulokkeen dynaamisten ominaisuuksien kuvaus ja niiden yhdistäminen biokemiallisen aktiivisuuden muutoksiin tässä työssä osoittivat, että uloke on yksi avainkomponenteissa fytokromin signaalinvälityksessä.

Avainsanat: Allosteria; enstyymiaktiivisuus; histidiinikinaasi; proteiinin muokkaukset; spektroskopia; valosensori.

Moona Kurttila, Nanotiedekeskus, Jyväskylän yliopisto, Bio- ja ympäristötieteiden laitos, PL 35, 40014, Jyväskylän yliopisto

Author's address Moona Kurttila
Nanoscience Center
Department of Biological and Environmental Science
P.O. Box 35
FI-40014 University of Jyväskylä
Finland
moona.k.m.kurttila@jyu.fi

Supervisors Prof. Janne Ihalainen
Nanoscience Center
Department of Biological and Environmental Science
P.O. Box 35
FI-40014 University of Jyväskylä
Finland

Dr. Heikki Takala
Nanoscience Center
Department of Biological and Environmental Science
P.O. Box 35
FI-40014 University of Jyväskylä
Finland

Reviewers Prof. Katrina Forest
Department of Bacteriology
The University of Wisconsin–Madison
Madison, WI
United States

Prof. Andreas Barth
Department of Biochemistry and Biophysics
Stockholm University
10691 Stockholm
Sweden

Opponent Prof. Klaas J. Hellingwerf
Swammerdam Institute for Life Sciences
University of Amsterdam
Science Park 904
1098 XH Amsterdam
The Netherlands

CONTENTS

ORIGINAL PUBLICATIONS

LIST OF ORIGINAL PUBLICATIONS

The thesis is based on the following publications which in the text are referred to by their Roman numerals I-IV.

I Rumfeldt J., Kurttila M., Takala, H. & Ihalainen J.A. 2021. The hairpin extension controls solvent access to the chromophore binding pocket in a bacterial phytochrome: a UV–vis absorption spectroscopy study. *Photochemical & Photobiological Sciences* 20: 1173–1181.

II Kurttila M., Etzl S., Rumfeldt J., Takala H., Galler N., Winkler A. & Ihalainen J.A. 2022. The structural effect between the output module and chromophore-binding domain is a two-way street via the hairpin extension. *Photochemical & Photobiological Sciences* 21: 1881–1894.

III Kurttila M., Rumfeldt J., Takala H. & Ihalainen J.A. 2023. The interconnecting hairpin extension "arm": an essential allosteric element of phytochrome activity. *Structure* 31: 1–9.

IV Kurttila M., Stucki-Buchli B., Rumfeldt J., Scroeder L., Häkkänen H., Liukkonen A., Takala H., Kottke T. & Ihalainen J.A. 2021. Site-by-site tracking of signal transduction in an azidophenylalanine-labeled bacteriophytochrome with step-scan FTIR spectroscopy. *Physical Chemistry Chemical Physics* 23: 5615–5628.

The author′s contribution to the original publications:

I The author planned the concept of the paper with J.R. and J.A.I., conducted part of the pH jump experiments and helped with data analysis.

II The author expressed and purified one of the sample systems, performed FTIR spectroscopy on all samples, planned and performed the kinetic activity assays on phosphatases. The cyclase activity assays and sequence conservation analysis were performed by N.G. and A.W., respectively. The author prepared the figures (all except Fig. 5) and wrote the manuscript together with J.A.I. and A.W.

III The author cloned one of the construct (others and overall design done by H.T.), expressed and purified all tongueless systems, performed all activity assays except for apoprotein (by H.T) and all spectroscopic measurements except for temperature dependent UV-vis (by J.R.) and dark reversion of wild-type systems (by J.A.I.). The author crystallized the PSM tongueless and collected the diffraction data with H.T, who solved the crystal structure. The author had the main responsibility of data analysis supported by J.A.I and J.R. The author did the majority of writing and prepared all the graphics.

IV The author planned the research with B.S-B. and J.A.I., performed the research with other authors, analyzed the data with J.R., T.K. and J.A.I, wrote the paper with T.K. and J.A.I., and prepared all the graphics.

ABBREVIATIONS

Agp1	phytochrome 1 from *Agrobacterium fabrum*
BphP	bacterial phytochrome protein
BV	biliverdin IXα
CBD	chromophore-binding domain
CD	circular dichroism
Cph1	phytochrome from cyanobacterium *Synechocystis* sp. strain PCC6803
*Dr*BphP	bacterial phytochrome from *Deinococcus radiodurans*
*Dr*PSM	photosensory module of *Dr*BphP
DrRR	response regulator of *Dr*BphP
FL	full-length
FTIR	Fourier-transform infra-red
GAF	cGMP phosphodiesterase/adenylate cyclase/FhlA
HK	histidine kinase
IR	infrared
OPM	output module
PaaC	phytochrome-activated adenylate cyclase
PAS	Pern/Arnt/Single-minded
pAzF	p-azidophenylalanine
Pfr	far-red light absorbing state of phytochromes
PHY	phytochrome specific (domain)
Pr	red light absorbing state of phytochromes
PSM	photosensory module
p-RR	phosphorylated response regulator
RR	response regulator
SADS	species-associated difference spectrum
T_m	melting temperature
UV–vis	ultaviolet–visible
WT	wild-type

1 INTRODUCTION

All living systems must adapt to their ambient environment. One of the factors affecting the growth and development in almost all living systems is light. Perception of light in cells requires special tools that can convert light signals into biochemical signaling cascades. These tools are called photosensors that bind a ligand, a light absorbing chromophore, which makes them specific for particular wavelengths of light (Fraikin *et al.*, 2013)). The response to light absorption by the choromophore results in changes in the structure and dynamics, or "jiggling and wiggling" of atoms (Feynman *et al.* 1963), which ultimately alter the biochemical activity of the system. In nature, a combination of different photoreceptors covers the visible light spectrum and thus allows organisms to respond to multiple environmental cues like time of the day or year, or leaf canopy (Möglich *et al.* 2010). Furthermore, applicability of photosensors have created a new field of optogenetics, where natural photoreceptors are engineered and modified for spatiotemporal and non-invasive control of cellular events by light. This field is rapidly growing and requires profound understanding of function and allosteric mechanisms of photosensors (Ziegler and Möglich 2015).

Phytochromes are a family of red and far-red light sensing photoreceptors found in plants, bacteria, fungi, and algae. In plants, they control for example seed germination and shade avoidance (Quail 2002). The effect of phytochromes can be observed, for example, as seedlings that grow towards the sun, or in a uniform sunflower field where all flowers are the same height. Different phytochromes use a variety of effector modules, which allows regulation of multiple cellular events (Rockwell and Lagarias 2010). On the contrary, the photosensory module of phytochromes is relatively conserved across species. Therefore, bacterial phytochromes (BphP) serve as excellent model systems for plant phytochromes which are more difficult to produce in amounts required for research purposes. Phytochrome research can increase our understanding of plant physiology and growth regulation, which can be beneficial also for example to agriculture during the progressing climate crisis.

Due to their light-absorbing and structural properties, BphPs hold enormous potential for optogenetic applications to control desired cellular events with light. However, any applications or engineering of phytochromes require basic understanding of the dynamics, photocycle and allostery of the system. Phytochromes can, in principle, switch eternally between the two distinguishable, red and far-red absorbing, states. Therefore, they are also excellent model systems to study structure-function relationships of proteins in general. Therefore, phytochrome research can help us understand the tips and turns of nature in many ways.

This thesis enlightens the dynamics and regulation of the output activity in a bacterial phytochrome. The central focus is in the role and dynamics of an intriguing hairpin extension in the photosensory module, also called the "tongue". Although the amino acid sequence is said to determine the secondary structural fold of the protein, the tongue changes its fold upon photoactivation (Takala *et al.* 2014a). The tongue extends from a distinct part of the protein to the vicinity of the chromophore. This thesis combines structural modifications of the protein to a variety of spectroscopic techniques and biochemical activity assays, which together enable describing the dynamics of the tongue within the resting state, site-specific changes during the photocycle, and finally the role of the tongue in coupling the light-sensing chromophore site and the effector site to control the biochemical activity.

2 LITERATURE REVIEW

2.1 Light sensing in nature

2.1.1 Photosensors

Light is electromagnetic radiation, emitted by the sun in nature. The solar spectrum includes the visible range of light (380-740 nm) accompanied by ultraviolet (UV) and infrared (IR) light at the blue and red end of the spectrum, respectively (Fig. 1). The energy of a photon is defined by the wavelength; the shorter the wavelength, the higher the energy the photon has. Light is used as the energy source in photosynthesis but it is also a factor that affects growth, development or behaviour in almost all living systems. In nature, the total and relative amount of different wavelengths of light vary depending on the time of the day and for example the canopy. Therefore, that cannot move, in particular plants, must adapt to their ambient light environment (Millar 2003, Chen *et al.* 2004, Rodriguez-Romero *et al.* 2010). Living organisms use a set of photosensors to perceive light and to translate light signals into biochemical signaling cascades in cells (Fig. 1).

Detection of light requires a light absorbing chromophore, and as they absorb particular wavelengths of visible light, chromophores play a key role in making photoreceptors functional (Möglich and Moffat 2010). Photoreceptors use variety of chromophores that respond to light with different photochemical mechamisms. In bilin chromophores of phytochromes and retinal of rhodopsins, a *cis-trans* isomerization of the double C=C bond occurs (Sharrock 2008, Nogly *et al.* 2018). The function of flavin-based chromophores relies on charge transfer reactions in cryptochromes and blue-light sensors using flavin (BLUF) (Losi and Gärtner 2012), and on formation of a covalent bond with cysteine residue in light-oxygen-voltage (LOV) sensing domains (Polverini *et al.* 2020). The plant UVR8 photoreceptors do not bind an external cofactor but instead use coordinated tryptophans as UV-light absorbing chromophores where electron transfer chain ultimately leads to monomerization of the UVR8 dimer (Jenkins 2014, Li *et al.* 2022b). Together different photoreceptors cover the whole visible light spec-

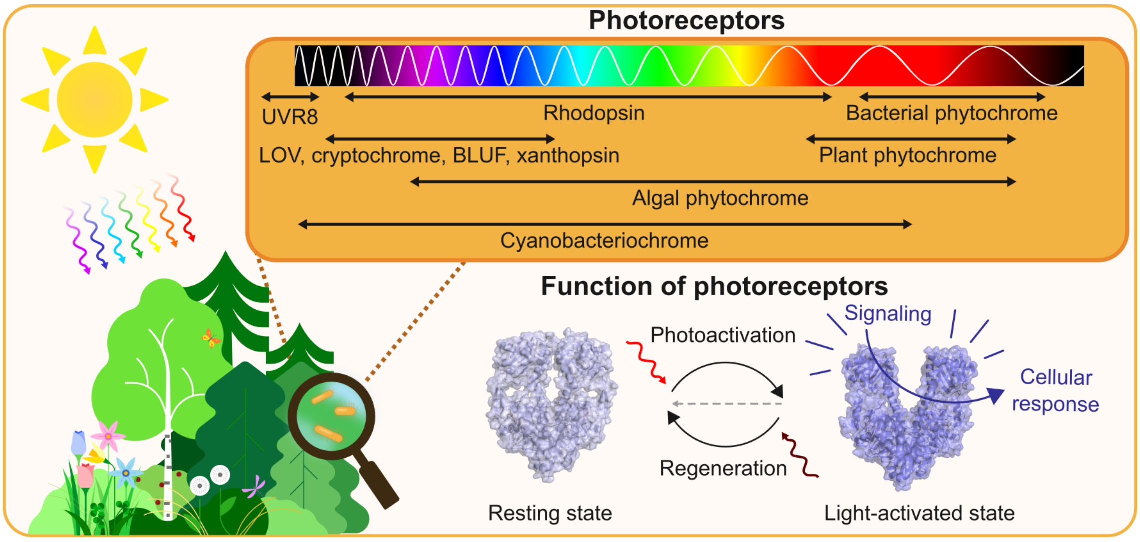

FIGURE 1 Combination of different photoreceptors found in plants, bacteria, and algae covers the whole visible range of light spectrum. In general, absorption of light results in photoactivation of the photoreceptor, and ultimately in a cellular response. Some systems return to resting state by absorption of a different wavelength of light or through thermal reversion in darkness (grey dashed line). Abbreviations: light-oxygen-voltage (LOV); blue light sensor using flavin (BLUF); UV RESISTANCE LOCUS8 (UVR8).

trum, and a combination of multiple photoreceptors allows organisms to respond to the changing light conditions. Different plant and bacterial photoreceptors with their respective light detection range is presented in Figure 1.

Photoreceptors often consist of a light-detecting sensory module which binds the chromophore ligand and is structurally coupled to a biochemically active output module (OPM) triggering the cellular response (Ziegler and Möglich 2015). Photoreceptors are allosteric systems where photon absorption by the chromophore results in perturbation at an allosteric chromophore binding site and alterations in the structure and dynamics of the photoreceptor (Nussinov and Tsai 2013). Ultimately, the system is driven into a light-activated state where the biochemical activity or molecular interactions of the OPM become altered at the functional site (Hellingwerf 2000). As a result, a cellular response, for example to transcription of a specific gene, is triggered according to the ambient light environment (Fig. 1). For example, bacterial phytochromes, which are the main focus of this thesis, often function as histidine kinases in two-component signalling performing (de)phosphorylation of their cognate response regulators (RR) (Bhoo *et al.* 2001, Karniol and Vierstra 2003). In some photosensors the photocycle is reversible, i.e. they can return to the resting state either by absorption of another wavelength of light or by thermal reversion (Fig. 1) (Sharrock 2008).

2.1.2 Red light-sensing phytochromes

The effect of light on plant seeding and growth has been an interest for a long time. Already back in 1935, Flint and McAlister discovered that lettuce seed germination is promoted by red light. Later, far-red light was shown to stop the germination and withdraw the red-light initiated effect, which suggested that plants include a reversible photoresponsive system (Borthwick *et al.* 1952). These observations were rationalized in 1959, when Butler *et al.* spectroscopically identified a red and far-red light absorbing pigment system, named phytochrome. During the 1960s and 1970s the phytochrome responses in plants as well as related chromophores were studied (e.g. Lane *et al.* 1963, Linschitz and Kasche 1966, Krauss *et al.* 1980), and in 1983 the first phytochrome from oat was successfully purified (Vierstra and Quail 1983). The primary sequence from the same phytochrome species was determined only two years later (Hershey *et al.* 1985). These breakthroughs allowed for a more thorough study of the spectroscopic properties of phytochromes as well as sequence comparison of phytochromes from different species.

In plants, phytochromes control for example seed germination, shade avoidance, flowering and plant architecture (reviewed in Franklin and Quail 2010), meaning that phytochromes play a major role in controlling the growth and development of all green vegetation on Earth. In seed plants, phytochromes with distinct functions exist, and they fall into three clades: *PHYA*, *PHYB/E*, and *PHYC* (Mathews 2010). The most studied model system from plant phytochromes is *Arabidopsis thaliana*, which has five different phytochromes (*At*PhyA–PhyE) with different functions (Quail 2002, Legris *et al.* 2019). PhyB has been show to control shade avoidance (Franklin 2008), to entrain the circadian rhythms together with a cryptochorome and UV-B receptor (Fankhauser and Staiger 2002, Millar 2004), and to promote seed germination in tandem with PhyA or PhyE, depending on the temperature (Heschel *et al.* 2007). In plant phytochromes, the light signal often results in transcriptional reprogramming of the system through interactions directly with transcriptional factors or with other transcription-regulating proteins (Leivar and Monte 2014, Legris *et al.* 2019).

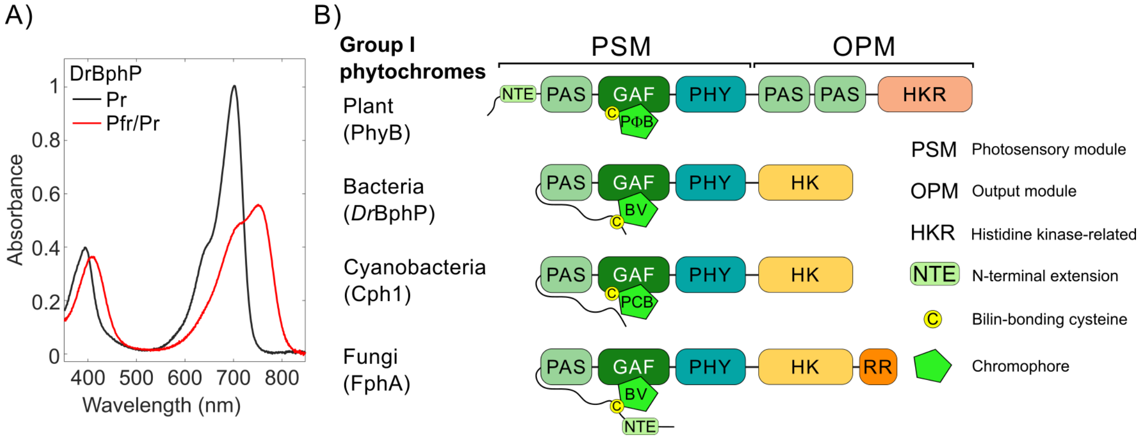

FIGURE 2 Absorption and modular structure of phytochromes. A) Phytochromes absorb red and far-red light, which is shown in the absorption spectrum under far-red light or darkness (black, Pr state), and under red light (red, Pfr-state). The absorption maxima are tuned by the chromophore and its environment depending on the species. B) The usual modular structure of group I phytochromes with example from each kingdom.

Initially, phytochromes were thought to exist only in plants. However, in 1996, the genome of cyanobacterium *Synechocystis* sp. strain PCC6803 was reported, revealing a sequence of a phytochrome-like protein among other plant related genes (Kaneko *et al.* 1996). In 1997, a recombinant protein from the same gene was expressed in *Escherichia coli* and purified (Hughes *et al.* 1997). After addition of a bilin chromophore, a photo-switchable prokaryotic phytochrome was revealed and shown to function as a light regulated histidine kinase, nowadays known as Cph1 (Yeh *et al.* 1997). Soon after, the knowledge of existing phytochromes was expanded to bacterial phytochromes (BphP) with red and far-red sensitivity, also in non-photosyntetic organisms *Deinococcus radiodurans* and *Pseudomonas aeruginosa* (Davis *et al.* 1999) (Fig. 2A). In addition to cyanobacteria, other photosynthetic bacteria can have phytochromes to control the synthesis of photosynthetic apparatus (Giraud *et al.* 2002). Today, phytochromes are known to exist also in fungi (Blumenstein *et al.* 2005) and algae where the absorption properties cover nearly the whole visible spectrum (Rockwell *et al.* 2014) (Fig. 1). Cyanobacteriochromes are distantly phytochrome-related photoreceptors that also bind a bilin chromophore but their absorption spans the whole UV–visible spectrum (Yoshihara *et al.* 2004).

The domain composition of phytochromes has proven to be very similar in all group I phytochromes where the photosensory module (PSM) consists of three domains: PAS (Per/Arnt/Sim), GAF (cGMP phosphodiesterase/adenylyl cyclase /Fhl1), which together form the chromophore binding domain (CBD), and PHY (phytochrome-specific) (Fig. 2) (Rockwell and Lagarias 2020). The group includes plant, bacterial, cyanobacterial and fungal phytochromes. Different species use different output modules (OPM), and thus molecular sizes vary from 80 kDa in bacterial phytochromes to 120 kDa in plant and even 200 kDa in fungal phytochromes (Rockwell and Lagarias 2010). PAS-less phytochromes phytochromes, like Cph2, belong to group II (Anders *et al.* 2011), and cyanobacteriochromes with less conserved PSM composition form the group III (Fushimi and Narikawa 2019).

All phytochromes bind a tetrapyrrole bilin chromophore through a covalent thioether linkage between the bilin A-ring vinyl side chain and a cysteine, but the attachment site and type of bilin vary between species (Fig. 2) (Rockwell and Lagarias 2006). In plant and cyanobacterial phytochromes, the cysteine is located in GAF domain but the bilin is differs: in plants, the chromophore is phytochromobilin (PΦB) (Kohchi *et al.* 2001), and in cyanobacteria phycocyanobilin (PCB) (Frankenberg *et al.* 2001). Bacterial as well as fungal phytochromes use biliverdin IXα (BV) that binds to a cysteine in PAS domain (Bhoo *et al.* 2001, Giraud *et al.* 2002, Lamparter *et al.* 2003, Blumenstein *et al.* 2005). Some phytochromes include an N-terminal extension (NTE) suggested to play a role in signal transduction (Escobar *et al.* 2017).

The largest variation between phytochrome species lies in their OPM. Many prokaryotic phytochromes have histidine kinase (HK) as their OPM (Quail 1997), whereas plant phytochromes have a histidine kinase-related OPM and function as serine/threonine kinases (Yeh and Lagarias 1998). Prokaryotic phytochromes are recombinantly expressed and purified more easily than the eukaryotic ones, which is a great advance in studying their functional and structural properties.

The similar PSM composition has allowed the use of, prokaryotic phytochromes as a model systems to understand the molecular mechanisms of signal transduction in higher phytochromes as well.

2.2 Structure of bacterial phytochromes

Phytochromes are modular homodimeric proteins where the protomers are organized either in parallel (Yang *et al.* 2008, Li *et al.* 2010, Takala *et al.* 2014a) or antiparallel (Essen *et al.* 2008, Mailliet *et al.* 2011, Bellini and Papiz 2012), and the dimerization is dictated by interactions of helices that extend from GAF to PHY, and from PHY to OPM forming the so-called helical spine of the system (Fig. 3A) (Li *et al.* 2010, Ulijasz and Vierstra 2011, Auldridge *et al.* 2012, Burgie and Vierstra 2014, Takala *et al.* 2014b). During the 21st century, the amount of structural data has expanded greatly from structures of CBD (Wagner *et al.* 2005, 2007) to photosensory modules in resting (Essen *et al.* 2008, Yang *et al.* 2008) and illuminated states (Takala *et al.* 2014a, Burgie *et al.* 2016), to full-length structures of different BphPs (Bellini and Papiz 2012, Otero *et al.* 2016, Gourinchas *et al.* 2017, Etzl *et al.* 2018), and finally to a full-length cryo-EM structures of a BphP with HK output module in Pr and Pfr states (Wahlgren *et al.* 2022).

The so-called CBD is the smallest photoswitchable fragment of phytochromes. The first crystal structures of CBD of a BphP from *Deinococcus radiodurans* (*Dr*BphP) revealed the general organization of CBD as well as the interactions of BV with the chromophore binding pocket in the Pr state (Wagner *et al.* 2005, 2007). An interesting feature found was the knot formed by PAS and GAF domains (Wagner *et al.* 2005). There, a mostly random coil segment of PAS goes through a loop from the GAF domain (Fig. 3B). The role of the knot is not yet well understood as also

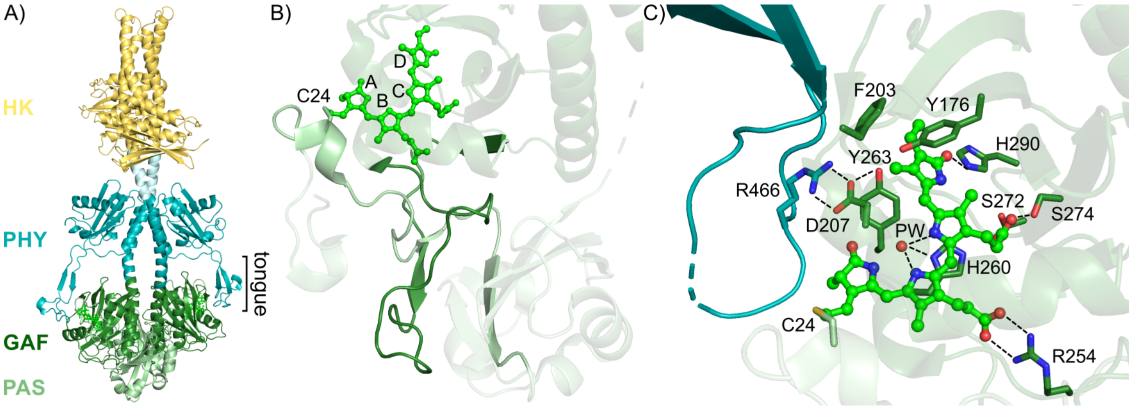

FIGURE 3 Structural organization of *Dr*BphP A) The secondary structure cartoon representation of *Dr*BphP from the model created by Björling *et al.* (2016). B) In CBD, a knot between the PAS and GAF is formed. The N-terminal PAS (pale green) has a covalent bond with BV at C24 after which the domain proceeds through a loop from the GAF domain (dark green). C) The interactions of the chromophore binding pocket. PDB: in panels B and C 5K5B (CBD) and 4O0P (tongue, in cyan)

knotless phytochromes exist (Gan *et al.* 2014, Xu *et al.* 2020). Although BV covalently binds to the cysteine close to the N-terminus in PAS (at C24 in *Dr*BphP), it forms multitude of weak interactions with the residues in the chromophore binding pocket inside the GAF cleft (Fig. 3C). In Pr state, the residues F203 and Y176 (*Dr*BphP numbering) form a hydrophobic pocket for the BV D-ring that additionally forms a hydrogen bond (H-bond) with H290 (Van Thor *et al.* 2007). The propionates of the C- and B-ring are stabilized with H-bonds with S272 and S274, and in the latter with R254, which is part of the knot sequence. Coordinated by the pyrrole rings of BV, a special water molecule termed pyrrole water is found in the center of the chromophore. This pyrrole water forms bonds with the NH-groups of the rings as well as with H260 that is in a different plane than BV (Burgie *et al.* 2014a).

In the PSM, the PHY domain extends from the GAF domain and forms an additional connection with CBD via an extension, a hairpin, often referred to as a "tongue" (Fig. 3C) (Essen *et al.* 2008). The first two structures of bacterial PSM from different species were published in the same issue, but with differently folded tongues (Essen *et al.* 2008, Yang *et al.* 2008). In the prototypical Cph1 in Pr, the tongue is folded in a β-sheet (Essen *et al.* 2008), fold shown in Figure 3, and in the Pfr state of a bathy system, the tongue has an α-helical fold (Yang *et al.* 2008). Therefore, a question if the folding of the tongue is species or state dependent was left open.

For dimerization, important interactions are formed in in the CBD-unit as well as in the OPM (Li *et al.* 2010, Auldridge *et al.* 2012, Bellini and Papiz 2012, Takala *et al.* 2015, Otero *et al.* 2016, Gourinchas *et al.* 2017, Etzl *et al.* 2018, Wahlgren *et al.* 2022) (Fig. 3A). The interactions between the OPM monomers can be necessary for the function (Otero *et al.* 2016, Gourinchas *et al.* 2018, Kumarapperuma *et al.* 2023). The complete crystal structures of HK bearing BphPs are still lacking to date, most probably due to long helical sections often included in HKs (Bhate *et al.* 2015). The recent cryo-EM structures of *Dr*BphP required linking the RR to the HK, and still the system was so dynamic or heterogenous that the OPM of the structure is poorly resolved (Wahlgren *et al.* 2022).

2.3 Function of phytochromes

2.3.1 The two metastable states

Phytochromes have two metastable states, the red light absorbing Pr state and the far-red light absorbing Pfr state between which phytochromes can switch reversibly (Fig. 4). Upon photoconversion, the structural features of the chromophore are altered, meaning that light can be used to switch the activity. Alternatively, the system can return to the resting state thermally in darkness. Most phytochromes are prototypical where the Pr state, often also referred as the dark state, is the resting state as described in Figure 4. However, some phytochromes are bathy phytochromes, and they thermally revert to Pfr state (Giraud *et al.* 2002, Karniol and Vierstra 2003).

The Pr and Pfr states are most often defined by the conformation of BV. In

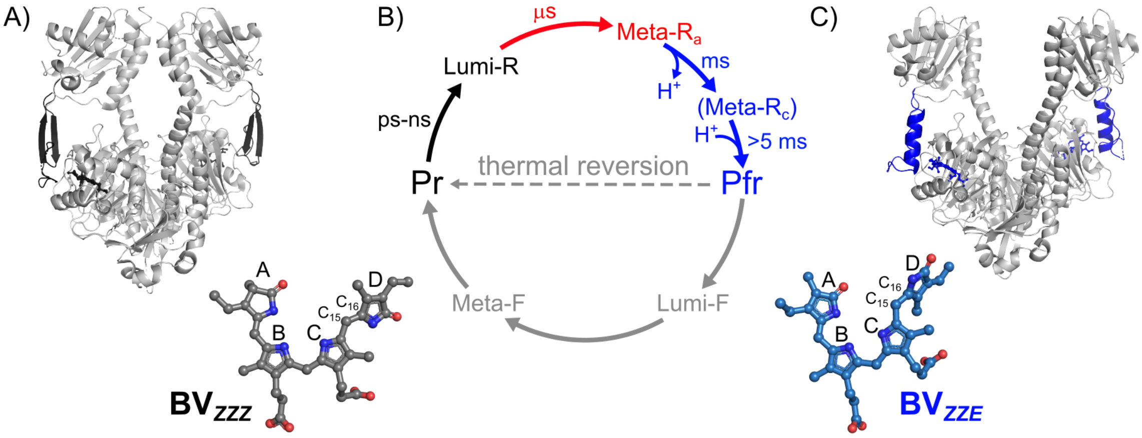

FIGURE 4 Photocycle of prototypical phtochromes. A) In Pr, the biliverdin (BV, ball-and-sticks) is in ZZZ conformation, the rings are indicated with letters. The overall structure of PSM is shown, the tongue conformation shown in black. (PDB: 4O0P) B) The intermediate states and their approximate time scales. The Meta-R state can be devided into two in case photocycle includes proton release and uptake. C) In Pf state, the D-ring of BV has flipped at the C_{15}=C_{16} double bond. Ultimately, this leads to structural rearrangement of the PSM where the tongue refolding to α-helix is shown in blue. (PDB:5C5K)

Pr state, the chromophore is in ZZZ conformation, and in Pfr ZZE conformation due to isomerization of C15=C16 double bond (Fig. 4) (Hahn *et al.* 2008, Yang *et al.* 2011, Song *et al.* 2013). The isomerization results in rotation of the chromophore D-ring, which alters the interactions in the chromophore binding pocket, and ultimately the biochemical activity of the system (Gourinchas *et al.* 2018, Wahlgren *et al.* 2022).

The most characteristic structural change of phytochromes is refolding of the tongue upon photoconversion (Fig. 4) (Takala *et al.* 2014a). In Pr state, the tongue folds into a β-sheet, and in Pfr it adopts an α-helical fold (Takala *et al.* 2014a). Based on the crystal structures, a large secondary structural difference signal in FTIR spectra has been interpreted as refolding of the tongue in BphPs (Stojković *et al.* 2014, Xu *et al.* 2020). The refolding of the tongue has also been observed by NMR (Gustavsson *et al.* 2020).

The isomerization of the chromophore results in structural rearrangements in the chromophore binding pocket, which have been observed in crystal structures from Pr and Pfr states (Takala *et al.* 2014a, Burgie *et al.* 2016). As the D-ring rotates, the interactions in Pr are modified (Fig. 5). The aromatic F203 and Y176 are forced to change their side chain orientation, and the latter forms an H-bond with the C-ring propionate. H201, pointing away from the chromophore in Pr, flips towards the D-ring in Pfr to stabilize the BV conformation after isomerization. The tongue refolding also alters the interactions between the CBD and the tongue: D207 bonds with S468 in Pfr instead of R466, both of which are residues from the conserved PRXSF motif. The residue Y263 strengthens the interactions between CBD and the tongue. In Pr, the Y263F mutation results in decoupling between the chromophore and tongue, which leads to α-helical fold despite the

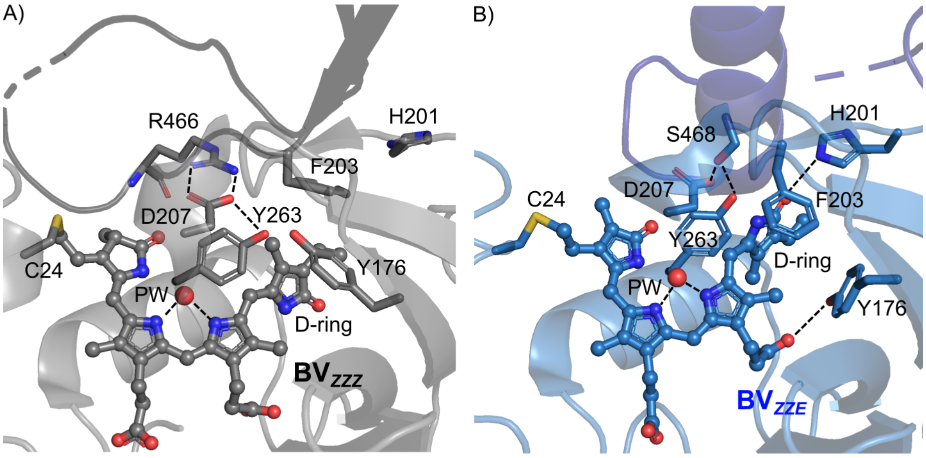

FIGURE 5 Reorganization of the chromophore binding pocket A) In Pr, the BV (ball-and-sticks) is in ZZZ conformation, some of the binding pocket residues are shown in sticks. The pyrrole water (PW) is coordinated in the center of BV. (PDB: 4Q0H (CBD), tongue from 4O0P). B) In the Pfr state, the D-ring of BV has flipped, resulting in structural rearrangements in BV binding pocket. The refolded tongue in α-helix is shown also in PSM (PDB: 5C5K).

ZZZ conformation of the chromophore (Takala *et al.* 2018). The pyrrole water remains in the approximately same position, although it has been suggested to dissociate early in the photocycle (Claesson *et al.* 2020).

Structural data reveal the atomic organization of the system, and are almost essential for unraveling the molecular mechanisms of signal transduction. However, photoswitchable phytochromes are also excellent systems to study with various spectroscopic methods. Spectroscopic measurements are usually performed in solution where dynamics of the protein can be captured. Spectroscopic data can be used to complement structural data or to study the absorption properties of the system upon structural modifications. For example 2D IR is a complex but powerful tool capture intramolecular dynamics and interactions. With 2D IR, the D-ring in the Pr state has been shown to exhibit at least two different H-bonding environments (Chenchiliyan *et al.* 2023), and an α-helical tongue to stabilize the chromophore in Pfr through dipole coupling (Buhrke *et al.* 2022). Further, chromophore protonation states are accessible with spectroscopic methods (Van Thor *et al.* 2005, Rumfeldt *et al.* 2019).

Thermal reversion from Pfr to Pr (or *vice versa* in bathy systems) can also be studied spectroscopically. The dark reversion rates vary from minutes to days, depending on the species, possible modifications of the protein subunits or single sites, and the temperature (Lamparter *et al.* 2002, Medzihradszky *et al.* 2013, Takala *et al.* 2014b, Legris *et al.* 2016). The mechanism of dark reversion is not yet well understood. Yet, in phytochrome research, the dark reversion rate affects they way experiments can successfully be conducted. Under constant illumination, phytochromes are in a photoequilibrium in a certain Pr/Pfr ratio. During illumination, the equilibrium is maintained by the system continuously converting between the two states. Therefore, for example resolving an illuminated-state crystal structure requires relatively slow dark reversion so that decent population can be driven and stays in the Pfr state long enough to form crystals. This is the case for *Dr*PSM, the system from which the illuminated state crystal structure was first solved (Takala *et al.* 2014a). By introducing a mutation slowing the reversion even more, a second crystal structure with more resolved changes in comparison to the dark state was solved (Burgie *et al.* 2016).

Ultimately the photoactivation results in regulation of the output activity. Even so, BphPs still lack a complete structural model of the molecular mechanisms behind the output activation. X-ray solution scattering studies on *Dr*BphP have proposed a 'rotation' model where the OPM slightly rotates relative to PSM upon light activation (Björling *et al.* 2016). This model is supported by observed activation mechanisms in other histidine kinase systems (Jacob-Dubuisson *et al.* 2018). Moreover, rearrangements in HK domains observed using spin labels (Kacprzak *et al.* 2017) and recently determined high resolution cryo-EM structures of dark and illuminated states of BphP support the 'rotation' model (Wahlgren *et al.* 2022). The cryo-EM structures revealed a small divergence in the helices extending from PHY to HK and increased asymmetry and disorder in the HK domains in Pfr. These structures overtook the previously proposed model, based on low-resolution cryo-EM structures with complete opening of the HK domains (Burgie *et al.* 2014b, Burgie and Vierstra 2014). The mechanisms seem to vary between species, possibly also depending on the output activity. A 'register switching' model has been proposed for a BphP from *Idiomariana* with adenylate cyclase activity (Gourinchas *et al.* 2018). Their crystal structures proposed asymmetric activation of the dimer, observed in the PSM protomers, resulting rearrangement of the coiled-coil helix to a different register at the sensor-OPM interface (Gourinchas *et al.* 2017).

2.3.2 Intermediate states of the photocycle

In translation of a photosignal into biochemical signal in a cell, the signal must propagate a distance of over 7 nm from the chromophore binding pocket to the active site in the OPM. The photocycle from Pr to Pfr, or *vice versa*, proceeds through at least two intermediate states: Lumi-R (Lumi-F in the reverse direction) and Meta-R (Meta-F) (Fig. 4) (Linschitz and Kasche 1966, Eilfeld and Rüdiger 1985, Van Thor *et al.* 2001, Borucki *et al.* 2005, Mroginski *et al.* 2007, Song *et al.* 2013, Ihalainen *et al.* 2018, Kübel *et al.* 2021). Time-resolved (Piwowarski *et al.* 2010, Ihalainen *et al.* 2018) and ultrafast spectroscopy (Sineshchekov 1995, Van Thor *et al.* 2007, Ihalainen *et al.* 2015), time-resolved X-ray crystallography (Claesson *et al.* 2020, Carrillo *et al.* 2021), X-ray solution scattering (Takala *et al.* 2014a, Björling *et al.* 2016) as well as cryo-trapping of the intermediate states for spectroscopy (Foerstendorf *et al.* 1996, 2001, Borucki *et al.* 2005, Rohmer *et al.* 2010) and structural data (Yang *et al.* 2011, Woitowich *et al.* 2018) have been used to understand the molecular mechanisms and time scales of the photocycle in various phytochromes. The full photocycle from Pr to Pfr state can take 1-1000 ms to complete, depending on the system (Van Thor *et al.* 2001, Björling *et al.* 2016). The back reaction via Lumi-F and Meta-F follows a different molecular mechanism (Foerstendorf *et al.* 1996) Here, the forward Pr to Pfr reaction is reviewed.

The photocycle is initiated by a photon absorption by the chromophore after which, the chromophore is excited to a higher energy state. The excited state is short lived (picoseconds), and has three probable outcomes. The chromophore can either return to the ground state by (1) non-radiative relaxation or (2) fluorescence. Absorption can also result in (3) isomerization of the D-ring, which drives the system into the first phase of photocycle, Pr to Lumi-R transition (Heyne *et al.* 2002). The Lumi-R state is reached within pico to nanoseconds (Schumann *et al.* 2007, Toh *et al.* 2011, Lenngren *et al.* 2018). The quantum yield of Pr to Pfr photoreaction is mainly defined by the gateway reaction from Pr to Lumi-R, although in some species a back reaction from Lumi-R to Pr can be observed after 100 ns (Mathes *et al.* 2015). The isomerization results in new hydrogen bonding networks around the chromophore and rather small changes in the secondary structures, already in Lumi-R state (Foerstendorf *et al.* 1996, Toh *et al.* 2011, Ihalainen *et al.* 2018, Carrillo *et al.* 2021).

The Lumi-R state decays thermally to Meta-R state in microseconds (Van Thor *et al.* 2001, Borucki *et al.* 2005, Björling *et al.* 2016). In some bacterial systems, like in Cph1 and Agp1, the Meta-R state is divided into Meta-R_a and Meta-R_c, which include proton release and uptake by the chromophore, respectively (Van Thor *et al.* 2001, Borucki *et al.* 2005). This mechanism has not been shown to take place in *Dr*BphP which also has a faster photocycle (< 5ms) in comparison to Cph1 and Agp1 (>100 ms) (Björling *et al.* 2016, Ihalainen *et al.* 2018). However, in all those systems, the chromophore is fully protonated in both Pr and Pfr states (Song *et al.* 2013, Velazquez Escobar *et al.* 2015, Modi *et al.* 2019). The largest structural rearrangements in the protein moiety have been suggested to take place during the Meta-R_c (or Meta-R) to Pfr transition where the photoactivated state becomes finalized (Ihalainen *et al.* 2018, Björling *et al.* 2016, Kraskov *et al.* 2020).

2.4 Biochemical activity of phytochromes

2.4.1 Bacteriophytochromes in two-component signalling

Two-component sensor HKs are allosteric components that play a central role in adaptation to environmental factors in prokaryotes (West and Stock 2001). HKs are often membrane bound systems paired with a variety of multi-domain sensory modules (Bhate *et al.* 2015). These sensory modules include at least one allosteric site which perceives environmental stimuli and transduces the signal to the the functional site in HK initiating (de)phosphorylation of its cognate RR (Fig. 6). As a second component of the signaling cascade, the RR usually triggers the cellular response by regulating the transcription of associated genes (Zschiedrich *et al.* 2016). Most prokaryotic phytochromes have a HK output module and in they act as red light sensors in two-component signalling (Quail 1997).

Kinase activity involves ATP-dependent autophosphorylation of a catalytic histidine in DHp (dimerization histidine phosphotransfer domain) (Casino and Miguel-Romero 2014). This requires interaction between the acidic residue next to the catalytic histidine (H+1) of DHp and an asparagine in N-box of CA (catalytic ATP-binding) domain (Multamäki *et al.* 2021). In two BphPs from *R. palustris*, the autophosphorylation occurs between the protomers (*trans*) and is light-dependent (Kumarapperuma *et al.* 2023). The autophosporylation is followed

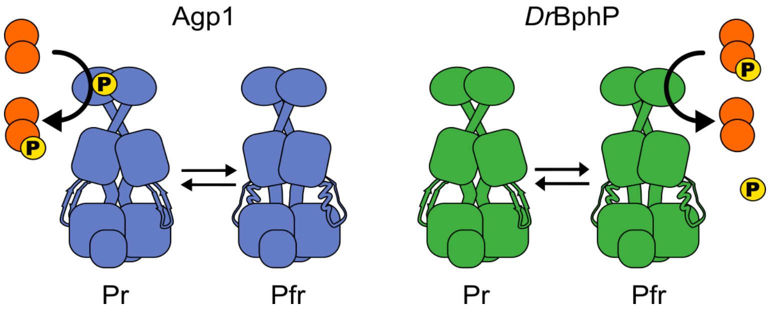

FIGURE 6 Activity of BphPs from *A. fabrum* (Agp1) and *D. radiodurans Dr*BphP. Agp1 is a red light suppressed kinase that that phosphorylates it cognate response regulator (RR, in orange). *Dr*BphP is a light activated phophatase cleaves off the phosphate from its RR.

by phosphotransfer reaction where the phosphate is transferred to a conserved aspartate of the receiver domain of an RR. The RR binds to the HK OPM and catalyzes its phosphotrasfer reaction (West and Stock 2001, Herrou *et al.* 2017, Multamäki *et al.* 2021). HKs usually also act as phosphatases that cleave off the phosphate from the phosphorylated RR (p-RR) by hydrolyzing the phospho-aspartyl bond (Goulian 2010).

Genetic analysis has revealed HK-like output modules in prokaryotic phytochromes (Hughes *et al.* 1997, Quail 1997), and kinase activity in different light conditions has been confirmed with radiolabeled kinase assay (Yeh *et al.* 1997, Lamparter *et al.* 2002). With this method, phytochromes with light suppressed (Yeh *et al.* 1997, Lamparter *et al.* 2002, Giraud *et al.* 2005, Baker *et al.* 2016) (Fig. 6) and light induced (Bhoo *et al.* 2001, Karniol and Vierstra 2003) kinase activity have been shown to exist. Despite extensive efforts, the output activity of the common model phytochrome *Dr*BphP was not revealed until recently (Multamäki *et al.* 2021). Multamäki *et al.* adopted a phosphorylation assay from McCleary and Stock (1994) to pre-phosphorylate RRs, and applied PhosTag gels to detect mobility of p-RR and non-phosphorylated RR. With this method, they revealed the light activated phosphatase activity of *Dr*BphP by demonstrating the disappearance of phosphorylated cognate RR (Fig. 6).

In addition to HK, HK-RR pairs (Jaubert *et al.* 2007), other types of OPMs are found from BphPs (Auldridge and Forest 2011). BphPs with GGDEF and EAL domain (names derived from key amino acids) can act as diguanylate cyclases or phosphodiesterases and they regulate the cyclic-dimeric-GMP levels in the cell (Galperin *et al.* 2001, Tarutina *et al.* 2006, Gourinchas *et al.* 2017, Böhm *et al.* 2022). PAS domains in the C-terminal OPM do not have any predicted enzymatic activity and therefore most probably mediate protein-protein interactions (Giraud *et al.* 2002, Möglich *et al.* 2009, Otero *et al.* 2016).

2.4.2 Applications and potential of bacteriophytochromes

Bacterial phytochromes have many properties that make them applicable fluorescent probes and optogenetic tools, especially in mammalian systems. In optogenetics, sensory photoreceptors are harnessed to control cellular processes by light. Fluorescent probes are used in non-invasive *in vivo* imaging in cells and tissues (Fischer and Lagarias 2004). The advantages of BphPs include the BV chromophore, which is readily available from heme degradation (Kapitulnik and Maines 2012). The absorption of BV in BphP is the most red shifted in comparison to other photosensors (Fig. 1). Red and near IR (NIR) light scatter relatively little and therefore penetrate deeper into tissue where the effect is initiated (Jacques 2013). Phytochromes can also be photoactivated by two-photon absorption where absorption of two lower energy photons results in the same effect as one with higher energy (here a red light) photon (Sokolovski *et al.* 2021) so even IR light could be used. In phytochromes, the activity can be reversibly controlled with two distinct wavelengths, and therefore the effect can be deactivated and reactivated. The thermal reversion rate to ground state can be modified to either sustain or diminish the effect (Burgie *et al.* 2014b). The modular sensor-effector structure of phytochromes gives great advantage for defining of the desired output activity. A variety of different native output modules already exist (Gourinchas *et al.* 2019), and artificial systems have also been successfully created (Etzl *et al.* 2018, Multamäki *et al.* 2021, Multamäki *et al.* 2022).

Upon excitation, BV fluoresces in the near IR (NIR) region and therefore could be used as NIR-fluorophores. The quantum yield of fluorescence in the native BphPs is relatively small, but point mutations have increased it significantly with the cost of decreased photoconversion (Auldridge *et al.* 2012, Lehtivuori *et al.* 2015). Fluorescent probes derived from BphPs are already available and their use has been demonstrated in applications (Filonov *et al.* 2011, Shcherbakova *et al.* 2016, Tran *et al.* 2014, Shcherbakova *et al.* 2015).

Various optogenetic tools already exist and are used for example in neuroscientific studies. However, the majority of the available tools function with strongly scattering and more damaging light at the blue end of the visible spectrum (De Mena *et al.* 2018). Most of the phytochrome based optogenetic tools are derived from a common plant phytochrome *At*PhyB despite them requiring an extracellular chromophore (Lehtinen *et al.* 2022). The first optogenetic systems based on BphPs were introduced in 2016. Light control of cellular morphology by intracellular translocation of target proteins and light induced gene expression was demonstrated in mammalian cells and mice tissue using the BphP from *R. palustris* (Kaberniuk *et al.* 2016). In another example, the control over kinase and phosphatase activity by *Dr*PSM (Multamäki *et al.* 2021) was utilized to suppress and induce bacterial gene expression, visually demonstrated by expression of fluorescent DsRed marker protein (Multamäki *et al.* 2022).

Improvements in the existing and upcoming NIR fluorophores require further definitions on structural and fluorescent properties of BphPs to increase their quantum yield and brightness in mammalian systems. Moreover, designing sophisticated, functional and efficient optogenetic tools requires understanding of the photoactivation and regeneration of the sensory part of the system and the allosteric communication between the sensor and OPM. Especially when creating novel artificial systems, understanding the different activation mechanisms of the OPM is essential.

3 AIMS OF THE STUDY

The aim of this thesis was to study signal transduction pathways, intramolecular allostery and regulation of the output activity in a bacterial phytochrome from *Deinococcus radiodurans* (*Dr*BphP). The main focus in this thesis was on the dynamic hairpin extension, "tongue", known to change its fold during the photocycle, and especially on its role in coupling the light-sensing chromophore to the functional output module. The specific aims for each publication were as follows.

I) Provide and demonstrate a method to study solvent access to the protein interior by UV–vis spectroscopy. Describe gating of the chromophore binding pocket by the dynamic tongue in a bacterial phytochrome using the method.

II) Study the cross-talk between the chromophore and the output module via the tongue in a wild-type and artificial bacterial phytochromes with a modified output module. Describe the effect of the output module on the stability of the tongue. Demonstrate how the structural (un)coupling between the chromophore and tongue results in (un)coupling of the biochemical activity and chromophore conformation.

III) To elucidate allosteric coupling in phytochromes and the role of the tongue in phytochrome signaling. Unravel the effects of the tongue dynamics in Pr and Pfr states. Describe the thermal stability of *Dr*BphP variants.

IV) To elucidate site-specific structural changes and their timescales during the photocycle of a *Dr*BphP fragment. Trace the timescales of the tongue refolding, and describe the role of specific residues in the chromophore binding pocket in signal propagation. Demonstrate the use of a vibrational label to study signal transduction in phytochromes in micro to milliseconds timescale.

4 METHODS

The thesis combines structural, spectroscopic and biochemical data, collected from a variety of *Dr*BphP fragments and their variants. The summary of the methods used in this thesis is presented in Table 1. Selected key methods of the thesis, which are useful for studying photosensors in general, are described below in more detail with a background.

TABLE 1 Summary of methods used in the presented work. Original publications are shown in Roman numerals.

Method	Publication
Protein modifications	
Point mutations and amino acid deletions	I, II, III, IV
Site-selective vibrational labelling*	IV
Production of proteins	
Overexpression of recombinant proteins	I, II, III, IV
Affinity and size-exclusion chromatography	I, II, III, IV
Spectroscopic methods	
UV–vis spectroscopy*	I, II, III, IV
Solvent accessibility by pH jump and UV–vis detection*	I, II
Flash-photolysis by UV–vis detection	IV
FTIR spectroscopy*	II, III, IV
Time-resolved step-scan FTIR spectroscopy*	IV
CD spectroscopy	III
Structural methods	
X-ray crystallography	III
Biochemical methods	
PhosTag activity assay*	II, III
Cyclase activity assays *in vivo* and *in vitro*	II

* Described in more detail in the subsections.

4.1 Detection of chromophore absorption by UV–vis

4.1.1 UV–vis absorption spectroscopy

In photosensory proteins, chromophores, by definition, absorb UV–visible light, which can be utilized to study the properties of the chromophore and its environment. The absorption properties of chromophores are affected by the protein environment, pH, and light conditions. In this thesis, UV–vis spectroscopy was applied in a number of ways to study absorption properties of the BV chromophore (Fig. 7).

The absorption spectrum of BV changes when it covalently binds the apoprotein, where it becomes responsive to red and far-red light (Fig. 7A–C) (Hughes *et al.* 1997, Lamparter *et al.* 2003, Wagner *et al.* 2008, Rumfeldt *et al.* 2019). The two

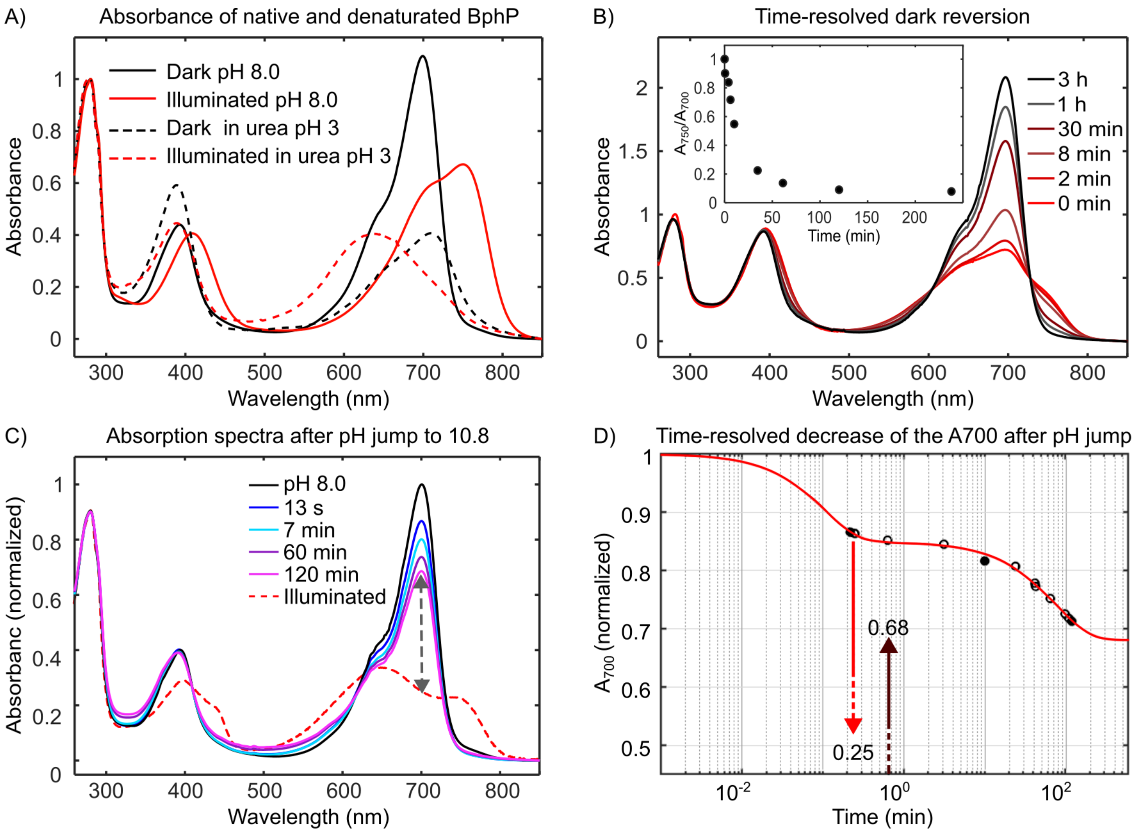

FIGURE 7 The variety of UV–vis experiments used in this thesis. A) Absorption of the chromophore in dark and illuminated states in native and urea denaturated *Dr*BphP PSM. B) Dark reversion studied by recording absorbance as a function of time after turning off red illumination. As an example, dark reversion of CBD is visualized. C) When the buffer pH is rapidly increased above BV pK_a, the absorbance at 700 nm decreases upon deprotonation of BV. The system can still responds to illumination (arrow). D) The deprotonation followed by the change in absorption at 700 nm as a function of time. The data is fit with a bi-exponential function in Eq. 1 (solid line). The figure in D was reproduced with modifications from publication I.

metastable states of phytochromes are named after their absorption properties: red (r) light absorbing Pr and far-red (fr) absorbing Pfr (Vierstra and Quail 1983). The states are often described based on their absorption maxima, 700 and 750 nm in *Dr*BphP, but the absorbance covers a broader range of the spectrum (Fig. 2A and 7A) (Wagner *et al.* 2008).

The Soret band around 400 nm is present in both Pr and Pfr states and slightly redshifts from the Pr to Pfr state (Fig. 7A). The absorption peak in the red region is referred to as the Q-band, which in the Pr state covers the region from 550 nm to 720 nm and in the Pfr state its spectral region expands from 560 nm to 800 nm. This also posses a challenge: the Pfr and Pr spectra overlap, and therefore the red illumination (660 nm LED was used in experiments in I-IV) does not result in a pure Pfr spectrum but in a photoequilibrium between the two states, estimated to be 64 % Pfr (Takala *et al.* 2014a). Conversely, a pure Pr spectrum can be reached by illumination with far-red wavelength that exceeds the absorbance in the Pfr state, for example 785 nm which was used in most experiments in this thesis (I-III).

The relative photoconversion yield to Pfr, where the chromophore is converted by illumination to ZZE, can be studied by UV–vis spectroscopy by denaturation of the system with urea (Fig. 7A). Even if the tertiary structure surrounding protein is denatured, the ZZZ/ZZE conformation of the chromophore is relatively stable (Lehtivuori *et al.* 2022). Without the protein interactions, the spectra of ZZZ and ZZE conformations still have distinct spectra which are comparable between different systems since the spectral shape depends mainly on the isomerization yield (III).

The UV–vis spectra in this thesis are analyzed from the perspective of spectral changes that result from different illumination conditions, solvent pH and protein modifications. The spectral changes were also analyzed in time-resolved manner. The photocycle in the chromophore was studied with flash-photolysis where the absorption of BV was monitored after red-light flash from micro-to milliseconds (IV). Dark reversion rates were studied by first illuminating the system to the illuminated state photoequilibrium, i.e. maximal Pfr yield, and then monitoring the time-resolved change in absorbance in darkness (III). There the A_{750}/A_{700} ratio reveals the relative population that has reverted to the resting Pr state at each time point (Fig. 7B). Below, a method where time-resolved UV–vis is combined with a rapid change in buffer pH is described.

4.1.2 Solvent accessibility by pH jumps

The protein environment affects the protonation state of BV and in principle sets some limits for it. Within those boundaries, protonation of BV is dictated by pH (Velazquez Escobar *et al.* 2017, Rumfeldt *et al.* 2019). This means that by changing the pH of the environment (solvent), the protonation state of BV can be modified. The protonation-dependent absorption properties of BV in PSM were utilized to study the solvent access to the protein interior, which in this case is the chromophore binding pocket in the dark adapted Pr state (I). The study resulted in a method that allows detection of solvent access gating, by rapid increase of solvent pH followed with time-resolved UV–vis spectroscopy.

In pH 8.0, the BV is fully protonated, here designated $(\text{BV-H}_4)^+$ (Song *et al.*

2013, Velazquez Escobar *et al.* 2015, Modi *et al.* 2019). The pK_a of BV in *Dr*BphP PSM (*Dr*PSM) in the Pr state is about 10.8 (Rumfeldt *et al.* 2019), which was reconfirmed by pH titration and plotting the A_{700} (S2 in I). At a pH equal to the pK_a, half of the BV population is deprotonated, by definition (Creighton 2010). The titration and acquired pK_a values indicated that in pH 8.0, used as a standard pH, BV in *Dr*BphP systems is protonated. An increase of pH above pK_a results in significant deprotonation, which causes a decrease in absorbance at 700 nm (Rumfeldt *et al.* 2019, I).

To study the time-resolved deprotonation process in the Pr state, the phytochrome sample was freshly diluted with water resulting in 3 mM Tris pH 8.0 buffer concentration. Then, mixing the fresh protein dilution to 60 mM glycine buffer with pH of 10.8 in ratio 1:1 resulted in rapid increase of the solvent pH. The absorbance was monitored with a diode-array UV–vis spectrophotometer (Cary 8454, Agilent Technologies) at different time points jumping the pH to 10.8 until the new equilibrium in the BV protonation state (Fig. 7C–D). Each sample was measured only once to eliminate the effect of the spectrophotometer light driving the sample to the illuminated state, where the BV gets completely deprotonated at once (Fig. 7D, red arrow). The functionality of the system remained in high pH, which was tested by illuminating the sample with red light, measuring the spectrum and recovering the system back to Pr by far-red illumination (Fig. 7C, shown by arrows).

A_{700} values at different time points were normalized to the A_{700} value at pH 8.0 (acquired by replacing the glycine buffer with 60 mM Tris pH 8.0), i.e. to time zero. The data were plotted as a function of time and fit to the exponential Eq. 1:

$$A_{measured}(t) = \sum_{i=1}^{n} A_i \times e^{-k_i \times t} + A_{endpoint} \tag{1}$$

where $A_{measured}$ is the normalized absorbance at 700 nm, A_i and k_i are the amplitude and rate constant for the i^{th} component, respectively, t is time and $A_{endpoint}$ is the A_{700} in the equilibrium at pH 10.8 (Fig. 7D).

The time-resolved measurements revealed a single exponential deprotonation in CBD (n=1) within the dead time of the experiment (13 seconds) resulting from manual mixing. In monophasic deprotonation, the whole system deprotonated uniformly (Fig. 3 in I), which suggested that the solvent had a direct access to the chromophore binding pocket. However in PSM, which includes the hairpin extension, the experiment resulted in a bi-exponential deprotonation curve (n=2). There, the first phase took place again within seconds, and the second phase during tens of minutes.

The observed bi-phasic deprotonation process is analogous to the Linderstrøm-Lang model for amide proton exchange (Hvidt and Nielsen 1966) in which proton exchange can take place once the amide backbone is exposed to solvent:

$$Closed \underset{k_{cl}}{\overset{k_{op}}{\rightleftharpoons}} Open \xrightarrow{k_{int}} Exchanged \tag{2}$$

There, "Closed" is a protected protonation state (exchange cannot take place), "Open" state is unprotected where exchange is possible. The system can revesibly fluctuate between these states by opening and closing with the rate constants k_{op}

and k_{cl}, respectively. Finally, "Exchanged" is the deuterated state. In "Open" state, the amide hydrogen-deuterium exchange happens with the is the intrinsic rate constant k_{int} (Bai *et al.* 1993).

Based on the bi-phasic deprotonation and adapted from the Linderstrom-Lang model, the Equation 1 can be expressed as follows:

$$[(BV-H_4)^+]_c \underset{k_{cl}}{\overset{k_{op}}{\rightleftharpoons}} [(BV-H_4)^+]_o \xrightarrow{k_{dep}} (BV-H_3)+H^+ \tag{3}$$

where $[(\mathrm{BV\text{-}H_4})^+]_c$ represents the fully protonated BV in the solvent protected form, and $[(\mathrm{BV\text{-}H_4})^+]_o$ represents the solvent exposed form, k_{op} and k_{cl} are the rate constants for opening and closing, respectively. The constant k_{dep} is the rate of deprotonation of the solvent exposed chromophore $[(\mathrm{BV\text{-}H_4})^+]_o$, and $[\mathrm{BV\text{-}H_3}]$ is the deprotonated form. The solvent gating structure of the system is most probably the tongue that fluctuates between "open" and "closed" conformations, and thus regulates the solvent access to the protein interior.

In the manual mixing regime, the dead time of the experiment is relatively long, 13 seconds. Therefore, the method was developed further by applying a stopped-flow mixer device (II). The stopped-flow allowed use of smaller sample volumes, fast automatized mixing of the phytochrome sample and the high pH glycine buffer, decreasing the dead time to 1-2 ms. After mixing, the sample was automatically moved to a measurement cell, and visible absorbance was monitored as a function of time (II). Otherwise, the experimental setup was not changed, and stopped-flow allowed recording of the kinetic changes of absorption properties of BV in the sub-second time-scale with better accuracy. However, in the stopped-flow device, the probe light was continuous. The light intensity was set as low as possible while at the same time maintaining a sufficient signal to noise ratio, but to prevent photoconversion during the measurement. The effect of the probe light was followed by time-resolved measurement of the sample in buffer with a pH 8.0, where no other effect than photoconversion was expected. The data was cut at 1 s because after that time the probe light started to affect the A_{700}.

The pH jump with stopped-flow is a complementary method to manual mixing. It allows observation of immediate deprotonation in the fast phase, which takes place during the first second, and from that, determination of k_{dep} (Eq. 3). The end point of the deprotonation, which is needed to determine the ratio of the fast and slow phases, is achieved by manual mixing (Fig. 7D). The fraction of the fast phase, detectable by stopped-flow, predicts the dynamics of the system: the smaller the fraction of the fast phase, the smaller the "open" population and thus, the more stable the tongue in the system is. Therefore, use of stopped-flow adds crucial accuracy to the method.

4.2 Vibrational spectroscopy of phytochromes

4.2.1 FTIR difference spectroscopy

In phytochromes, perturbation by red light causes isomerization of the chromophore, and ultimately structural changes of the protein moiety. These can include changes in H-bonding interactions, side chain orientations, and even refolding of secondary structure (Takala *et al.* 2014a). The changes in the molecular interactions between Pr and Pfr states were studied with Fourier-transform infrared (FTIR) spectroscopy that simultaneously probes changes in both chromophore and protein vibrations. FTIR spectroscopy utilizes absorption of infrared (IR) light to detect molecular vibrations that arise from stretching and bending of covalent bonds between atoms (Siebert and Hildebrant 2008, Creighton 2010). The vibrational frequency describes the vibrational energy of the bond, which depends on the mass of the bonding atoms as well as the bond strength, and is tuned by weak molecular interactions with neighbouring atoms (Barth 2007). The vibrational spectrum of a molecule, in principle, comprises all the information about the molecular structure and intramolecular interactions, and therefore FTIR is a sensitive and powerful tool to study these properties (Kottke *et al.* 2017).

FTIR spectrophotometers use a polychromatic IR source and the Michelson interferometer which first guides the light is to a beam splitter that divides the light half to stationary and moving mirror (Barth 2007, Creighton 2010) (Fig. 8A). The mirrors reflect the light back to the beam splitter where it is recombined and directed to the sample compartment. Depending on the phase of the light wave, determined by the position of the moving mirror, constructive or destructive interference takes place when the beams are combined. Therefore, at each mirror position intensity of some wavelengths of light is amplified while others are suppressed. The resulting interferogram pattern, excluding absorbed wavelengths, is recorded in relation to the mirror position. By changing the position of the moving mirror, the amplified wavelengths are changed, and the full spectrum can be covered. Finally, all the collected interferograms are converted into a spectrum through Fourier transformation (FT) process. The FT method enables better signal-to-noise ratio than could be achieved with a monochromatic IR with same resources (Uhmann *et al.* 1991).

A nonlinear molecule with N atoms has 3N - 6 normal modes. Therefore, in the case of proteins and other large biomolecular complexes, vibrations arise from thousands of bonds, many of which have overlapping vibrational frequencies (Barth 2007). To make any meaningful interpretations, a filter to reveal the relevant signals is needed. In phytochromes, the special interest lays in structural changes between the dark Pr and illuminated Pfr states as well as their short-lived intermediate photoproducts (see Section 4.2.2). Therefore, FTIR difference spectroscopy was used. There the photoactivated Pfr state, or the intermediate states, is measured directly in comparison to the Pr state. Changes in the structure and protonation state upon photoconversion modify the molecular interactions, which also affect the vibrations in perturbed areas (Kottke *et al.* 2017). Thus, difference spectra reveal the spectral changes between the two states.

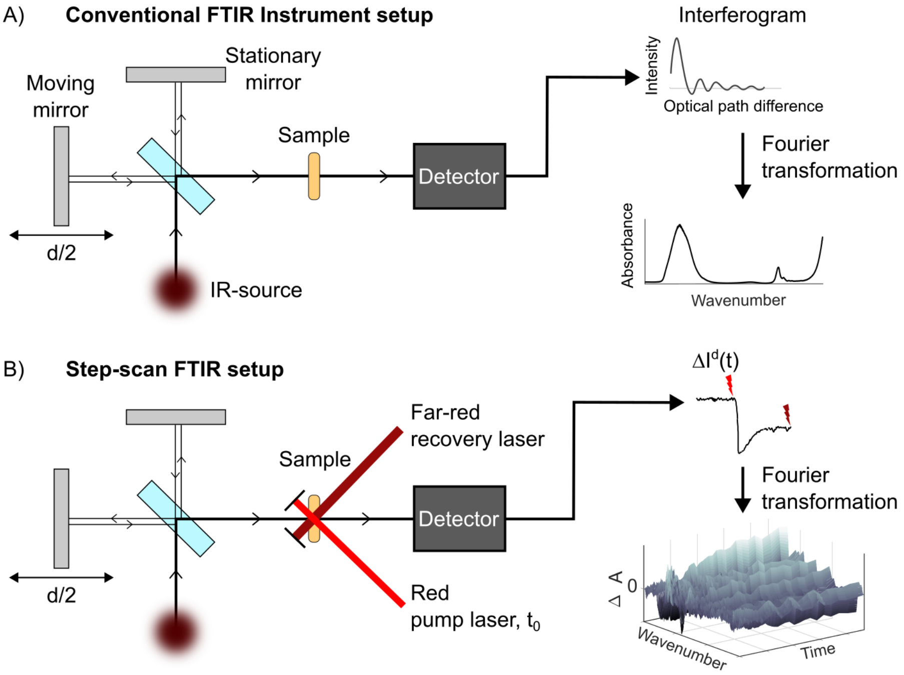

FIGURE 8 Principle of conventional and two-color step-scan FTIR. A) Beam splitter divides the IR beam onto two mirrors, stationary and moving. The recombined light is directed through the sample to the detector that records an interferogram relative to the mirror position. The interferograms collected at different mirror positions are finally combined into one FTIR spectrum through Fourier transformation, and can finally be presented for example as absorbance. B) In step-scan, interferograms are collected at each mirror position as a function of time, synchronized with the pump laser, here red, causing perturbation in the sample. In two-color step-scan, a recovery laser, for phytochromes far-red, is used to recover the sample back to a non-perturbed state to repeat the process in the next mirror position. Finally, the interferograms collected at same time point are combined into a spectrum, resulting a three-dimensional spectrum as functions of wavenumber and time.

To collect difference spectra, the phytochrome sample was concentrated to a high, about 2 mM or 300 mg/ml, concentration with Vivaspin 500 10K centrifugal concentrators, and filtered prior sandwiching it between CaF_2 windows (II-IV). Glisseal N grease (Borer Chemie) was used to seal the sample between the windows, resulting in a path length of about 10 μm. High concentration and short path length were used to minimize the absorption of water that overlaps with the amide I vibrations at around 1650 cm^{-1}. The optical path length was adjusted by tightening the cuvette until the maximal absorbance at 1650 cm^{-1} was 0.7-1.0 to gain maximal signal but still allowing enough light to pass through the sample. This allowed us to retain an acceptable signal-to-noise ratio as the difference signal was about a thousand times smaller than the absolute absorbance. Some samples were also measured also in D_2O to shift the water absorbance to lower wavenumbers, allowing the use of a 50 μm path length with a corresponding Teflon spacer and lower protein concentrations (II, IV). LEDS of 660 nm and 775 nm wavelength were used to switch the sample between the Pr and Pfr states. One of these states was used as a background for the other. Due to small signal size, at least 25 spectra in both directions (Pfr *minus* Pr and *vice versa*) were measured and averaged together, resulting in a good signal-to-noise ratio.

One of the advantages and at the same time challenges of FTIR is that it collects all structural information in solution. Due to a large amount of overlapping vibrations, assignment of the signals is very demanding. To some extent, successful interpretations have been achieved by means of isotope labelling of the chromophore (Foerstendorf *et al.* 2001) and protein (Van Thor *et al.* 2005, Ihalainen *et al.* 2018, Takala *et al.* 2018), truncations (Takala *et al.* 2016), point mutations (Lenngren *et al.* 2018) and computations (Van Thor *et al.* 2007, Takiden *et al.* 2017). In the thesis, the assignments were made based on literature (for example Barth 2007, Stojković *et al.* 2014, Zhang *et al.* 2018, Brielle and Arkin 2021), and cross-comparison between the variants including point mutations (II, IV), truncations (II, III), and ^{13}C ^{15}N isotope labelling of the protein (III).

4.2.2 Time-resolved step-scan FTIR

Step-scan FTIR was used to study the intermediate states in the photocycle of *Dr*BphP variants (IV). Step-scan allows time-resolved FTIR experiments from nanoseconds to seconds time-scale (Uhmann *et al.* 1991, Kottke *et al.* 2017), and is therefore a suitable method to study the photocycle of phytochromes (Fig. 4). In conventional as well as in time-resolved rapid scan FTIR, all mirror positions and thus the whole interferogram is measured in one sequence, which takes 5-20 ms (Siebert and Hildebrant 2008). To reach time-resolution faster than that, in step-scan FTIR, interferograms at each mirror position are measured with time-stamps (Fig. 8B). A perturbation, for example a light signal from a laser, gives an electrical trigger to the detector, and the interferograms are recorded as a function of time. When the whole time-range is covered at one mirror position, the mirror is moved to the next position (Uhmann *et al.* 1991, Siebert and Hildebrant 2008, Kottke *et al.* 2017). At each mirror position, the sample is recovered to the initial state and the reaction is re-initiated. Once all the mirror positions are measured, all interferograms at each time point are converted into a an FTIR spectrum through Fourier transformation (Kottke *et al.* 2017).

Reversible systems can utilize two-color step-scan, where a laser pulse initiates the reaction in the sample. After measurement of one sequence, the back reaction can be accelerated with a different color laser pulse, hence two-color (Fig. 8B). This way the same sample can be recovered for the next measurement sequence, and a fresh sample is not required after each initiating laser pulse (Kottke *et al.* 2017). To cover all mirror positions, even multiple times, step-scan measurements often requires hundreds of repeats; therefore, two-color step-scan saves a considerable amount of sample material. On the other hand, a rather high laser power is needed as the concentration of the sample is high. First, a majority of the population needs to be triggered to enter the photocycle and then, subsequently be reverted back before a new cycle. The high power laser pulses can be tolerated for only a limited amount of cycles, and therefore the samples are not eternal.

The samples were monitored in 316 discrete mirror positions in spectral window of 988–2256 cm^{-1} after a 660 nm laser pulse (10 ns, 4.5 mJ/cm^2) with 1000 time slices of 5 μs and 8 coadditions resulting in 8 cm^{-1} spectral resolution and time resolution of 2.5 μs (IV). The samples were reverted back to the Pr state with a 751 nm laser pulse (40 ms, 500 mW/cm^2). The components were synchronized with a DG645 (Stanford Research System) pulse generator. The same sample was used for up to three experiments corresponding to less than 8000 excitation pulses. The temperature was maintained at 20°C with a circulating water path.

To reveal the intermediate components from the data, a weighed global analysis was performed (Stokkum *et al.* 2004). A sequential model with three intermediates was used as demonstrated in Ihalainen *et al.* (2018) corresponding to the photocycle presented in Figure 4 (without splitted Meta-R). If fewer components were sufficient to fit the data, only two components were used. The global analysis resulted in species associated difference spectra (SADS) with a concentration profile and a time constant, and the SADS were associated with the intermediate states based on time constants and spectral features.

4.2.3 Vibrational labelling of proteins

Assignment of the IR difference spectra to a specific amino acid or even just the chromophore is challenging since the numerous frequencies and spectral overlap result in a complex spectra. To gain site-specific information on the structural changes, vibrational labelling was applied (IV). A relatively small unnatural amino acid p-azidophenylalanine (pAzF) was selected as the vibrational probe (Fig. 9A) (Ye *et al.* 2009, Thielges *et al.* 2011). Not present in proteins naturally, the asymmetric stretching vibrations of the N_3 azide group absorb at a distinct region from protein and water vibrations, at about 2100 cm^{-1} (Fig. 9C). The azide group has a relatively high extinction coefficient in comparison to other vibrational probes (Choi *et al.* 2008, Ma *et al.* 2015). Further, the azide vibrations are sensitive to the local electrostatic environment, especially to local H-bonding environment, which reflects to its vibrational spectral position and shape (Wolfshorndl *et al.* 2012, Maj *et al.* 2016, Creon *et al.* 2018). In phytochromes, they therefore have potential to report photoconversion-induced changes in the structure in a site-specific manner.

The monomeric photosensory module from *Dr*BphP (*Dr*PSM$_{mon}$) with monomerizing mutations F145S, L311E and L314E (Auldridge *et al.* 2012) was labelled with pAzF at nine separate positions, each one separately from others (Fig 9B). In general aromatic ring containing residues tyrosine and phenylalanine were replaced with pAzF due to their similar structure and size. The labelled positions were selected based on where a change was expected: two in the tongue (F469, Y472) and four in the chromophore binding pocket (Y176, F203, S257, Y263). One position (R228) was chosen in the knot of CBD (Wagner *et al.* 2005), and one (Y307) at the dimerization interface. One label (F372) was inserted at a position which was assumed to not change during photoswitching in PHY as a control.

The labels were inserted using amber codon suppression technology (Chin *et al.* 2002, Liu and Schultz 2010, Young *et al.* 2010). There, the nonsense amber codon (TAG) was mutated to the desired position in the monomeric phytochrome

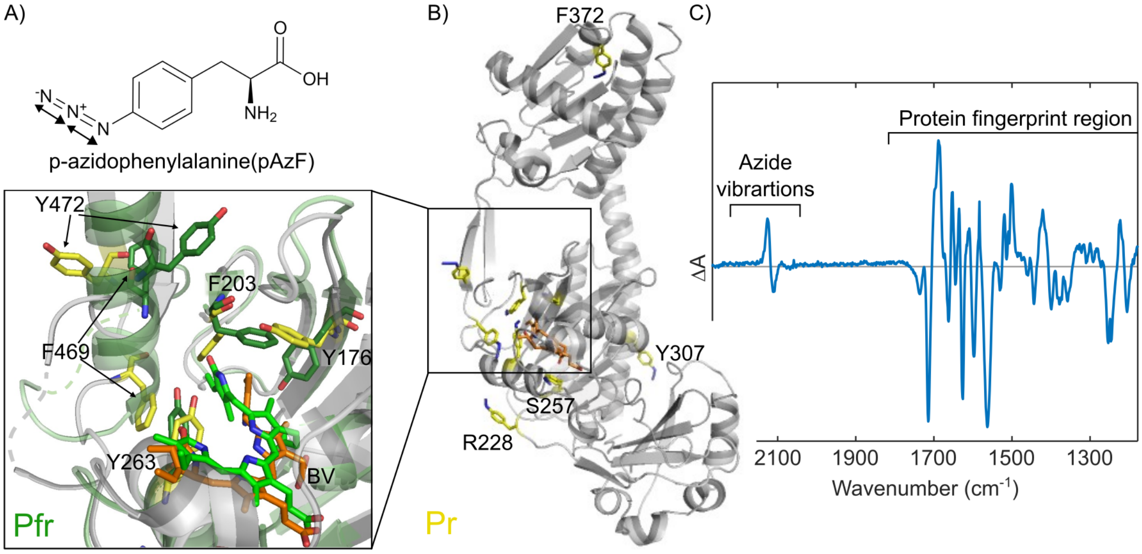

FIGURE 9 Vibrational labelling with p-azidophenylalanine (pAzF) A) The molecular structure of the unnatural amino acid pAzF. The asymmetric vibrations of the azide group are indicated with arrows. B) Label positions in the monomeric photosensory module of *Dr*BphP. The label molecules are modelled at the labelled positions in the structures, the inset shows the label positions near the chromophore and in the tongue in both Pr (yellow) and Pfr (green) states. (PDB: Pr, 4O0P and Pfr, 4O01). C) In the IR spectrum, the azide vibrations locate around 2100 cm^{-1}, in a spectral window free from protein vibrations below 1750 cm^{-1}. The azide signal in a difference spectrum reports on a change in the label environment. The figure was reproduced with modifications from publication IV.

sequence (Takala *et al.* 2016) using QuikChange Lightning Multi Site-directed Mutagenesis kit (Agilent Technologies). The plasmid (pET21b$^+$) containing the mutated phytochrome sequence was co-transformed into *E. coli* BL21(DE3) with amber codon suppression machinery that consists of an orthogonal aminoacyl-tRNA synthetase/suppressor tRNA$_{CUA}$ pair in pEVOL-pAzF plasmid (Addgene #31186, gifted by Peter Schultz). The amber codon suppression machinery allows reassessment of the amber codon to encode the unnatural amino acid pAzF (Liu and Schultz 2010, Young *et al.* 2010).

The labelling was done *in vivo* by first inducing the suppression machinery at the OD$_{600}$ value of 0.2 with 0.02 % (w/v) arabinose and 600 μg/ml of pAzF (Bachem). The phytochrome expression was induced with 1 mM IPTG when OD$_{600}$ reached 0.8 after which the expression was continued in darkness to prevent any light-induced reactions of pAzF. The phytochrome sequence was complemented with a C-terminal His$_6$-tag for affinity chromatography, which ensured prematurely truncated systems would by-pass the column into waste during purification. Use of monomeric system prevented formation of heterodimers of complete and truncated systems. The biliverdin chromophore was added externally during purification (Lehtivuori *et al.* 2013).

Three of the pAzF labelled samples, Y176pAzF, F203pAzF and Y472pAzF, were confirmed to be photoswitchable with UV–vis spectroscopy with a difference signal in the label region with FTIR difference spectra. Therefore, they were identified as suitable candidates and selected for step-scan measurements (IV, Supplementary information). The path length of the step-scan samples was adjusted $A_{1650} > 1.1$ to increase the signal in the label region, while keeping the protein concentration the same as in the steady-state experiments to ensure a sufficient hydration of the sample. The resulting high water absorption in the amide I region caused a saturation in the spectral region from 1610 to 1670 cm^{-1}, which was therefore left out in the global analysis of the time-resolved difference spectra. In the labelled samples, the global analysis was performed separetely for the label region (2060–2175 cm^{-1}) and the fingerprint region of the protein and chromophore (1200–1765 cm^{-1}), which allowed observing the photocycle at the labelled site and of the system as a whole independently.

4.3 Detection of biochemical activity with PhosTag assay

Changes in the biochemical activity of *Dr*BphP variants was studied with the PhosTag activity assay, adopted from Multamäki *et al.* (2021) (II, III). The assay allows detection of phosphatase and kinase activity of phytochromes on their cognate RR. Detection of phosphatase activity in *DrBphP* requires pre-phosphorylation of the DrRR. For that, 1.4 mg/ml of purified DrRR were incubated an assay buffer (25 mM Tris/HCl pH 7.8, 5 mM $MgCl_2$, 4 mM 2-mercaptoethanol, 5 % ethylene glycol) supplemented with 100 mM acetyl phosphate at +37°C for 30 min. The buffer was exchanged back to 30 mM Tris pH 8.0 with successive dilution-concentration cycles using centrifugal filters (Amicon®Ultra 10 KDa).

SDS-PAGE gels (9 %) containing 20 μM PhosTag acrylamide (Wako Chemicals) were used for the mobility shift detection of non-phosphorylated RR and p-RR proteins. The samples were run on the PhosTag gel at room temperature with 40 mA according to the Zn^{2+}-Phos-tag®SDS-PAGE assay protocol (Wako Chemicals). The PhosTag gel separates phosphorylated and non-phosphorylated proteins by decelerating the mobility of the phosphorylated ones. Therefore the p-RR band is detected above the RR (19 kDa) band on the stained gel (Fig. 10A).

For the activity detection, 0.4 mg/ml of *Dr*BphP variant was incubated with 0.4 mg/ml of p-DrRR in the assay buffer at +25°C either in the dark or under constant red light illumination. The maximum Pr or illuminated state equilibrium was ensured by pre-illumination with either 780 nm laser (Thorlabs, 20 sec, 80 mW/cm^2) or saturating red LED (660 nm, 5 min, on average 13 mW/cm^2) prior to initiating the reaction with 1 mM ATP. The reactions were stopped after 10 min with 5x SDS loading buffer and run on PhosTag gels as described above. The same method allows detection of kinase activity if the p-RR is replaced with non-phosphorylated RR in the reaction. Then, kinase activity is detected as the appearance of a p-RR band in the gel. This method was used to study the activity of tongueless *Dr*BphP and *Dr*BphP Chimera, where the OPM was replaced by the HK from Agp1 (III), described in Multamäki *et al.* (2021).

The method is qualitative, and does not determine the dynamic range, i.e., the ratio of the minimal and maximal activity of the system (Ziegler and Möglich 2015). The method was developed further by adding a time-resolved dimension

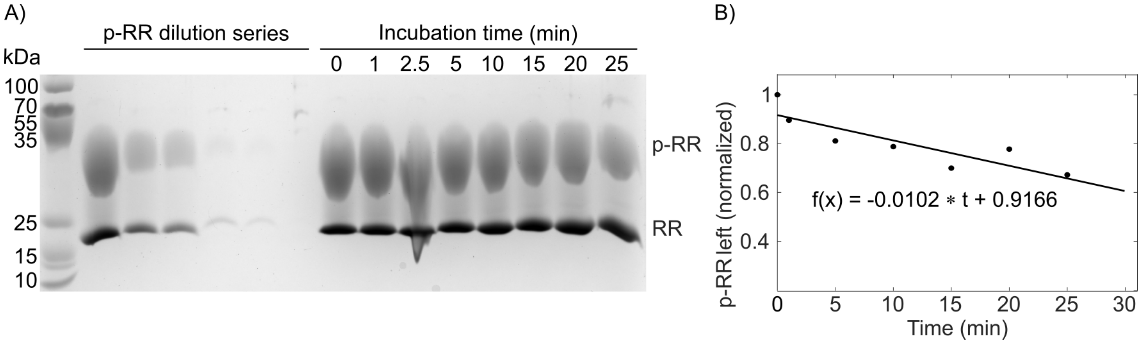

FIGURE 10 Mobility detection of p-RRs and RRs in the PhosTag gel. A) A mixture of RR and p-RR was run on a PhosTag gel, where PhosTag slows phosphorylated proteins (p-RR) down, to separate them from each other. The dilution series was made until the RR band became non-saturated to determine the relative intensity of p-RR and RR bands, which was 50 %. The varying incubation times of p-RR at +25°C were used to determine the spontaneous breakage of p-RR to RR. B) The normalized relative intensity of p-RR was plotted as a function of time, and fit to a single-polynomial function. The slope of the fit equals the rate of spontaneous breakage. The figure was reproduced from publication II.

to the experiment (II). The dephosphorylation reaction catalyzed by *Dr*BphP variant was followed at various time points and assumed to proceed as in Eq. 4.

$$[E] + [S] \underset{k_{-1}}{\overset{k_1}{\rightleftharpoons}} [ES] \xrightarrow{k_2} [E] + [P], \tag{4}$$

where ES is the enzyme-substrate complex (i.e., p-RR bound to the phytochrome), and P is the product (dephosphorylated RR).

The incubation time of *Dr*BphP variants with p-RRs was altered from 1 min to 20 min in dark and illuminated states (Fig. 11A). The concentration of *Dr*BphP variants was adjusted to 0.4 mg/ml in the dark and to 0.06 mg/ml in the illuminated state to maintain the p-RR levels detectable throughout the selected time scale. The experiments were repeated at least three times.

For determination of the specific activity, the molar concentration ratio of p-RR and phytochrome was calculated. The phytochrome concentration was known and the same at each time point, but the p-RR concentration decreased (Eq. 4). Pre-phosphorylation of RR does not result in 100 % phosphorylation efficacy, but a mixture of RR and p-RR (Fig. 10A). To determine the initial p-RR concentration, the phosphorylation efficacy of acetyl phosphate treatment was estimated from the relative intensity of the p-RR and RR bands from the gel using ImageJ analysis program (Schneider *et al.* 2002), which revealed 50 % phosphorylation efficacy (Fig. 10A).

When kept at +25°C, the p-RRs spontaneously dephosphorylate during the reaction. The time series with only p-RR/RR mixture were performed to determine the rate of spontaneous breakage of p-RR at +25°C (Fig. 10A). The band intensities fit to a single polynomial function, where the slope is the rate for spontaneous breakage (Fig. 10B).

The relative fraction of p-RR that had been dephosphorylated by *Dr*BphP

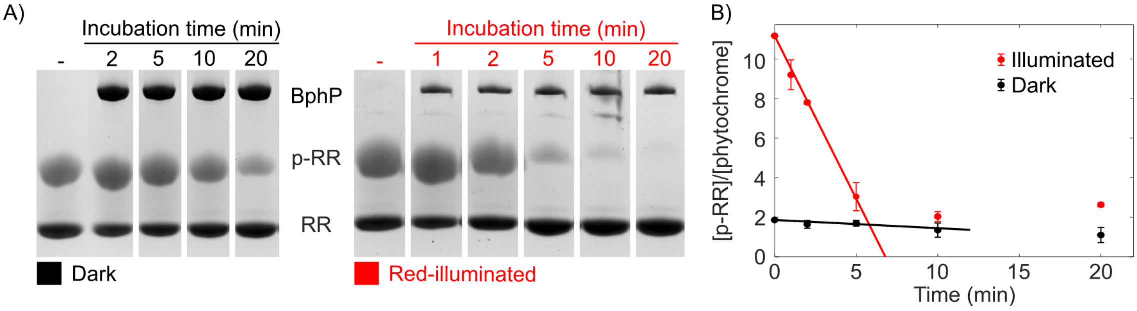

FIGURE 11 Determination of the specific phosphatase activity. A) BphP was incubated at +25°C with pre-phosphorylated RR (p-RR), and the reaction was stopped at different timepoints and run on a PhosTag gel to separate the remaining p-RR and RR. Using an image analysis program, the intesity of the remaining p-RR was determined and plotted in B. B) The normalized relative intensity of p-RR relative to the phytochrome concentration was plotted as a function of time, and fit to a single-polynomial function. The slope is the initial velocity of the reaction and equals the rate of breakage. The figure was reproduced with modifications from publication II.

variant during the reaction was quantified using ImageJ at each time point and calculated in relation to the initial concentration (Fig. 11). The concentration values at each time point were corrected with the slope of spontaneous breakage to investigate the phytochrome activity alone. Finally, the decreasing [p-RR]/[phytochrome] ratio was plotted as a function of time (Fig. 11B).

RR and p-RR competitively bind to *Dr*BphP (Multamäki *et al.* 2021), and therefore it was assumed that k_1 becomes the rate limiting step of the reaction as the amount of available p-RR decreases with time. Therefore, the first four time points of the reaction were fit to a linear function to derive the initial velocity V_0. The V_0 resulted in the specific activity for the *Dr*BphP variants under the described conditions, in dark or illuminated state.

5 RESULTS AND DISCUSSION

5.1 Dynamics of the Pr state

5.1.1 Fluctuations of the tongue

Many protein systems include dynamic loops and other types of structural features that gate solvent or for example ligand access to the protein interior (Gora *et al.* 2013). To study solvent access to the protein interior, a method applying rapid change of solvent pH and time-resolved UV–vis spectroscopy was established (see Section 4.1.2, I). In the context of phytochromes, the method is based on changes in biliverdin absorption upon deprotonation (Velazquez Escobar *et al.* 2017, Rumfeldt *et al.* 2019). Yet, the method can be expanded to any system with pH-dependent absorption properties. The studies on *Dr*BphP samples resulted in a model that describes solvent access to the chromophore binding pocket, gated by the tongue in the Pr state (Fig. 12A).

The tongue extends from the PHY domain to the vicinity of the chromophore, and based on the crystal structures, folds as a β-sheet in the Pr state (Fig. 4) (Anders *et al.* 2013, Takala *et al.* 2014a, Burgie and Vierstra 2014, Yang *et al.* 2014, Gourinchas *et al.* 2017, Nagano *et al.* 2016, Li *et al.* 2022a, Wahlgren *et al.* 2022). The structural data suggests that in that state, dictated by the conserved interactions with the CBD, the tongue blocks solvent access to the chromophore binding pocket (Fig. 1 in I). However, in solution, proteins are dynamic systems that populate a variety of pre-existing conformational states, most of which cannot be recorded in crystal structures (Frauenfelder *et al.* 1991, Hilser *et al.* 2012, Nussinov and Tsai 2013, Motlagh *et al.* 2014). However, random coil conformation of the tongue, mixed with β-folded tongue, has been recorded by NMR (Gustavsson *et al.* 2020).

The pH jump data of *Dr*PSM fragment revealed a bi-phasic deprotonation process (Fig. 12B). This supports solvent gating by the tongue which can adopt at least two conformations: "closed", where deprotonation does not take place because the solvent access to the chromophore is blocked, and "open", where the solvent can access the protein interior and immediate deprotonation of BV takes

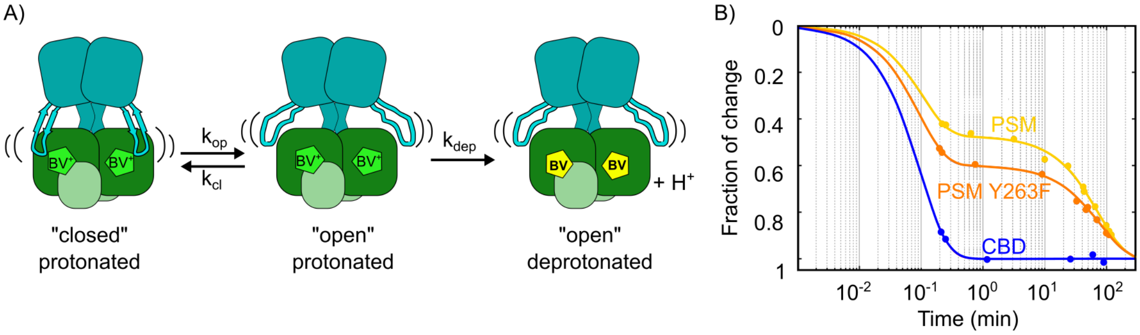

FIGURE 12 Solvent access to chromophore binding pocket in *Dr*BphP fragments. A) A model of BV deprotonation in the Pr state of PSM. The chromophore binding domain is shown in green and the PHY domain in cyan. The fluctuations of the tongue are dictated by rate constants for opening and closing, k_{op} and k_{cl}, respectively. The deprotonation takes place according to k_{dep}, which the model assumes to take place only when the tongue is in the "open" conformation. B) Kinetics of deprotonation in three *Dr*BphP samples. In the PSM fragment, deprotonation is bi-phasic, whereas in CBD it takes place in one phase in (sub)second time scale. The data is plotted as the total amplitude change. Subfigures A and B were reproduced with modifications from publications II and I, respectively, with permission from Springer Nature.

place (Fig. 12A). CBD, which lacks the tongue, deprotonated in one phase in (sub)second time scale (Fig. 12B).

The fits of data revealed deprotonation rate constants k_{dep} for all three studied systems, PSM, PSM Y263F, and CBD, and rate constants of the tongue fluctuations, k_{op} and k_{cl}, for the PSM fragments (Fig. 3 and Table 1 in I). The k_{dep} was very similar in all systems, about 10 min^{-1}, but the deprotonation took place beyond the time resolution of the experiment. In both PSM variants, the rate constants for tongue fluctuations were also very similar to each other, and showed that the tongue fluctuations take place with minute time scales.

Depending on the system, the BV absorption and pK_a can vary slightly resulting in different end points, and amplitudes. Therefore, plotting the kinetics as a function of the fractional amplitude change allows easier comparison between systems. Between PSM and PSM Y263F, the largest difference was in the relative amplitudes of the fast and slow phase, corresponding to the "open" and "closed" population, respectively. In wild-type PSM the fraction of the fast amplitude was 47 %, whereas in PSM Y263F, where the tongue has been decoupled from the chromophore by the mutation (Takala *et al.* 2018), the amplitude raised to 60 % (Fig. 12B). The solvent gating tongue might have a role in a (de)protonation process of the system. Here, the power of the method and the model is that together they can be used to compare the relative dynamics of the tongue between systems.

After implementation of the method (I), the Pr state dynamics of the tongue were studied in a set of *Dr*BphP (derived) system by the pH jump method using rapid mixing by stopped-flow, and complemented with FTIR difference spectroscopy (II). *Dr*PSM, full-length *Dr*BphP and artificial phytochrome activated

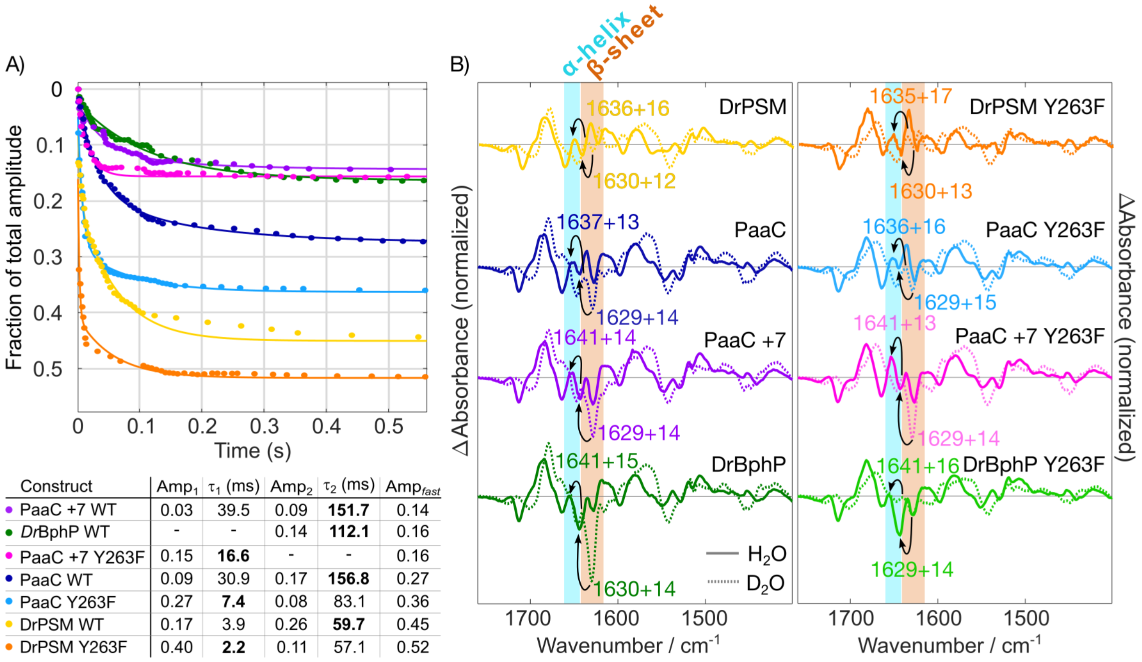

Construct	Amp_1	τ_1 (ms)	Amp_2	τ_2 (ms)	Amp_{fast}
● PaaC +7 WT	0.03	39.5	0.09	**151.7**	0.14
● *Dr*BphP WT	-	-	0.14	**112.1**	0.16
● PaaC +7 Y263F	0.15	**16.6**	-	-	0.16
● PaaC WT	0.09	30.9	0.17	**156.8**	0.27
● PaaC Y263F	0.27	**7.4**	0.08	83.1	0.36
● DrPSM WT	0.17	3.9	0.26	**59.7**	0.45
● DrPSM Y263F	0.40	**2.2**	0.11	57.1	0.52

FIGURE 13 Spectroscopic properties of the Pr state A) The fast phase of deprotonation after pH jump from pH 8.0 to 10.8. The table shows the fits of the data, and in most cases two components were needed. The Amp_{fast} is the amplitude of the fast phase determined at the plateau after 0.5 s. B) FTIR difference spectra (Pfr *minus* Pr) measured in H_2O (solid line) and D_2O (dotted line) for different phytochrome samples. The regions corresponding to α-helical and β-sheet signals are highlighted at amide I. The shift of signals from D_2O to H_2O are shown with arrows and wavenumbers. Reproduced with modifications from publication II with permission from Springer Nature.

adenylyl cyclases (PaaC) and PaaC +7 were compared. PaaC systems have a *Dr*PSM combined with adenylyl cyclase output module (Etzl *et al.* 2018). In PaaC +7, seven extra amino acids between in the helix connecting the PSM and OPM result in an extra turn. On top of the wild-type systems, the Y263F variant from each system was included into the comparison.

The main interest was on the fast phase of the deprotonation to determine the fraction of the "open" population. The fast phase was best accessible by stopped flow measurement with sub-second experimental dead time (see Section 4.1.2). The deprotonation was recorded until the first stationary phase, which we interpreted as completion of the fast phase (Fig. 13A). With better time-resolution, the fast phase required a bi-exponential fit, possibly due to complex deprotonation mechanics in the systems. The complexity is emphasized especially in the early time points from 20 to 80 ms, where the signal is the most challenging to fit. The sum of these two components was considered the fast phase amplitude A_{fast}. The amplitude of the total change was recorded separately for determining the fraction of change in the fast phase, which corresponds to the "open" population (Fig. 12B).

The smallest fast phase amplitude was in PaaC +7 WT (14 %) followed by *Dr*BphP WT and PaaC +7 Y63F (16 %) (Fig. 13A). The amplitudes imply that in the dark state photo-equilibrium, in 86 % (PaaC +7 WT) and 84 % (*Dr*BphP WT and PaaC +7 Y263F) of the population the tongue is in "closed" conformation and therefore more stable, or less dynamic, than in the five other systems. In PaaC WT and PaaC Y263F, the "open" fraction of systems was 27 % and 36 %, respectively, which is larger than in other full-length systems, but smaller than in PSM fragments. In PSM WT and PSM Y263F, the fast phase amplitudes were 45 % and 52 %, respectively.

The pH jump experiments with seven systems showed two trends. First, the uncoupling of the tongue and the chromophore environment in the Y263F mutation increased the fast phase amplitude. This suggests that the uncoupling also increases dynamics of the tongue in comparison to their wild-type systems (Fig. 13A). Secondly, the full-length systems had a smaller fast phase amplitude than the PSM fragment. This suggests that in the complete systems, the tongue is more stable, possibly stabilized by OPM. The additional turn in the PaaC helix in PaaC +7 seems to bring more stability, even in the Y263F variant, in which the tongue stability was same as in the native *Dr*BphP system.

The two observed time constants, or only one in *Dr*BphP WT and PaaC +7 Y263F, explain the complex deprotonation in the systems, to some extent. In all systems, one of the time constants is more dominating than the other, meaning that the amplitude of the component is larger (Fig. 13A). In the wild-type systems, the time constant is in the time scale of tens of milliseconds, whereas in Y263F only of milliseconds. The data is not adequate to resolve the deprotonation mechanism in the systems, but the comparison of the mutated and wild-type systems suggests that the residues of the chromophore binding pocket play a role in the process. The complex deprotonation process possibly reflects the heterogeneity of the chromophore in the Pr state, observed by other methods (Velazquez Escobar *et al.* 2017, Chenchiliyan *et al.* 2023).

FTIR difference spectra (Pfr *minus* Pr) were recorded from the eight samples in H_2O and D_2O to detect tongue dynamics with another spectroscopic method (II). FTIR difference spectra, in principle, captures all structural changes that take place upon photoconversion from Pr to Pfr. Negative signals arise from the Pr state vibrations that are absent in the Pfr state, and conversely, positive signals are those that shift upon photoconversion and appear only in the Pfr state (Kottke *et al.* 2017). Here, the FTIR comparison focused on the amide I signals of the different secondary structures, especially the β-sheet signals that should be observable around 1623–1641 cm^{-1} in H_2O and 1615–1638 cm^{-1} in D_2O. Apparent effects of the Y263F mutation on the chromophore vibrations, especially the positive signal at 1685 cm^{-1}, have been discussed earlier (Takala *et al.* 2018). The large β-sheet to α-helix shift in the amide I region, often associated with the tongue refolding, has been shown in different phytochrome species (Stojković *et al.* 2014, Xu *et al.* 2020) but is not as apparent in *Dr*BphP as there seem to be overlapping signals from the CBD and even the chromophore (Takala *et al.* 2018). However, similar signal pattern has been identified from ^{13}C ^{15}N isotope labelled *Dr*PSM (Takala *et al.* 2018, Ihalainen *et al.* 2018).

Based on the solvent access experiments, full-length variants, *Dr*BphP, PaaC and PaaC +7, with a small fraction in the open conformation should have a larger β-sheet signal than *Dr*PSM. In H_2O, a negative signal at 1642–1644 cm^{-1} was detected in all systems, which is the middle one from the three negative signals in the amide I region (1620–1680 cm^{-1}) (Fig. 13B). The signal intensity clearly increased from *Dr*PSM to full-length systems. However, when measured in H_2O, the observed frequencies were just outside the reported β-sheet extremes (Barth 2007). In the ^{13}C ^{15}N labelled *Dr*PSM, the negative signal is at 1597 cm^{-1} (Ihalainen *et al.* 2018), downshifted by 45–47 cm^{-1} from the frequency observed here. The shift is in the expected range for amide I (C=O) stretches caused ^{13}C ^{15}N labelling (Brielle and Arkin 2021).

When measured in D_2O, a similar negative peak pattern was observed in all systems (Fig. 13B). The negative signal in the middle had shifted to 1629–1630 cm^{-1} by 12-15 cm^{-1}, which align with β-sheet frequencies (Fig. 13B) (Barth 2007). Therefore, this negative contribution was interpreted as a disappearing β-sheet content in the Pr state. In both H_2O and D_2O, the negative signal is accompanied by a small up-shifted positive contribution at 1650–1656 cm^{-1} and 1635–1641 cm^{-1}, respectively (Fig. 13B). In water, the frequencies matched with the reported frequencies for α-helical structures (Barth 2007, Stojković *et al.* 2014, Xu *et al.* 2020). However, in most cases, notable differences in signal intensity were not observed, most probably due to strong suppression by other vibrations, and here the focus is on the β-sheet signal.

In H_2O, the intensity of the β-sheet signal in Pr was smallest in *Dr*PSM and PaaC variants and largest in *Dr*BphP variants (Fig. 13B). Between *Dr*PSM WT and Y263F, there was no clear difference in signal intensity, but in PaaC and PaaC +7, the β-sheet signal was bleached upon Y263F mutation. In *Dr*BphP, surprisingly, the signal intensity of Y263F was larger than in WT. However, when switched to D_2O, the signals were significantly more intensive in all full-length WT systems.

In D_2O, the signal intensities followed the trend of the pH jump experiment. The largest β-sheet intensities, correlating with smallest "open" amplitude, were found in *Dr*BphP WT, PaaC +7 WT, and PaaC +7 Y263F. In *Dr*BphP Y263F, missing from the pH jump experiments, the signal became strongly suppressed. This was expected based on the increased solvent access *Dr*PSM Y263F in comparison to WT. Based in FTIR data, the Y263F mutation increased the "open" population also in full-length *Dr*BphP (Fig. 13A). Correlating with solvent accessibility, the signal intensity in PaaC WT is slightly smaller than in other full-length WT systems. Also, the β-sheet signal intensity in PaaC is more suppressed upon Y263F mutation. The β-sheet signal intensity of both PaaC +7 variants was very similar, like in the pH jump experiment (Fig. 13). In *Dr*PSM, both signals are strongly suppressed by overlapping vibrations, as previously discussed (Takala *et al.* 2016, 2018).

A suggestion of the origin of the overlapping signals from CBD was made based on observed frequencies, isotope labelling and structural data (III). A negative-negative-positive (1660(–), 1645(–), 1634(+) cm^{-1}) peak pattern was identified from CBD and found to shift for 42–44 cm^{-1} in ^{13}C ^{15}N labelled CBD (Fig. S5 in III), matching the expected shift of C=O vibrations upon isotope labelling (Brielle and Arkin 2021). The two negative peaks, 1660 cm^{-1} and 1645 cm^{-1}, in the Pr state match with β-sheet turns and disorder frequencies, respectively (Barth 2007). The positive signal at 1634 cm^{-1} in Pfr matches with the frequency of increasing β-sheet content. Increase of the β-sheet content was found by comparing the *Dr*PSM crystal structures in Pr and Pfr. The structures show that the β-sheet strands in PAS grow longer upon photoconversion. Therefore, the contribution of the turns and disordered structures becomes smaller in Pr, and the lengthening of the strands is observed as increasing β-sheet content in Pfr. The above observed β-sheet signals in Pr therefore compete with these contributions.

In CBD (Fig. S5 in III) and even in PSM (Fig.13B), the positive 1634 cm^{-1} signal had a large positive contribution. In full-length systems, with increasing negative contribution at 1644 cm^{-1}, the positive contributions became more and more suppressed and upshifts by 1–2 cm^{-1}. In D_2O, the signal was suppressed by the negative contribution of the β-sheet, most probably from the tongue, which has competing vibrations at very similar frequencies. The slight difference in the signal can be explained by the nature of the β-folded structure. The increasing β-fold in PAS locates in a slightly bent sheet of five strands, whereas the tongue is a dynamic hairpin structure with only two strands.

5.1.2 Effects of the tongue on the properties of the Pr state

The solvent accessibility studies showed that the tongue fluctuates in the Pr state. The amount of dynamics is decreased by 1) the coupling between the chromophore and the tongue and 2) stabilization by the OPM (Fig. 13). To elucidate the role of the tongue in phytochrome signaling directly, the tongue was removed from *Dr*BphP. PSM tongueless and full-length (FL) tongueless variants were introduced (III). There, the tongue segment (R446-G478) was replaced with a sequence "GGGS".

The Pr state crystal structure of the PSM tongueless was resolved up to 2.6 Å resolution (Fig. 14). The dimer symmetry and dimerization angle were affected by removal of the tongue. The connecting helices between CBD and PHY domains position at a smaller angle, 50°, in the PSM tongueless in comparison to 80° in the wild-type PSM (Fig. 14A–B). The bending of the helices is not symmetrical in the PSM tongueless, but in one protomer, the PHY domain is leaning towards its corresponding CBD. Most probably this is due to lack of support from the tongue, which allows the PHY domains to organize more freely. The resulting organization is a crystallization artefact, explained by the smaller B-factor in the docked PHY domain in comparison to the other (Fig. S2 in III). Despite, the altered dimer symmetry, organization of the chromophore binding pocket was highly similar to that of PSM (Fig. 14C). The chromophore as well as the conserved residues of the chromophore binding pocket had adopted very similar conformations in the Pr state.

The similar organization of the chromophore binding pocket in the crystal structure was supported by the spectroscopic measurements in solution. The dark UV–vis spectra (Fig. 2A in III) as well as urea-denatured dark state systems (Fig. S3A in III) showed that the chromophore absorption is same as in wild-type systems and adapted ZZZ conformation. The FTIR difference spectra of tongueless constructs contain the same negative signals for the chromophore vibrations in Pr as their wild-type counterparts (Fig. 2B in III).

Although the chromophore binding pocket remained unaltered, the tongue dynamics had effects on the full-length system, especially its OPM activity. *Dr*BphP

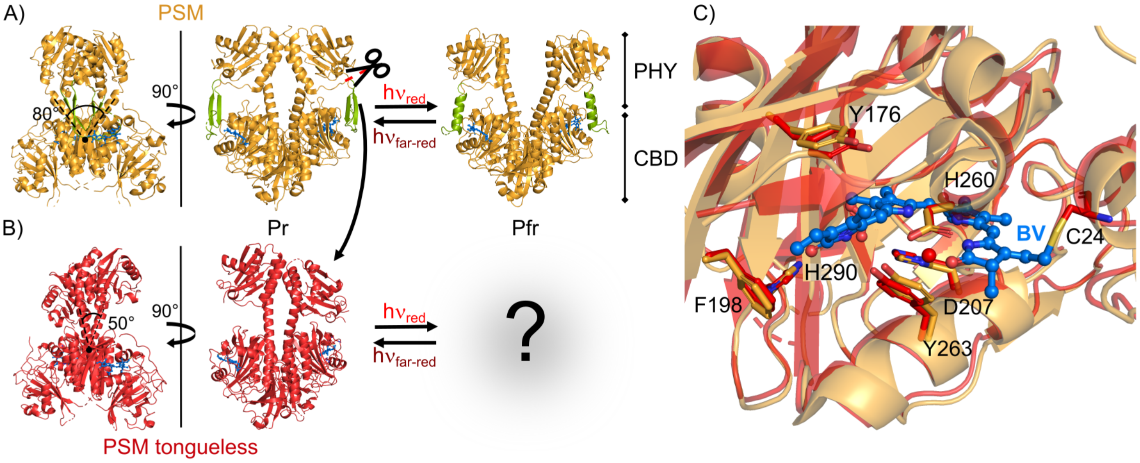

FIGURE 14 Structural comparison of PSM and PSM tongueless. A) *Dr*PSM crystal structure in Pr and Pfr-like states. The 90° rotated view is shown from the Pr structure. The BV (blue) is buried inside the chromophore binding domain (CBD) and the tongue extending from the PHY domain is shown in green. B) The resolved crystal structure of PSM tongueless in the dark state. The pivot angle of the protomers is illustrated in the 90° rotated view. C) Chromophore binding pocket organization of PSM (yellow) and PSM tongueless (red). Conserved residues are shown as sticks, and the chromophore (blue) is shown only from the PSM tongueless structure with balls-and-sticks. PDB codes: 4O0P (PSM in Pr), 5C5K (PSM in Pfr), 8BOR (PSM tongueless). Reproduced with modifications from publication III with permission from Elsevier.

is a light-activated phosphatase, but the activity analyses of *Dr*BphP wild-type (WT) and *Dr*BphP Y263F reveal that when the tongue is present, the dark-state activity increases (Fig. 15A). When the tongue was removed and no fluctuations can take place in *Dr*BphP tongueless, nearly no cleavage of the phosphate from RR was observed, which is observed as similar p-RR bands in p-RR and dark tongueless lanes.

In the *Dr*BphP WT, with the tongue, the p-RR band was less intense in the darkness than in the tongueless variant, resulting from enzymatic activity of the system (Fig. 15A). When the Y263F variant, with increased tongue dynamics, was incubated with p-RR in darkness, higher activity than in WT was observed. The dark state activities were determined (see Section 4.3) for *Dr*BphP WT and Y263F, revealing about two times higher specific activity in Y263F in comparison to WT (Fig. 15B). PaaCs are light-activated cyclases, and there, like in *Dr*BphP, the Y263F mutation also resulted in two times higher dark state activity of than in PaaC WT (Fig. 15B). Previously, Takala *et al.* (2018) described the uncoupling of the tongue from the chromophore in structural terms, and here the effect of uncoupling was shown in biochemical terms.

The importance of the tongue became apparent in stabilization of the *Dr*BphP structure. Temperature dependent CD spectroscopy allowed determination of the melting temperatures (T_m) of the PHY and OPM by following the temperature dependent molar ellipticity at 222 nm, separately from CBD denaturation which was traced at 281 nm (III). In both PSM WT and PSM tongueless, the T_m of

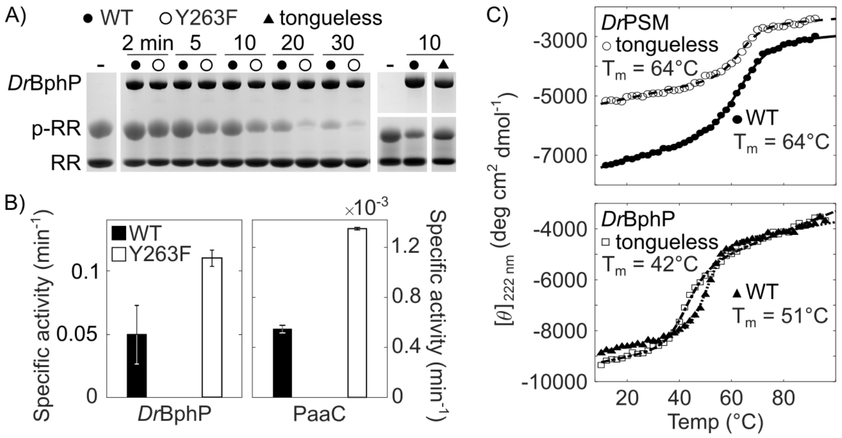

FIGURE 15 Effect of the tongue to biochemical activity and thermal stability in the Pr state. A) Time-resolved activity assay of *Dr*BphP phosphatase activity in WT and Y263F. On the right, the dark state activity of WT and tongueless variants after 10 min incubation. B) The specific dark state activities of WT and Y263F variants of *Dr*BphP and PaaC in the Pr state. C) Temperature-dependent CD signal at 222 nm in *Dr*PSM and PSM tongueless, and full-length *Dr*BphP WT and tongueless. The fitted T_ms reflect the thermal stability of the systems. Subfigures A and B were reproduced with modifications from publication II and I with permission from Springer Nature, and the subfigure C from publication III with permission from Elsevier.

PHY was 64°C, and therefore not dictated by the tongue (Fig. 15C). This suggests that even the dimer asymmetry of the tongueless variant revealed by the crystal structure (Fig. 14B) does not affect the thermal stability. However, in *Dr*BphP, where the OPM is included, the removal of the tongue resulted in nearly ten degrees lower T_m (Fig. 15C). The difference in the T_ms indicates that the tongue significantly increases the thermal stability of the system. Interestingly, the output module decreases the fluctuations of the tongue considerably (Fig. 13); and conversely, the tongue increases the stability of the OPM. The biochemical activity assays underline the functional coupling between these elements (Fig. 15), but the pH jump and thermal stability data together show that the coupling is also structural.

5.2 Stability of the Pfr state

5.2.1 The tongue stabilizes the Pfr state

In the Pfr state, the chromophore has isomerized to ZZE. In the tongueless systems, where the hairpin extension has been removed, the switching between the Pr and Pfr states was demonstrated spectroscopically (Fig. 16A). The tongueless systems could be switched back and forth between Pr and Pfr, and their illuminated state UV–vis spectra resembled that of CBD. There, the spectral shape is altered and absorption at NIR increases, although shift of the absorption maximum to 750 nm is not observed as in PSM or full-length systems. The chromophore iso-

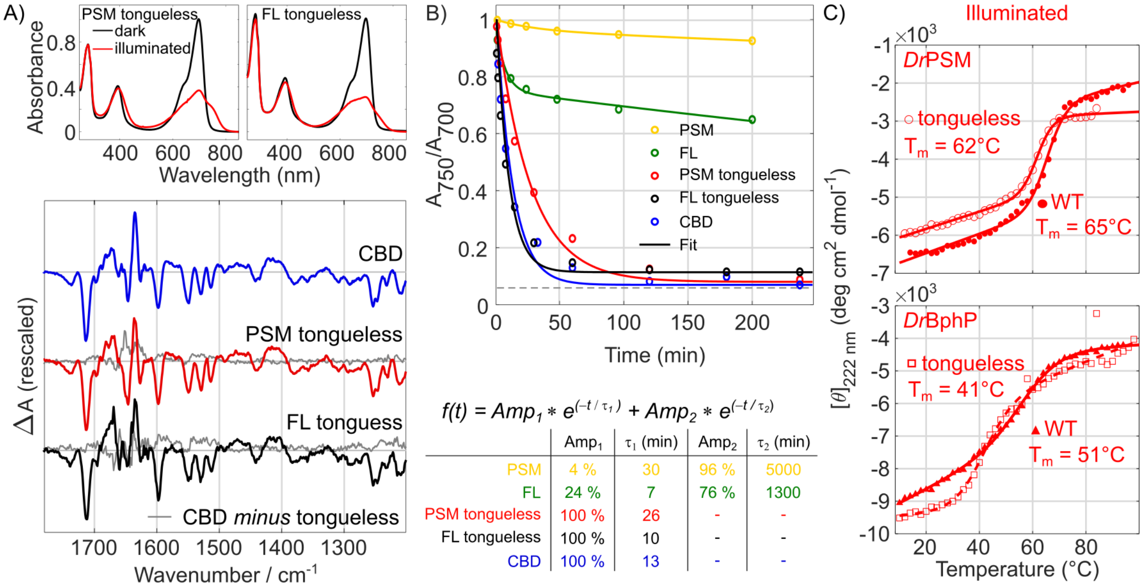

FIGURE 16 The spectroscopic features of the Pfr state A) The dark and illuminated UV–vis spectra and FTIR difference (Pfr *minus* Pr) spectra of tongueless fragments. *Dr*PSM tongueless and *Dr*BphP tongueless can be switched reversibly between the two states and have very similar spectra to CBD. B) The dark reversion of tongueless *Dr*PSM and *Dr*BphP show that they revert back in one phase with time constant of minutes like CBD, whereas their wild-type counterparts have bi-phasic and much slower reversion. C) Thermal CD data shows that the tongue increases the thermal stability of the illuminated state structure. Reproduced with modifications from publication III with permission from Elsevier.

merization was confirmed with urea denatured UV–vis spectra of the dark and illuminated state (Fig. S3 in III). Whereas CBD isomerizes to same extent as PSM (Lehtivuori *et al.* 2022), both tongueless systems yielded a bit smaller ZZE population than PSM.

The FTIR difference spectra of both tongueless fragments were nearly identical to CBD meaning altered photo-activated state in comparison to their WT counterparts (Fig. 16A). As in WT systems, in tongueless fragments the H-bonding interactions of the D-ring carbonyl increased from Pr to Pfr, observed as a smaller frequency. The D-ring carbonyl vibrations, shift from 1712 cm $^{-1}$ in Pr to 1685 cm^{-1} Pfr upon interactions with H201 and S468 sites (Ihalainen *et al.* 2018). In tongueless, the carbonyl vibrations were bleached and spread to a wider region as interactions with the tongue were not available. Also the signals at 1200–1250 cm^{-1} mainly originated from BV, according to isotope labelling (Fig. S5A in III). In tongueless, those signals deviated from the PSM and full-length WT, again suggesting a different BV environment. In conclusion, the tongueless spectra resembled the spectrum of CBD and significantly deviated from their wild-type counterparts, which suggests that without the tongue, the signal is trapped inside the CBD.

The thermal reversion from Pfr back to Pr in darkness was recorded with UV–vis spectroscopy. In PSM and FL, the reversion took hours, and the data required bi-exponential fit (Fig. 16B). However, when the tongue was removed, the dark reversion progress accelerated significantly, and took place in one phase with a time constant between 10 and 30 minutes, like in CBD. In PSM and FL, the first component was very similar to CBD and tongueless based on the time-constants of the fits. The bi-exponential dark reversion suggests that their Pfr state could be heterogeneous and consist of two sub-populations with different dark reversion rates, or that dark reversion takes place through an intermediate. Without the tongue, the long-lasting Pfr conformation could be reached, most probably due to missing interactions between the tongue and CBD, reflected to BV.

In PSM, the thermal stability of the wild-type slightly increased upon photoconversion, whereas in tongueless it slightly decreased from 64°C (Fig. 13C and 16C). In full-length *Dr*BphP, the T_m in the illuminated state remained the same as in dark, whereas in tongueless it decreased by one degree. Interestingly, the coupling between the tongue and the BV could be observed as a change in BV absorption upon melting of the tongue in PSM and full-length WT (Fig. 4 and S9B in III).

In dark and illuminated states, the thermal stability of full-length systems was significantly lower than PSM, which suggests that the HK unit decreased the thermal stability of the system (Fig. 13C and 16C). Moreover, the slope of *Dr*BphP WT in the illuminated state was smaller than in dark. This means that the denaturation was not as cooperative as in darkness, and the data possibly includes a multi phase denaturation process (Fig. 16C) (Vermeer and Norde 2000). This is in line with recently published cryo-EM structures of *Dr*BphP in the Pr and Pfr states (Wahlgren *et al.* 2022). In both structures, the PSM part is well resolved, but especially in the Pfr state, the HK appears very dynamic and heterogeneous, and is therefore only partially resolved. The denaturation curve of *Dr*BphP could reflect the heterogeneity of the Pfr state, where different sub-populations denature at different temperatures.

5.2.2 Light control of the enzymatic activity

*Dr*BphP is a red-light activated phosphatase (Multamäki *et al.* 2021), but has some activity also in the dark state (Fig. 15B). In the *Dr*BphP tongueless variant, the dark state activity was suppressed in comparison to WT (Fig. 15A). Upon illumination, the phosphatase activity of the WT is switched on, observed as diminished p-RR band (Fig. 17A). However, in the tongueless variant, the band remained equivalent to the dark state suggesting that the tongueless system cannot be switched on (Fig. 17B).

To confirm that the removal of the tongue did not distort the functionality of OPM, Chimera variants, which have the PSM from *Dr*BphP, OPM (HK) from Agp1, and acts as a light suppressed kinase (Multamäki *et al.* 2021), were applied to the activity assay. With the Chimera, non-phosphorylated RR was incubated in the reaction, and the dark state activity was observed as an appearance of p-RR band (Fig. 17A). In the illuminated state, the activity was suppressed and no p-RR band was observed. The Chimera tongueless revealed that the OPM can be functional even if the tongue is removed. The Chimera tongueless acts in darkness as a kinase, like the Chimera WT, but the activity could not be switched

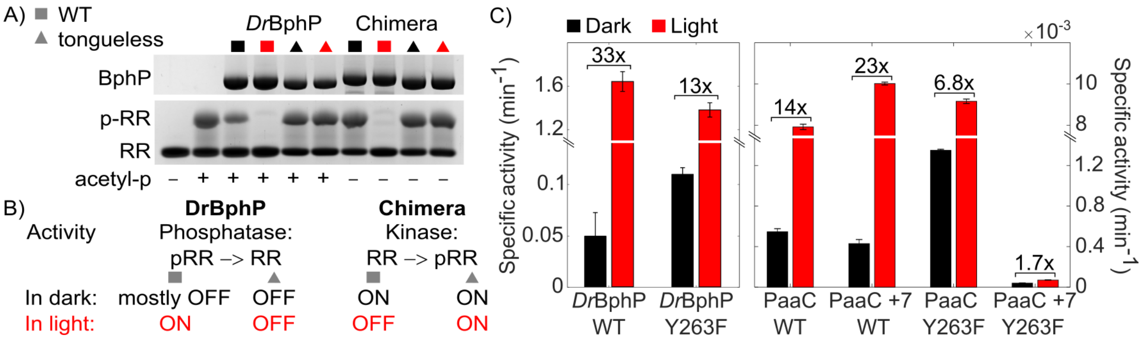

FIGURE 17 Light control of output activity A) The dark and illuminated state phosphatase activities of *Dr*BphP WT and Y263F, and adenylate cyclase activities of WT and Y263F variants of PaaC and PaaC +7 in dark and illuminated states. The y-axes have breaks to better display the low activity levels. The numbers above specific activities refer to the dynamic range of the system, i.e. ratio between the maximal and minimal activity. B) PhosTag activity assay with *Dr*BphP WT and tongueless and a light deactivated kinase Chimera WT and tongueless. The phosphatase activity of *Dr*BphP variants is observed as diminished p-RR band, and the kinase activity of Chimeras is observed as appearance of p-RR bands. C) The interpretation of the gel results. Subfigures A and B reproduced from publications III, with permission from Elsevier, and II with permission from Springer Nature, respectively.

off with red light (Fig. 17B).

The specific activities for *Dr*BphP WT and Y263F as well as for the four PaaC variants were determined in the dark and light states (Fig. 17C). In all of the systems, the activity increased upon light-activation. The ratio of the minimal and maximal activity in each system resulted in the dynamic range. The dynamic range reports how effectively the signalling of the system can be controlled, in this context, with light (Ziegler and Möglich 2015).

Above, the effect of Y263F mutation was shown to considerably increase the dark state activity (Fig. 15B). In all systems, the illumination increased the phosphatase or, in PaaC variants, the cyclase activity (Fig. 17C). For example, in *Dr*BphP WT, the specific activity increased from 0.05 min^{-1} to 1.65 min^{-1}, which resulted in a 33-fold increase in activation. In *Dr*BphP, the Y263F mutation slightly decreased the illuminated state activity, but in PaaC, the WT had a smaller specific activity in the illuminated state than the Y263F variant. Mainly due to the increased dark state activity, the dynamic range of Y263F was not more than half of the dynamic range or their WT counterparts (Fig. 17C).

In the artificial PaaC systems, the extra turn increased the dynamic range of the system from 14-fold activation to 23-fold (Fig. 17C). The PaaC +7 Y263F variant was an exception in the comparison as it had almost negligible cyclase activity in the dark and light states. The pH jump and FTIR data of PaaC +7 Y263F did not make a large difference to PaaC +7 WT and showed a rather stable tongue conformation, which correlates with the inhibited state of the variant.

The dynamic range of a system depends on the magnitude of the equilibrium shift between the active and inactive conformations upon perturbation, which here is a light signal (Tsai and Nussinov 2014). Therefore, in efficient systems, the perturbation and functional sites must be strongly coupled, which results in a large dynamic range. In the tongueless systems, the activity cannot be controlled with light, and therefore the dynamic range is close to one (Fig. 17A, B). In Y263F variants the dynamic range is less than half of the dynamic range of their WT counterparts (Fig. 17C). In both cases the decrease in the dynamic range results from decoupling between the chromophore and OPM. In the tongueless, the removal of tongue results in complete uncoupling of the system. In Y263F, the tongue is partially uncoupled from the chromophore in the dark state, observed as increased fluctuations of the tongue and resulting in increased dark state activity. In the illuminated state, the Y263F variants function nearly like WT systems.

The results show that the tongue is an essential allosteric element in controlling the output activity of these bacterial phytochromes with light. In the dark state, the strong coupling between chromophore and tongue is required to keep the tongue locked to β-sheet conformation. The tongueless systems showed that the tongue is not required to suppress the activity, but the increased activity of Y263F rather results from tongue fluctuations and strong coupling of the OPM to the tongue. Signal transduction from CBD through the helical spine to the OPM has been suggested (Gourinchas *et al.* 2017, Isaksson *et al.* 2021), but our results indicate that also that route would be controlled by the tongue. The tongue is needed to transduce the signal further from the CBD and to switch on (or off) the activity of the OPM upon light activation.

5.3 Signal propagation from the Pr to Pfr state

To study the photocycle (Fig. 4) site-specifically, a monomeric *Dr*PSM was labelled at selected sites with an IR-label pAzF (IV). The pAzF label has a vibrational frequency distinguishable from the protein fingerprint vibrations below 1750 cm^{-1} and sensitive to its electrostatic environment (Adhikary *et al.* 2017). Therefore, it allows detection of site specific changes during the photocycle (Hall *et al.* 2019, Krause *et al.* 2019) with time-resolved IR spectroscopy (see Sections 4.2.3 and 4.2.2). The label was successfully introduced to the tongue (at Y472) and to two sites in the chromophore binding pocket (Y176 and F203).

5.3.1 Response of the tongue

The residue Y472 is located in the tongue and therefore allowed to follow the refolding of the tongue during photoconversion (Takala *et al.* 2014a). The crystal structures predict a solvent exposed side chain in Pr and protein pointing conformation in the Pfr state (Takala *et al.* 2014a, Burgie *et al.* 2016). Therefore the refolding was expected to change the relative position and thus the electrostatic environment of the pAzF label at Y472. A difference signal at the label region (2060–2175 cm^{-1}), reporting a change, was detected for Y472pAzF (Fig. 18A).

The steady-state FTIR difference spectra were used to interpret the local environment of the label in the two states, Pr and Pfr. In solution, the pAzF signal consists of asymmetric azide stretch band which is accompanied by Fermi resonance bands on both sides (Gai *et al.* 2011, Thielges *et al.* 2011). The Fermi resonances re-

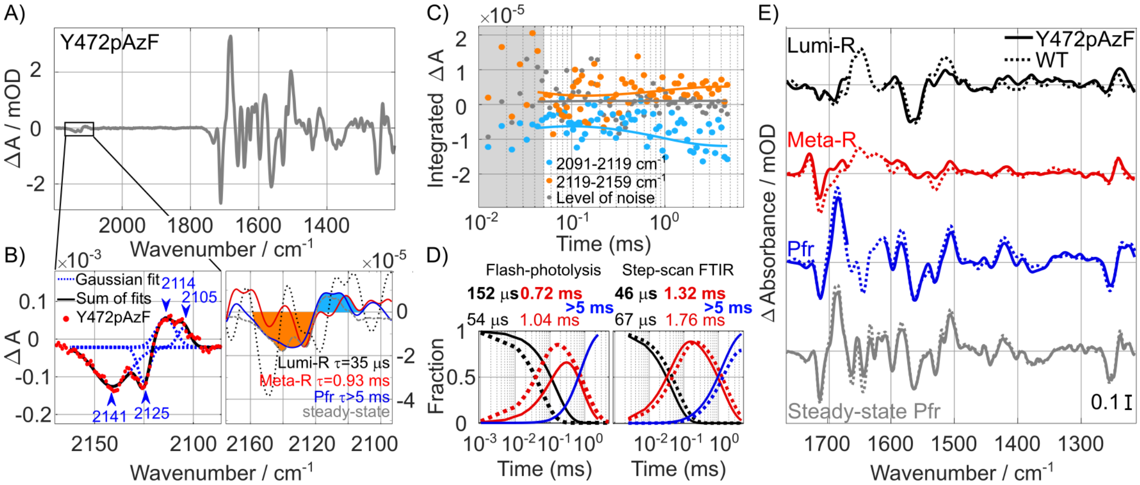

FIGURE 18 Spectroscopic analysis of the Y472pAzF variant A) The steady-state FTIR difference spectrum (Pfr *minus* Pr) of Y472pAzF. B) The left panel shows fit of the steady-state label signal with three Gaussian bands. The maxima of fits are shown in numbers. The right panel shows the intermediate states of the label extracted from the time-resolved step-scan data independently from other protein vibrations. The Lumi-R spectrum is shown in dotted line due to its low signal-to-noise ratio. For each intermediate, the decay times are indicated. With orange and light blue are shown the integrated are shown in C. C) The integrated signal of the label peaks as a function of time. The fits are performed according to the intermediate time constants. The gray area until 40 μs corresponds to noise in the data. D) Decay times and population development of intermediates in the chromophore and protein, extracted from the flash photolysis and step-scan data, respectively. The time constants of Y472pAzF are shown above in bold and WT in normal font below. E) The intermediate and steady-state spectra of Y472pAzF and WT in the fingerprint region. Reproduced with modifications from publication IV with permission from the Royal Society of Chemistry.

sult from vibrational coupling of the asymmetric azide stretch with combination modes of the phenyl modes and symmetric azide stretch of pAzF (Lieber *et al.* 1963, Zhang *et al.* 2018). The position of all contributing bands was revealed by fitting the Y472pAzF difference signal with a sufficient number of Gaussians (Fig. 18B) (Waegele *et al.* 2011, Maj *et al.* 2016, Zhang *et al.* 2018). Based on previous studies, the maximum frequency of the asymmetric azide stretch was assumed to appear within the limits of 2110–2130 cm^{-1} (Maj *et al.* 2016, Zhang *et al.* 2018). In this range, an upshift of the frequency indicates increased H-bonding strength, and the bands outside the range are identified as Fermi resonance bands (Choi *et al.* 2008, Wolfshorndl *et al.* 2012, Maj *et al.* 2016, Zhang *et al.* 2018).

In the steady-state FTIR difference spectrum of Y472pAzF, the pAzF signal maximum shifted from 2125 cm^{-1} in Pr to 2114 cm^{-1} in Pfr (Fig. 18B). The azide maxima are accompanied by Fermi resonance bands at 2141 cm^{-1} and 2105 cm^{-1} in Pr and Pfr, respectively. The decrease in pAzF frequency from Pr to Pfr indicated disappearing of an H-bond or decrease in H-bonding strength (Choi *et al.* 2008, Wolfshorndl *et al.* 2012, Maj *et al.* 2016, Zhang *et al.* 2018). The detected change is supported by the crystal structures: in Pr, the residue forms a strong

H-bond, most probably with solvent H_2O, and the interactions change in Pfr, most probably upon refolding of the tongue, when the residue turns towards the protein moiety. In the Pr state, the label did not reveal a difference between the "open" and "closed" conformations of the tongue, which could be explained by solvent exposed conformation of the residue, and therefore a similar local environment in both cases. However, the relatively small signal size could in principle be affected by the tongue fluctuations.

The time-resolved step-scan FTIR was measured from 2.5 μs to 4.7 ms to capture early and late steps of the photocycle (Kübel *et al.* 2020). The label region (2060–2175 cm^{-1}) and the protein fingerprint region (1200–1765 cm^{-1}) were analyzed separately using global analysis with suitable number of components to extract the previously observed species associated difference spectra (SADS) of the intermediate states Lumi-R and Meta-R and Pfr from the data (Stokkum *et al.* 2004, Ihalainen *et al.* 2018). The SADS were interpreted to the corresponding intermediate states based on their time constants.

The time-resolved data of the label region were utilized to detect in which time scales the observed changes between the Pr and Pfr states in the labelled positions arise. The fingerprint region was used to compare the photocycle of the labelled systems with the non-labelled *Dr*PSM$_{mon}$ to understand the effect of the labelling to the photocycle and thus the role of the native residue. Flash-photolysis in the visible region was recorded separately to study response of the chromophore independently from the label and protein moiety. The separate time-resolved data from the chromophore, the label and from the whole system allowed direct comparison of the time scales of the photocycle at different sites.

The global analysis of the label region in Y472pAzF showed that the label signal evolves in three components (Fig. 18B). This means that the label site responded to the photoactivation in all three phases of the photocycle, Lumi-R and Meta-R, and finally Pfr. The intensity of the label signal in Y472pAzF was small, and therefore the first intermediate state, Lumi-R (τ = 35 μs) spectrum of the label was dominated by relatively large noise. Yet, integration of the negative and positive peak regions in all time points reveals that the signal appears already during tens of microseconds upon changes at the label site, suggests that the tongue responds to the photosignal already during the first stage of the photocycle (Fig. 18C). In the second intermediate Meta-R (τ = 0.93 ms), the label spectrum had four peaks. Two negative and two positive signals located at similar positions as in the steady-state difference spectrum of the label, but with different relative intensities (Fig. 18B). The last Pfr spectrum (τ > 5 ms) matched the steady-state signal, which suggests that the changes in the tongue were finalized within the experimental time frame (4.7 ms). The intermediate spectra of pAzF were different from the Pfr spectrum, which suggests that the tongue refolding is a complex process during the photocycle, and is finalized during Meta-R to Pfr transition, as previously suggested (Ihalainen *et al.* 2018).

The global analysis of the protein fingerprint region and chromophore by flash-photolysis showed that photocycle in Y472pAzF variant proceeded very similarly to the wild-type *Dr*PSM$_{mon}$ (Fig. 18E). The spectral features of the intermediate states resembled the unlabelled system, and most of the usual characteristics, for example the positive band at 1730 cm^{-1} in Meta-R, were present.

The photocycle also proceeded in similar time scales as the wild-type (Fig. 18D). In flash-photolysis as well as in step-scan data, the Meta-R state of Y472pAzF decayed slightly faster than the wild-type, which could possibly be explained by the less pronounced 1712 cm^{-1} signal. Like in WT, also Y472pAzF the spectral features of the fingerprint region finalized within 5 ms, which is seen as the matching step-scan and steady-state Pfr spectra (Fig. 18E). All peaks were not as well resolved with 8 cm^{-1} spectral resolution in step-scan as in 2 cm^{-1} resolution steady-state spectra. Also the chromophore finalized the photocycle within 5 ms in Y472pAzF, and also in the two other variants (Y176pAzF and F203pAzF) (Fig. S9 and S10 in IV). The highly similar photocycle of the Y472pAzF variant means that either the hydroxyl group of the native tyrosine is not crucial for the photocycle or that the azide group can replace its function. More importantly, the unaltered photocycle tells that the changes and time scales reported by the label are real and trustworthy.

5.3.2 Response of the chromophore binding pocket

Y176pAzF and F203pAzF provided information on the role of the hydrophobic pocket around the chromophore (IV). According to crystal structures, their side chain orientation changes during photoconversion, and in the Pfr state, the OH-group of the Y176 forms a chromophore-stabilizing H-bond with the C-ring propionate (Yang *et al.* 2008, Takala *et al.* 2014a, Burgie *et al.* 2016). With Y176pAzF, formation of an H-bond was demonstrated as the label frequency shifted from 2112 cm^{-1} in Pr to 2125 cm^{-1} in Pfr (Fig. 3A in IV). The global analysis of the label region revealed that the label signal develops in two components (Fig. 3B in IV). The first response is observed in Meta-R state, and the H-bond is finalized in the last phase of the photocycle (Fig. 19). Labelling of Y176pAzF altered the photocycle to some extent (Fig. 3E in IV), but the position was sufficient to provide information on the local changes and the role of the residue in the photocycle.

In F203pAzF, the label was in action in all three intermediate states, and most probably the label experienced a strong H-bond in the Pfr state (Fig. 4 in IV). The time constants of the intermediate states observed at the label were very similar to the *Dr*PSM WT photocycle. However, label at F203 accelerated the photocycle by completely diminishing the Meta-R state in the chromophore as well as in the protein moiety (Fig. 4D-F in IV). This was observed both in the time constants from the global analysis as well as completely missing Meta-R specific spectral features, like the positive signal at 1730 cm^{-1}.

The pAzF label at F203 did not provide site-specific information that would be convertible to action of the native residue in the wild-type photocycle. On the other hand, the labelling revealed information on the role of the native phenylalanine in the photocycle. During the photocycle, the D-ring rotates and its carbonyl group forms new interactions with H201 that flips towards D-ring. In Pfr, this interaction results in carbonyl vibration at 1685 cm^{-1}. In Meta-R, the D-ring has rotated, but the carbonyl group is not yet flipped towards it. As a result, the lack of H-bond to the H201, the frequency of the D-ring carbonyl upshifts to 1730 cm^{-1} (Ihalainen *et al.* 2018, Takala *et al.* 2018). It is possible that in the wild-type system, hydrophobic F203 is the residue that hinders the movement of H201 during Meta-

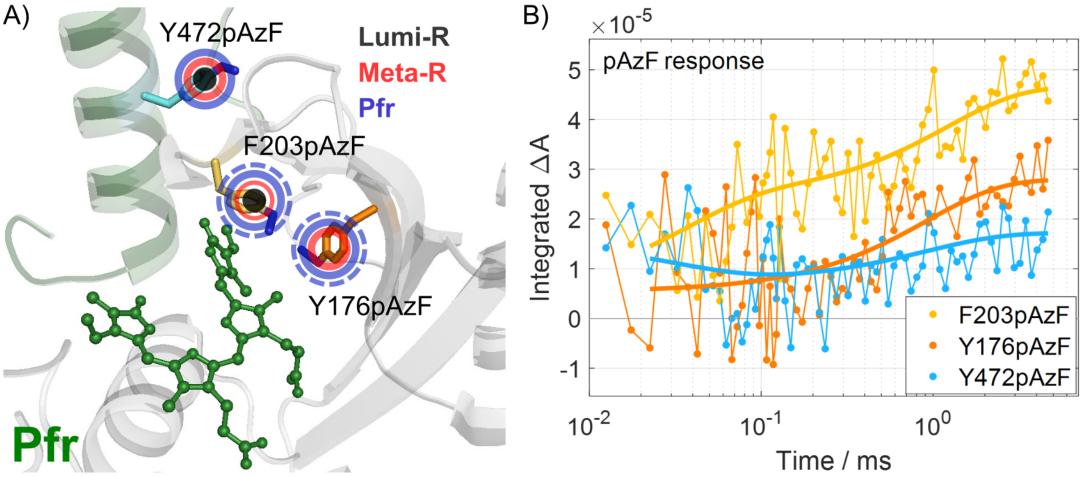

FIGURE 19 The contribution of the three labelled position to the photoactivation of *Dr*PSM. A) Position of the native residues, which were labelled, in the Pfr state (PDB: 5C5K). The responses of the labels to the photocycle are highlighted with colored circles that correspond to the intermediate states. The dashed blue line in F203pAzF and Y176pAzF indicate that in those variants, further equilibration took place after the chromophore had finalized its photocycle in 5 ms. B) The integrated label signals (region of 2100-2160 cm^{-1}) and their fits (solid line) from the three labelled variants. The time-constants of the fits were acquired from global analysis of the label region. Reproduced from publication IV with permission from the Royal Society of Chemistry.

R and thus delays the formation of the H-bond to Meta-R to Pfr transition. The azide group brings polarity to the F203 position, and thus lowers the barrier of the H201 movement. As a result, F203pAzF accelerates the photocycle and suppresses the formation of the Meta-R state in chromophore-protein interactions.

5.3.3 Detection of local electrostatic changes using IR probes

The benefit of using IR spectroscopy in combination with an IR label is yielding information concomitantly on the global protein mechanism from the fingerprint region and on site-specific changes in the label environment from the signal around 2100 cm^{-1} (Blankenburg *et al.* 2019). Furthermore, the separate time-resolved data from the chromophore, from the label, and from the system as a whole allowed comparison of the time scales of the photocycle at different sites.

The use of pAzF in site-specific tracking of the changes during the photocycle was successfully demonstrated in *Dr*PSM. The labels in the three different positions, Y47pAzF, Y176pAzF, and F203pAzF, reported on the local changes during the photocycle (Y472pAzF, Y176pAzF) or on the role of the native residue (F203pAzF, Y176pAzF) (Fig. 19). Y472 was a successful location as there the native residue did not have a significant role that would have been disturbed by replacement with the label. On the other hand, the labels in the chromophore binding pocket demonstrated that some sites are less tolerant for changes than other. This was also observed in the six other labelled sites (Fig. 9B) that were not used in the time-resolved experiments: some could not be purified due to structural impairment, and some did not report any changes (see Supplementary information in IV). However, with Y176pAzF the formation of a strong H-bond during the last phase of the photocycle was observed. F203pAzF revealed valuable information on the role of the native hydrophobic residue in formation of the Meta-R intermediate.

Based on our results, broad guidelines for IR-labelling to detect photocycle (or other structural changes) can be formatted. The azide group label has a large dipole moment, and therefore it can distort the structure or function if inserted in a hydrophobic pocket or to replace a hydrophobic residue, respectively. The azide group can accept but not donate an H-bond and therefore it necessarily cannot fulfil a role of for example a tyrosine. Therefore, the label should not be inserted to the center of action to replace conserved residues, for example like Y263, but rather to a neighbouring residue close to action. Mainly residues with an aromatic ring were replaced, but also other residues were shown to be suitable for labelling (see SI in IV).

The azidophenylalanine label is superior to other probes due to its high extinction coefficient (Choi *et al.* 2008, Ma *et al.* 2015). Furthermore, the pAzF frequency shifts reliably report on the changes in the H-bonding strength to the label (Wolfshorndl *et al.* 2012). However, challenges of using pAzF as a reporter molecule include its inconsistent responses to (a)polarity of the environment (Maj *et al.* 2016) as well as complicated accidental Fermi resonance bands (Wolfshorndl *et al.* 2012, Zhang *et al.* 2018). Solvatochromic models of azidophenyls have been built, but the models underline their complexity (Choi *et al.* 2008, Wolfshorndl *et al.* 2012) and work better with more straightforward nitrile probes (Bagchi *et al.* 2012, van Wilderen *et al.* 2014, Zhang *et al.* 2016). The Fermi resonance bands complicate the lineshapes and thus interpretation of the pAzF signals (Suydam *et al.* 2006, Lipkin *et al.* 2011, Fried and Boxer 2015). The Fermi resonances have successfully been suppressed by modifications of the probe (Lipkin *et al.* 2011, Zhang *et al.* 2018). On the other hand, the resonance bands of azide probes could yield additional information for example about the (a)polarity of the site. In cyano probes, the Fermi resonances are an indicator of the H-bonding status (Rodgers *et al.* 2017). Deeper understanding of the vibrational bands would allow utilizing the full potential of the azido probes to obtain site-selective signal propagation in sensory proteins.

6 CONCLUSIONS

Phytochromes are allosteric systems that relay light cues into structural changes that control the biochemical activity of the output module. In this thesis, structural and functional properties of a bacterial phytochrome from *D. radiodurans* were studied by means of spectroscopic, biochemical and structural methods. The main attention was focused on the hairpin structure, often referred as the "tongue", that extends from an interconnecting domain to the vicinity of the chromophore. It has been shown to refold from β-sheet to α-helix upon red light activation. Here, the structural and dynamic properties of the tongue and its role in signal transduction were unraveled. The results highlight the effects of the tongue on the structural stability, photoactivation and regulation of the output activity.

A straightforward and elegant method was developed to study solvent access to the protein interior by means of rapid pH change and UV-vis spectroscopy. The method was used to study the properties of phytochromes, but can be expanded to any system with pH-dependent absorption properties, for example another common photosensor rhodopsins. In phytochromes, relaying on the protonation dependent absorption profile of the chromophore, the method allowed studying the solvent access to chromophore binding pocket gated by the tongue. Based on existing structural data and the results, a model of the solvent access gating tongue was created. There, the tongue fluctuates between "closed" and "open" conformations in the resting state. The former blocks the solvent access to the chromophore binding pocket, and the latter allows it, which can be observed as deprotonation of the BV.

The tongue was shown to be stabilized by the OPM in the full-length systems. On the contrary, the dynamics of the tongue increased, when it was decoupled from the chromophore by a mutation. The tongue, or its fluctuations, did not seem to affect the chromophore environment in the dark state. However, the tongue fluctuations increased the dark state activity in the native systems and also in an artificial variant with an adenylate cyclase output module. The role of the tongue became crucial in the illuminated state where it is needed to finalize the chromophore environment in the binding pocket, and to stabilize the Pfr state. Without the tongue, the signal appeared "trapped" within the CBD, which also resulted in fast thermal reversion to the Pr state in darkness. Furthermore, the signal was not relayed to the output module, showing that the tongue is crucial for controlling the output activity. On the other hand, when the tongue couples the BV and OPM, activity yield similar to WT can be achieved even with an artificial system. To study the action of the tongue during the photocycle site-specifically, a vibrational labelling with pAzF and time-resolved step-scan FTIR spectroscopy were applied. An early response of the tongue to photoconversion was observed within tens of microseconds, with final structural changes occurring during the final phase of the photocycle, hand-in-hand with the chromophore.

The results in this thesis provided essential knowledge of photoactivation processes in bacteriophytochromes. The tongue is in a central role in the signal transduction process of phytochromes. Therefore, effort to understand the control of the refolding, and how the changes in tongue are relayed to the output module is needed next. Furthermore, the tongue seems to affect also the biphasic dark reversion rates. Especially for optogenetic applications, knowing the rate of diminishing or increasing activity in darkness is essential, and regulated by the tongue, it can differ from the dark reversion rates of the chromophore. In case of phosphatase activity, the time-resolved method introduced here can be accommodated for that purpose. The results also demonstrated that the dynamic range of an optogenetic tool can be decreased or increased by modifying the chromophore-tongue interactions as well as the connection between PSM and OPM, also in an artificial system.

Naturally, a complete picture of the signal transduction mechanism requires computational studies that visualize the signal transduction pathways on an atomic level in the form of free energy landscapes. At this time however, the computing power is not sufficient for the size and time-scales of this type of systems. When the day comes, simulations require experimental observables derived from the studies presented in this thesis which will provide guidelines for choosing correct physical models. This could open an avenue in understanding histidine kinase activation mechanisms, in general.

Acknowledgements

This thesis was carried out at University of Jyväskylä, Department of Biological and Environmental Science and Nanoscience center, in Division of Cell and Molecular Biology. The funding for the work between 2020-2023 was awarded by the Graduate School for Doctoral Studies. I am thankful for this funding which provided me the opportunity to carry out my PhD work in Jyväskylä.

I had a great privilege to join the research group of Prof. Janne Ihalainen already during my Master's studies in the Department of Biological and Environmental Science. Since day one, I felt very welcomed in the group. During the summer of 2018, I got to experience the fun of doing science as an intern, and the spark has lasted to this date. When I was offered a chance to accomplish my PhD and continue research in the group, the decision was rather easy. Now, I can also say that it was the right one. During the past five years, I have worked with very smart, inspiring, and fun people, had intriguing discussion about science and beyond, and shared offices with warmhearted people. All the people on the way made this experience as good as it could have ever been.

First and foremost, I would like to thank my supervisors, Prof. Janne Ihalainen and Dr. Heikki Takala. During this project, they have been strong support, forward pushing power, great teachers, and available when I needed help or reassurance. Janne, thank you for all the trust and believe you had in me since beginning. You saw the potential in me, and your actions and words often gave me a feeling that I can do anything. Maybe not anything, but many times encouraged by you, I accomplished goals, and wrote codes which I did not think I had in me. I enjoyed our countless conversations full of excitement, explaining results (one way another), and turning them into stories for papers. Thank you also for all the non-scientific lessons in squash, skiing, and life. Heikki, thank you for being the grounding system and realist during this project, especially when the speed was accelerating. Your calmness often reminded that everything cannot and does not have to be done at once, which saved me from a lot of trouble. I also appreciate your attention to detail and great sense of humour. Those made planning experiments, learning new methods and taking comments very enjoyable with you.

I also want to express my deepest gratitude to my co-workers in co-authors. Jessica Rumfeldt put a huge effort into all four publications. Jessica, without your experience and help, my thesis and past few years would have been very different. Thank you for taking the time to discuss protein folding and denaturation, temperature-dependent experiments with laws of thermodynamic on the side. Furthermore, thank you for all the other the office conversations. We solved many knots and made the world a little better on the way. Special thanks for the title and language check on the thesis. And for making me like running, at least for a while. Alli Liukkonen, thank you for putting up and managing a lab, where working was easy, straightforward, and everything was though out. The bar for my future labs is high, and I will do my best to reach the level of organization that you have. Thank you also for welcoming an unknown student into your office

and listening my excitement and disappointments, and always putting a smile on my face. I also want to thank Heikki Häkkänen for sharing some of your years of experience with me and introducing me to laser lab and building up a time-resolved setup. I am very proud of the effort we put into the flash-setup together. With Brigitte Stucki-Buchli, we had a chance to meet only shortly. However, she left me a great and fun project to work with and an excellent protocol, and I am very thankful for that. The project was a big turning point for what I wanted to do, it gave me a flying start for my theses, and without it I probably would not be here.

I would also like to thank the rest of the HoT'n'JuIcy group. They have pushed my work forward, directly or indirectly, and have always been very good company to be around. Special thanks for Iida Kettunen and Elina Multamäki. Iida, thank you for the countless hours together in the lab and for being the best peer support. Elina, thank you for helping me to master PhosTag in one of your excursions to Jyväskylä.

I would also like to thank the collaborators, the group of Prof. Tilman Kottke in Bielefeld University and the group of Prof. Andreas Winkler in Technical University of Graz. Both of the collaborations were fruitful in publications but also in eye-opening discussions. The trip to Bielefeld was one of the highlights of my early scientific career. I am also very happy that we could meet and discuss with Andreas in real life, although Covid had other plans.

Finally, I would like to thank my friends and family. During my Master's studies in Jyväskylä, I made life long friends, who have kept me going during the PhD journey. They understand, to some extent, what I have been doing, and having friends outside of work to share challenges and success with was very valuable. Peipet, I am forever grateful that biology brought us together and having you in my life. After deciding to stay another four years in Jyväskylä, the second best decision was to take up Finnish baseball again. Thanks to Pesisgisulit for the space where I did not have to be a scientist or think about science. I want to thank especially the teammates who turned into friends. With you, the most fun and unexpected things happen and I love it. Last, I want to thank my family. Mum and dad, thank you for letting me find my path and supporting me and my decisions, even when it was not easy for you. I know you always have my back.

YHTEENVETO (RÉSUMÉ IN FINNISH)

Jalalla koreasti valon tahtiin: bakteerifytokromin signaalinvälitysreitit

Luonnossa eliöiden kuten kasvien, eläinten ja mikrobien on havainnoitava ja sopeuduttava elinympäristöönsä. Yksi tärkeistä eliöiden kasvua ja käyttäytymistä ohjaavista ympäristötekijöistä on valo. Valon aistiminen tapahtuu solutasolla ja vaatii erityisiä työkaluja, joita kutsutaan valoreseptoreiksi. Esimerkiksi ihmisen valoreseptorit löytyvät silmästä ja mahdollistavat näkemisen. Paikallaan kasvavilla kasveilla niitä taas löytyy useista kasvin osista, mikä maksimoi ympäristön havainnointikyvyn. Solut, joilla ei ole valoreseptoreita, eivät voi aistia valoa.

Aurinko säteilee valon eri aallonpituuksia sisältäen UV-valon, näkyvän valon ja infrapunavalon aallonpituudet. Yksi valoreseptori ei riitä kattamaan koko auringon spektriä, vaan niitä on useita erilaisia. Ne aistivat valon eri aallonpituuksia ja yhdessä kattavat miltei kaikki aallonpituudet. Eri valoreseptorit myös toimivat soluissa eri tavoin. Sekä valon havaitsemismekanismi että eteenpäin välitetty viesti voi olla erilainen. Kaikille on kuitenkin yhteistä fysikaalisen valosignaalin kääntäminen solulle ymmärrettävään muotoon eli biokemialliseksi signaaliksi. Solussa tämä signaali laukaisee sen toimintaa muuttavan ja lopulta koko eliön toimintaa ohjaavan tapahtumasarjan vallitsevien valo-olo-suhteiden mukaisesti. Tätä tapahtuu luonnossa, minkä lisäksi valoreseptoreja voidaan valjastaa esimerkiksi biolääketieteen käyttöön. Optogenetiikassa soluihin siirrettyjä valoreseptoreita käytetään laukaisemaan haluttu toiminto solussa valon avulla.

Fytokromit ovat punaista ja pidemmän aallonpituuden punaista eli kaukopunaista valoa havaitsevia valoreseptoreja kasveissa, bakteereissa ja sienissä. Kasveissa ne säätelevät esimerkiksi itämistä ja varjojen välttelyä. Juuri fytokromien ansiosta esimerkiksi loppukesän auringonkukat kasvavat pelloilla tasakorkuisina, varjostamatta toinen toisiaan. Useiden ominaisuuksiensa vuoksi fytokromeissa on myös paljon potentiaalia optogeneettisiin sovelluksiin. Sekä kasvien kasvun säätelyn ymmärtäminen että fytokromien käyttö sovelluksissa vaatii ymmärrystä fytokromien toiminnasta ja säätelystä.

Fytokromit, kuten muutkin valoreseptorit, ovat proteiineja, jotka koostuvat kymmenistä, usein sadoista aminohapoiksi kutsutuista rakennuspalikoista. Aminohappoketju rakentuu solussa geneettisen koodin mukaisesti 20 erilaisesta aminohaposta, joiden järjestys määrittää proteiinin kolmiulotteista rakennetta. Aminohappoketjun lisäksi kaikkiin valoreseptoreihin on sitoutunut erillinen molekyyli, kromofori, joka on systeemin valoa "imevä" eli absorboiva osa. Luonnossa fytokromit ovat usein dimeerejä, eli kaksi samanlaista aminohappoketjua niihin kiinnittyneine kromoforeineen on sitoutunut yhteen ja toimivat yhdessä.

Vaikka fytokromissa kromoforin sitova proteiiniosa on yhtenäinen aminohappoketju, se voidaan kuitenkin rakenteellisesti jakaa kahteen eri yksikköön. Valosensoriyksiköstä löytyy kromofori ja se on ylipäätään hyvin samankaltainen eri lajien fytokromeilla. Toiminnallinen yksikkö taas on fytokromin biokemiallisesti aktiivinen, signaloiva osa, joka voi olla toiminnaltaan hyvinkin erilainen eri lajien fytokromeissa. Valosensoriyksikkö voidaan vielä jakaa rakenteellisesti kahteen eri osaan: kromoforin sitovaan osaan sekä fytokromispesifiseen osaan, joka yhdistää rakenteellisesti kromoforin ympäristön toiminnalliseen yksikköön. Fytokromispesifisessä osassa on erikoinen uloke, joka kuroutuu silmukan tai hiuspinnin tavoin lähelle kromoforia.

Fytokromin toiminta perustuu valon absorptioon kromoforissa ja siitä seuraaviin rakenteellisiin muutoksiin, jotka lopulta säätelevät toiminnallisen yksikön aktiivisuutta. Fytokromit vaihtelevat edestakaisin kahden tilan, lepotilan ja valoaktivoidun tilan välillä. Lepotilassa punaisen valon absorptio kromoforissa aiheuttaa valokemiallisen reaktion ja muuttaa kromoforin rakennetta. Tämä taas johtaa muutoksiin kromoforin ja sitä ympäröivien aminohappojen vuorovaikutuksissa ja sensoriyksikön kolmiulotteisessa rakenteessa. Lopulta rakenteellinen uudelleenjärjestäytyminen muuttaa toiminnallisen osan aktiivisuutta eli kytkee sen päälle tai pois päältä. Systeemi palautuu valoaktivoidusta tilasta lepotilaa, kun se absorboi kaukopunaista valoa tai on pimeässä riittävän kauan. Palauduttuaan, systeemi voidaan jälleen aktivoida punaisella valolla. Joitain rakenteellisia muutoksia kahden tilan välillä on pystytty selvittämään. Kuitenkaan tarkkaa rakenteellista mekanismia, jolla systeemi päätyy valoaktivoituun tilaan, ja miten sensoriyksikkö säätelee toiminnallisen yksikön aktiivisuutta ei tunneta.

Tässä työssä tutkittiin erään bakteerifytokromin signaalinvälitysreittejä eli niitä proteiinin paikallisia rakenteellisia muutoksia, jotka ovat välttämättömiä systeemin aktiivisuuden säätelemiseksi. Erityinen huomio työssä oli hiuspinniulokkeessa. Ulokkeesta erikoisen tekee sen rakenteen muutokset lepotilan ja valoaktivoidun tilan välillä. Uloke nimittäin laskostuu uudelleen β-levystä α-kierteeksi valoaktivaation seurauksena, vaikka laskoksen tyypin sanotaan useimmiten määräytyvän pelkän aminohappojärjestyksen perusteella. Työn tavoitteena oli ymmärtää ulokkeen roolia ja uudelleenlaskostumisen merkitystä toiminnallisen yksikön aktiivisuuden säätelyssä.

Työssä hyödynnettiin useita eri menetelmiä. Valtaosa kokeista tehtiin puhdistetusta nesteeseen liuenneesta fytokrominäytteestä eli solujen ulkopuolella. Muokkaukset tehtiin proteiinin geeniin, minkä jälkeen niitä tuotettiin bakteereissa hyödyntämällä bakteerien proteiinin tuottokoneistoa. Bakteerien hajottamisen jälkeen fytokromiproteiinit erotettiin muista vesiliukoisista proteiineista rakenteeseen ja kokoon perustuvia puhdistusmenetelmiä käyttämällä. Fytokromien valovaihtuvuutta, eli absorptio-ominaisuuksien ja rakenteen muutoksia punaisen valon absorption seurauksena, tutkittiin spektroskooppisin menetelmin. Spektroskopiassa näytteen ominaisuuksia tutkitaan valon avulla mittaamalla, kuinka paljon ja mitä valon aallonpituuksia näyte absorboi. Näytteen absorboimat aallonpituudet muodostavat spektrin. Spektrin muodosta ja sen muutoksista eri valo-olosuhteissa sekä näytteiden välillä voidaan tehdä päätelmiä näytteen omi-naisuuksista ja toiminnasta. Näkyvän valon alueella absorboi pelkkä kromofo-ri. Pidemmillä aallonpituuksilla, niin kutsutulla infrapuna-alueella, absorboivat kromoforin lisäksi myös proteiinin aminohapot. Siksi infrapunaspektroskopiaa käytettiin koko fytokromissa tapahtuvien rakenteellisten muutosten selvittämiseen.

Ensimmäisessä osatyössä kehitimme menetelmän, jolla voidaan seurata liuoksen pääsyä proteiinin sisälle. Menetelmä hyödyntää näkyvän valon absorptio-ominaisuuksia ja niiden muutoksia nopean pH:n muutoksen seurauksena. Fytokromissa kromofori absorboi näkyvää punaista valoa, mutta absorption määrä laskee kun kromofori joutuu korkeaan pH:hon ja luovuttaa protoneita liuokseen eli deprotonoituu. Menetelmää käyttäen näytimme, että fytokromijoukossa kaikki kromoforit eivät deprotonoidu samanaikaisesti liuoksen nopean pH:n nousun jälkeen. Osoitimme tämän johtuvan siitä, että fytokromin lepotilassa uloke säätelee liuoksen pääsyä proteiinin sisälle kromoforin sitovaan taskuun. Uloke voi olla "kiinni", mikä estää veden pääsyn kromoforin ympäristöön, tai "auki", jolloin vesi pääsee sisään. Fytokromeja voidaan muunnella ja mutatoida. Tiettyjen muutosten seurauksena uloke suosii "auki"-rakennetta, kun taas täysin villityypin eli muuntelemattomassa fytokromissa "kiinni" on ulokkeen vallitseva tila. Mitä enemmän uloke on "kiinni"-tilassa, sitä stabiilimpi se on, sillä ulokkeen "aukeaminen" on seurausta sen lisääntyneestä liikehdinnästä.

Toisessa osatyössä määritimme, kuinka tehokkaasti tutkimamme bakteerifytokromi pystytään aktivoimaan valolla. Lepotilassa tutkimamme bakteerifytokromi on miltei kokonaan epäaktiivinen ja punainen valo kasvatti sen aktiivisuuden 33-kertaiseksi. Samalla tutkimme myös keinotekoista fytokromia, jossa tuttu valosensoriyksikkö oli yhdistetty erilaisesta reseptorista peräisin olevaan toiminnalliseen yksikköön. Pystyimme näyttämään, että tällainen keinotekoinen systeemi aktivoituu lähes yhtä tehokkaasti kuin villityyppi, vaikka biokemiallinen toiminta onkin eri. Toisessa osatyössä osoitimme myös, että biokemiallinen aktiivisuus on kytkeytynyt ulokkeen liikehdintään, mikä pystyttiin havaitsemaan epäaktiivisessa lepotilassa. Lisääntynyt liikehdintä johti toiminnallisen yksikön osit-taiseen aktivoitumiseen ja siten epäspesifiseen signalointiin niin villityypin kuin keinotekoisessa fytokromissa. Näytimme myös aiemmin kehittämäämme mene-telmää käyttäen, että toiminnallisella osalla on rooli ulokkeen vakauttamisessa.

Kolmannessa osatyössä ulokkeen roolia tutkittiin poistamalla se kokonaan. Ratkaisimme ulokkeettoman fytokromin kolmiulotteisen kiderakenteen lepotilassa, minkä avulla pystyimme näyttämään, että ulokkeen liikehdintä ei oikeastaan vaikuta kromoforin ympäristöön. Lepotilassa ulokkeen merkittävin rooli vaikutti olevan koko fytokromin rakenteen tukeminen. Pystyimme osoittamaan, että valoaktivoitumisessa ja biokemiallisen aktiivisuuden säätelyssä uloke on välttämätön. Ilman uloketta valon laukaisema signaali ei pääse etenemään kromoforin sitovasta osasta eteenpäin ja näin ollen myöskään biokemiallista aktiivisuutta ei voida säädellä valon avulla. Siksi ulokkeen aiemmin havaitut rakenteelliset muutokset vaikuttaisivat olevan välttämättömiä signaloinnille.

Neljännessä osatyössä käytettiin infrapunaspektroskopiaa sekä siihen soveltuvaa reportterimolekyyliä signaalin etenemisen havaitsemiseen. Reportterimolekyyli asetettiin tarkasti valittuihin paikkoihin fytokromissa, mm. ulokkeeseen sekä kromoforin läheisyyteen. Reportterimolekyylin avulla fytokromien rakennemuutoksia pystyttiin havaitsemaan paikkaspesifisesti. Lepotilan ja valoaktivoidun tilan välillä on nopeita välitiloja, jotka katoavat mikro- ja millisekuntien kuluessa valon absorption jälkeen. Mittaamalla valoaktivaation aiheuttamia muutoksia aikaerotteisesti pystyimme osoittamaan, että uloke on toiminnassa molemmissa välitiloissa, ja sen rakennemuutokset ovat valmiita yhtä aikaa kromoforin kanssa. Onnistuimme näyttämään, kuinka reportteria voidaan parhaimmillaan hyödyntää proteiinin rakennemuutosten tutkimisessa. Reportterin käyttö ei kuitenkaan ole täysin suoraviivaista ja ongelmatonta. Väärässä paikassa se voi vääristää proteiinin toimintaa, ja toisaalta sen lähettämien viestien tulkitseminen ei aina ole yksiselitteistä. Myös näitä haasteita tutkimuksemme nosti esille.

Tässä työssä tutkittiin useita eri fytokromimuunnoksia spektroskooppisia, rakenteellisia ja biokemiallisia menetelmiä käyttäen. Osoitimme ulokkeen rakenteellisten muutosten kytkeytyvän kromoforin muutoksiin ja lopulta toiminnallisen yksikön aktiivisuuteen. Punainen valo laukaisee fytokromissa signaalinvälityksen, ja tässä työssä paljastettiin fytokromin bravuuriliikkeen merkitys sen toiminnalle. Tutkielmassa saadut tulokset edistävät fytokromitutkimusta, mutta asettuvat myös laajempaan viitekehykseen. Ensimmäisessä osatyössä kehitettyä menetelmää voidaan hyödyntää myös muissa proteiineissa esiintyvien silmukkarakenteiden dynaamisuuden tutkimisessa. Toisessa ja kolmannessa osatyössä taas osoitettiin, mikä samankaltaisten rakenteiden merkitys rakenteen stabiilisuuden ylläpidossa ja toiminnan säätelyssä voi olla.

Vaikka ulokkeen merkitys signaalinvälitykselle vahvistettiin, on fytokromin tarkan signalointimekanismin ratkaisuun vielä matkaa. Esimerkiksi jo ulokkeen uudelleenlaskostumisen takana olevat tekijät eivät ole täysin selvillä. Täydellisen signaalinvälitysmekanismin ratkaiseminen taas vaatii lopulta tietokonesimulaatioita, joissa jokainen yksityiskohta ja aikaskaala voidaan tarkasti mallintaa. Fytokromin kokoinen systeemi sisältää kuitenkin niin monta muuttujaa, ja valoaktivaatio tapahtuu molekyylitasolla suhteellisen pitkässä aikaskaalassa, minkä vuoksi nykyisten koneiden teho ei vielä ole riittävä kaikkien yksityiskohtien laskemiseen. Kuitenkin, kun resurssit simulointiin tulevaisuudessa riittävät, esimerkiksi tässä työssä esitetyt tulokset ovat avainroolissa simulaatioiden viitekehyksen ja raja-arvojen asettamisessa.

REFERENCES

Adhikary R., Zimmermann J. & Romesberg F., 2017. Transparent Window Vibrational Probes for the Characterization of Proteins with High Structural and Temporal Resolution. *Chem. Rev.* 117: 1927–1969.

Anders K., Daminelli-Widany G., Mroginski M.A., von Stetten D. & Essen L.O., 2013. Structure of the Cyanobacterial Phytochrome 2 Photosensor Implies a Tryptophan Switch for Phytochrome Signaling. *J. Biol. Chem.* 288: 35714–35725.

Anders K., von Stetten D., Mailliet J., Kiontke S., Sineshchekov V.A., Hildebrandt P., Hughes J. & Essen L.O., 2011. Spectroscopic and Photochemical Characterization of the Red-Light Sensitive Photosensory Module of Cph2 from *Synechocystis* PCC 6803. *Photochem. PhotobioL.* 87: 160–173.

Auldridge M.E. & Forest K., 2011. Bacterial phytochromes: More than meets the light. *Crit. Rev. Biochem. Mol. Biol.* 46: 67–88.

Auldridge M.E., Satyshur K., Anstrom D. & Forest K., 2012. Structure-guided engineering enhances a phytochrome-based Infrared fluorescent protein. *J. Biol. Chem.* 287: 7000–7009.

Bagchi S., Fried S.D. & Boxer S.G., 2012. A solvatochromic model calibrates nitriles′ vibrational frequencies to electrostatic fields. *J. Am. Chem. Soc.* 134: 10373–10376.

Bai Y., Milne J.S., Mayne L. & Englander S.W., 1993. Primary structure effects on peptide group hydrogen exchange. *Proteins* 17: 75.

Baker A.W., Satyshur K.A., Moreno Morales N. & Forest K.T., 2016. Arm-in-arm response regulator dimers promote intermolecular signal transduction. *J. Bacteriol.* 198: 1218–1229.

Barth A., 2007. Infrared spectroscopy of proteins. *Biochim Biophys Acta Bioenerg* 1767: 1073–1101

Bellini D. & Papiz M.Z., 2012. Structure of a bacteriophytochrome and light-stimulated protomer swapping with a gene repressor. *Structure* 20: 1436–1446.

Bhate M.P., Molnar K.S., Goulian M. & DeGrado W.F., 2015. Signal transduction in histidine kinases: insights from new structures. *Structure* 23: 981–994.

Bhoo S., Davis S., Walker J., Karniol B. & Vierstra R., 2001. Bacteriophytochromes are photochromic histidine kinases using a biliverdin chromophore. *Nature* 414: 776–779.

Björling A., Berntsson O., Lehtivuori H., Takala H., Hughes A.J., Panman M., Hoernke M., Niebling S., Henry L., Henning R., Kosheleva I., Chukharev V., Tkachenko N.V., Menzel A., Newby G., Khakhulin D., Wulff M., Ihalainen J.A. & Westenhoff S., 2016. Structural photoactivation of a full-length bacterial phytochrome. *Sci Adv* 2: e1600920. doi: 10.1126/sciadv.1600920.

Blankenburg L., Schroeder L., Habenstein F., Błasiak B., Kottke T. & Bredenbeck J., 2019. Following local light-induced structure changes and dynamics of the photoreceptor PYP with the thiocyanate IR label. *Phys. Chem. Chem. Phys.* 21: 6622–6634.

Blumenstein A., Vienken K., Tasler R., Purschwitz J., Veith D., Frankenberg-Dinkel N. & Fischer R., 2005. The Aspergillus nidulans phytochrome FphA represses sexual development in red light. *Curr. Biol.* 15: 1833–1838.

Böhm C., Gourinchas G., Zweytick S., Hujdur E., Reiter M., Trstenjak S., Sensen C.W. & Winkler A., 2022. Characterisation of sequence-structure-function space in sensor-effector integrators of phytochrome-regulated diguanylate cyclases. *Photochem. Photobiol. Sci.* 21: 1761–1779.

Borthwick H.A., Hendricks S.B., Parker M.W., Toole E.H. & Toole V.K., 1952. A Reversible Photoreaction Controlling Seed Germination. *Proc. Nat. Ac. Sci.* 38: 662–666.

Borucki B., Stetten D.V., Seibeck S., Lamparter T., Michael N., Mroginski M.A., Otto H., Murgida D.H., Heyn M.P. & Hildebrandt P., 2005. Light-induced proton release of phytochrome is coupled to the transient deprotonation of the tetrapyrrole chromophore. *J. Biol. Chem.* 280: 34358–34364.

Brielle E.S. & Arkin I.T., 2021. Isotope-Edited Amide II Mode: A New Label for Site-Specific Vibrational Spectroscopy. *J. Phys. Chem. Lett.* 12: 6634–6638.

Buhrke D., Michael N. & Hamm P., 2022. Vibrational couplings between protein and cofactor in bacterial phytochrome Agp1 revealed by 2D-IR spectroscopy. *Proc. Nat. Ac. Sci.* 119: e2206400119. doi: 10.1073/pnas.2206400119.

Burgie E.S., Bussell A.N., Walker J.M., Dubiel K. & Vierstra R.D., 2014a. Crystal structure of the photosensing module from a red/far-red light-absorbing plant phytochrome. *Proc. Nat. Ac. Sci.* 111: 10179–10184.

Burgie E.S. & Vierstra R.D., 2014. Phytochromes: An atomic perspective on photoactivation and signaling. *Plant Cell* 26: 568–4583.

Burgie E.S., Wang T., Bussell A.N., Walker J.M., Li H. & Vierstra R.D., 2014b. Crystallographic and electron microscopic analyses of a bacterial phytochrome reveal local and global rearrangements during photoconversion. *J. Biol. Chem.* 289: 24573–24587.

Burgie E.S., Zhang J. & Vierstra R.D., 2016. Crystal structure of *Deinococcus* phytochrome in the photoactivated state reveals a cascade of structural rearrangements during photoconversion. *Structure* 24: 448.

Butler W.L., Norris K.H., Siegelman H.W. & Hendricks S.B., 1959. Detection, Assay, and Preliminary Purification of the Pigment Controlling Photoresponsive Development of Plants. *Proc. Nat. Ac. Sci.* 45: 1703–1708.

Carrillo M., Pandey S., Sanchez J., Noda M., Poudyal I., Aldama L., Malla T.N., Claesson E., Wahlgren W.Y., Feliz D. *et al.*, 2021. High-resolution crystal structures of transient intermediates in the phytochrome photocycle. *Structure* 29: 743–754.

Casino P., Miguel-Romero L. & Marina A., 2014. Visualizing autophosphorylation in histidine kinases. *Nat Commun.* 5: 3258. doi: 10.1038/ncomms4258.

Chen M., Chory J. & Fankhauser C., 2004. Light Signal Transduction in Higher Plants. *Annu. Rev. Genet.* 38: 87–117.

Chenchiliyan M., Kübel J., Ooi S.A., Salvadori G., Mennucci B., Westenhoff S. & Maj M., 2023. Ground-state heterogeneity and vibrational energy redistribution in bacterial phytochrome observed with femtosecond 2D IR spectroscopy. *J. Chem. Phys.* 158: 085103. doi: 10.1063/5.0135268.

Chin J.W., Santoro S.W., Martin A.B., King D.S., Wang L. & Schultz P.G., 2002. Addition of p-azido-L-phenylalanine to the genetic code of *Escherichia coli*. *J. Am. Chem. Soc.* 124: 9026–9027.

Choi J.H., Oh K.I. & Cho M., 2008. Azido-derivatized compounds as IR probes of local electrostatic environment: Theoretical studies. *J. Chem. Phys.* 129: 174512. doi: 10.1063/1.3001915.

Claesson E., Wahlgren W.Y., Takala H., Pandey S., Castillon L., Kuznetsova V., Henry L., Panman M., Carrillo M., Kübel J., Nanekar R., Isaksson L., Nimmrich A., Cellini A., Morozov D., Maj M., Kurttila M., Bosman R., Nango E., Tanaka R., Tanaka T., Fangjia L., Iwata S., Owada S., Moffat K., Groenhof G., Stojković E.A., Ihalainen J.A., Schmidt M. & Westenhoff S., 2020. The primary structural photoresponse of phytochrome proteins captured by a femtosecond x-ray laser. *eLife* 9: 53514. doi: 10.7554/eLife.53514.

Creighton T.E., 2010. The Physical and Chemical Basis of Molecular Biology. Helvetian Press.

Creon A., Josts I., Niebling S., Huse N. & Tidow H., 2018. Conformationspecific detection of calmodulin binding using the unnatural amino acid p-azido-phenylalanine (AzF) as an IR-sensor. *Struct. Dyn.* 5: 064701. doi: 10.1063/1.5053466.

Davis S.J., Vener A.V. & Vierstra R.D., 1999. Bacteriophytochromes: phytochrome-like photoreceptors from nonphotosynthetic eubacteria. *Science* 286: 2517–2520.

De Mena L., Rizk P. & Rincon-Limas D.E., 2018. Bringing light to transcription: the optogenetics repertoire. *Front. Genet* 9: 518. doi: 10.3389/fgene.2018.00518

Eilfeld P. & Rüdiger W., 1985. Absorption spectra of phytochrome intermediates. *Z. Naturforsch., C, J. Biosci.* 40: 109–114.

Escobar F.V., Buhrke D., Lopez M.F., Shenkutie S.M., von Horsten S., Essen L.O., Hughes J. & Hildebrandt P., 2017. Structural communication between the chromophore-binding pocket and the N-terminal extension in plant phytochrome phyB. *FEBS Letters* 591: 1258–1265.

Essen L.O., Mailliet J. & Hughes J., 2008. The structure of a complete phytochrome sensory module in the Pr ground state. *Proc. Nat. Ac. Sci.* 105: 14709–14714.

Etzl S., Lindner R., Nelson M.D. & Winkler A., 2018. Structure-guided design and functional characterization of an artificial red light–regulated guanylate/adenylate cyclase for optogenetic applications. *J. Biol. Chem.* 293: 9078–9089.

Fankhauser C. & Staiger D., 2002. Photoreceptors in *Arabidopsis thaliana*: light perception, signal transduction and entrainment of the endogenous clock. *Planta* 216: 1–16.

Feynman R., Leighton R. & Sands M., 1963. The Feynman: Lectures on Physics, Basic Books, New Millenium Edition.

Filonov G.S., Piatkevich K.D., Ting L.M., Zhang J., Kim K. & Verkhusha V.V., 2011. Bright and stable near-infrared fluorescent protein for in vivo imaging. *Nat. biotechnol* 29: 757–761.

Fischer A.J. & Lagarias J.C., 2004. Harnessing phytochrome's glowing potential. *Proc. Nat. Ac. Sci.* 101: 17334–17339.

Flint L.H. & McAlister E.D., 1935. Wave lengths of radiation in the visible spectrum inhibiting the germination of light-sensitive lettuce seed. *Smithsonian Misc. Collect.* 94: 1–11.

Foerstendorf H., Benda C., Gärtner W., Storf M., Scheer H. & Siebert F., 2001. FTIR studies of phytochrome photoreactions reveal the C=O bands of the chromophore: Consequences for its protonation states, conformation, and protein interaction. *Biochemistry* 40: 14952–14959.

Foerstendorf H., Mummert E., Schäfer E., Scheer H. & Siebert F., 1996. Fourier-Transform Infrared Spectroscopy of Phytochrome : Difference Spectra of the Intermediates of the Photoreactions. *Biochemistry* 35: 10793–10799.

Fraikin G.Y., Strakhovskaya M. & Rubin A., 2013. Biological photoreceptors of light-dependent regulatory processes. *Biochemistry (Moscow)* 78: 1238–1253.

Frankenberg N., Mukougawa K., Kohchi T. & Lagarias J.C., 2001. Functional genomic analysis of the HY2 family of ferredoxin-dependent bilin reductases from oxygenic photosynthetic organisms. *The Plant Cell* 13: 965–978.

Franklin K.A., 2008. Shade avoidance. *New Phytologist* 179: 930–944.

Franklin K.A. & Quail P.H., 2010. Phytochrome functions in *Arabidopsis* development. *J. Exp. Bot.* 61: 11–24.

Frauenfelder H., Sligar S.G. & Wolynes P.G., 1991. The energy landscapes and motions of proteins. *Science* 254: 1598.

Fried S.D. & Boxer S.G., 2015. Measuring electric fields and noncovalent interactions using the vibrational stark effect. *Acc. Chem. Res.* 48: 998–1006.

Fushimi K. & Narikawa R., 2019. Cyanobacteriochromes: photoreceptors covering the entire UV-to-visible spectrum. *Curr. Opin. Struct. Biol.* 57: 39–46.

Gai X.S., Coutifaris B.A., Brewer S.H. & Fenlon E.E., 2011. A Direct Comparison of Azide and Nitrile Vibrational Probes. *Phys. Chem. Chem. Phys.* 13: 5926–5930.

Galperin M.Y., Nikolskaya A.N. & Koonin E.V., 2001. Novel domains of the prokaryotic two-component signal transduction systems. *FEMS Microbiol. Lett.* 203: 11–21.

Gan F., Zhang S., Rockwell N.C., Martin S.S., Lagarias J.C. & Bryant D.A., 2014. Extensive remodeling of a cyanobacterial photosynthetic apparatus in far-red light. *Science* 345: 1312–1317.

Giraud E., Fardoux J., Fourrier N., Hannibal L., Genty B., Bouyer P., Dreyfus B. & Verméglio A., 2002. Bacteriophytochrome controls photosystem synthesis in anoxygenic bacteria. *Nature* 417: 202–205.

Giraud E., Zappa S., Vuillet L., Adriano J.M., Hannibal L., Fardoux J., Berthomieu C., Bouyer P., Pignol D. & Verméglio A., 2005. A new type of bacteriophytochrome acts in tandem with a classical bacteriophytochrome to control the antennae synthesis in Rhodopseudomonas palustris. *J. Biol. Chem.* 280: 32389–32397.

Gora A., Brezovsky J. & Damborsky J., 2013. Gates of enzymes. *Chem. Rev.* 113: 5871–5923.

Goulian M., 2010. Two-component signaling circuit structure and properties.*Curr. Opin. Microbiol.* 13: 184–189.

Gourinchas G., Etzl S., Göbl C., Vide U., Madl T. & Winkler A., 2017. Long-range allosteric signaling in red light-regulated diguanylyl cyclases. *Sci Adv.* 3: e1602498. doi: 10.1126/sciadv.1602498.

Gourinchas G., Etzl S. & Winkler A., 2019. Bacteriophytochromes – from informative model systems of phytochrome function to powerful tools in cell biology. *Curr. Opin. Struct. Biol.* 57: 72–83.

Gourinchas G., Heintz U. & Winkler A., 2018. Asymmetric activation mechanism of a homodimeric red light-regulated photoreceptor. *eLife* 7: e34815. doi: 10.7554/eLife.34815

Gustavsson E., Isaksson L., Persson C., Mayzel M., Brath U., Vrhovac L., Ihalainen J.A., Karlsson B.G., Orekhov V. & Westenhoff S., 2020. Modulation of Structural Heterogeneity Controls Phytochrome Photoswitching. *Biophys. J.* 118: 415–421.

Hahn J., Strauss H.M. & Schmieder P., 2008. Heteronuclear NMR investigation on the structure and dynamics of the chromophore binding pocket of the cyanobacterial phytochrome Cph1. *J. Am. Chem. Soc.* 130: 11170–11178.

Hall C.R., Collado J.T., Iuliano J.N., Gil A.A., Adamczyk K., Lukacs A., Greetham G.M., Sazanovich I., Tonge P.J. & Meech S.R., 2019. Site-Specific Protein Dynamics Probed by Ultrafast Infrared Spectroscopy of a Noncanonical Amino Acid. *J. Phys. Chem. B* 123: 9592–9597.

Hellingwerf K.J., 2000. Key issues in the photochemistry and signalling-state formation of photosensor proteins. *J. Photochem. Photobiol.* 54: 94–102.

Herrou J., Crosson S. & Fiebig A., 2017. Structure and function of HWE/HisKA2–family sensor histidine kinases. *Current Opinion in Microbiology* 36: 47–54.

Hershey H.P., Barker R.F., Idler K.B., Lissemore J.L. & Quail P.H., 1985. Analysis of cloned cDNA and genomic sequences for phaytochrome: Complete amino acid sequences for two gene products expressed in etiolated Avena. *Nucleic Acids Res.* 13: 8543–8559.

Heschel M.S., Selby J., Butler C., Whitelam G.C., Sharrock R.A. & Donohue K., 2007. A new role for phytochromes in temperature-dependent germination. *New Phytologist* 174: 735–741.

Heyne K., Herbst J., Stehlik D., Esteban B., Lamparter T., Hughes J. & Diller R., 2002. Ultrafast dynamics of phytochrome from the cyanobacterium Synechocystis, reconstituted with phycocyanobilin and phycoerythrobilin. *Biophys. J.* 82: 1004–1016.

Hilser V.J., Wrabl J.O. & Motlagh H.N., 2012. Structural and Energetic Basis of Allostery. *Annu. Rev. Biophys.* 41: 585–609.

Hughes J., Lamparter T., Mittmann F., Hartmann E., Gartner W., Wilde A. & Borner T., 1997. A prokaryotic phytochrome. *Nature* 386: 663.

Hvidt A. & Nielsen S.O., 1966. Hydrogen exchange in proteins. *Adv. Protein Chem.* 21: 287.

Ihalainen J.A., Gustavsson E., Schroeder L., Donnini S., Lehtivuori H., Isaksson L., Thöing C., Modi V., Berntsson O., Stucki-Buchli B., Liukkonen A., Häkkänen H., Kalenius E., Westenhoff S. & Kottke T., 2018. Chromophore-Protein Interplay during the Phytochrome Photocycle Revealed by Step-Scan FTIR Spectroscopy. *J. Am. Chem. Soc.* 140: 12396–12404.

Ihalainen J.A., Takala H. & Lehtivuori H., 2015. Fast photochemistry of canonical Bacteriophytochrome proteins - a species-specific comparison. *Front. Mol. Biosci.* 2: 75. doi: 10.3389/fmolb.2015.00075.

Isaksson L., Gustavsson E., Persson C., Brath U., Vrhovac L., Karlsson G., Orekhov V. & Westenhoff S., 2021. Signaling Mechanism of Phytochromes in Solution. *Structure* 29: 151–160.

Jacob-Dubuisson F., Mechaly A., Betton J.M. & Antoine R., 2018. Structural insights into the signalling mechanisms of two-component systems. *Nat. Rev. Microbiol* 16: 585–593.

Jacques S.L., 2013. Optical properties of biological tissues: a review. *Phys. Med. Biol.* 58: 5007–5008.

Jaubert M., Lavergne J., Fardoux J., Hannibal L., Vuillet L., Adriano J.M., Bouyer P., Pignol D., Giraud E. & Verméglio A., 2007. A singular bacteriophytochrome acquired by lateral gene transfer. *J. Biol. Chem.* 282: 7320–7328.

Jenkins G.I., 2014. The UV-B Photoreceptor UVR8: From Structure to Physiology. *The Plant Cell* 26: 21–37.

Kaberniuk A., Shemetov A.A. & Verkhusha V.V., 2016. A bacterial phytochrome-based optogenetic system controllable with near-infrared light. *Nat. Methods* 13: 591–597.

Kacprzak S., Njimona I., Renz A., Feng J., Reijerse E., Lubitz W., Krauss N., Scheerer P., Nagano S., Lamparter T. & Weber S., 2017. Intersubunit distances in full-length, dimeric, bacterial phytochrome Agp1, as measured by pulsed electron-electron double resonance (PELDOR) between different spin label positions, remain unchanged upon photoconversion. *J. Biol. Chem.* 292: 7598– 7606.

Kaneko T., Sato S., Kotani H., Tanaka A., Asamizu E., Nakamura Y., Miyajima N., Hirosawa M., Sugiura M., Sasamoto S. *et al.*, 1996. Sequence analysis of the genome of the unicellular cyanobacterium Synechocystis sp. strain PCC6803. II. Sequence determination of the entire genome and assignment of potential protein-coding regions. *DNA Res.* 3: 109–136.

Kapitulnik J. & Maines M.D., 2012. The role of bile pigments in health and disease: effects on cell signaling, cytotoxicity, and cytoprotection. *Front Pharmacol.* 13:136. doi: 10.3389/fphar.2012.00136.

Karniol B. & Vierstra R.D., 2003. The pair of bacteriophytochromes from *Agrobac-terium tumefaciens* are histidine kinases with opposing photobiological properties. *Proc. Nat. Ac. Sci.* 100: 2807–2812.

Kohchi T., Mukougawa K., Frankenberg N., Masuda M., Yokota A. & Lagarias J.C., 2001. The Arabidopsis HY2 gene encodes phytochromobilin synthase, a ferredoxin-dependent biliverdin reductase. *The Plant Cell* 13: 425–436.

Kottke T., Lórenz-Fonfría V.A. & Heberle J., 2017. The grateful infrared: Sequential protein structural changes resolved by infrared difference spectroscopy. *J. of Phys. Chem. A* 121: 335–350.

Kraskov A., Nguyen A.D., Goerling J., Buhrke D., Velazquez Escobar F., Fernandez Lopez M., Michael N., Sauthof L., Schmidt A., Piwowarski P., Yang Y., Stensitzki T., Adam S., Bartl F., Schapiro I., Heyne K., Siebert F., Scheerer P., Mroginski M.A. & Hildebrandt P., 2020. Intramolecular Proton Transfer Controls Protein Structural Changes in Phytochrome. *Biochemistry* 59: 1023–1037. PMID: 32073262.

Krause B.S., Kaufmann J.C., Kuhne J., Vierock J., Huber T., Sakmar T.P., Gerwert K., Bartl F.J. & Hegemann P., 2019. Tracking Pore Hydration in Channelrhodopsin by Site-Directed Infrared-Active Azido Probes. *Biochemistry* 58: 1275–1286.

Krauss C., Bubenzer C. & Scheer H., 1980. Studies on plant bile pigments. 6. Photochemically assisted reaction of A-dihydrobilindione with nucleophiles as a model for phytochrome interconversion. *Photochem. Photobiol.* 30: 473–477.

Kübel J., Chenchiliyan M., Ooi S.A., Gustavsson E., Isaksson L., Kuznetsova V., Ihalainen J.A., Westenhoff S. & Maj M., 2020. Transient IR spectroscopy identifies key interactions and unravels new intermediates in the photocycle of a bacterial phytochrome. *Phys. Chem. Chem. Phys.* 22: 9195–9203.

Kübel J., Westenhoff S. & Maj M., 2021. Giving voice to the weak: Application of active noise reduction in transient infrared spectroscopy. *Chem. Phys. Lett.* 783: 139059. doi: 10.1016/j.cplett.2021.139059.

Kumarapperuma I., Tom I.P., Bandara S., Montano S. & Yang X., 2023. Mode of autophosphorylation in bacteriophytochromes RpBphP2 and RpBphP3. *Photochem. Photobiol. Sci.* 22: 1257-1266.

Lamparter T., Michael N., Caspani O., Miyata T., Shirai K. & Inomata K., 2003. Biliverdin Binds Covalently to *Agrobacterium* Phytochrome Agp1 via Its Ring A Vinyl Side Chain. *J. Biol. Chem.* 278: 33786–33792.

Lamparter T., Michael N., Mittmann F. & Esteban B., 2002. Phytochrome from *Agrobacterium tumefacienshas* unusual spectral properties and reveals an N-terminal chromophore attachment site. *Proc. Nat. Acad. Sci.* 99: 11628–11633.

Lane H.C., Siegelman H.W., Butler W.L. & Firer E.M., 1963. Detection of Phytochrome in Green Plants. *Plant Physiol.* 38: 414–416.

Legris M., Ince Y.Ç. & Fankhauser C., 2019. Molecular mechanisms underlying phytochrome-controlled morphogenesis in plants. *Nat. Commun* 10: 5219. doi: 10.1038/s41467-019-13045-0.

Legris M., Klose C., Burgie E.S., Rojas C.C., Neme M., Hiltbrunner A., Wigge P.A., Schäfer E., Vierstra R.D. & Casal J.J., 2016. Phytochrome B integrates light and temperature signals in *Arabidopsis*. *Science* 354: 897–900.

Lehtinen K., Nokia M.S. & Takala H., 2022. Red Light Optogenetics in Neuroscience. *Front. Cell. Neurosci.* 15: 778900. doi: 10.3389/fncel.2021.778900.

Lehtivuori H., Bhattacharya S., Angenent-Mari N.M., Satyshur K.A. & Forest K.T., 2015. Removal of chromophore-proximal polar atoms decreases water content and increases fluorescence in a near infrared phytofluor. *Front. in Mol. Biosci* 2: 65. doi: 10.3389/fmolb.2015.00065.

Lehtivuori H., Rissanen I., Takala H., Bamford J., Tkachenko N.V. & Ihalainen J.A., 2013. Fluorescence properties of the chromophore-binding domain of bacteriophytochrome from *Deinococcus radiodurans*. *J. Phys. Chem. B* 117: 11049–11057.

Lehtivuori H., Rumfeldt J., Mustalahti S., Kurkinen S. & Takala H., 2022. Conserved histidine and tyrosine determine spectral responses through the water network in Deinococcus radiodurans phytochrome. *Photochem. Photobiol. Sci.* 21: 1975–1989.

Leivar P. & Monte E., 2014. PIFs: systems integrators in plant development. *The Plant Cell* 26: 56–78.

Lenngren N., Edlund P., Takala H., Stucki-Buchli B., Rumfeldt J., Peshev I., Häkkänen H., Westenhoff S. & Ihalainen J.A., 2018. Coordination of the biliverdin D-ring in bacteriophytochromes. *Phys. Chem. Chem. Phys.* 20: 18216–18225.

Li H., Burgie E.S., Gannam Z.T.K., Li H. & Vierstra R.D., 2022a. Plant phytochrome B is an asymmetric dimer with unique signalling potential. *Nature* 604: 127–133.

Li X., Liu Z., Ren H., Kundu M., Zhong F.W., Wang L., Gao J. & Zhong D., 2022b. Dynamics and mechanism of dimer dissociation of photoreceptor UVR8. *Nat. Commun* 13: 93. doi: 10.1038/s41467-021-27756-w.

Li H., Zhang J., Vierstra R.D. & Li H., 2010. Quaternary organization of a phy-tochrome dimer as revealed by cryoelectron microscopy. *Proc. Nat. Ac. Sci.* 107: 10872–10877.

Lieber E., Rao C., Thomas A., Oftedahl E., Minnis R. & Nambury C., 1963. Infrared spectra of acid azides, carbamyl azides and other azido derivatives: Anomalous splittings of the N3 stretching bands. *Spectrochimica Acta* 19: 1135–1144.

Linschitz H. & Kasche V., 1966. The kinetics of phytochrome conversion. *J. Biol. Chem.* 241: 3395–3403.

Lipkin J.S., Song R., Fenlon E.E. & Brewer S.H., 2011. Modulating accidental fermi resonance: What a difference a neutron makes. *J. Phys. Chem. Lett.* 2: 1672–1676.

Liu C.C. & Schultz P.G., 2010. Adding new chemistries to the genetic code. *Annu Rev. Biochem.* 79: 413–444.

Losi A. & Gärtner W., 2012. The Evolution of Flavin-Binding Photoreceptors: An Ancient Chromophore Serving Trendy Blue-Light Sensors. *Annu Rev Plant Biol.* 63: 49–72.

Ma J., Pazos I.M., Zhang W., Culik R.M. & Gai F., 2015. Site-specific infrared probes of proteins. *Annu Rev Phys Chem.* 66: 357–377.

Mailliet J., Psakis G., Feilke K., Sineshchekov V., Essen L.O. & Hughes J., 2011. Spectroscopy and a High-Resolution Crystal Structure of Tyr263 Mutants of Cyanobacterial Phytochrome Cph1. *J Mol. Biol.* 413: 115–127.

Maj M., Ahn C., Błasiak B., Kwak K., Han H. & Cho M., 2016. Isonitrile as an Ultrasensitive Infrared Reporter of Hydrogen-Bonding Structure and Dynamics. *J. Phys. Chem. B* 120: 10167–10180.

Mathes T., Ravensbergen J., Kloz M., Gleichmann T., Gallagher K.D., Woitowich N.C., Peter R.S., Kovaleva S.E., Stojković E.A. & Kennis J.T., 2015. Femto- to Microsecond Photodynamics of an Unusual Bacteriophytochrome. *J. Phys. Chem. Lett.* 6: 239–243.

Mathews S., 2010. Evolutionary studies illuminate the structural-functional model of plant phytochromes. *The Plant Cell* 22: 4–16.

McCleary W.R. & Stock J.B., 1994. Acetyl phosphate and the activation of two-component response regulators. *J. Biol. Chem.* 269: 31567– 31572.

Medzihradszky M., Bindics J., éva ádám, Viczián A., éva Klement, Lorrain S., Gyula P., Mérai Z., Fankhauser C., Medzihradszky K.F., Kunkel T., Schäfer E. & Nagy F., 2013. Phosphorylation of phytochrome B inhibits light-induced signaling via accelerated dark reversion in Arabidopsis. *Plant Cell* 25: 535–544.

Millar A.J., 2003. A suite of photoreceptors entrains the plant circadian clock. *J. Biol. Rhythms* 18: 217–226.

Millar A.J., 2004. Input signals to the plant circadian clock. *J. Exp. Bot.* 55: 277–283.

Modi V., Donnini S., Groenhof G. & Morozov D., 2019. Protonation of the Biliverdin IXα Chromophore in the Red and Far-Red Photoactive States of a Bacteriophytochrome. *J. Phys. Chem. B* 123: 2325–2334.

Möglich A., Ayers R.A. & Moffat K., 2009. Structure and signaling mechanism of Per-ARNT-Sim domains. *Structure* 17: 1282–1294.

Möglich A. & Moffat K., 2010. Engineered photoreceptors as novel optogenetic tools. *Photochem. Photobiol. Sci.* 9: 1286–1300.

Möglich A., Yang X., Ayers R.A. & Moffat K., 2010. Structure and function of plant photoreceptors. *Annu Rev of Plant Biol* 61: 21–47.

Motlagh H.N., Wrabl J.O., Li J. & Hilser V.J., 2014. The ensemble nature of allostery. *Nature* 508: 331–339.

Mroginski M.A., Murgida D.H. & Hildebrandt P., 2007. The chromophore structural changes during the photocycle of phytochrome: A combined resonance Raman and quantum chemical approach. *Acc. Chem. Res.* 40: 258– 266.

Multamäki E., Nanekar R., Morozov D., Lievonen T., Golonka D., Wahlgren W.Y., Stucki-Buchli B., Rossi J., Hytönen V., Westenhoff S., Ihalainen J., Möglich A. & Takala H., 2021. Comparative analysis of two paradigm bacteriophytochromes reveals opposite functionalities in two-component signaling. *Nat Commun.* 12: 4394. doi: 10.1038/s41467-021-24676-7.

Multamäki E., Garc'ıa de Fuentes A., Sieryi O., Bykov A., Gerken U., Ranzani A.T., Köhler J., Meglinski I., Möglich A. & Takala H., 2022. Optogenetic control of bacterial expression by red light. *ACS Synth. Biol.* 11: 3354–3367.

Nagano S., Scheerer P., Zubow K., Michael N., Inomata K., Lamparter T. & Krauß N., 2016. The Crystal Structures of the N-terminal Photosensory Core Module of *Agrobacterium* Phytochrome Agp1 as Parallel and Anti-parallel Dimers. *J. Biol. Chem.* 291: 20674–20691.

Nogly P., Weinert T., James D., Carbajo S., Ozerov D., Furrer A., Gashi D., Borin V., Skopintsev P., Jaeger K., Nass K., Båth P., Bosman R., Koglin J., Seaberg M., Lane T., Kekilli D., Brünle S., Tanaka T., Wu W., Milne C., White T., Barty A., Weierstall U., Panneels V., Nango E., Iwata S., Hunter M., Schapiro I., Schertler G., Neutze R. & Standfuss J., 2018. Retinal isomerization in bacteriorhodopsin captured by a femtosecond x-ray laser. *Science* 361: eaat0094. doi: 10.1126/science.aat0094.

Nussinov R. & Tsai C.J., 2013. Allostery in Disease and in Drug Discovery. *Cell* 153: 293–305.

Otero L.H., Klinke S., Rinaldi J., Velázquez-Escobar F., Mroginski M.A., López M.F., Malamud F., Vojnov A.A., Hildebrandt P., Goldbaum F.A. & Bonomi H.R., 2016. Structure of the Full-Length Bacteriophytochrome from the Plant Pathogen *Xanthomonas campestris* Provides Clues to its Long-Range Signaling Mechanism. *J. Mol. Biol.* 428: 3702–3720.

Piwowarski P., Ritter E., Hofmann K.P., Hildebrandt P., von Stetten D., Scheerer P., Michael N., Lamparter T. & Bartl F., 2010. Light-induced activation of bacterial phytochrome Agp1 monitored by static and time-resolved FTIR spectroscopy. *ChemPhysChem* 11: 1207–1214.

Polverini E., Schackert F.K. & Losi A., 2020. Interplay among the "flipping" glutamine, a conserved phenylalanine, water and hydrogen bonds within a blue-light sensing LOV domain. *Photochem. Photobiol. Sci.* 19: 892– 904.

Quail P.H., 1997. An emerging molecular map of the phytochromes. *Plant Cell Environ* 20: 657–665.

Quail P.H., 2002. Phytochrome photosensory signalling networks. *Nat. Rev. Mol. Cell Biol.* 3: 85–93.

Rockwell N.C., Duanmu D., Martin S.S., Bachy C., Price D.C., Bhattacharya D., Worden A.Z. & Lagarias J.C., 2014. Eukaryotic algal phytochromes span the visible spectrum. *Proc. Nat. Ac. Sci.* 111: 3871–3876.

Rockwell N.C. & Lagarias J.C., 2006. The structure of phytochrome: a picture is worth a thousand spectra. *Plant Cell* 18: 4–14.

Rockwell N.C. & Lagarias J.C., 2010. A brief history of phytochromes. *ChemPhysChem* 11: 1172–1180.

Rockwell N.C. & Lagarias J.C., 2020. Phytochrome evolution in 3D: deletion, duplication, and diversification. *New Phytologist* 225: 2283–2300.

Rodgers J.M., Abaskharon R.M., Ding B., Chen J., Zhang W. & Gai F., 2017. Fermi resonance as a means to determine the hydrogen-bonding status of two infrared probes. *Phys. Chem. Chem. Phys.* 19: 16144–16150.

Rodriguez-Romero J., Hedtke M., Kastner C., Müller S. & Fischer R., 2010. Fungi, Hidden in Soil or Up in the Air: Light makes a difference. *Annu Rev Microbiol.* 64: 585–610.

Rohmer T., Lang C., Bongards C., Gupta K.B.S.S., Neugebauer J., Hughes J., Gärtner W. & Matysik J., 2010. Phytochrome as molecular machine: Revealing chro-mophore action during the Pfr → Pr photoconversion by magic-angle spinning NMR spectroscopy. *J. Am. Chem. Soc.* 132: 4431–4437.

Rumfeldt J., Takala H., Liukkonen A. & Ihalainen J., 2019. UV-Vis Spectroscopy Reveals a Correlation Between Y263 and BV Protonation States in Bacteriophytochromes. *Photochem. Photobiol.* 95: 969–979.

Schneider C.A., Rasband W.S. & Eliceiri K.W., 2002. NIH Image to ImageJ: 25 years of image analysis. *Nat Methods* 9: 671–675.

Schumann C., Groß R., Michael N., Lamparter T. & Diller R., 2007. Subpicosecond mid-infrared spectroscopy of phytochrome Agp1 from *Agrobacterium tumefaciens*. *ChemPhysChem* 8: 1657–1663.

Sharrock R.A., 2008. The phytochrome red/far-red photoreceptor superfamily. *Genome Biology* 9:230. doi: 10.1186/gb-2008-9-8-230.

Shcherbakova D.M., Baloban M., Emelyanov A.V., Brenowitz M., Guo P. & Verkhusha V.V., 2016. Bright monomeric near-infrared fluorescent proteins as tags and biosensors for multiscale imaging. *Nat Commun.* 7: 12405. doi: 10.1038/ncomms12405.

Shcherbakova D.M., Baloban M. & Verkhusha V.V., 2015. Near-infrared fluo-rescent proteins engineered from bacterial phytochromes. *Curr. Op. Chem. Biol.* 27: 52–63.

Siebert F. & Hildebrant P., 2008. Vibrational Spectroscopy in Life Science. Tutorials in Biophysics. Wiley.

Sineshchekov V.A., 1995. Photobiophysics and photobiochemistry of the heterogeneous phytochrome system. *Biochim Biophys Acta Bioenerg* 1228: 125–164.

Sokolovski S.G., Zherebtsov E.A., Kar R.K., Golonka D., Stabel R., Chichkov N.B., Gorodetsky A., Schapiro I., Möglich A. & Rafailov E.U., 2021. Two-photon conversion of a bacterial phytochrome. *Biophys. J.* 120: 964–974.

Song C., Rohmer T., Tiersch M., Zaanen J., Hughes J. & Matysik J., 2013. Solid-state NMR spectroscopy to probe photoactivation in canonical phytochromes. *Photochem. Photobiol.* 89: 259–273.

Stojković E.A., Toh K.C., Alexandre M.T.A., Baclayon M., Moffat K. & Kennis J.T.M., 2014. FTIR Spectroscopy Revealing Light-Dependent Refolding of the Conserved Tongue Region of Bacteriophytochrome. *J. Phys. Chem. Lett.* 15: 2512–2515.

Stokkum I.H.V., Larsen D.S. & Grondelle R.V., 2004. Global and target analysis of time-resolved spectra. *Biochim Biophys Acta Bioenerg* 1657: 82–104.

Suydam I.T., Snow C.D., Pande V.S. & Boxer S.G., 2006. Electric Fields at the Active Site of an Enzyme: Direct Comparison of Experiment with Theory. *Science* 313: 200–204.

Takala H., Björling A., Berntsson O., Lehtivuori H., Niebling S., Hoernke M., Kosheleva I., Henning R., Menzel A., Ihalainen J.A. & Westenhoff S., 2014a. Signal amplification and transduction in phytochrome photosensors. *Nature* 509: 245.

Takala H., Björling A., Linna M., Westenhoff S. & Ihalainen J.A., 2015. Light-induced changes in the dimerization interface of bacteriophytochromes. *J. Biol. Chem.* 290: 16383–16392.

Takala H., Lehtivuori H., Berntsson O., Hughes A., Nanekar R., Niebling S., Panman M., Henry L., Menzel A., Westenhoff S. & Ihalainen J.A., 2018. On the (un)coupling of the chromophore, tongue interactions, and overall conformation in a bacterial phytochrome. *J. Biol. Chem.* 293: 8161–8172.

Takala H., Lehtivuori H., Hammarén H., Hytönen V.P. & Ihalainen J.A., 2014b. Connection between absorption properties and conformational changes in *Deinococcus radiodurans* phytochrome. *Biochemistry* 53: 7076.

Takala H., Niebling S., Berntsson O., Björling A., Lehtivuori H., Häkkänen H., Panman M., Gustavsson E., Hoernke M., Newby G., Zontone F., Wulff M., Menzel A., Ihalainen J.A. & Westenhoff S., 2016. Light-induced structural changes in a monomeric bacteriophytochrome. *Struct. Dyn.* 3: 054701. doi: 10.1063/1.4961911.

Takiden A., Velazquez-Escobar F., Dragelj J., Woelke A.L., Knapp E.W., Piwowarski P., Bart F., Hildebrandt P. & Mroginski M.A., 2017. Structural and Vibrational Characterization of the Chromophore Binding Site of Bacterial Phy-tochrome Agp1. *Photochem. Photobiol.* 93: 713–723.

Tarutina M., Ryjenkov D.A. & Gomelsky M., 2006. An unorthodox bacteriophytochrome from Rhodobacter sphaeroides involved in turnover of the second messenger c-di-GMP. *J. Biol. Chem.* 281: 34751–34758.

Thielges M.C., Axup J.Y., Wong D., Lee H.S., Chung J.K., Schultz P.G. & Fayer M.D., 2011. Two-dimensional IR spectroscopy of protein dynamics using two vibrational labels: A site-specific genetically encoded unnatural amino acid and an active site ligand. *J. Phys. Chem. B* 115: 11294–11304.

Toh K.C., Stojković E.A., Rupenyan A.B., van Stokkum I.H.M., Salumbides M., Groot M.L., Moffat K. & Kennis J.T.M., 2011. Primary reactions of bacteriophytochrome observed with ultrafast mid-infrared spectroscopy. *J. Phys. Chem. A* 115: 3778–3786.

Tran M.T.N., Tanaka J., Hamada M., Sugiyama Y., Sakaguchi S., Nakamura M., Takahashi S. & Miwa Y., 2014. *In vivo* image analysis using iRFP transgenic mice. *Exp. Anim.* 63: 311–319.

Tsai C.J. & Nussinov R., 2014. A Unified View of "How Allostery Works". *PLOS Comput. Biol.* 10: 1–12.

Uhmann W., Becker A., Taran C. & Siebert F., 1991. Time-Resolved FT-IR Absorption Spectroscopy Using a Step-Scan Interferometer. *Appl Spectrosc.* 45: 390–397.

Ulijasz A.T. & Vierstra R.D., 2011. Phytochrome structure and photochemistry: recent advances toward a complete molecular picture. *Curr. Opin. Plant Biol.* 14: 498–506.

Van Thor J.J., Borucki B., Crielaard W., Otto H., Lamparter T., Hughes J., Hellingwerf K.J. & Heyn M.P., 2001. Light-induced proton release and proton uptake reactions in the cyanobacterial phytochrome Cph1. *Biochemistry* 40: 11460–11471.

Van Thor J.J., Fisher N. & Rich P.R., 2005. Assignments of the Pfr - Pr FTIR difference spectrum of cyanobacterial phytochrome Cph1 using ^{15}N and ^{13}C isotopically labeled phycocyanobilin chromophore. *J. Phys. Chem. B* 109: 20597–20604.

Van Thor J.J., Ronayne K.L. & Towrie M., 2007. Formation of the early photoproduct Lumi-R of cyanobacterial phytochrome Cph1 observed by ultrafast mid-infrared spectroscopy. *J. Am. Chem. Soc.* 129: 126–132.

van Wilderen L.J.G.W., Kern-Michle D., Müller-Werkmeister H. & Bredenbeck J., 2014. Vibrational dynamics and solvatochromism of the label SCN in various solvents and hemoglobin by time dependent IR and 2D-IR spectroscopy. *Phys. Chem. Chem. Phys.* 16: 19643–19653.

Velazquez Escobar F., Lang C., Takiden A., Schneider C., Balke J., Hughes J., Alexiev U., Hildebrandt P. & Mroginski M.A., 2017. Protonation-dependent structural heterogeneity in the chromophore binding site of cyanobacterial phy-tochrome Cph1. *J. Phys. Chem. B* 121: 47–57.

Velazquez Escobar F., Piwowarski P., Salewski J., Michael N., Lopez M.F., Rupp A., Qureshi B.M., Scheerer P., Bartl F., Frankenberg-Dinkel N., Siebert F., Mroginski M.A. & Hildebrandt P., 2015. A protonation-coupled feedback mechanism controls the signalling process in bathy phytochromes. *Nat Chemistry* 7: 423–430.

Vermeer A.W. & Norde W., 2000. The Thermal Stability of Immunoglobulin: Unfolding and Aggregation of a Multi-Domain Protein. *Biophys. J.* 78: 394– 404.

Vierstra R.D. & Quail P.H., 1983. Purification and Initial Characterization of 124–Kilodalton Phytochrome from Avena. *Biochemistry* 22: 2498–2505.

Waegele M.M., Culik R.M. & Gai F., 2011. Site-specific spectroscopic reporters of the local electric field, hydration, structure, and dynamics of biomolecules. *J. Phys. Chem. Lett.* 2: 2598–2609.

Wagner J.R., Brunzelle J.S., Forest K.T. & Vierstra R.D., 2005. A light-sensing knot revealed by the structure of the chromophore-binding domain of phytochrome. *Nature* 438: 325–331.

Wagner J.R., Zhang J., Brunzelle J.S., Vierstra R.D. & Forest K.T., 2007. High resolution structure of *Deinococcus* bacteriophytochrome yields new insights into phytochrome architecture and evolution. *J. Biol. Chem.* 282: 12298–12309.

Wagner J.R., Zhang J., Stetten D.V., Günther M., Murgida D.H., Mroginski M.A., Walker J.M., Forest K.T., Hildebrandt P. & Vierstra R.D., 2008. Mutational analysis of *Deinococcus radiodurans* bacteriophytochrome reveals key amino acids necessary for the photochromicity and proton exchange cycle of phytochromes. *J. Biol. Chem.* 283: 12212–12226.

Wahlgren W.Y., Claesson E., Tuure I., Trillo-Muyo S., Bódizs S., Ihalainen J.A., Takala H. & Westenhoff S., 2022. Structural mechanism of signal transduction in a phytochrome histidine kinase. *Nat. Commun* 13: 7673. doi: 10.1038/s41467-022-34893-3.

West A.H. & Stock A.M., 2001. Histidine kinases and response regulator proteins in two-component signaling systems. *Trends Biochem. Sci.* 26: 369–376.

Woitowich N.C., Halavaty A.S., Waltz P., Kupitz C., Valera J., Tracy G., Gallagher K.D., Claesson E., Nakane T., Pandey S., Nelson G., Tanaka R., Nango E., Mizohata E., Owada S., Tono K., Joti Y., Nugent A.C., Patel H., Mapara A., Hopkins J., Duong P., Bizhga D., Kovaleva S.E., Peter R.S., Hernandez C.N., Ozarowski W.B., Roy-Chowdhuri S., Yang J.H., Edlund P., Takala H., Ihalainen J.A., Brayshaw J., Norwood T., Poudyal I., Fromme P., Spence J.C., Moffat K., Westenhoff S., Schmidt M. & Stojković E.A., 2018. Structural basis for light control of cell development revealed by crystal structures of a myxobacterial phytochrome. *IUCrJ* 5: 619–634.

Wolfshorndl M., Baskin R., Dhawan I. & Londergan C., 2012. Covalently bound azido groups are very specific water sensors, even in hydrogen-bonding environments. *J. Phys. Chem. B* 116: 1172–1179.

Xu Q.Z., Goett-Zink L., Gärtner W., Zhao K.H. & Kottke T., 2020. Tongue Refolding in the Knotless Cyanobacterial Phytochrome All2699. *Biochemistry* 59: 2047–2054.

Yang X., Kuk J. & Moffat K., 2008. Crystal structure of *Pseudomonas aeruginosa* bacteriophytochrome: Photoconversion and signal transduction. *Proc. Nat. Ac. Sci.* 105: 14715–14720.

Yang Y., Linke M., von Haimberger T., Matute R., González L., Schmieder P. & Heyne K., 2014. Active and silent chromophore isoforms for phytochrome Pr photoisomerization: An alternative evolutionary strategy to optimize photore-action quantum yields. *Struct. Dyn.* 1: 14701. doi: 10.1063/1.4865233.

Yang X., Ren Z., Kuk J. & Moffat K., 2011. Temperature-scan cryocrystallography reveals reaction intermediates in bacteriophytochrome. *Nature* 479: 428–431.

Ye S., Huber T., Vogel R. & Sakmar T.P., 2009. FTIR analysis of GPCR activation using azido probes. *Nature Chemical Biology* 5: 397–399.

Yeh K. & Lagarias J.C., 1998. Eukaryotic phytochromes: Light-regulated serine/threonine protein kinases with histidine kinase ancestry. *Proc. Nat. Ac. Sci.* 95: 13976–13981.

Yeh K., Wu S., Murphy J. & Lagarias J., 1997. A cyanobacterial phytochrome two-component light sensory system. *Science* 277: 1505–1508.

Yoshihara S., Katayama M., Geng X. & Ikeuchi M., 2004. Cyanobacterial Phytochrome-like PixJ1 Holoprotein Shows Novel Reversible Photoconversion Between Blue- and Green-absorbing Forms. *Plant and Cell Physiology* 45: 1729–1737.

Young T.S., Ahmad I., Yin J.A. & Schultz P.G., 2010. An Enhanced System for Unnatural Amino Acid Mutagenesis in *E. coli*. *J. Mol. Biol.* 395: 361–374.

Zhang W., Markiewicz B.N., Doerkse R.S., Smith A.B. & Gai F., 2016. CRN stretching vibration of 5–cyanotryptophan as an infrared probe of protein local environment: what determines its frequency? *Phys. Chem. Chem. Phys.* 18: 7027–7034.

Zhang J., Wang L., Zhang J., Zhu J., Pan X., Cui Z., Wang J., Fang W. & Li Y., 2018. Identifying and Modulating Accidental Fermi Resonance: 2D IR and DFT Study of 4–Azido-l-phenylalanine. *J. Phys. Chem B* 122: 8122– 8133.

Ziegler T. & Möglich A., 2015. Photoreceptor engineering. *Front. Mol. Biosci.* 2: 30. doi: 10.3389/fmolb.2015.00030.

Zschiedrich C.P., Keidel V. & Szurmant H., 2016. Molecular mechanisms of two-component signal transduction. *J. Mol. Biol.* 428: 3752–3775.

ORIGINAL PAPERS

I

THE HAIRPIN EXTENSION CONTROLS SOLVENT ACCESS TO THE CHROMOPHORE BINDING POCKET IN A BACTERIAL PHYTOCHROME: A UV–VIS ABSORPTION SPECTROSCOPY STUDY

by

Jessica Rumfeldt, Moona Kurttila, Heikki Takala & Janne A. Ihalainen 2021

Photochemical & Photobiological Sciences 20: 1173–1181

https://doi.org/10.1007/s43630-021-00090-2

Photochemical & Photobiological Sciences (2021) 20:1173–1181
https://doi.org/10.1007/s43630-021-00090-2

ORIGINAL PAPERS

The hairpin extension controls solvent access to the chromophore binding pocket in a bacterial phytochrome: a UV–vis absorption spectroscopy study

Jessica Rumfeldt[1] · **Moona Kurttila**[1] · **Heikki Takala**[1] · **Janne A. Ihalainen**[1]

Received: 19 May 2021 / Accepted: 9 August 2021 / Published online: 30 August 2021

Abstract

Solvent access to the protein interior plays an important role in the function of many proteins. Phytochromes contain a specific structural feature, a hairpin extension that appears to relay structural information from the chromophore to the rest of the protein. The extension interacts with amino acids near the chromophore, and hence shields the chromophore from the surrounding solvent. We envision that the detachment of the extension from the protein surface allows solvent exchange reactions in the vicinity of the chromophore. This can facilitate for example, proton transfer processes between solvent and the protein interior. To test this hypothesis, the kinetics of the protonation state of the biliverdin chromophore from *Deinococcus radiodurans* bacteriophytchrome, and thus, the pH of the surrounding solution, is determined. The observed absorbance changes are related to the solvent access of the chromophore binding pocket, gated by the hairpin extension. We therefore propose a model with an "open" (solvent-exposed, deprotonation-active on a (sub)second time-scale) state and a "closed" (solvent-gated, deprotonation inactive) state, where the hairpin fluctuates slowly between these conformations thereby controlling the deprotonation process of the chromophore on a minute time scale. When the connection between the hairpin and the biliverdin surroundings is destabilized by a point mutation, the amplitude of the deprotonation phase increases considerably. In the absence of the extension, the chromophore deprotonates essentially without any "gating". Hence, we introduce a straightforward method to study the stability and fluctuation of the phytochrome hairpin in its photostationary state. This approach can be extended to other chromophore-protein systems where absorption changes reflect dynamic processes of the protein.

Keywords Protein dynamics · Solvent gating · Conformational substates · Chromophore protein systems · pH jump

1 Introduction

The view of proteins as static structures obtained from X-ray crystallography, has evolved to a more biologically relevant understanding of proteins as dynamic molecules in solution [1–3]. This is in part due to advances in experimental techniques, which are able to detect the sparsely populated, transitory states. Such methods include nuclear magnetic resonance (NMR) [4], hydrogen–deuterium exchange (H/D) [5], single molecule fluorescence methods [6], and more recently time-resolved crystallography [7] and time-resolved serial femtosecond crystallography [8, 9]. Notwithstanding, elaborated molecular dynamics simulations have often indicated the role of the dynamics of proteins in their function [2].

A complete overview of protein motion requires experimentation on a range of timescales covering over ten orders of magnitude: from picosecond side-chain rotations, to larger amplitude collective motions taking place on timescales from nanosecond to milliseconds, as well as global or subglobal unfolding events with time constants of seconds to hours. The goal is to determine the relationship between these motions and the function of the protein [10]. For example, the exact role dynamics plays in enzyme catalysis is

---

Pushing the limits of flash photolysis to unravel the secrets of biological electron and proton transfer—a topical issue in honour of Klaus Brettel.

✉ Janne A. Ihalainen
janne.ihalainen@jyu.fi

[1] Nanoscience Center, Department of Biological and Environmental Science, University of Jyväskylä, 40014 Jyväskylä, Finland

still not fully understood or agreed upon [11–13]. There are numerous examples of enzymes where the active site is protected by loops that open to let substrate in and close to protect the reaction from solvent [14, 15].

Often, solvent dynamics can be linked to the dynamic nature of proteins [16–18]. Furthermore, solvent exchange reactions involving water from bulk solvent to the protein interior influence the activity of the enzymes.

Recent studies have reported a link between a decrease in bilin-specific absorption and the deprotonation of the positively charged chromophore, which is embedded within a binding pocket of the phytochrome [19, 20]. Rather than using the above-mentioned extensive methods, we describe here a straightforward measurement approach where the deprotonation process of the biliverdin is linked to a sub-global protein motion, and further, solvent accessibility to the protein interior.

Phytochromes are red light-sensing, multidomain proteins, which generally consist of an N-terminal photosensory module and a C-terminal output module. Here we study the photosensory module of a bacteriophytochrome from *Deinococcus radiodurans* (*Dr*BphP). This CBD-PHY fragment consists of a chromophore binding domain (CBD) and a phytochrome-specific GAF-related domain (PHY). In the dark, CBD-PHY maintains the structural features characteristic of red-light absorbing state (Pr) shown in ribbon representation in Fig. 1a. The biliverdin (BV) chromophore is covalently bound in a pocket of the CBD, and shown as ball and sticks in Fig. 1a. Absorption of red light in Pr causes isomerization of the BV D-ring which leads to formation of the far red-light absorbing state (Pfr) (Fig. S1), which is accompanied by large-scale structural changes within the CBD-PHY [21]. This photo-conversion acts as a control switch for activity of the output module, like enzymatic activity in two-component signaling [22]. Through these structural processes, phytochromes convert the ambient light cues to the host of biological processes within the cell.

A peculiar structural feature of phytochromes is a hairpin extension (circled in Fig. 1a) that initiates from the PHY domain and extends to form close contacts with the CBD [25]. Along the photoactivation of the protein, this extension has been shown to change its fold from β-sheet structure in Pr, to α-helix in Pfr, with each fold forming unique interactions with the CBD [21]. In Pr, these interactions are extensive enough to completely cover the binding pocket and protect BV from solvent [25] as shown in Fig. 1b. In

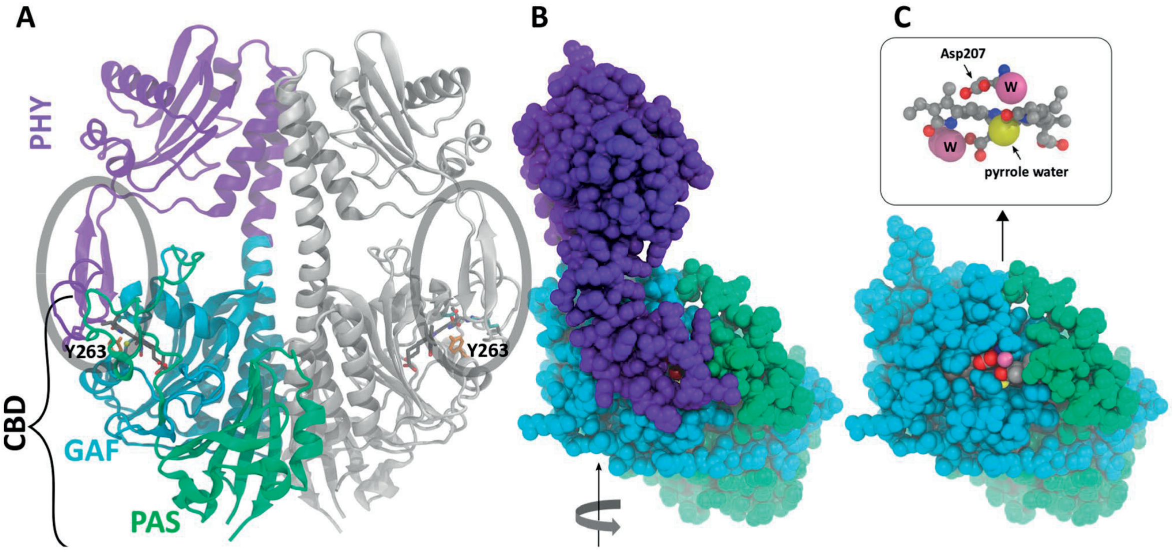

Fig. 1 Structure of *Dr*BphP constructs showing solvent protection of the BV binding pocket by the β-stranded hairpin extension A) Ribbon structure of the CBD-PHY dimer with one monomer coloured grey and the other coloured according to domains: the PHY domain is coloured purple and domains that make up the CBD, Per/ARNT/Sim (PAS) and cGMP phosphor diesterase/adenyl cyclase/FhlA (GAF), are coloured green and blue, respectively. The BV chromophore is represented as sticks with carbons coloured grey, nitrogens blue and oxygens red. The pyrrole water is shown as a yellow sphere. The hairpin is circled and tyrosine 263 is shown in yellow in both monomers. B) The coloured monomer subunit in A is shown in space fill representation with an ~ 90° rotation out of the page along the vertical axis. The BV is protected from solvent by the hairpin extension with only the carbonyl oxygen from the BV A-ring and the pyrrole water visible. C) The CBD is shown in the same orientation as B. Since the PHY domain is absent, the BV binding pocket is more exposed to solvent in this truncated construct. The exposed atoms include oxygen from the BV A-ring (red), the pyrrole water (yellow), an ordered water (pink), as well as the oxygens of the D207 side chain. These atoms are also indicated in the magnification of BV above. The figure was prepared using PDB 4q0j [23] and VMD [24]

the truncated CBD construct, shown in Fig. 1c, the BV is solvent-exposed due to the absence of the hairpin extension. Here, we link the movement of the hairpin extension in the dark state to the (de)protonation process of the BV-molecule under basic conditions. This is based on the assumption that the solvent access to the CBD pocket facilitates the proton transfer reaction (Fig. 2). Thus, by inducing a rapid pH change of (sub-)second time-scale and detecting the spectral changes of the biliverdin chromophore due to the changes of the BV protonation state, we are able to indirectly detect slow time-scale fluctuation of the hairpin extension and its effect on the solvent exposure to the CBD domain in the phytochrome in its Pr state.

2 Results and discussion

The rate of BV deprotonation in the Pr state was determined for three different *Dr*BphP samples, wild-type CBD-PHY (WT), CBD-PHY Y263F variant, and CBD. From previous studies it was shown that a decrease in absorbance at 700 nm with a concomitant increase at 600 nm can be associated with BV deprotonation in *Dr*BphP [20]. Here, a jump to pH 10.8, near the pH titration midpoint for all three samples (Fig. S2), produces a clearly observable change of absorption at 700 nm, describing the decreased population of the protonated form $(BV\text{-}H_4)^+$, while maintaining the functionality of the protein. The time it takes to equilibrate from the "fully protonated" to the "deprotonated" state ($BV\text{-}H_3$) at pH 10.8 gives information about the solvent access to the binding site.

To confirm the functionality under the experimental conditions, the protein was left at pH 10.8 for 2.5 h and then illuminated with red light (Fig. S3). Consequently, the absorbance decreased at 700 nm and increased at 750 nm, as expected due to photoisomerization of the BV from Pr to Pfr [26]. This transition is reversible: the absorbance spectrum returned to the original state after illumination with far-red light (Fig. S3). However, very long incubation times (four hours or more) tend to lead to protein degradation (Fig. S4). By switching using red and far-red light illuminations, transitions between Pr and Pfr at pH 10.8, with final far-red illumination, can produce the endpoint absorbance values for the Pr state as well (Figs. 3 and S4). In this case, the switching between the states causes unfolding/folding of the hairpin which opens the hairpin extension and allows solvent access to the BV leading to fast deprotonation.

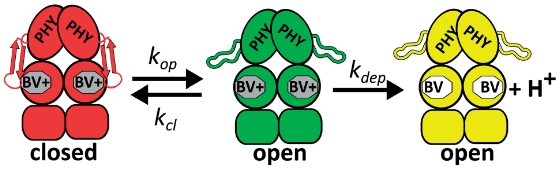

Fig. 2 Cartoon model of BV deprotonation in CBD-PHY in its Pr state. The opening and closing of the hairpin extension is governed by the rate constants k_{op} and k_{cl} respectively. When the hairpin extension is open, BV is exposed to solvent and is deprotonated with a rate constant k_{dep}. In this model, it is assumed that in the closed state (red CBD-PHY) BV deprotonation does not occur

For kinetic data, the absorbance of the samples was measured after 13 s and up to 120 mins after dilution (Fig. 3). Each time point was measured separately after dilution to avoid illumination artifacts. The deprotonation process was followed using the absorbance at 700 nm, which is plotted as function of incubation time after the pH jump (Fig. 3, lower panel). The absorbance kinetics of the CBD-PHY WT and the Y263F variant are best fit to two exponential phases while one is sufficient for CBD (Eq. 1, Table 1). The fitted end-point absorbance for each construct is very similar to corresponding values from pH titrations (Fig. S2), and photoisomerization at pH 10.8 (Fig. S4) confirming little to no measurement artifacts.

2.1 Fast and slow BV deprotonation is observed

For all samples, there is a significant absorbance decrease that occurs within the 13 s experimental dead time. An exponential fit gives a rate constant of about 10 min^{-1} for this phase (k_1), reflecting a process of about 6 s and therefore being beyond the time-resolution limit of the experiment. A second, slower phase (k_2) with a rate constant of 0.013 min^{-1} corresponding to a time constant of about 76 min (Table 1), exists for the CBD-PHY WT and Y263F samples.

In addition to the rate constants, the amplitudes of the phases give important information. Since each protein has different BV absorbance properties and slightly different pK_a values, the total absorbance change from pH 8.0 to 10.8 is variable (Fig. 3). For easier comparison, the kinetics are plotted as a function of total amplitude change in Fig. 4. From this and Table 1, the fast phase amplitude A_1 for CBD-PHY WT and Y263F is 47 and 60 % of the total absorbance change. For CBD, only a fast phase is observed and therefore makes up 100% of the amplitude change.

2.2 Two-state model for BV deprotonation

Although the pH titrations for CBD and CBD-PHY are similar (Fig. S2), CBD deprotonates within seconds while CBD-PHY takes over 2 h to reach the expected endpoint. This is attributed to gating of solvent access to the BV binding site by the extension as outlined in Fig. 2. In theory, the hairpin may assume many conformations and multiple deprotonation pathways; however, the model assumes two general cases: closed and open, which prevents and

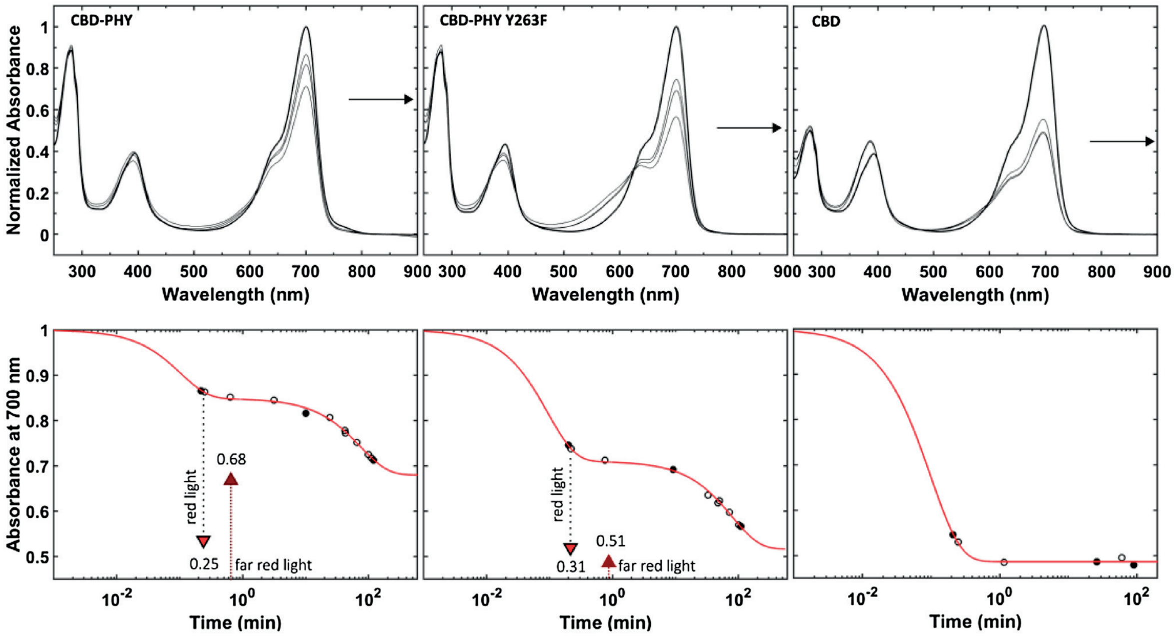

Fig. 3 Absorbance-monitored BV deprotonation Top row: absorbance spectra of **A** CBD-PHY, **B** CBD-PHY Y263 and **C** CBD in the Pr state monitored after a jump from pH 8 (thick lines) to pH 10.8 (thin lines). Spectra are normalized to the absorbance at 700 nm of the protein in pH 8.0 buffer. The representative spectra correspond to the time points of the filled circles in the plots below. The equilibrium absorbance at pH 10.8 determined by pH titration experiments (Fig. S2) is indicated by an arrow to the right-hand side axes. Bottom row: The normalized absorbance value at 700 nm is plotted against time (circles), and according to Eq. 1, a free parameter fit to a double or single exponential (red line) is presented. The 700 nm absorbance expected at equilibrium was determined by a jump to pH 10.8, followed by immediate illumination with red light (down arrow) and then driving the sample back to Pr with far red-light (up arrow)(Fig. S4)

Table 1 Parameters derived from fitting deprotonation kinetics to one or two exponentials as in Eq. 1

Construct	Fast phase		Slow phase						
	Amp_1	k_1	Amp_2	k_2	$A_{endpoint}$ [b]	$fAmp_1$ [c]	K_{eq} [d]	k_{op} [e]	k_{cl} [f]
CBD-PHY	0.15	9.7	0.17	0.013	0.65	0.47	0.89	0.013	0.015
CBD-PHY Y263F	0.29	10.7	0.19	0.013	0.52	0.60	1.5	0.013	0.008
CBD [a]	0.51	10.1			0.49	1			

Rate constants have units of $\min^{-1}$

[a] CBD fit to single exponential

[b] Obtained by fitting the deprotonation transitions. Similar values obtained by switching the sample between Pr and Pfr Fig. S4

[c] Fraction of the fast phase amplitude Amp_1 where the total amplitude equals $Amp_1 + Amp_2$

[d] Equilibrium constant calculated using $K_{eq} = fAmp_1/(1\text{-}fAmp_1)$, reflects initial conditions, pH 8

[e] k_{op} set to k_2, and reflects the opening rate constant at pH 10.8

[f] If k_{op} and k_{cl} are independent of pH, then $k_{cl} = k_{op}/K_{eq}$

allows deprotonation, respectively. At neutral pH, the positively charged BV is highly favoured and there is no net change in the protonation state. If the pH is increased above the pK_a of BV, the deprotonation reaction becomes significant. The amplitude of the fast phase reflects the distribution of states at the initial conditions [27]; therefore, the K_{eq} is reflective of the open and closed populations at pH 8.0.

For CBD, all of the molecules are considered to be in the open state. Hence, the observed single exponential rate constant is taken as a limiting value for k_{dep}. For PHY-containing proteins, the observed deprotonation kinetics are a

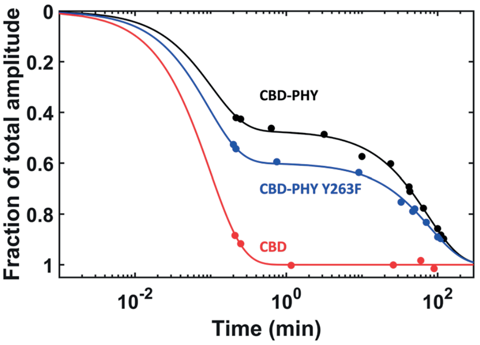

Fig. 4 Kinetics of BV deprotonation scaled according to the fraction of total amplitude and modelled as in Fig. 2. Absorbance values (filled circles) have been converted to fraction of total amplitude of the exponential fits for easier comparison. At the top, 0 represents no change and 1 represents 100% of the total change. The black (CBD-PHY WT) and blue (CBD-PHY Y263F) solid lines were generated by substituting the corresponding rate constants for k_{op}, k_{cl} and k_{dep} in Table 1 into Eqs. S4 and S5.

combination of the microscopic rate constants that define each step in Fig. 2. Since this deprotonation model is analogous to the Linderstrom-Lang model used for H/D exchange (Eq. 3), we can use equations derived for H/D to analyse the deprotonation to obtain k_{op} and k_{cl} from the observed kinetics (reviewed in [5, 28]).

The two phases observed for PHY-containing proteins are taken to reflect the relative population of the closed and open states that exist at time zero [27]. This is expected when k_{cl} and k_{op} are of similar magnitude so that both the closed and open states are significantly populated [27]. The simplified equations typically used for H/D are therefore not applicable (see Supplementary Information); deprotonation kinetics require the full equation for exchange, described in detail by Qian and Chan [27] and outlined in Supplementary Information in Eqs. S4 and S5.

For CBD-PHY WT and Y263F, the fractional amplitude change of the fast phase is 0.47 and 0.6, respectively. Since these values indicate the fraction of molecules that exist in solution, the values can be used to calculate the equilibrium constant (K_{eq}) for the transition from open to closed states as shown in Table 1. The remaining slow phase amplitude is due to the population of PHY domain-containing proteins in the closed state. The rate of deprotonation in this case is limited by k_{op} and can, therefore, be assigned to the rate constant measured for this phase (see Table 1) [27]. This condition is considered the EX1 limit of exchange as in Eq. S3. Using this value for k_{op} and K_{eq}, the value for k_{cl} can be calculated as shown in Table 1. These rate constants were substituted into **Eqs.** S4 and S5 to generate the lines for CBD-PHY WT and Y263F in Fig. 4, demonstrating the applicably of this model. These equations have also used to simulate deprotonation time courses to better understand how the microscopic rate constants affect the observed kinetics (Fig. S6).

Comparison of $fAmp_1$ in WT and Y263F CBD-PHY suggests more molecules are in the open state in solution for the mutant. Since the slow rate constant is the same for WT and Y263F, this results in a decreased value of k_{cl} for the mutant. An example of the effect, an even larger selective decrease of k_{cl} has on deprotonation is shown in the simulated black and red solid lines in Fig. S6.

The results of Y263F are in line with our previous study which shows that the conformation of the hairpin becomes partially uncoupled from the Pr/Pfr transition of the biliverdin chromophore [29]. Specifically, the extension in Y263F is more likely to adopt Pfr-like α-helical architecture even when BV remains in the Pr state. According to the crystal structure, the hairpin in the Pfr conformation does not protect BV from solvent (Fig. S5) which is observed experimentally as fast deprotonation when CBD-PHY is in the Pfr conformation (Fig. S4). The "closed" hairpin in Y263F likely adopts conformations that behave as open ones, granting solvent access to the binding site.

2.3 Dynamics of the extension

The minute timescales of opening and closing of the extension determined using this method are much slower than typically observed in protein dynamics and for loops in particular [30]. It is not particularly surprising that the dynamics of the extension differs from other mobile loops presented so far: it is formed by 37 residues (Pro443 to His484) and is, therefore, much longer than most loops. Further, it contains clear secondary structures and thus does not fall neatly into any one category of loop architecture [31]. In light of this, it can be even considered as a separate subdomain. Indeed the dynamic behaviour is more like subglobal unfolding; for example, unfolding of the lysozyme β-domain occurs on the second timescale in the naturally occurring mutants I156T and D67H [32]. The opening and closing of the Ω -loop in cytosolic phosphoenolpyruvate carboxykinase [33] and in cytochrome c [34] have also been described as folding and unfolding transitions as opposed to active site loops that remain rigid like a swinging gate [14, 15]. To note, dynamic events in the hairpin extension in the dark-adapted phytochromes have been reported by means of NMR (internal dynamics on the μs to ms timescale) [35] and by H/D exchange studies (on the second time-scale) [36].

A folding transition of the extension is known to occur as a part of the function of phytochrome: it readily adopts an α-helical structure in the light-activated Pfr state shown in Fig. S1 [21, 37]. The idea that proteins have pre-existing pathways of structural organization has gained attention in the last decade [2, 38]. Specifically, the alternate conformations adopted after ligand binding or other modifiers are always accessible to the protein as dynamic substates, even in the absence of the triggering event. It is therefore conceivable that conformational dynamics of the extension occurs in the absence of any light induced BV isomerization. Especially extension residues 472–477 that form a solvent exposed β-strand in the crystal structure [21, 23, 25] but are actually predicted to form an α-helix based on the primary sequence (Fig. S1).

The stability of the extension in the context of the Pr state as a whole may only be slightly tipped in favour of β -sheet structure. This coincides with the determined K_{eq}, indicating the closed and open states have similar energy levels (Table 1). For Y263F, which disrupts an interaction between the extension and the CBD, the balance seems to be further tipped away from retaining the β-sheet conformation. Although the closed and open states may be close in energy, the slow interconversion suggests a high energy barrier between them. If pre-existing pathways are considered, the extension needs to break contacts with the CBD, unfold, fold to an α-helix, unfold, and then fold back to a β-sheet reforming contacts. The k_{op} and k_{cl} includes a rate constant for all these unfolding and refolding processes.

The ability to act as a solvent gate to the BV binding site is similar to other loops that gate solvent and substrate access to the active site, like in triosephosphate isomerase [39] and lactate dehydrogenase [40]. Presently, a clear functional purpose for this type of gate is missing, although (dynamic) interactions between water molecules and the biliverdin have been indicated, both in the resting state as well as in the intermediate states of the photocycle [41–43].

3 Conclusions

Here, we show a method that uses the intrinsic pH dependence of BV absorbance to monitor the equilibrium and kinetic properties of the PHY domain hairpin extension; an interesting and unusual structural feature of phytochromes for which the function has yet to be established.

The method assumes that access to bulk solvent is required for BV deprotonation to proceed and that this access is gated by the extension (Fig. 2). The observed deprotonation kinetics, monitored by absorbance at 700 nm after a jump to high pH, reflect the energetic transition of the hairpin extension from a closed solvent protected, to an open solvent exposed state. To demonstrate that the effect observed in this study originates from the stability of the hairpin extension, we use a truncated construct CBD which lacks the PHY domain, and a CBD-PHY Y263F mutant, which has been shown to drive the equilibrium population of the extension from β-strand to α-helical structure [21, 29]. For CBD, deprotonation is complete within seconds, while the Y263F mutation increases the amplitude of this fast phase relative to CBD-PHY WT. The rate of BV deprotonation is, therefore, dependent on the presence/stability of the PHY domain.

Energetic parameters were extracted from the observed kinetics using Eqs. S5 and S4 (Table 1). They indicate that the closed and open states are similar in energy but have a high energy barrier between them. This interpretation derives from the fast and slow phases of CBD-PHY WT and Y263F deprotonation: the fast phase coinciding with the significant population of open state at equilibrium, and the slow phase due to rate limiting opening of the extension. We note that with this approach, we are unable to access the mechanism of the proton transfer reaction from the chromophore to the solvent, or the proton exchange reactions within the chromophore binding pocket. To expand the knowledge about these proton transfer events, faster detection methods and additional mutations at the chromophore vicinity would be required.

4 Experimental

4.1 Protein purification

The expression constructs, *Dr*BphP coding domains CBD (residues 1–321) and CBD-PHY (residues 1–502) were kindly provided by the laboratories of Prof. R. D. Vierstra and Prof. K. T. Forest. Cloning of the CBD-PHY Y263F mutant is described elsewhere [29]. For all constructs, the expression vector pET21b(+) containing a C-terminal His6-tag (Novagen) was used. Proteins were expressed and purified as previously outlined [21, 44]. Purified proteins from the final size exclusion chromatography step were concentrated to 30 mg mL^{-1} in 30 mM Tris pH 8, flash-frozen and stored at −80°C.

4.2 UV–vis spectroscopy

The absorbance measurements were carried out using a Cary 8454 UV–vis spectrometer (Agilent Technologies). For pH jump experiments on a given day, a stock of phytochrome protein was made in 3 mM Tris pH 8.0 with an absorbance value at 700 nm of 0.5. The stock was mixed 1+1 with either 60 mM Tris pH 8.0 or 60 mM glycine pH 10.8 giving a final buffer concentration of 31.5 mM Tris pH 8.0 or 1.5 mM Tris and 30 mM glycine pH 10.8 (confirmed with a pH meter). The final concentration of phytochrome after mixing gave an absorbance at 700 nm of 0.25. The absorption spectrum at pH 8.0 was used as a zero time point and for normalization. For kinetic data, absorbance spectra were measured at specific time intervals after the dilution into pH 10.8 buffer. Using this manual mixing set up, the smallest possible time interval between dilution and measurement is 13 s and is referred to as the experimental dead-time. The longest time interval was 250 min. As each measurement exposes the phytochrome to UV and visible light, repeated measurements were not taken to avoid illumination artifacts; instead, a separate dilution was made for every time interval.

4.3 Data processing and analysis

Absorbance scans were normalized to the absorbance at 700 nm of the time zero pH 8.0 spectra measured on the same day. These absorbance values were plotted as a function of time and fit to the exponential Eq. 1

$$A_{measured} = \sum_{i=1}^{n} A_i \times e^{-k_i \times t} + A_{endpoint} \tag{1}$$

where $A_{measured}$ is the normalized absorbance measured at 700 nm, A_i and k_i are the amplitude and rate constant for the i^{th} phase, respectively, t is time and $A_{endpoint}$ is the final absorbance value.

The equation for BV deprotonation demonstrated in Fig. 2 is written below:

$$[(BV - H_4)^+]_c \underset{k_{cl}}{\overset{k_{op}}{\rightleftharpoons}} [(BV - H_4)^+]_o \xrightarrow{k_{dep}} (BV - H_3) + H^+ \tag{2}$$

where $[(\text{BV-H}_4)^+]_c$ represents the fully protonated BV in the solvent protected form with the extension in close contact with the GAF domain and $[(\text{BV-H}_4)^+]_o$ represents the solvent exposed form when the extension is separated from GAF, k_{op} and k_{cl} are the rate constants for opening and closing of the extension and k_{dep} is the rate constant for deprotonation of the solvent exposed $[(\text{BV-H}_4)^+]$.

This approach is analogous to the Linderstrom-Lang model for amide exchange [45]:

$$Closed \underset{k_{cl}}{\overset{k_{op}}{\rightleftharpoons}} Open \xrightarrow{k_{int}} Exchanged \tag{3}$$

in which closed represents the closed (protected), protonated state, open represents the open (unprotected) protonated state where exchange is possible and exchanged represents the deuterated state. The k_{op} and k_{cl} are the opening and closing rate constants for the structural event leading to exchange, k_{int} is the intrinsic rate constant for amide hydrogen-deuterium exchange in the open state [46].

Supplementary Information The online version contains supplementary material available at https://doi.org/10.1007/s43630-021-00090-2.

Acknowledgements The authors thank Alli Liukkonen and Heikki Häkkänen for help in protein purification procedures and in the spectroscopic experimental settings, respectively. The research was supported by the Academy of Finland (Grants 332742 for JAI and 330678 for HT).

Funding Open access funding provided by University of Jyväskylä (JYU).

Declarations

Conflict of interest The authors declare that they have no conflict of interest.

References

1. Frauenfelder, H., Sligar, S., & Wolynes, P. (1991). The energy landscapes and motions of proteins. *Science, 254*(5038), 1598.
2. Bahar, I., Chennubhotla, C., & Tobi, D. (2007). Intrinsic dynamics of enzymes in the unbound state and relation to allosteric regulation. *Current Opinion in Structural Biology, 17*(6), 633.
3. Frauenfelder, H. (2017). Physical concepts in biology—past and future. *Physical Biology, 14*(1), 010402.
4. Peng, J. W. (2012). Exposing the moving parts of proteins with NMR spectroscopy. *The Journal of Physical Chemistry Letters, 3*(8), 1039.
5. Konermann, L., Pan, J., & Liu, Y. (2011). Hydrogen exchange mass spectrometry for studying protein structure and dynamics. *Chemical Society Reviews, 40*(3), 1224.
6. Schuler, B., Lipman, A., & Everett, W. E. (2002). SProbing the free-energy surface for protein folding with single-molecule fluorescence spectroscopy. *Nature, 419,* 743.
7. Mehrabi, P., Schulz, E. C., Dsouza, R., Müller-Werkmeister, H. M., Tellkamp, F., Miller, R. J. D., & Pai, E. F. (2019). Time-resolved crystallography reveals allosteric communication aligned with molecular breathing. *Science, 365*, 1167.
8. Nogly, P., Weinert, T., James, D., Carbajo, S., Ozerov, D., Furrer, A., et al. (2018). Retinal isomerization in bacteriorhodopsin captured by a femtosecond x-ray laser. *Science, 361,* eaat0094.
9. Claesson, E., Wahlgren, W. Y., Takala, H., Pandey, S., Castillon, L., Kuznetsova, V., Henry, L., Panman, M., Carrillo, M., Kübel, J., Nanekar, R., Isaksson, L., Nimmrich, A., Cellini, A., Morozov, D., Maj, M., Kurttila, M., Bosman, R., Nango, E., Tanaka, R., Tanaka, T., Fangjia, L., Iwata, S., Owada, S., Moffat, K., Groenhof, G., Stojković, E. A., Ihalainen, J. A., Schmidt, M., & Westenhoff, S. (2020). The primary structural photoresponse of phytochrome proteins captured by a femtosecond X-ray laser. *eLife, 9*, e53514.
10. Henzler-Wildman, K., Lei, M., Thai, V., Kerns, S., Karplus, M., & Kern, D. (2007). A hierarchy of timescales in protein dynamics is linked to enzyme catalysis. *Nature, 450*(7171), 913.

11. Kamerlin, S.C. & Warshel, A. (2010). At the dawn of the 21st century: Is dynamics the missing link for understanding enzyme catalysis?. *Proteins*, *78*(6), 1339.
12. Olsson, M. H., Parson, W. W., & Warshel, A. (2006). Dynamical contributions to enzyme catalysis: Critical tests of a popular hypothesis. *Chemical Reviews, 106*(5), 1737.
13. Zhao, Q. (2017). On the indirect relationship between protein dynamics and enzyme activity. *Progress in Biophysics and Molecular Biology, 125*, 52.
14. Gerstein, M., Arthur, M., & Chothia, C. (1994). Structural mechanisms for domain movements in proteins. *Biochemistry, 33*(22), 6739.
15. Gora, A., Brezovsky, J., & Damborsky, J. (2013). Gates of enzymes. *Chemical Reviews, 113*(8), 5871.
16. Frauenfelder, H., Fenimore, P. W., & Young, R. D. (2007). Protein dynamics and function: Insights from the energy landscape and solvent slaving. *IUBMB Life, 59*(8–9), 506.
17. Frauenfelder, H., Fenimore, P., Chen, G., & McMahon, B. (2006). Protein folding is slaved to solvent motions. *Proceedings of the National Academy of Sciences of the United States of America, 103*(42), 15469.
18. Lewandowski, J. R., Halse, M. E., Blackledge, M., & Emsley, L. (2015). Direct observation of hierarchical protein dynamics. *Science, 348*(6234), 578.
19. Escobar, F. V., Lang, C., Takiden, A., Schneider, C., Balke, J., Hughes, J., et al. (2017). Protonation-dependent structural heterogeneity in the chromophore binding site of cyanobacterial phytochrome Cph1. *Journal of Physical Chemistry B, 121*(1), 47–57.
20. Rumfeldt, J. A., Takala, H., Liukkonen, A., & Ihalainen, J. A. (2019). UV-Vis spectroscopy reveals a correlation between Y263 and BV protonation states in bacteriophytochromes. *Photochemistry Photobiology, 95*(4), 969.
21. Takala, H., Björling, A., Berntsson, O., Lehtivuori, H., Niebling, S., Hoernke, M., Kosheleva, I., Henning, R., Menzel, A., Ihalainen, J. A., & Westenhoff, S. (2014). Signal amplification and transduction in phytochrome photosensors. *Nature, 509*(7499), 245.
22. Multamäki E., Nanekar R., Morozov D., Lievonen T., Golonka D., Wahlgren W. Y., Stucki-Buchli B., Rossi J., Hytönen V. P., Westenhoff S., Ihalainen J. A., Möglich A., Takala H. (2021). Comparative analysis of two paradigm bacteriophytochromes reveals opposite functionalities in two-component signaling. *Nat Commun, 12*(1), 4394.
23. Burgie, E. S., Wang, T., Bussell, A. N., Walker, J. M., Li, H., & Vierstra, R. D. (2014). Crystallographic and electron microscopic analyses of a bacterial phytochrome reveal local and global rearrangements during photoconversion. *Journal of Biological Chemistry, 289*(35), 24573.
24. Humphrey, W., Dalke, A., & Schulten, K. (1996). VMD: Visual molecular dynamics. *Journal of Molecular Graphics, 14*(1), 33.
25. Essen, L. O., Mailliet, J., & Hughes, J. (2008). The structure of a complete phytochrome sensory module in the Pr ground state. *Proceedings of the National Academy of Sciences, 105*(38), 14709.
26. Takala, H., Lehtivuori, H., Hammarén, H., Hytönen, V. P., & Ihalainen, J. A. (2014). Connection between absorption properties and conformational changes in Deinococcus radiodurans phytochrome. *Biochemistry, 53*(45), 7076.
27. Qian, H., & Chan, S. I. (1999). Hydrogen exchange kinetics of proteins in denaturants: A generalized two-process model. *Journal of Molecular Biology, 286*(2), 607.
28. Englander, S. W., Downer, N. W., & Teitelbaum, H. (1972). Hydrogen exchange. *Annual Review of Biochemistry, 41*(1), 903.
29. Takala, H., Lehtivuori, H. K., Berntsson, O., Hughes, A., Nanekar, R., Niebling, S., et al. (2018). On the (un)coupling of the chromophore, tongue interactions, and overall conformation in a bacterial phytochrome. *Journal of Biological Chemistry, 293*(21), 8161.
30. Fenwick, R., Esteban-Martín, S., & Salvatella, X. (2011). Understanding biomolecular motion, recognition, and allostery by use of conformational ensembles. *European Biophysics Journal, 40*(12), 1339.
31. Oliva, B., Bates, P. A., Querol, E., Avilés, F. X., & Sternberg, M. J. (1997). An automated classification of the structure of protein loops. *Journal of Molecular Biology, 266*(4), 814.
32. Dumoulin, M., Canet, D., Last, A. M., Pardon, E., Archer, D. B., Muyldermans, S., et al. (2005). Reduced global cooperativity is a common feature underlying the amyloidogenicity of pathogenic lysozyme mutations. *Journal of Molecular Biology, 346*(3), 773.
33. Cui, D. S., Broom, A., Mcleod, M. J., Meiering, E. M., & Holyoak, T. (2017). Asymmetric anchoring is required for efficient o-loop opening and closing in cytosolic phosphoenolpyruvate carboxykinase. *Biochemistry, 56*(15), 2106.
34. Krishna, M. M., Lin, Y., Rumbley, J. N., & Englander, S. W. (2003). Cooperative omega loops in cytochrome c: Role in folding and function. *Journal of Molecular Biology, 331*(1), 29.
35. Gustavsson, E., Isaksson, L., Persson, C., Mayzel, M., Brath, U., Vrhovac, L., et al. (2020). Modulation of structural heterogeneity controls phytochrome photoswitching. *Biophysics of Journal, 118*(2), 415.
36. Gourinchas, G., Etzl, S., Göbl, C., Vide, U., Madl, T., & Winkler, A. (2017). Long-range allosteric signaling in red light-regulated diguanylyl cyclases. *Science Advances, 3,* e1602498.
37. Burgie, E. S., Zhang, J., & Vierstra, R. D. (2016). Crystal structure of Deinococcus phytochrome in the photoactivated state reveals a cascade of structural rearrangements during photoconversion. *Structure, 24*(3), 448.
38. Haliloglu, T., & Bahar, I. (2015). Adaptability of protein structures to enable functional interactions and evolutionary implications. *Current Opinion in Structural Biology, 35*, 17.
39. Kursula, I., Salin, M., Sun, J., Norledge, B., Haapalainen, A., Sampson, N., & Wierenga, R. (2004). Understanding protein lids: Structural analysis of active hinge mutants in triosephosphate isomerase. *Protein Engineering, Design and Selection, 17*(4), 375.
40. McClendon, S., Zhadin, N., & Callender, R. (2005). The approach to the Michaelis complex in lactate dehydrogenase: The substrate binding pathway. *Biophysical Journal, 89*(3), 2024.
41. Wagner, J. R., Brunzelle, J. S., Forest, K. T., & Vierstra, R. D. (2005). A light-sensing knot revealed by the structure of the chromophore-binding domain of phytochrome. *Nature, 438*(7066), 325.
42. Lenngren, N., Edlund, P., Takala, H., Stucki-Buchli, B., Rumfeldt, J., Peshev, I., et al. (2018). Coordination of the biliverdin D-ring in bacteriophytochromes. *Physical Chemistry Chemical Physics, 20*(27), 18216.
43. Ihalainen, J. A., Gustavsson, E., Schroeder, L., Donnini, S., Lehtivuori, H., Isaksson, L., et al. (2018). Chromophore-protein interplay during the phytochrome photocycle revealed by step-scan FTIR spectroscopy. *Journal of the American Chemical Society, 140*(39), 12396.
44. Lehtivuori, H., Rissanen, I., Takala, H., Bamford, J., Tkachenko, N. V., & Ihalainen, J. A. (2013). Fluorescence properties of the chromophore-binding domain of bacteriophytochrome from Deinococcus radiodurans. *The Journal of Physical Chemistry B, 117*(38), 11049.
45. Hvidt, A., & Nielsen, S. O. (1966). Hydrogen exchange in proteins. *Advances in Protein Chemistry, 21,* 287.
46. Milne, B. Y. J., & Englander, L. M. (1993). Primary structure effects on peptide group hydrogen exchange. *Proteins, 17*(1), 75.

47. Drozdetskiy, A., Cole, C., & Procter, J. B. G. (2015). Pred4: A protein secondary structure prediction server. *Nucleic Acids Research, 43*(W1), W389.
48. Wildes, D., & Marqusee, S. (2004). Hydrogen-Exchange Strategies Applied to Energetics of Intermediate Processes in Protein Folding. *Methods in Enzymology, 380*, 328.
49. Clarke, J., & Itzhaki, L. S. (1998). Hydrogen exchange and protein folding. *Current Opinion in Structural Biology, 8*(1), 112.

The hairpin extension controls solvent access to the chromophore binding pocket in a bacterial phytochrome.

1 Supplementary Information

1.1 Introduction to amide exchange-model

The rate of amide exchange in an unstructured random-coil polypeptide is dependent on temperature, pH as well as the primary structure. Using data from model peptides, this intrinsic rate of exchange (k_{int}) can be easily predicted for each amide in a given protein sequence [4]. In a folded protein, the observed rate constants for amide protons are often much slower than the predicted k_{int}. This is due to solvent inaccessibility, protection by H-bonds or both [5]. Exchange occurs in the protected amides by exposure to solvent due to an opening event as outlined in the two-state model in **Eq.** 3.
These opening events can be small fluctuations that expose only a single amide, local unfolding of a larger segment of structure or global unfolding of the protein [6]. Exchange may also occur by small non-cooperative fluctuations that allow water into the protein interior through solvent channels however **Eq.** 3 does not apply in this case [6].
In a typical experiment, the protein is exchanged into deuterium solution and monitored by NMR and/or mass spectrometry [5]. Assuming the two-state model in **Eq.** 3, the observed rate constant for exchange, k_{obs}, is dependent on the microscopic rate constants k_{op}, k_{cl} respectively and k_{int}. Under native conditions, $k_{cl} \gg k_{op}$ and the observed rate constant for exchange, k_{obs}, is given by [5]:

$$k_{obs} = \frac{k_{op} k_{int}}{k_{cl} + k_{int}} \tag{S1}$$

Two limits exist for exchange depending on the relative magnitudes of the rate constants. At the EX2 limit, $k_{cl} \gg k_{int}$ and k_{obs} simplifies to:

$$k_{obs} = \frac{k_{op}}{k_{cl}} k_{int} \tag{S2}$$

At the EX1 limit, $k_{int} \gg k_{cl}$ and therefore k_{op} becomes rate limiting and k_{obs} simplifies to:

$$k_{obs} = k_{op} \tag{S3}$$

When k_{cl} and k_{op} are of similar magnitude, the kinetics usually have two phases with rate constants [7]:

$$k_{1,2} = \frac{B \pm \sqrt{B^2 - 4A}}{2} \tag{S4}$$

where $A = k_{op} k_{int}$ and $B = k_{op} + k_{cl} + k_{int}$
and amplitudes [7]:

$$A_1 = \frac{k_2 - k_{int} f_o}{k_2 - k_1}, A_2 = \frac{k_{int} f_o - k_1}{k_2 - k_1}, A_1 + A_2 = 1 \tag{S5}$$

where f_o is the fraction of molecules in the open state at time zero which can be written in terms of K_{eq}: $f_o = K_{eq}/(1 + K_{eq})$ where $K_{eq} = k_{op}/k_{cl}$.

1.2 SI Materials and Methods

For pH titration measurements, the stock solutions of the phytochromes in the dark state were diluted into solutions buffered between pH 6 and 11: Mes buffer was used for pH 6 to 7.1, Tris for pH 7.2 to 9.2 and glycine for pH 9.3 to 11. The final concentration of buffer was 30 mM with constant ionic strength maintained at all pH values using NaCl. The final concentrations of the protein constructs were ~2 μM giving an absorbance at 700 nm of about 0.25 at pH 8. incubating in the dark for approximately 3 hours, the absorbance spectrum of each sample was measured in the dark using a Cary 8454 UV-vis spectrometer (Agilent Technologies).
The pH jump in the illuminated Pfr state was performed as described in the main text except, before the dilution, the sample was illuminated with a red LED light (655 nm with output power of 7 mW corresponding a photon flux of about 490 μmol m^{-2} s^{-1}) for 2 min. For CBD-PHY, the dark reversion is very slow with about 2 % conversion to Pr in 50 min [8] and so had minimal effect on the observed kinetics.

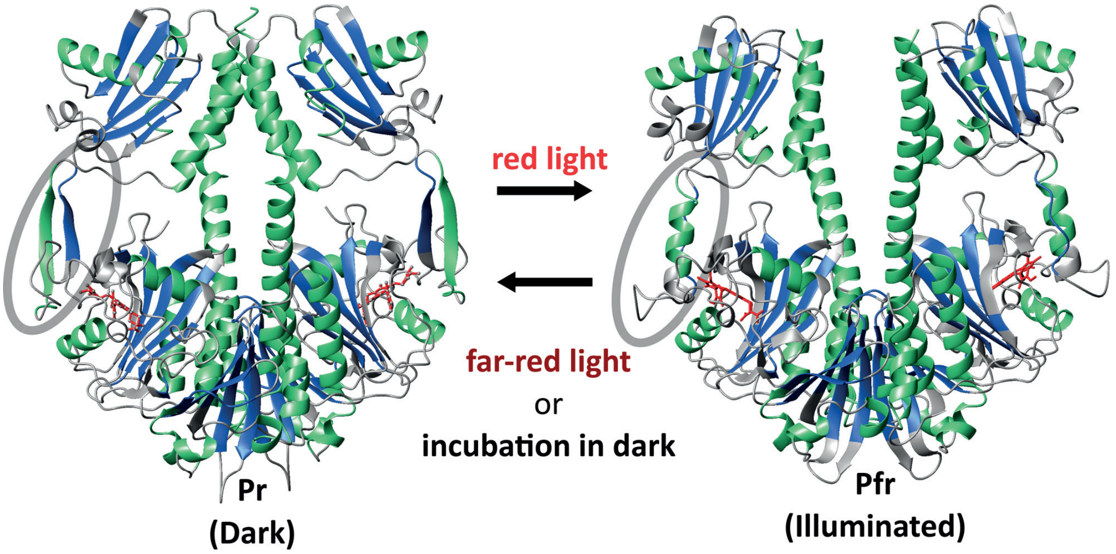

Fig. S1 Structure of CBD-PHY in the Pr and Pfr state The crystal structure of CBD-PHY in the Pr and Pfr state are shown colour coded according to the secondary structure predicted using Jpred 4 [1] (predicted α-helix is green, predicted β-strand is blue, the remaining is grey). The BV chromophore is shown as sticks coloured red. The predicted structure type generally matches with the structure type observed in crystals except for the hairpin extension circled in grey. Figure made using PDB files 4O0P [2] and 5C5K [3].

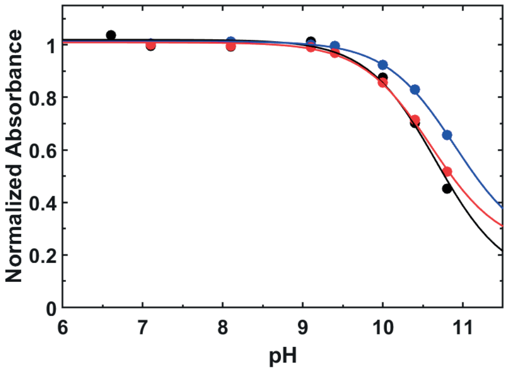

Fig. S2 Absorbance-monitored pH titration The absorbance at 700 nm as a function of pH is plotted for CBD-PHY WT[9] (blue), CBD-PHY Y263F[9] (red), and CBD (black). Experimental details can be found in Supplementary Materials and Methods. Lines represent a fit to a single pK_a model with pK_a values of 10.9, 10.6 and 10.7 for CBD-PHY WT, CBD-PHY Y263F and CBD respectively. Note that the model is under-determined by the data and any fitted parameters are therefore an approximation (See more details in [9])

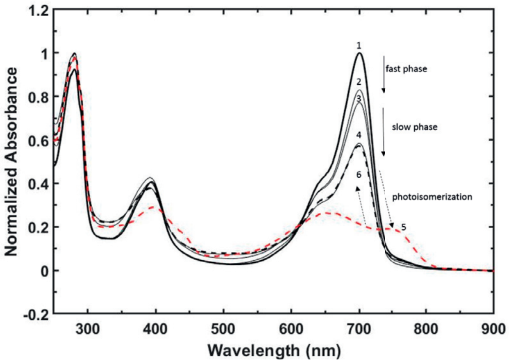

Fig. S3 Absorbance monitored pH jump of CBD-PHY in the dark Pr state and reversible photoisomerization after long incubation at pH 10.8 Spectra are normalized to the absorbance at 700 nm of CBD-PHY in the Pr state in pH 8.0 buffer (scan 1, thick solid line). Absorbance scans are taken after 13 seconds (scan 2) 12 minutes (scan 3) and 150 minutes (scan 4) after dilution into pH 10.8 (thin solid lines). Red light illumination of the sample with prolonged pH 10.8 incubation results in a typical "Pfr" peak at 750 nm (scan 5, short dashed red line, see also **Fig.** S4) which can be reversed to the same Pr spectrum upon illumination with far red light (scan 6, short dashed black line).

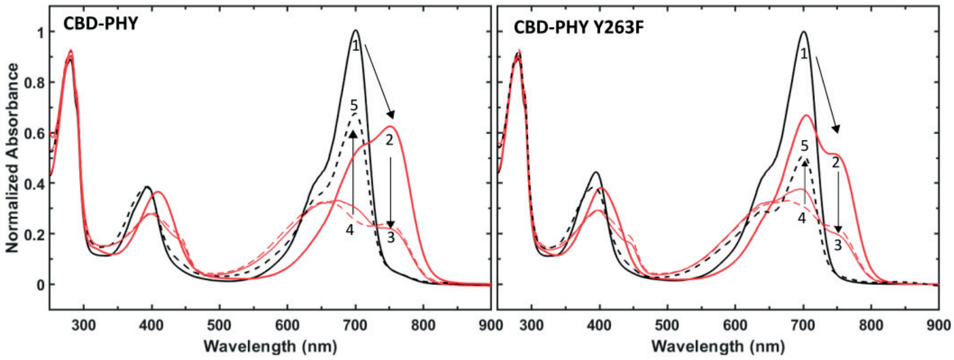

Fig. S4 Determination of endpoint absorbance for pH jump kinetics and fast deprotonation observed in the Pfr state Spectra are normalized to the absorbance at 700 nm in the Pr state in pH 8.0 buffer (scan 1, solid black line). The Pfr state at pH 8.0 is formed after illumination with red light indicated by the increased absorbance at 750 nm (scan 2, solid red line). Approximately 30 % of the population remains in the Pr state due to overlapping Pr and Pfr spectra. A decrease in absorbance is observed 13 seconds after a pH jump from 8.0 to 10.8 (scan 3, thin red line). Measurement at later time points shows a small decrease in absorbance in the 700 nm "Pr peak" but not in the 750 nm "Pfr peak". This indicates deprotonation is fast in the Pfr state and that BV is not protected from solvent exchange. Further illumination with red light slightly increases the 750 nm absorbance indicating the population can be driven further to the Pfr state at high pH (scan 4, red dashed line). Note that the resulting spectra is the same if the phytochrome in the Pr is first diluted into pH 10.8 and then illuminated with red light. Formation of the Pr state at pH 10.8 is observed after illumination with far red light (scan 5, dashed black line). This is the absorption spectrum that is expected for the phytochrome protein at equilibrium protonation at pH 10.8.

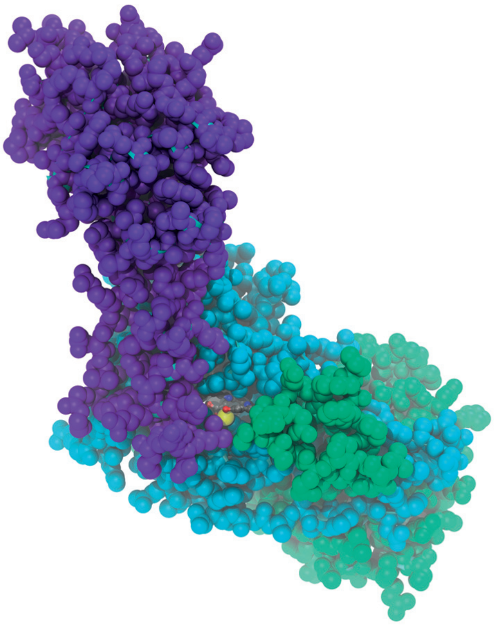

Fig. S5 Solvent exposure of the CBD-PHY binding site in the Pfr state Crystal structure of CBD-PHY in the illuminated Pfr state coloured according to domains as in **Fig.** 1.

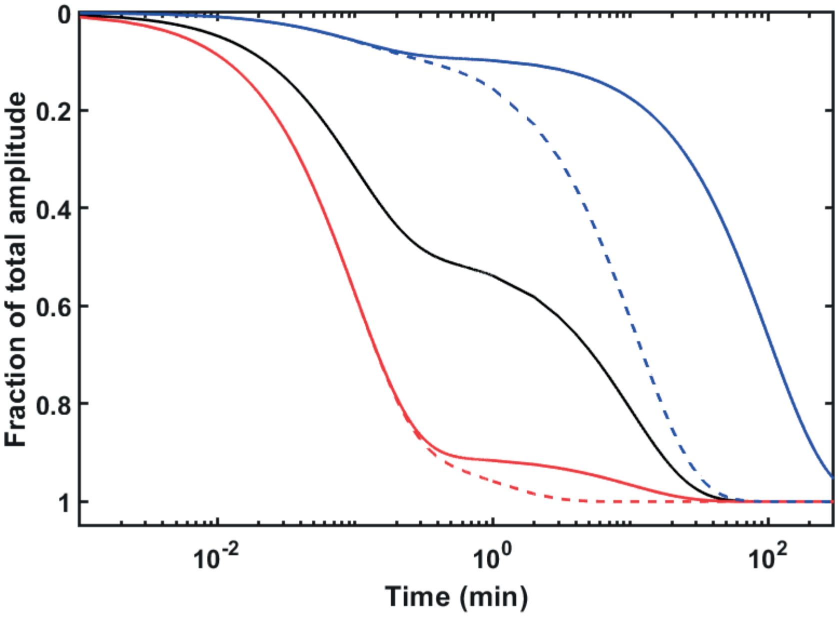

Fig. S6 Effect of k_{op} and k_{cl} on the observed kinetics and relative amplitudes of BV deprotonation Data was simulated using **Eqs.** S4 and S5. The k_{op} was 10 min^{-1} for all simulations. The other rate constants with units of min^{-1} were as follows:

— Blue solid $k_{op} = 0.01$ and $k_{cl} = 0.1$, $K_{eq} = 0.1$ and $fAmp_1$ is 0.1
--- Blue dashed $k_{op} = 0.1$ and $k_{cl} = 1$, $K_{eq} = 0.1$ and $fAmp_1$ is 0.1
— Black solid $k_{op} = 0.1$ and $k_{cl} = 0.1$, $K_{eq} = 1$ and $fAmp_1$ is 0.5
— Red solid $k_{op} = 0.1$ and $k_{cl} = 0.01$, $K_{eq} = 10$ and $fAmp_1$ is 0.9
--- Red dashed $k_{op} = 1$ and $k_{cl} = 0.1$, $K_{eq} = 10$ and $fAmp_1$ is 0.9

References

1. A. Drozdetskiy, C. Cole, J. Procter, B. G.J., Nucleic Acids Res **43**(W1), W389 (2015)
2. H. Takala, A. Björling, O. Berntsson, H. Lehtivuori, S. Niebling, M. Hoernke, I. Kosheleva, R. Henning, A. Menzel, J.A. Ihalainen, S. Westenhoff, Nature **509**(7499), 245 (2014)
3. E.S. Burgie, J. Zhang, R.D. Vierstra, Structure **24**(3), 448 (2016)
4. B. Y, J. Milne, L. Mayne, Englander, Proteins. **17**(1), 75 (1993)
5. D. Wildes, S. Marqusee, in *Energetics of Biological Macromolecules, Part E*, *Methods in Enzymology*, vol. 380 (Academic Press, 2004), pp. 328–349
6. J. Clarke, L.S. Itzhaki, Current Opinion in Structural Biology **8**(1), 112 (1998)
7. H. Qian, S.I. Chan, Journal of Molecular Biology **286**(2), 607 (1999)
8. H. Takala, H. Lehtivuori, H. Hammarén, V.P. Hytönen, J.A. Ihalainen, Biochemistry **53**(45), 7076 (2014)
9. J.A. Rumfeldt, H. Takala, A. Liukkonen, J.A. Ihalainen, Photochem. Photobiol. **95**(4), 969 (2019)

II

THE STRUCTURAL EFFECT BETWEEN THE OUTPUT MODULE AND CHROMOPHORE-BINDING DOMAIN IS A TWO-WAY STREET VIA THE HAIRPIN EXTENSION

by

Moona Kurttila, Stefan Etzl, Jessica Rumfeldt, Heikki Takala, Nadine Galler,
AndreasWinkler & Janne A. Ihalainen 2022

Photochemical & Photobiological Sciences 21: 1881–1894

https://doi.org/10.1007/s43630-022-00265-5

Photochemical & Photobiological Sciences (2022) 21:1881–1894
https://doi.org/10.1007/s43630-022-00265-5

ORIGINAL PAPERS

The structural effect between the output module and chromophore-binding domain is a two-way street via the hairpin extension

Moona Kurttila[1] · Stefan Etzl[2] · Jessica Rumfeldt[1] · Heikki Takala[1] · Nadine Galler[2] · Andreas Winkler[2] · Janne A. Ihalainen[1]

Received: 13 May 2022 / Accepted: 30 June 2022 / Published online: 19 August 2022

Abstract

Signal transduction typically starts with either ligand binding or cofactor activation, eventually affecting biological activities in the cell. In red light-sensing phytochromes, isomerization of the bilin chromophore results in regulation of the activity of diverse output modules. During this process, several structural elements and chemical events influence signal propagation. In our study, we have studied the full-length bacteriophytochrome from *Deinococcus radiodurans* as well as a previously generated optogenetic tool where the native histidine kinase output module has been replaced with an adenylate cyclase. We show that the composition of the output module influences the stability of the hairpin extension. The hairpin, often referred as the PHY tongue, is one of the central structural elements for signal transduction. It extends from a distinct domain establishing close contacts with the chromophore binding site. If the coupling between these interactions is disrupted, the dynamic range of the enzymatic regulation is reduced. Our study highlights the complex conformational properties of the hairpin extension as a bidirectional link between the chromophore-binding site and the output module, as well as functional properties of diverse output modules.

1 Introduction

Protein function is influenced to a large degree by the biophysical properties of the 20 proteinogenic amino acids and their 3-dimensional arrangement. While a diversity of ligand-binding sites or active centers can be formed this way, the versatility of protein function can be even further expanded by interactions of proteins with non-protein-based organic compounds or metal ions—so called cofactors. Not only do they provide access to chemistry otherwise infeasible, but they also enable photoreceptor proteins to sense light ranging from the blue region all the way to the near-infrared end of the electromagnetic spectrum [41]. In the case of photoreceptors, cofactors not only need to absorb light of their corresponding spectral regions, but they also should allow signal integration via functional interactions with regulatory parts of the protein. To this end, characteristic hydrogen-bonding interactions are typically formed with polar amino acid side chains or water molecules in the cofactor binding site. Eventually, these interactions can be modulated during the formation of a photoactivated state and, subsequently, the local structural rearrangements can be propagated over long distances to enable allosteric regulation of different output functionalities or modulation of biological interactions [14]. These light-induced structural rearrangements are an active area of research but their description at a molecular level is frequently complicated by the dynamic nature of these processes. A comprehensive understanding requires an integrative approach that enables analysis over different time and length scales [8, 19, 23, 25, 49].

As far as red light-sensing phytochromes are concerned, these are typically multi-domain sensor systems with a

---

This publication is dedicated to Prof. Silvia E. Braslavsky, a pioneer in photobiology and photobiophysics, on the occasion of her 80th birthday.

✉ Andreas Winkler
andreas.winkler@tugraz.at

✉ Janne A. Ihalainen
janne.ihalainen@jyu.fi

[1] Nanoscience Center, Department of Biological and Environmental Science, University of Jyväskylä, 40014 Jyväskylä, Finland

[2] Institute of Biochemistry, Graz University of Technology, Petersgasse 12/II, 8010 Graz, Austria

variety of linked output functionalities across different species [1, 23, 48]. The reactions of phytochromes start with the photoisomerization of a covalently bound bilin molecule inside the chromophore-binding PAS (Per/Arnt/Sim) and GAF (cGMP phosphodiesterase/adenylyl cyclase/FhlA) domains (Fig. 1) [64]. For canonical Group I phytochromes [46], photoactivation initiates structural changes in the photosensory module (PSM), consisting of PAS, GAF, and PHY (phytochrome specific) domains, including local changes in side chain rotamers around the bilin chromophore [74], the refolding of the N-terminal extension preceding the PAS domain [22], and the refolding of the hairpin extension in the PHY domain, also referred to as the tongue, from β-sheet (as in Fig. 1) to α-helix in the photoactivated state [11, 54, 56]. Phytochromes thereby frequently cycle between a red light absorbing Pr and a far-red light absorbing Pfr state. Because of the initial bilin isomerization from *ZZZssa* conformation in Pr to *ZZEssa* in Pfr [63, 70] and the coupled rearrangements in local hydrogen-bonding interactions, the photostates can be fairly simply tracked with UV–Vis spectroscopy (Fig. S1). Eventually, the structural changes in the PSM enable the regulation of a variety of biochemical activities in diverse output modules, such as enzymatic activities or biomolecular interactions [23, 74].

In plants, phytochromes regulate a diversity of key processes related to their growth and development, such as shade avoidance and seed germination [36, 47]. Phytochromes exist also in prokaryotic cells, including photosynthetic and non-photosynthetic bacteria, cyanobacteria and algae, as well as in fungi [4, 6, 27, 46]. Due to their less complex domain architecture and simpler requirements for cofactor maturation, a lot of structural and functional studies have recently addressed biliverdin-binding bacteriophytochromes. Even with this subgroup of phytochromes it has, however, been challenging to link atomic-level structural information of both photostates to their corresponding biochemical activities. In some cases, like with *Agrobacterium fabrum* phytochrome (Agp) [4, 30, 35], activity assays have been available but structural information has been lacking. In other cases, like with *Deinococcus radiodurans* bacteriophytochrome (*Dr*BphP) [11, 56], structural information has been available, even if only for the PSM alone, but the enzymatic readout has been missing. Furthermore, the dynamic nature of the underlying signaling processes has been overlooked or its influence underestimated. To date, these shortcomings start to alleviate as structural information for Agp becomes available [53], enzymatic output for the *Dr*BphP has been revealed [73], and the dynamic perspective of the protein subunits in their photostationary states has been reported [24, 51].

Reports of atomic structures for wild-type bacteriophytochoromes including the histidine kinase output modules have been rare, mainly relying on homology models [5], but full-length structural studies of bacteriophytochromes with other types of output modules have been reported [3, 44, 43]. Full-length structural data could be also

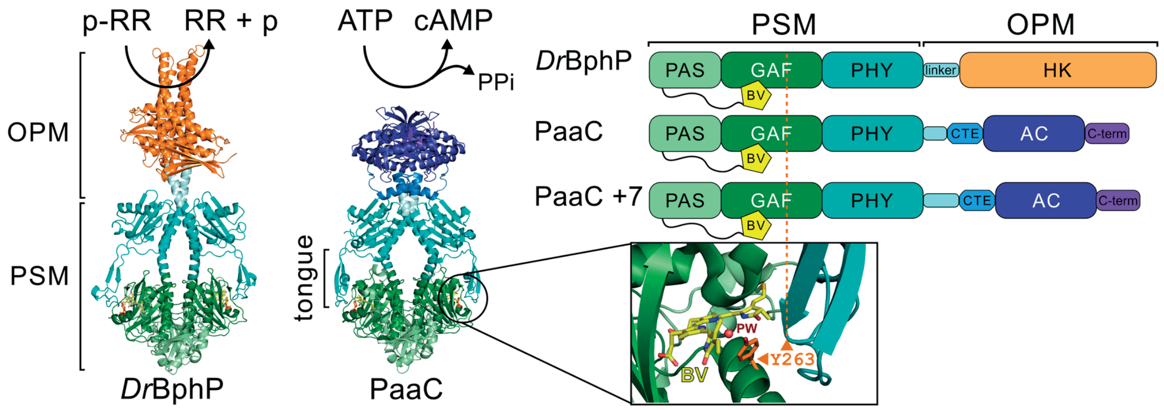

Fig. 1 The structures of the phytochromes used in the study. The *Deinococcus radiodurans* bacteriophytochrome (*Dr*BphP) photosensory module (PSM) consists of a PAS domain with a preceding N-terminal extension where the biliverdin (BV) is covalently attached, a GAF domain that physically buries the BV cofactor, and the PHY domain that includes a structurally flexible tongue that extends close to the BV binding site. The GAF domain provides a highly conserved tyrosine residue (amino acid 263 according to *Dr*BphP numbering), which is highlighted in the close-up of the binding site to show its interaction with the cofactor, the central pyrrole water (PW), and the tongue element. The function of the photoreceptor is defined by the output module (OPM) that is linked to the PSM via a linker region. In wild-type *Dr*BphP, this is a histidine kinase (HK). Replacing the HK domain with an adenylate/guanylate cyclase (AC/GC) from *Synechocystis* sp. including its cognate cyclase transducer element (CTE) created functional chimeras with PaaC and the 7 residue longer linker variant PaaC +7 providing red light regulated cyclase activity [16]. The full-length *Dr*BphP structure is based on a homology model from Björling et al. [5], and the PaaC structure is based on the PDB coordinates 6FHT [16]

obtained for a system, where the PSM is naturally linked to a diguanylate cyclase effector domain, allowing to correlate structural changes of the protein with a direct linkage to the enzymatic activity [21]. In the latter case, even structural rearrangements propagating all the way from the cofactor environment through the sensor-effector linker to the active site of the OPM could be described [22]. With respect to synthetic constructs, a guanylate cyclase (GC) from *Synechocystis* sp. including its cyclase transducer element (CTE) was functionally linked to the PSM of *Dr*BphP system creating a phytochrome activated guanylate cyclase that can easily be switched to an adenylate specific cyclase (PaaC), rendering it a versatile optogenetic tool [16]. Functional properties of this synthetic fusion and its linker region could be correlated with structural details of its full-length structure to provide a detailed picture of its signal transduction mechanism [16].

As indicated above, for *Dr*BphP, not only are structural data available for both Pr and Pfr states [11, 56], but recently also functional insights have been enriched [73]. Mutagenesis of critical amino acids has been performed on a large scale [37, 38, 50, 66], and the PSM has been successfully employed for the generation of artificial optogenetic tools [12, 16, 20, 29, 76]. Still, unexpected insights can be observed. For example, the substitution of the tyrosine at position 263 with a phenylalanine [60], resulting in uncoupling of the tongue and chromophore interactions, thus allowing structural properties of Pfr, such as the α-helical tongue to be observed in an otherwise Pr-state biliverdin environment. Importantly, the effect of the Y263F substitution was in part correlated with an altered water coordination in the BV environment, a property that could directly be linked to differences in protonation of the cofactor in various photocycle states [9, 33, 50, 60]. With two different enzymatic readouts, coupled to the same kind of PSM, at hand [16, 73], we set out to study in detail the effect of this Y263F substitution in the context of full-length proteins (Fig. 1).

To that end, we studied the relation between the dynamics of the tongue and the output module by means of solvent accessibility of the chromophore [51], FTIR spectroscopy, and biochemical activity assays. In our studies, we used full-length *Dr*BphP and its fragment lacking the output module (*Dr*PSM), as well as an artificial variant with an adenylate cyclase output module and two different functional sensor-effector linker lengths (PaaC and PaaC +7) [16]. Based on the combination of these four variants and their different output module compositions, we show that the output module stabilizes the conformation of the tongue in the dark state, in which it has been shown to switch between folded (β-sheet) and random coil conformations [24, 51]. With all phytochrome variants and their Y263F mutants we show that the uncoupling between the tongue and the chromophore environment decreases the dynamic range of the enzyme, i.e., the ratio of the enzymatic activities in the dark-adapted and in the light-activated signaling states [76].

Eventually, these insight are helpful for understanding central properties of light-regulated systems, such as the dynamic range of activation. Tunability of the dynamic range over several orders of magnitude and the favorable tissue penetration of red light could enable more advanced optogenetic tools for mammalian systems [72]. Therefore, understanding the relation between biliverdin conformation, chromophore environment and structural, as well as dynamic alterations of the overall structure to regulate the activity of the output domain, is crucial for an improved understanding of the underlying molecular mechanisms.

2 Materials and methods

2.1 Protein expression and purification

2.1.1 *Dr*BphP variants

The expression plasmids coding for wild-type *Dr*BphP fragments (*Dr*PSM with amino acids 1–502, full-length with amino acids 1–755) were kindly provided by the laboratories of Prof. R. D. Vierstra and Prof. K. T. Forest [10, 64, 65]. The point mutations (Y263F) were introduced by QuikChange Lightning Multi Site-Directed Mutagenesis Kit (Agilent Technologies) and confirmed by sequencing. The $(His)_6$-tagged constructs were expressed in *Escherichia coli* BL21(DE3) as described previously [58]. Purification was performed by means of affinity chromatography followed by size-exclusion chromatography in 30 mM Tris pH 8.0, as described in Ihalainen et al. [28]

2.1.2 PaaC variants

Genes encoding for the uncoupled variants of PaaC and PaaC +7 were created by mutagenesis PCR of the codon required for the *Dr*BphP Y263F amino acid exchange in the pETM-11-based vectors of PaaC and PaaC +7 [16] according to the procedure of Liu and Naismith [39]. The primers for the codon optimized sequences are presented in Table S1. The resulting plasmids were sequence verified and transformed in *E. coli* BL21 (DE3) *cya*$^-$ pT7Ho1 competent cells for plate screenings and *E. coli* BL21 (DE3) pT7Ho1 for protein expression and purifcation as described previously [16]. The proteins were stored and studied in 10 mM Tris (pH 8.0), 150 mM NaCl, and 2 mM $MgCl_2$.

2.2 Activity assays

2.2.1 Phosphatase PhosTag activity assay

The PhosTag activity assay was performed as in [73]. The *Dr*BphP WT and *Dr*BphP Y263F were introduced with pre-phosphorylated response regulator (RR) from *D. radiodurans*. The phosphorylation of the RR was conducted at +37°C for 2.8 mg/ml of RR in the presence of 100 mM acetyl phosphate. For the gels in darkness and red light conditions, 0.4 mg/ml and 0.06 mg/ml of phytochrome concentrations were used, respectively. The samples were pre-illuminated with saturating red LED (660 nm, 5 min, on average 13 mW/cm^2) or far-red laser (> 780 nm, Thorlabs, 20 s, 80 mW/cm^2) to reach the Pfr or Pr state, respectively during a 5-min incubation at +25°C. The dephosphorylation reactions were initiated with 1 mM ATP and the samples were incubated either under red light (as above) or in the dark at +25°C during the reaction, and stopped at corresponding time point with 5x SDS loading buffer. For the mobility shift detection of phosphorylated RR (p-RR) proteins, Zn^{2+}-Phostag® SDS-PAGE assay (Wako Chemicals) was applied. The reactions were run in the 9% SDS-PAGE gels containing 20 μM PhosTag acrylamide at room temperature with 40 mA according to the instructions of the manufacturer.

To determine the concentration of the p-RR and the rate of the spontaneous breakage of p-RR to RR, a separate control gel without phytochrome samples was run otherwise as described above. First, the concentration of the p-RR from the RR/p-RR mixture was quantified from their intensity ratio, obtained by ImageJ program, revealing a 50% phosphorylation rate (Fig. S2A). Second, a time series with *Dr*BphP WT and Y263F, where the reactions were kept at +25°C for different times (otherwise on ice), were made. The band intensities were normalized to the zero time point and fitted to a single polynomial function. The slope was used to correct the activity assay gel results to investigate the phytochrome activity alone (Fig. S2B).

The reaction catalyzed by *Dr*BphP WT and Y263F at each time point was followed by plotting the p-RR and phytochrome concentration ratio at each time point. The gels for dark and red light conditions were both repeated three times (Fig. S3) from which the value for each time point was averaged, and errors as standard deviation were calculated. The reaction is assumed to proceed as in the following equation:

$$[E] + [S] \underset{k_{-1}}{\overset{k_1}{\rightleftharpoons}} [ES] \xrightarrow{k_2} [E] + [P]. \tag{1}$$

Assuming that the k_2 is the rate limiting step of the reaction, the first four time points of the reaction were fitted to a linear function to derive the initial velocities for reactions in dark and red light conditions for *Dr*BphP WT and Y263F (Fig. S4).

2.2.2 Adenylate cyclase activity assays

Adenylate cyclase activity assays were performed according to the procedure described in [16]. Briefly, reactions were set up using 20 μM PaaC and PaaC +7 at a substrate concentration of 1 mM ATP at 20°C. For light state measurements, samples were pre-illuminated for 10 min using a 660 nm LED (Thorlabs) at 34 mW/cm^2. Dark state measurements were performed under non-actinic conditions with indirect dim green light. After various incubation times, reactions were stopped by heat inactivation at 95°C for 1 min. The soluble part was subsequently analyzed by HPLC and substrate and product concentrations quantified. Measurements were done for various time points and initial velocities were derived from linear fits weighted by the standard deviation of three independent replicates.

The plate screening assay for adenylate cyclase activity was performed as described in [16]. Briefly, *E. coli* BL21 (DE3) *cya*$^-$ cells containing the helper plasmid pT7Ho1 were transformed with plasmids encoding the adenylate cyclase variants. As a negative control, a pETM-11 plasmid with a gene encoding for a non-cyclase blue light-sensitive photoreceptor protein (AppAΔC) was transformed [67]. Cells were grown in LB medium supplemented with 0.36% glucose at 37°C. An aliquot was then harvested, the cells collected by centrifugation and resuspended to reach an OD600 of 20. 4 µl of the cell suspension were spotted on LB agar plates [10 µM IPTG, 60 µg/ml 5-bromo-4-chloro-3-indolyl-β-D-galactopyranoside (X-Gal), 10 µg/ml 5-aminolevulinic acid, antibiotics] and incubated in the dark or under constant red light illumination for several hours at 37°C, until a change in coloration of the colonies was observed.

2.3 Steady-state FTIR spectroscopy

By illuminating the sample with saturating 661 nm or 775 nm LED, providing Pfr or Pr state, respectively, the difference FTIR-signal between the states was measured using a Nicolet Magna IR-760 FTIR spectrometer as described in Kurttila et al. [34]. The procedure was repeated for H_2O diluted and D_2O diluted 30 mM Tris buffers at pH 8.0. The difference spectra were normalized to the negative biliverdin D-ring C=O stretch band [18] at 1712 cm^{-1} (in H_2O) or 1700 cm^{-1} (in D_2O).

2.4 pH jump with stopped-flow

The so called pH-jump experiment records kinetic changes of absorption properties of the phytochrome after rapid pH change of the solution. The method is adapted from Rumfeldt et al. [51] However, here the aim was to record absorbance changes in the sub-second time-scale. Therefore, a TgK Scientific Hi-Tech KinetAsyst Stopped-Flow system that has a dead time of 1–2 ms (instead of 13 s with manual mixing) was used.

The phytochrome samples were freshly prepared in 0.4 mM Tris pH 8.0 with an absorbance of about 0.4 at 700 nm. The stopped-flow device was used to rapidly mix 60 mM glycine pH 10.8 buffer with the initially prepared phytochrome mix, resulting in pH 10.8 in 30 mM glycine, 0.2 mM Tris buffer concentrations. The absorbance changes were detected with an integration time of 1.6 ms and low light intensity to minimize the photoconversion during the early time points. Control experiments in 15.4 mM Tris at pH 8.0 confirmed that the fast phase does not suffer from detection driven photoconversion. All the measurements were repeated at least 15 times, including measurements from separate sample batches, and with time intervals varying between 8 ms, 15 ms, 80 ms and 150 ms. All the measurements were averaged to reach an adequate signal-to-noise ratio. The measurements were carried out at 21°C.

The "slow phase" of the pH-jump measurement to determine the end point absorption was measured using manual mixing and a Cary 8454 UV–Vis spectrometer (Agilent Technologies) as described in [51] with the data analysis, described earlier.

The fast phase required a bi-exponential fitting function according to the following equation:

$$A_{\text{measured}} = A_1 \times e^{-k_1 t} + A_2 \times e^{-k_2 t} + A_{\text{fast endpoint}}, \tag{2}$$

where A_{measured} is the normalized absorbance measured at 700 nm, A_i and k_i are the amplitudes and rate constants for the fast phase, respectively, t is time and $A_{\text{fast endpoint}}$ is the final absorbance value of the fast phase. Further, the data were scaled in respect of the total change according to the final endpoint of the whole process.

2.5 Natural diversity in bacteriophytochrome sequence space and coevolution analysis

During characterization of sequence space of the PadC family [7], one family member was identified that naturally features F at the position corresponding to Y263 in *Dr*BphP. HHBlits searches with this sequence revealed several homologs featuring identical sensor-effector linker lengths with the same substitution. In addition, residues identified by Gremlin coevolution analysis [45] to correlate with the Y263 position [7] show interesting substitutions in this subfamily that indicate a different biliverdin environment, especially around the D-ring.

3 Results and discussion

3.1 The output module stabilizes the "closed" conformation of the tongue in its resting state

We recently introduced a method where solvent access to the chromophore-binding pocket can be studied by a quick pH jump [51]. This allows determination of the tongue fluctuation between "closed" and "open" conformations in the Pr state. In *Dr*BphP, the closed tongue conformation protects the BV environment from solvent and the open conformation allows solvent access to BV resulting in deprotonation of the cofactor at high pH (> 10.5). Deprotonation of BV decreases its absorption at the phytochrome Q-band (around 700 nm) (Fig. S1) [26, 61], and in terms of kinetics of the absorbance changes, two phases can be observed (Fig. S5). In the population responsible for the fast phase, the tongue is in the "open" conformation and BV thus deprotonates rapidly. The slow phase corresponds to the kinetics of tongue opening from its closed state [51].

The use of stopped-flow spectrophotometry enabled measuring absorbance changes on sub-second time-scales (Fig. 2). In most of the studied samples, the resulting kinetics required a minimum of two-exponential fits. We note that the kinetic signal in the range around 20 and 80 ms is challenging to fit with exponential functions. The signal in this time range probably reflects complex deprotonation mechanics in the studied systems. However, our major aim was to find out the dynamic nature of the tongue system. In all cases, the total amplitude of the decay (Amp_{fast} in Fig. 2) corresponds to the population of the open conformation present at the initiation of the jump. If the tongue is in a conformation that allows solvent access to the BV environment, deprotonation takes place essentially on the time-scale of 150 ms. To reveal the fraction of the fast phase amplitude relative to the total absorbance change, we also recorded the overall absorbance decrease (Fig. S5). The smallest fast phase amplitudes are observed in PaaC +7 (0.14), *Dr*BphP WT (0.16) and PaaC +7 Y263F (0.16). These numbers imply that in the dark state, 86% and 84% of the population, respectively, have the tongue in a "closed" conformation, i.e., folded as a β-sheet thereby preventing solvent access to biliverdin. The shorter the linker length is between PHY and OPM (PaaC vs. PaaC +7 and *Dr*BphP) or if the OPM is completely missing, the greater the fraction of the fast phase amplitude that is observed, up to values of 0.52 for *Dr*PSM Y263F mutant. This shows that the OPM, the linker region, and the tyrosine side chain in the 263 position stabilize the conformation of the tongue as a β-sheet in the dark state.

The Pr to Pfr spectral changes in the mid-IR-region reveal the changes of the biliverdin, its surroundings, and the protein scaffold upon photoactivation [18, 17, 28,

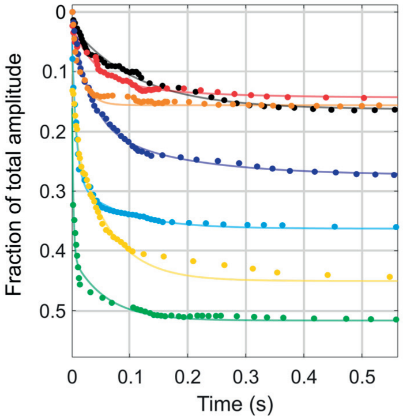

Construct	Amp_1	τ_1(ms)	Amp_2	τ_2(ms)	Amp_{fast}
● PaaC +7 WT	0.03	39.5	0.09	**151.7**	0.14
● *Dr*BphP WT	-	-	0.14	**112.1**	0.16
● PaaC +7 Y263F	0.15	**16.6**	-	-	0.16
● PaaC WT	0.09	30.9	0.17	**156.8**	0.27
● PaaC Y263F	0.27	**7.4**	0.08	83.1	0.36
● *Dr*PSM WT	0.17	3.9	0.26	**59.7**	0.45
● *Dr*PSM Y263F	0.40	**2.2**	0.11	57.1	0.52

Fig. 2 The BV deprotonation, followed at A_{700} as a function of time after a rapid pH jump from pH 8.0 to 10.8. The data (dots) is normalized to the A_{700} at pH 8.0, fitted to a double exponent function Eq. 2 (solid line), and scaled to the total amplitude of the whole reaction, shown in Fig. S5. The fitted time constants and their amplitudes are presented in the table on the left side. The more dominating fractions of the fits are marked in bold. The Y263F mutants are highlighted with grey. The sum of squared errors (SSE) of the fits are < 0.0067 for *Dr*PSM and < 0.0027 for the full-length systems

31, 34, 54, 62]. Already 25 years ago, Foerstendorf et al. performed extensive FTIR analysis of the phytochrome proteins, distinguishing the IR-signals from the chromophore from the protein scaffold. However, the link to the structural changes of the protein were hampered due to the lack of crystal structures in those early days [18, 17]. Later on, Stojković et al. determined clear changes in the amide I region between Pr and Pfr states for *Rhodopseudomonas palustris* systems, which they pinpointed to the tongue region [54].

In terms of *Dr*BphP, the secondary structural changes are slightly more difficult to observe [28, 38, 59], albeit the clear changes in the crystal structures [11, 56]. Most likely, this is due to compensating signals from the chromophore binding PAS-GAF domains [59]. Nevertheless, we can detect a clear Pr-related (negative signal in the Pfr *minus* Pr difference spectrum) signal at 1642–1644 cm^{-1} in *Dr*BphP in H_2O, which is down shifted to 1629–1630 cm^{-1} and better revealed in respect to intensity of other signals in D_2O (Fig. 3). We relate this signal to the disappearance of the β-sheet structure upon the photoconversion to the Pfr state [9, 32, 54, 60, 68]. The positive appearance of the α-helix in the Pfr-state is somewhat buried under other signals of the system but a small positive contribution at 1635–1641 cm^{-1} and 1650–1657 cm^{-1} in D_2O and H_2O, respectively, can be observed.

The constructs in our study reveal variation of the size of the negative signal (β-sheet in Pr) (Fig. 3A). The signal decreases in PaaC WT in comparison to *Dr*BphP WT, and is the smallest in *Dr*PSM. Relatively, the PaaC +7 has slightly bigger negative signal with respect to the PaaC. As this signal can be rather safely related to the changes in the tongue region, these observations correlate with the solvent accessibility study shown above: a shorter sensor-effector

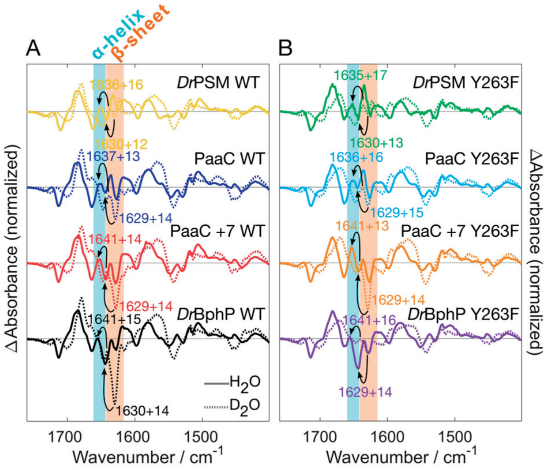

Fig. 3 The effect of the output module on the changes in amide I signals detected by FTIR. The difference spectra (Pfr *minus* Pr) were measured in H_2O (solid line) and D_2O (dotted line). The numbers with arrows indicate the shift from D_2O to H_2O of the negative signals within the β-sheet region (1615–1638 cm^{-1}, rust background) and the positive signals within the α-helix region (1642–1660 cm^{-1}, cyan background). **A** *D. radiodurans* photosensory module and all full-length systems without any point mutations, **B** Y263F variants of the same constructs. The H_2O and D_2O spectra are normalized according to the negative 1712 cm^{-1} peak and D_2O spectra are scaled with a factor of 0.5 to match the size of H_2O spectra

linker or a completely missing OPM results in a more flexible tongue region. Naturally, we can not rule out compensating effects of other signals among the different constructs.

Despite the lack of the prominent FTIR difference signal indicative of β-sheet to α-helix transition and the challenging deprotonation kinetics in the stopped-flow data, our results are in good agreement and support each other. The solvent accessibility phenomenon with pH-jump method has been studied so far only in *Dr*BphP [51]. However, in various prokaryotic phytochrome crystal structures, for example in *Rp*BphP2 [71], *Is*PadC [21], *Sa*BphP1 [75] and Cph1 [15], the β-folded tongue appears to block the solvent access to the chromophore-binding pocket, like in *Dr*BphP. Therefore, it would be interesting to see, if the solvent access is similar for example in *Rp*BphP2 or Cph1, that show relatively large β-sheet to α-helix transition in their FTIR difference spectra [54, 62]. On the other hand, some crystal structures of plant phytochromes, like *Gm*PhyB [42] and *At*PhyB [10], suggest that the tongue allows solvent access to the chromophore even in the Pr state. Therefore, the pH-jump method would help to verify this observation in solution.

3.2 Tongue flexibility affects the biochemical activity of phytochromes

The flexibility of the tongue region may also relate to the biochemical activity of the constructs. *Dr*BphP functions as a phosphatase and its activity can be switched on with red light [73]. Also, the cyclase activity of the PaaC variants switches on with red light [16]. Thus, in the dark state, *Dr*BphP and the PaaC variants should, in principle, be inactive. In spite of this, the dynamic tongue fluctuates between 'closed' and 'open' conformations in the dark state [24, 51]. To understand the consequence of tongue dynamics on the activity, we ran an activity assays of *Dr*BphP and PaaC variants (Fig. 4), and the switching between Pr and Pfr states was confirmed with UV–Vis spectroscopy (Fig. S1). The phosphatase activity of *Dr*BphP was followed by tracking the disappearance of the substrate p-RR with a PhosTag activity assay [73] in dark and red light conditions (Fig. 4A, all gels available in SI Fig. S3), taking into account the spontaneous breakage of p-RR (Fig. S2). The specific activities of *Dr*BphP in dark and red light conditions, derived from the initial velocity of the reactions (Fig. S4), reveal that *Dr*BphP is not completely inactive in the dark state (Fig. 4B). In the dark, *Dr*BphP WT has specific activity of 0.050 min^{-1}. Under red light, the specific activity increases to 1.65 min^{-1}, 33 times higher than in darkness. The ratio between the red light and dark state-specific activities corresponds to the dynamic range of the system.

The specific activities of the PaaC variants reveal that also all of them have some dark state activity (Fig. 4C). Here, the same output activity allows the comparison between PaaC and PaaC +7 revealing that the specific dark state activity in PaaC (0.5*10^{-3} min^{-1}) is higher than in PaaC +7 (0.4*10^{-3} min^{-1}). This correlates with the more dynamic tongue region in PaaC compared to PaaC +7 as seen in the pH-jump and FTIR experiments (Figs. 2 and 3A). The lower dark state activity in PaaC +7 WT in comparison to PaaC WT is also visible in the cell-based screening, where green color indicates enzymatic activity of the PaaC variants (Fig. 4D). The introduction of the additional turn in the linker region in

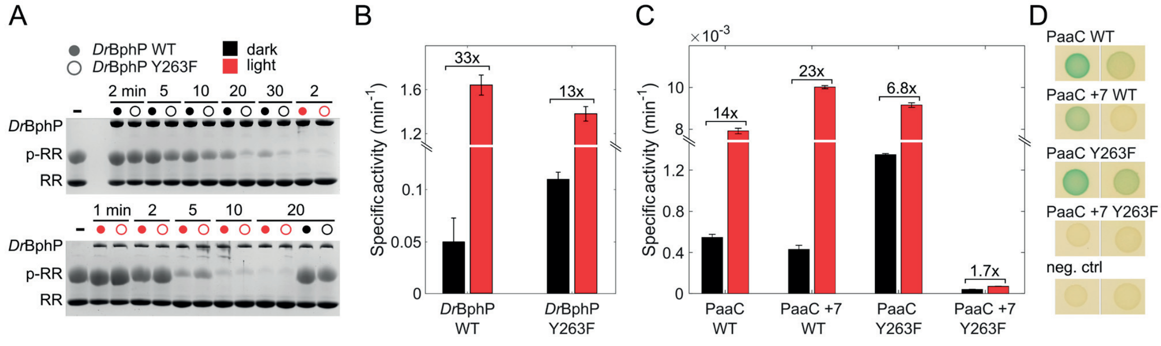

Fig. 4 Phosphatase and cyclase activity of the phytochrome variants in dark and red light. **A** The declining amount of phosphorylated response regulator (p-RR) upon phosphatase activity was followed at different time points in the dark (top panel) and under red light (bottom) for *Dr*BphP WT and Y263F with a PhosTag assay. The phytochrome (enzyme) concentration used in the bottom gel is 6 times less than on the top. **B** The specific activity of *Dr*BphP WT and Y263F in dark and red light were determined from the gels in A (the kinetic plots in Fig. S4). A y-axis break was introduced between 0.14 and 1.1 min^{-1} for better visualization of the dark state activity. The numbers on top indicate the dynamic range for *Dr*BphP WT and Y263F. **C** Specific activities of PaaC variants. Black bars correspond to dark state activities, while red bars reflect specific activities in the illuminated states. A y-axis break was introduced between 0.0015 and 0.0075 min^{-1} to enable better visualization of the low PaaC +7 Y263F activity. **D** Representation of adenylate cyclase screening of the PaaC variants in cyclase deficient *E. coli* cells, grown at 37 °C

PaaC +7 WT increases the dynamic range also by increasing the specific activity under red light from ($8*10^{-3}$ min^{-1}) to ($10*10^{-3}$ min^{-1}) (Fig. 4C). As a result, the fold change in PaaC +7 WT is 23-fold, which is 64% higher than the 14-fold change in PaaC WT.

Due to the different chemical outputs, the specific activities between *Dr*BphP and PaaC variants are difficult to compare. Still, the dynamic ranges are comparable (Fig. 4B, C). They show that the natural system *Dr*BphP has the highest fold change (33-fold). The artificial PaaC variants do not reach the dynamic range of the natural system with 23-fold and 14-fold changes in PaaC +7 WT and PaaC WT, respectively, but they still operate at comparable levels. We note that none of the systems is completely inactive in the dark in vitro. This suggests that organisms must have developed coupled regulatory mechanisms to control the on and/or off states of signaling components.

3.3 Influence of the Y263F mutation on the tongue dynamics and further to the enzymatic activity

Above, we have shown that the full-length linker and OPM strengthen the stability of the tongue, which also influences the dynamic range of the enzyme activity. Previously, the effect of the uncoupling between the chromophore and the tongue by the Y263F mutation has been demonstrated in structural terms in *Dr*BphP PSM [60]. Now, we link the uncoupling effect to the tongue dynamics and enzymatic activity in full-length *Dr*BphP and PaaC variants. The activity assays of *Dr*BphP and PaaC WT and Y263F mutants show that the Y263F mutation increases the dark state activity (Fig. 4B, C). In *Dr*BphP Y263F and PaaC Y263F, the dark state activity is 2 and 2.5 times higher, respectively, than in their respective WT. The red light activity is slightly lower in *Dr*BphP Y263F and slightly higher in PaaC Y263F than in their WT counterparts. However, the evident decrease of the dynamic range in both *Dr*BphP and PaaC appears to be mainly due to the increase of the dark state activity in the Y263F mutants.

Interestingly, almost negligible cyclase activity for PaaC +7 Y263F was revealed. Compared to the fully functional PaaC +7 construct, which has a relatively high dynamic range, the light state activity is approximately 140 times smaller in PaaC +7 Y263F (Fig. 4C). However, there is still a slight difference in activity between dark and red light conditions. The results of the in vitro activity assay are to some extend repeated in vivo, (Fig. 4D). Both PaaC and PaaC Y263F have green color in the light state, and some dark state activity when grown at 37 °. PaaC +7 also shows light state activity, but not with the same intensity as PaaC and PaaC Y263F. PaaC +7 Y263F shuts down also in vivo and no activity is observed in dark or light conditions.

The FTIR spectra show that the Y263F mutation decreases the intensity of the negative Pr-related β-sheet signal in PaaC and *Dr*BphP in comparison to WT, seen in particular in D_2O measurement (Fig. 3). In PaaC WT and PaaC +7 WT the β-sheet signal in H_2O is bigger in comparison to their Y263F mutants, but in *Dr*BphP WT it is smaller than in its Y263F variant, most probably due to overlapping signals. In contrast, in D_2O, the PaaC +7 Y263F presents slightly increased signal intensity in comparison to the WT. This might indicate a stabilized tongue architecture even in the Y263F variant due to the more stabilized coiled-coil effector of this system, which would also correspond to the decreased overall activity. The typically decreased refolding of the tongue in the Y263F variant has been shown earlier in *Dr*PSM, discussed together with other spectral changes caused by the mutation [60].

The uncoupling of the chromophore and the tongue due to the Y263F mutation affects the solvent accessibility, as expected. In all Y263F mutants, the amplitude of the fast change due to deprotonation is bigger than in their WT counterparts (Fig. 2) meaning that due to uncoupling, the solvent accessibility to the chromophore is increased. This has been showed before in the photosensory module [51] and here also in full-length variants (Fig. 2). The increased tongue dynamics are observed in FTIR as well as solvent accessibility studies, and we connect these fluctuations to the increased dark state enzymatic activity (Fig. 4B, C). In PaaC +7 WT vs. Y263F counterparts, the difference in the tongue dynamics is rather small, observed both by FTIR (Fig. 3) and the solvent accessibility. Nevertheless, this variant features a rather inhibited state, which correlates with a stabilized Pr tongue conformation (Fig. 4).

A closer look at the fast phase time constants of the solvent accessibility studies reveals a difference between the Y263F mutants and their wild-type counterparts (Fig. 2). In all Y263F variants, the dominating amplitude has a time constant of 10 ms. When the hydroxyl group at residue 263 is present, the time constant of the dominating component is around 100 ms. The difference between dominating time constants is observed even in both PaaC +7 s, although the total amplitude remains similar despite the Y263F mutation. This suggests that the Y263 has a role in the BV (de) protonation mechanism, possibly through water network interactions [13]. The sub-second deprotonation data possibly include information about the mechanism as the bi-exponential fit is not sufficient to capture all the features of the data. However, these data alone are inadequate to make interpretations about the (de)protonation mechanism in detail and will not be discussed further in this paper, but should be studied more carefully in the future.

3.4 The linkage of the tyrosine at 263 to other structural elements in bacteriophytochromes—coevolution alignment

Above, we demonstrated the influence of Y263 on tongue dynamics as well as for enzymatic activity in *Dr*BphP-based systems. The importance of tyrosine at this position can also be demonstrated by a small sequence alignment-coevolution study. While the vast majority of bacteriophytochromes, but also more distantly related phytochromes such as the fungal outgroup of the alignment (Fig. 5), show a strictly conserved tyrosine at this position, a small subfamily of bacteriophytochromes naturally features a replacement of tyrosine with phenylalanine Y/F263 (Fig. 5). Interestingly, members of this family show concomitant changes at other critical biliverdin-binding residues (red circles in Fig. 5). Apparently, different BV environments can fulfill similar functions for the stabilization of the intricate rearrangements accompanying light activation. Since these compensating mutations are not available in our Y263F variants, the apparently important regulatory network in the D-ring environment is missing and, therefore, negatively affects the dynamic ranges of the variants.

As shown above and in [60], the Y263F variant in *Dr*BphP causes uncoupling of the chromophore and the tongue and decreases the photoconversion efficiency [60]. Apparently, the productive formation of Pfr is reduced by an increased structural heterogeneity of the chromophore in the Pr state, which in turn allows sampling of Pfr-like conformations even in the dark. Along these lines, shorter constructs bearing only the chromophore-binding domain of *Dr*BphP system and featuring the same Y263F substitution have been shown to exhibit increased fluorescent yields, making them interesting candidates as fluorescent reporters [1]. Also for more distantly related bacteriophytochromes from *Rhodopseudomonas palustris* (*Rp*BphP), the analogous amino acid replacement was shown to only moderately affect Pfr formation in the classical Pr-Pfr converting *Rp*BphP2, whereas it completely abolishes Pr to Pnr formation in *Rp*BphP3. Interestingly, the region responsible for the uncommon photocycle characteristics can also be attributed to residues lining the biliverdin D-ring [69].

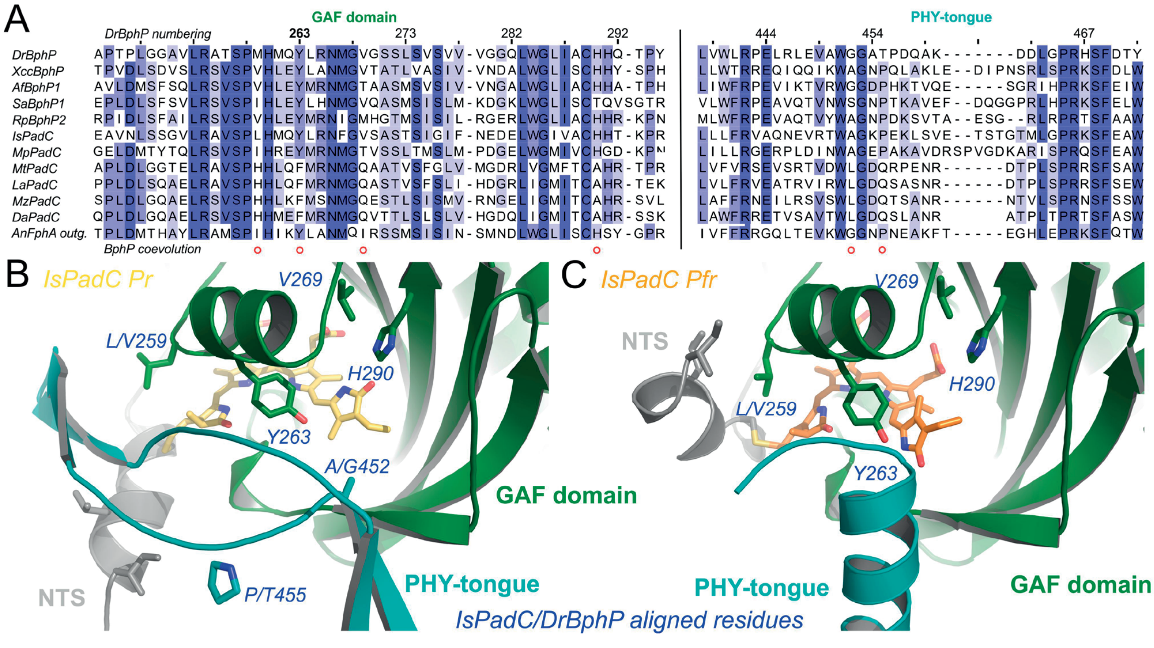

Fig. 5 Sequence conservation analysis of some well studied bacteriophytochromes compared to the subfamily of PadCs with a naturally occurring Y263F substitution. **A** Sequence alignment of two amino acid stretches involved in BV D-ring coordination. The fungal FphA outgroup is shown at the bottom of the alignment. The other sequences from top to bottom correspond to *Dr*BphP, *Xanthomonas campestris* BphP, *A. fabrum* BphP1 (Agp1), *Stigmatella aurantiaca* BphP1, *Rs. palustris* BphP2, *Idiomarina* species A28L Phytochrome activated diguanylate cyclase (PadC), *Marinobacter persicus* PadC, *Microbacterium trichothecenolyticum* PadC, *Leifsonia aquatica* PadC, *Mycetocola zhadangensis* PadC and *Demequina aestuarii* PadC. **B+C** Close ups of the three-dimensional structures corresponding to the closest homolog structure available for the PadC family with the natural Y263F substitution—*Is*PadC—in Pr [21] and Pfr conformations [22], respectively. The BV cofactor is shown in yellow and orange, respectively. Colors of individual domain elements are the same as used in Figure 1. Numbering correspond to *Dr*BphP

The most detailed characterization of a system featuring the corresponding Y263F substitution in Cph1 from *Synechocytsis* also revealed interesting parallels, while also showing important differences at a structural level [40]. In Cph1 the substitution of Tyr to Phe also increased the fluorescence yield and slowed down formation of an otherwise typical Pfr spectrum, which was attributed to different populations of structurally heterogeneous biliverdin substates in the Pr state. At a structural level, interesting changes of tongue residues in the region of biliverdin contact sites were also observed. However, it was unclear whether these are due to crystal contacts or due to the introduced amino acid substitution. Overall, the tongue architecture was still in a Pr-like conformation even though some potentially functionally relevant rearrangements of the photosensory module were observed by the changes in the PHY domain orientation relative to the chromophore-binding domain [40].

3.5 A short linker region between the OPM and tongue rationalizes the observed effects on the tongue dynamics and enzymatic activity

One of the main conclusion of our study is that the composition of the OPM influences to the properties of the tongue region. First, the presence of the OPM considerably stabilizes the tongue in its Pr state in comparison to with the PSM only. Both FTIR spectra and pH-jump experiments imply more loose tongue systems in the PSM construct. Secondly, by increasing the stability of the coiling linker helix towards the OPM, the stability of the tongue region increases.

A closer look at the crystal structures reveals an interesting detail about the link between the tongue and the OPM. There are only eight amino acids between the tongue and the helix at the C-terminal end of PHY domain that finally extends as the coiled-coil linker of the OPM, highlighted in purple in Fig. 6. The short linker between the tongue and OPM regions gives an intuitive picture of a direct channel between the structural changes in the tongue region and the properties of the OPM. Consequently, changes in the OPM are easily reflected back to the tongue, and hence in the chromophore-binding pocket (Fig. 6).

In photoreceptors, the enzymatic activity of the OPM can be either increased or suppressed with light [41]. For example, in the case of *A. fabrum* phytochrome, red light suppresses the kinase activity [4, 30, 35, 73]. In nature, the dynamic range in photoreceptors can cover at least three orders of magnitude. For example, a fold change of over 1000-fold has been recorded for the cGMP producing rhodopsinguanylyl cyclase from *Catenaria anguillulae*,

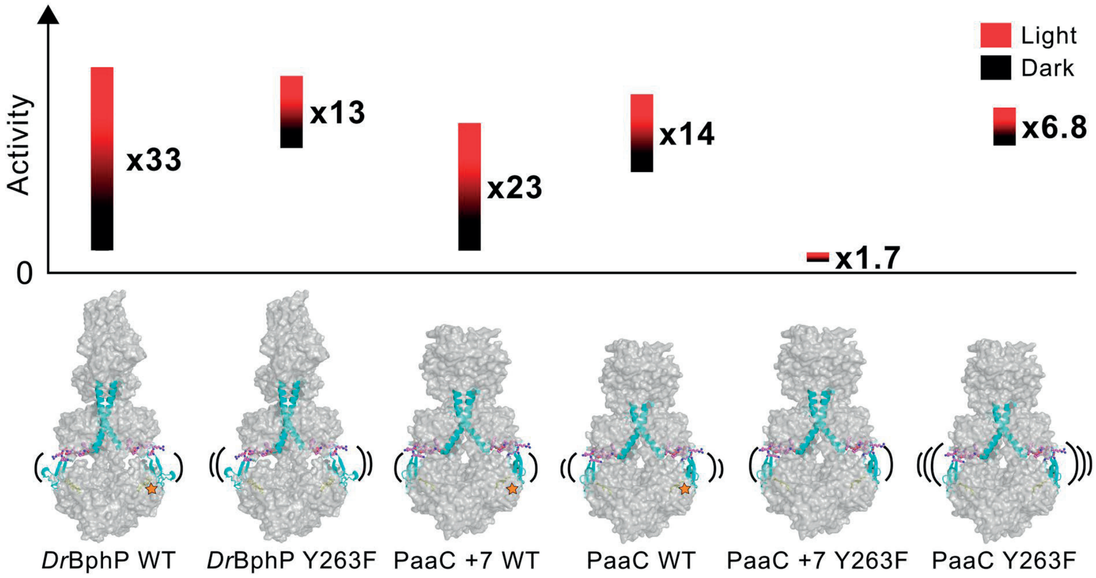

Fig. 6 Overview of dynamic ranges of *Dr*BphP and PaaC variants. The height of the bars represents the dynamic range of each construct, and the amount of activity in the dark or under red light is illustrated as the relative position of the bars on the y-axis in relation to each other. We interpret the changes in dynamic ranges either by (1) different output modules with increasing/decreasing cross-talk between the linker and the tongue or (2) by the uncoupling between the chromophore, tongue and thus output module due to the Y263F substitution. The tongue and the N-terminal PHY-helix that finally extends into the sensor-effector linker helix are directly connected *via* eight residue long chains, shown with ball-and-stick model in purple. The dynamics of the tongue are illustrated in the structures, and the presence of the coupling hydroxyl group at position 263 is marked with a star. The structure of the PaaC +7 variants is an illustration based on the PaaC structure with additional turns in the linker helix (cyan)

where the activity is switched on with green light [52]. The dynamic range of a LOV-domain-based photoswitch has been improved from 5- to 70-folds by rational mutations [55]. In our WT systems, the fold change varied from 14-fold in PaaC WT to 33-fold in *Dr*BphP WT. It has been pointed out by Ziegler and Möglich, that thermodynamically the magnitude of the dynamic range is mainly dependent upon how well the enzymatic activity can be shut off in the non-active state, in our case the dark state [76]. The more dynamic the tongue is, either due to weaker stabilization from the OPM, due to uncoupling between the chromophore and tongue, or due to other properties, the smaller the dynamic range. The cross-talk between the tongue and the OPM seems to be the one of the key tuning nobs of the dynamic range in the phytochromes, and the short linker provides an effective communication wire between them.

4 Conclusions

The signal transduction from the light absorbing chromophore to the enzymatically active OPM as well as stabilizing the light state conformation require delicate intramolecular regulation mechanisms. The structural events in bacteriophytochromes can be divided into tiers, where the small scale reactions take place around the chromophore, which are then linked to secondary structural changes of the tongue and the N-terminal segment [23], and finally to large-scale structural changes or to changes in the activity of OPM [23, 74]. Previously, the uncoupling of the different tiers of a phytochrome has been demonstrated in the photosensory module alone by Takala et al. [60]. They showed that the chromophore, the flexible tongue and the overall protein structure do not always act hand in hand. When the linkage between the chromophore and the tongue, a hydroxyl group in Y263F, is removed, even though the chromophore is in its Pr conformation (*ZZZssa*), the tongue and the globular structure can resemble the structures of the Pfr state. Here, we demonstrated the uncoupling phenomenon in terms of enzymatic activity: the same point mutation position (Y263F) in the full-length system leads to a more flexible tongue region, and further, to lower the dynamic range of the enzymes due to increased dark state activity. The results could be rationalized by a larger population of “open” tongue systems in the dark state. This highlights the role of the tyrosine in the position 263 in linking the PHY domain to the chromophore-binding pocket, and thus in the allosteric communication between the sensory and effector domains of *Dr*BphP.

Furthermore, a direct interplay between the OPM, the tongue, and thus the chromophore-binding pocket in a bacteriophytochrome is demonstrated. The composition of the OPM relates directly to the dynamics of the tongue, which again influences the dynamic range in enzymatic activity of the studied samples. With three different phytochrome constructs, wild-type *Dr*BphP, PaaC and PaaC +7 all bearing the same photosensory module from *Dr*BphP, we show that all the output modules stabilize the tongue in comparison to the photosensory module alone, and that the natural *Dr*BphP system operates with the largest dynamic range. However, the artificial red light-responsive adenylate cyclase PaaC +7 does not fall far behind. The reported fold changess of the wild-type systems range from 14-fold to 33-fold, which is promising for optogenetic applications.

The OPM is connected to the tongue, i.e., the hairpin extension, via a helical linker and a short connector between the linker helix and the tongue. All together, these structures and the coupling of the tongue and chromophore assure a stiff-but-controllable structural connection between the enzymatic activity and the photoactivated state of the chromophore, like a two-way street.

Supplementary Information The online version contains supplementary material available at https://doi.org/10.1007/s43630-022-00265-5.

Acknowledgements This work benefited from access to the Molecular Biophysics, Oulu, Finland, an Instruct-ERIC center. Financial support was provided by Instruct-ERIC (PID: 13173), Academy of Finland (332742 and 330678, for JAI and HT, respectively), and the Austrian Science Fund (FWF): P32022 (to AW). We thank Dr. Tiila-Riikka Kiema and Prof. Rikkert Wierenga for the discussions and the kind help with the pH-jump experiments.

Funding Open Access funding provided by University of Jyväskylä (JYU).

Declarations

Conflict of interest On behalf of all the authors, the corresponding authors state that there is no conflicts of interest.

References

1. Auldridge, M. E., & Forest, K. T. (2011). Bacterial phytochromes: More than meets the light. *Critical Reviews in Biochemistry and Molecular Biology, 46*(1), 67–88.
2. Auldridge, M. E., Satyshur, K. A., Anstrom, D. M., & Forest, K. T. (2012). Structure-guided engineering enhances a

phytochrome-based infrared fluorescent protein. *Journal of Biological Chemistry, 287*(10), 7000–7009.

3. Bellini, D., & Papiz, M. Z. (2012). Structure of a bacteriophytochrome and light-stimulated protomer swapping with a gene repressor. *Structure, 20*(8), 1436–1446.
4. Bhoo, S.-H., Davis, S. J., Walker, J., Karniol, B., & Vierstra, R. D. (2001). Bacteriophytochromes are photochromic histidine kinases using a biliverdin chromophore. *Nature, 414*(6865), 776–779.
5. Björling, A., Berntsson, O., Lehtivuori, H., Takala, H., Hughes, A. J., Panman, M., et al. (2016). Structural photoactivation of a full-length bacterial phytochrome. *Science Advances, 2*(8), e1600920.
6. Blumenstein, A., Vienken, K., Tasler, R., Purschwitz, J., Veith, D., Frankenberg-Dinkel, N., & Fischer, R. (2005). The aspergillus nidulans phytochrome FPHA represses sexual development in red light. *Current Biology, 15*(20), 1833–1838.
7. Böhm, C., Gourinchas, G., Zweytick, S. et al. (2022) Characterisation of sequence–structure–function space in sensor–effector integrators of phytochrome-regulated diguanylate cyclases. *Photochemical & Photobiological Sciences*. https://doi.org/10.1007/s43630-022-00255-7
8. Bostock, M. J., Solt, A. S., & Nietlispach, D. (2019). The role of NMR spectroscopy in mapping the conformational landscape of GPCRs. *Current Opinion in Structural Biology, 57,* 145–156.
9. Buhrke, D., Gourinchas, G., Müller, M., Michael, N., Hildebrandt, P., & Winkler, A. (2020). Distinct chromophore-protein environments enable asymmetric activation of a bacteriophytochrome-activated diguanylate cyclase. *Journal of Biological Chemistry, 295*(2), 539–551.
10. Burgie, E. S., Wang, T., Bussell, A. N., Walker, J. M., Li, H., & Vierstra, R. D. (2014). Crystallographic and electron microscopic analyses of a bacterial phytochrome reveal local and global rearrangements during photoconversion. *Journal of Biological Chemistry, 289*(35), 24573–24587.
11. Burgie, E. S., Zhang, J., & Vierstra, R. D. (2016). Crystal structure of Deinococcus phytochrome in the photoactivated state reveals a cascade of structural rearrangements during photoconversion. *Structure, 24*(3), 448–457.
12. Chernov, K. G., Redchuk, T. A., Omelina, E. S., & Verkhusha, V. V. (2017). Near-infrared fluorescent proteins, biosensors, and optogenetic tools engineered from phytochromes. *Chemical Reviews, 117*(9), 6423–6446.
13. Claesson, E., Wahlgren, W. Y., Takala, H., Pandey, S., Castillon, L., Kuznetsova, V., et al. (2020). The primary structural photoresponse of phytochrome proteins captured by a femtosecond x-ray laser. *eLife, 9,* e53514.
14. Ernst, O. P., Lodowski, D. T., Elstner, M., Hegemann, P., Brown, L. S., & Kandori, H. (2014). Microbial and animal Rhodopsins: Structures, functions, and molecular mechanisms. *Chemical Reviews, 114*(1), 126–163.
15. Essen, L.-O., Mailliet, J., & Hughes, J. (2008). The structure of a complete phytochrome sensory module in the PR ground state. *Proceedings of the National Academy of Sciences of the United States of America, 105*(38), 14709–14714.
16. Etzl, S., Lindner, R., Nelson, M. D., & Winkler, A. (2018). Structure-guided design and functional characterization of an artificial red light-regulated guanylate/adenylate cyclase for optogenetic applications. *Journal of Biological Chemistry, 293*(23), 9078–9089.
17. Foerstendorf, H., Mummert, E., Schäfer, E., Scheer, H., & Siebert, F. (1996). Fourier-transform infrared spectroscopy of phytochrome: Difference spectra of the intermediates of the photoreactions. *Biochemistry, 35*(33), 10793–10799.
18. Foerstendorf, H., Benda, C., Gärtner, W., Storf, M., Scheer, H., & Siebert, F. (2001). FTIR studies of phytochrome photoreactions reveal the C=O bands of the chromophore: Consequences for its protonation states, conformation, and protein interaction. *Biochemistry, 40*(49), 14952–14959.
19. Fushimi, K., & Narikawa, R. (2019). Cyanobacteriochromes: Photoreceptors covering the entire UV-to-visible spectrum. *Current Opinion in Structural Biology, 57,* 39–46.
20. Gasser, C., Taiber, S., Yeh, C.-M., Wittig, C. H., Hegemann, P., Ryu, S., et al. (2014). Engineering of a red-light–activated human camp/CGMP-specific phosphodiesterase. *Proceedings of the National Academy of Sciences of the United States of America, 111*(24), 8803–8808.
21. Gourinchas, G., Etzl, S., & Winkler, A. (2017). Long-range allosteric signaling in red light-regulated diguanylyl cyclases. *Science Advances, 3*(3), e1602498.
22. Gourinchas, G., Heintz, U., & Winkler, A. (2018). Asymmetric activation mechanism of a homodimeric red light-regulated photoreceptor. *eLife, 7,* e34815.
23. Gourinchas, G., Etzl, S., & Winkler, A. (2019). Bacteriophytochromes—from informative model systems of phytochrome function to powerful tools in cell biology. *Current Opinion in Structural Biology, 57*(57), 72–83.
24. Gustavsson, E., Isaksson, L., Persson, C., Mayzel, M., Brath, U., Vrhovac, L., et al. (2020). Modulation of structural heterogeneity controls phytochrome photo switching. *Biophysical Journal, 118*(2), 415–421.
25. Heath, G. R., & Scheuring, S. (2019). Advances in high-speed atomic force microscopy (hs-afm) reveal dynamics of transmembrane channels and transporters. *Current Opinion in Structural Biology, 57,* 93–102.
26. Hirose, Y., Rockwell, N. C., Nishiyama, K., Narikawa, R., Ukaji, Y., Inomata, K., et al. (2013). Green/red cyanobacteriochromes regulate complementary chromatic acclimation via a protochromic photocycle. *Proceedings of the National Academy of Sciences of the United States of America, 110*(13), 4974–4979.
27. Hughes, J., Lamparter, T., Mittmann, F., Hartmann, E., Gärtner, W., Wilde, A., & Börner, T. (1997). A prokaryotic phytochrome. *Nature, 386*(6626), 663–663.
28. Ihalainen, J. A., Gustavsson, E., Schroeder, L., Donnini, S., Lehtivuori, H., Isaksson, L., et al. (2018). Chromophore-protein interplay during the phytochrome photocycle revealed by step-scan FTIR spectroscopy. *Journal of the American Chemical Society, 140*(39), 12396–12404.
29. Kaberniuk, A. A., Shemetov, A. A., & Verkhusha, V. V. (2016). A bacterial phytochrome-based optogenetic system controllable with near-infrared light. *Nature Methods, 13*(7), 591–597.
30. Karniol, B., & Vierstra, R. D. (2003). The pair of bacteriophytochromes from Agrobacterium tumefaciens are histidine kinases with opposing photobiological properties. *Proceedings of the National Academy of Sciences of the United States of America, 100*(5), 2807–2812.
31. Kottke, T., Lórenz-Fonfría, V. A., & Heberle, J. (2017). The grateful infrared: Sequential protein structural changes resolved by infrared difference spectroscopy. *The Journal of Physical Chemistry B, 121*(2), 335–350.
32. Kraskov, A., Buhrke, D., Scheerer, P., Shaef, I., Sanchez, J. C., Carrillo, M., et al. (2021). On the role of the conserved histidine at the chromophore isomerization site in phytochromes. *The Journal of Physical Chemistry B, 125*(50), 13696–13709.
33. Kübel, J., Chenchiliyan, M., Ooi, S. A., Gustavsson, E., Isaksson, L., Kuznetsova, V., et al. (2020). Transient IR spectroscopy identifies key interactions and unravels new intermediates in the photocycle of a bacterial phytochrome. *Physical Chemistry Chemical Physics, 22*(17), 9195–9203.
34. Kurttila, M., Stucki-Buchli, B., Rumfeldt, J., Schroeder, L., Häkkänen, H., Liukkonen, A., et al. (2021). Site-by-site tracking of signal transduction in an azidophenylalanine-labeled

bacteriophytochrome with step-scan FTIR spectroscopy. *Physical Chemistry Chemical Physics, 23,* 5615–5628.

35. Lamparter, T., Michael, N., Mittmann, F., & Esteban, B. (2002). Phytochrome from Agrobacterium tumefaciens has unusual spectral properties and reveals an N-terminal chromophore attachment site. *Proceedings of the National Academy of Sciences of the United States of America, 99*(18), 11628–11633.
36. Legris, M., Ince, Y., & Fankhauser, C. (2019). Molecular mechanisms underlying phytochrome-controlled morphogenesis in plants. *Nature Communications, 10*(1), 5219.
37. Lehtivuori, H., Rissanen, I., Takala, H., Bamford, J., Tkachenko, N. V., & Ihalainen, J. A. (2013). Fluorescence properties of the chromophore-binding domain of bacteriophytochrome from *Deinococcus radiodurans*. *The Journal of Physical Chemistry B, 117*(38), 11049–11057.
38. Lenngren, N., Edlund, P., Takala, H., Stucki-Buchli, B., Rumfeldt, J., Peshev, I., et al. (2018). Coordination of the biliverdin D-ring in bacteriophytochromes. *Physical Chemistry Chemical Physics, 20*(27), 18216–18225.
39. Liu, H., & Naismith, J. H. (2008). Adding new chemistries to the genetic code. *BMC Biotechnology, 8*(91), 413–444.
40. Mailliet, J., Psakis, G., Feilke, K., Sineshchekov, V., Essen, L.-O., & Hughes, J. (2011). Spectroscopy and a high-resolution crystal structure of tyr263 mutants of cyanobacterial phytochrome cph1. *Journal of Molecular Biology, 413*(1), 115–127.
41. Möglich, A., Yang, X., Ayers, R. A., & Moffat, K. (2010). Structure and function of plant photoreceptors. *Annual Review of Plant Biology, 61,* 21–47.
42. Nagano, S., Guan, K., Shenkutie, S. M., Feiler, C., Weiss, M., Kraskov, A., et al. (2020). Structural insights into photoactivation and signalling in plant phytochromes. *Nature Plants, 6*(5), 581–588.
43. Otero, L. H., Klinke, S., Rinaldi, J., Velázquez-Escobar, F., Mroginski, M. A., López, F., et al. (2016). Structure of the full-length bacteriophytochrome from the plant pathogen *Xanthomonas campestris* provides clues to its long-range signaling mechanism. *Journal of Molecular Biology, 428*(19), 3702–3720.
44. Otero, L. H., Foscaldi, S., Antelo, G. T., Rosano, G. L., Sirigu, S., Klinke, S., et al. (2021). Structural basis for the pr-pfr long-range signaling mechanism of a full-length bacterial phytochrome at the atomic level. *Science Advances, 7*(48), eabh1097.
45. Ovchinnikov, S., Kamisetty, H., & Baker, D. (2014). Robust and accurate prediction of residue-residue interactions across protein interfaces using evolutionary information. *eLife, 3,* e02030.
46. Rockwell, N. C., & Lagarias, J. C. (2010). A brief history of phytochromes. *ChemPhysChem, 11*(6), 1172–1180.
47. Rockwell, N. C., & Lagarias, J. C. (2020). Phytochrome evolution in 3D: Deletion, duplication, and diversification. *New Phytologist, 225*(6), 2283–2300.
48. Rockwell, N. C., Su, Y.-S., & Lagarias, J. C. (2006). Phytochrome structure and signaling mechanisms. *Annual Review of Plant Biology, 57,* 837–858.
49. Roth, B. L. (2019). How structure informs and transforms chemogenetics. *Current Opinion in Structural Biology, 57,* 9–16.
50. Rumfeldt, J. A., Takala, H., Liukkonen, A., & Ihalainen, J. A. (2019). UV-vis spectroscopy reveals a correlation between Y263 and BV protonation states in bacteriophytochromes. *Photochemistry and Photobiology, 95*(4), 969–979.
51. Rumfeldt, J. A., Kurttila, M., Takala, H., & Ihalainen, J. A. (2021). The hairpin extension controls solvent access to the chromophore binding pocket in a bacterial phytochrome: A UV-vis absorption spectroscopy study. *Photochemical and Photobiological Sciences, 20*(9), 1173–1181.
52. Scheib, U., Broser, M., Constantin, O. M., Yang, S., Gao, S., Mukherjee, S., et al. (2018). Rhodopsin-cyclases for photocontrol of cgmp/camp and 2.3Å structure of the adenylyl cyclase domain. *Nature Communications, 9*(1), e2046.
53. Schmidt, A., Sauthof, L., Szczepek, M., Lopez, M. F., Escobar, F. V., Qureshi, B. M., et al. (2018). Structural snapshot of a bacterial phytochrome in its functional intermediate state. *Nature Communications, 9*(9), 4912.
54. Stojković, E. A., Toh, K. C., Alexandre, M. T. A., Baclayon, M., Moffat, K., & Kennis, J. T. M. (2014). FTIR spectroscopy revealing light-dependent refolding of the conserved tongue region of bacteriophytochrome. *The Journal of Physical Chemistry Letters, 15*(5), 2512–2515.
55. Strickland, D., Yao, X., Gawlak, G., Rosen, M. K., Gardner, K. H., & Sosnick, T. R. (2010). Rationally improving LOV domain-based photoswitches. *Nature Methods, 7*(8), 623–626.
56. Takala, H., Björling, A., Berntsson, O., Lehtivuori, H., Niebling, S., Hoernke, M., et al. (2014). Signal amplification and transduction in phytochrome photosensors. *Nature, 509*(7499), 245–248.
57. Takala, H., Lehtivuori, H., Hammarén, H., Hytönen, V. P., & Ihalainen, J. A. (2014). Connection between absorption properties and conformational changes in *Deinococcus radiodurans* phytochrome. *Biochemistry, 53*(45), 7076–7085.
58. Takala, H., Björling, A., Linna, M., Westenhoff, S., & Ihalainen, J. A. (2015). Light-induced changes in the dimerization interface of bacteriophytochromes. *Journal of Biological Chemistry, 290*(26), 16383–16392.
59. Takala, H., Niebling, S., Berntsson, O., Björling, A., Lehtivuori, H., Häkkänen, H., et al. (2016). Light-induced structural changes in a monomeric bacteriophytochrome. *Structural Dynamics, 3*(5), 12.
60. Takala, H., Lehtivuori, H. K., Berntsson, O., Hughes, A., Nanekar, R., Niebling, S., et al. (2018). On the (un)coupling of the chromophore, tongue interactions, and overall conformation in a bacterial phytochrome. *Journal of Biological Chemistry, 293*(21), 8161–8172.
61. Van Thor, J. J., Borucki, B., Crielaard, W., Otto, H., Lamparter, T., Hughes, J., et al. (2001). Light-induced proton release and proton uptake reactions in the cyanobacterial phytochrome Cph1. *Biochemistry, 40*(38), 11460–11471.
62. Van Thor, J. J., Fisher, N., & Rich, P. R. (2005). Assignments of the Pfr - Pr FTIR difference spectrum of cyanobacterial phytochrome Cph1 using ^{15}N and ^{13}C isotopically labeled phycocyanobilin chromophore. *The Journal of Physical Chemistry B, 109*(43), 20597–20604.
63. van Thor, J. J., Ronayne, K. L., & Towrie, M. (2007). Formation of the early photoproduct Lumi-R of cyanobacterial phytochrome Cph1 observed by ultrafast mid-infrared spectroscopy. *Journal of the American Chemical Society, 129*(1), 126–132.
64. Wagner, J. R., Brunzelle, J. S., Forest, K. T., & Vierstra, R. D. (2005). A light-sensing knot revealed by the structure of the chromophore-binding domain of phytochrome. *Nature, 438*(7066), 325–331.
65. Wagner, J. R., Zhang, J., Brunzelle, J. S., Vierstra, R. D., & Forest, K. T. (2007). High resolution structure of Deinococcus bacteriophytochrome yields new insights into phytochrome architecture and evolution. *Journal of Biological Chemistry, 282*(16), 12298–12309.
66. Wagner, J. R., Zhang, J., von Stetten, D., Günther, M., Murgida, D. H., Mroginski, M. A., et al. (2008). Mutational analysis of *Deinococcus radiodurans* bacteriophytochrome reveals key amino acids necessary for the photochromicity and proton exchange cycle of phytochromes. *Journal of Biological Chemistry, 283*(18), 12212–12226.
67. Winkler, A., Heintz, U., Lindner, R., Reinstein, J., Shoeman, R. L., & Schlichting, I. (2013). A ternary AppA-PpsR-DNA complex mediates light regulation of photosynthesis-related gene expression. *Nature Structural and Molecular Biology, 20*(7), 859–867.

68. Xu, Q.-Z., Gött-Zink, L., Gärtner, W., Zhao, K.-H., & Kottke, T. (2020). Tongue refolding in the knotless cyanobacterial phytochrome All2699. *Biochemistry, 59*(22), 2047–2054.
69. Yang, X., Stojković, E. A., Kuk, J., & Moffat, K. (2007). Crystal structure of the chromophore binding domain of an unusual bacteriophytochrome, rpbphp3, reveals residues that modulate photoconversion. *Proceedings of the National Academy of Sciences, 104*(30), 12571–12576.
70. Yang, Y., Linke, M., Von Haimberger, T., Hahn, J., Matute, R., González, L., et al. (2012). Real-time tracking of phytochrome's orientational changes during Pr photoisomerization. *Journal of the American Chemical Society, 134*(3), 1408–1411.
71. Yang, Y., Linke, M., von Haimberger, T., Matute, R., González, L., Schmieder, P., & Heyne, K. (2014). Active and silent chromophore isoforms for phytochrome Pr photoisomerization: An alternative evolutionary strategy to optimize photoreaction quantum yields. *Structural Dynamics, 1*(1), 014701.
72. Lehtinen, K., Nokia, M. S., & Takala, H. (2022). Red light optogenetics in neuroscience. Frontiers in Cellular Neuroscience *15*.
73. Multamäki, E., Nanekar, R., Morozov, D., Lievonen, T., Golonka, D., Yuan Wahlgren, W., Stucki-Buchli, B., Rossi, J., Hytönen, V. P., Westenhoff, S., Ihalainen, J. A., Möglich, A., & Takala, H.,(2021). Comparative analysis of two paradigm bacteriophytochromes reveals opposite functionalities in two-component signaling. *Nature Communications, 12*(4394).
74. Takala, H., Edlund, P., Ihalainen, Janne A., & Westenhoff, S. (2020). Tips and turns of bacteriophytochrome photoactivation. *Photochemical and Photobiological Sciences*.
75. Woitowich, N. C., Halavaty, A. S., Waltz, P., Kupitz, C., Valera, J., Tracy, G., Gallagher, K. D., Claesson, E., Nakane, T., Pandey, S., Nelson, G., Tanaka, R., Nango, E., Mizohata, E., Owada, S., Tono, K., Joti, Y., Nugent, A. C., Patel, H., Mapara, A., Hopkins, J., Duong, P., Bizhga, D., Kovaleva, S. E., St. Peter, R., Hernandez, C. N., Ozarowski, W. B., Roy-Chowdhuri, S., Yang, J.-H., Edlund, P., Takala, H., Ihalainen, J., Brayshaw, J., Norwood, T., Poudyal, I., Fromme, P., Spence, J. C. H., Moffat, K., Westenhoff, S., Schmidt, M., & Stojković, E. A., (2018). Structural basis for light control of cell development revealed by crystal structures of a myxobacterial phytochrome. *IUCrJ5*(5), 619–634.
76. Ziegler, T., & Möglich, A., (2015). Photoreceptor engineering. *Frontiers in Molecular Biosciences, 2*.

Supporting Information for The structural effect between the output module and chromophore binding domain is a two-way street via the hairpin extension

Moona Kurttila[a], Stefan Etzl[b], Jessica Rumfeldt[a], Heikki Takala[a],
Nadine Galler[b], Andreas Winkler[b*] and Janne A. Ihalainen[a**]
[a] *University of Jyväskylä, Nanoscience Center, Department of Biological and Environmental Science, 40014 Jyväskylä, Finland and*
[b] *Institute of Biochemistry, Graz University of Technology, Petersgasse 12/II, 8010 Graz, Austria*

TABLE S1: The primers for the codon optimized sequences used for PaaC and PaaC +7 Y263F.

Forward:	5'-ATGCAGTTTCTGCGTAATATGGGTGTTGGTAGCAGC
Reverse:	5'-ACGCAGAAACTGCATGTGCATCGGGCTGG

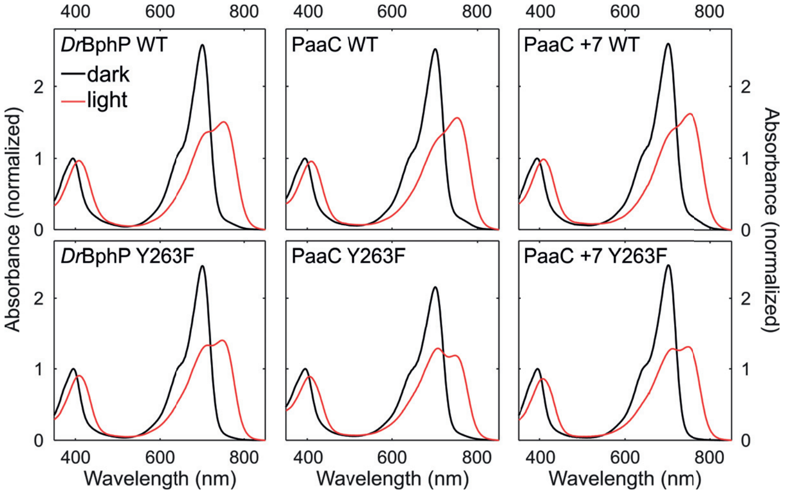

FIG. S1: Dark and light state UV-vis spectra of all the full-length *Dr*BphP, PaaC and PaaC +7 variants in this paper were measured to verify that all variants switch between the Pr and Pfr states. The spectra show that all the variants populate Pr and Pfr states in dark and red light, respectively. In Pr, the A_{700}/A_{280} ratio varies between the samples, but the spectral shape and maximum at 700 nm match the conventional Pr state spectrum.[1,4,5] The spectra are normalized at the maximum of the Soret band (394 nm) in the dark state. Dark spectra are acquired from samples kept in the dark or after far-red light (780 nm) illumination. Light samples are measured after saturated 661 nm LED illumination.

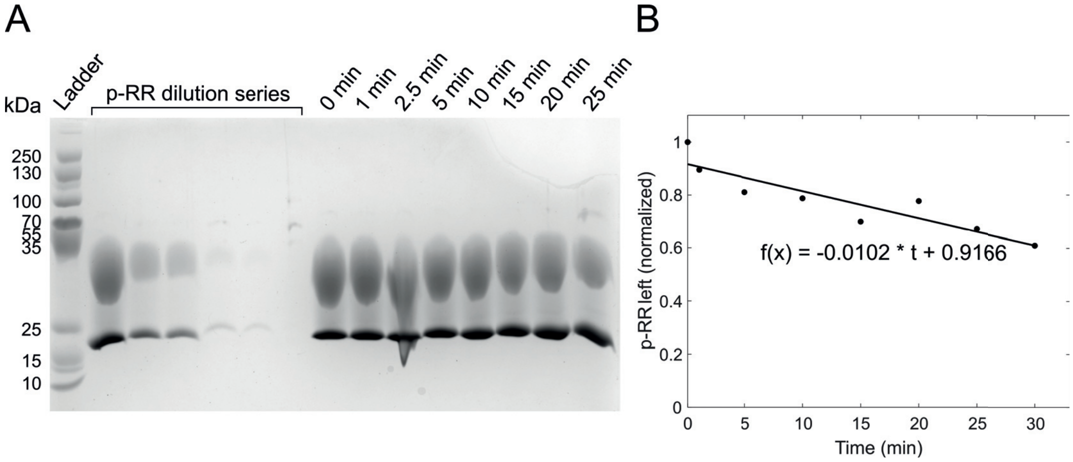

FIG. S2: A) 100% chemical phosphorylation of the response regulator (RR) population is not possible with our current methods. To determine the concentration of the phosphorylated RR (p-RR) a dilution series was performed. By determining the intensity of each band, 50.7% phosphorylation rate was revealed. Time series of p-RR (incubation time at +25°) follows the spontaneous breakage of p-RR. B) The intensities of p-RR bands in A were determined and normalized according to 0 min time point (dots). The single polynomial fit (solid line) was used as a correction line in determining the specific activity of *Dr*BphP (Fig. S4). The 2.5 min time point was not used and the 30 min time point is taken from a separate gel (Fig. S3 bottom left) with 0 min and 30 min time points.

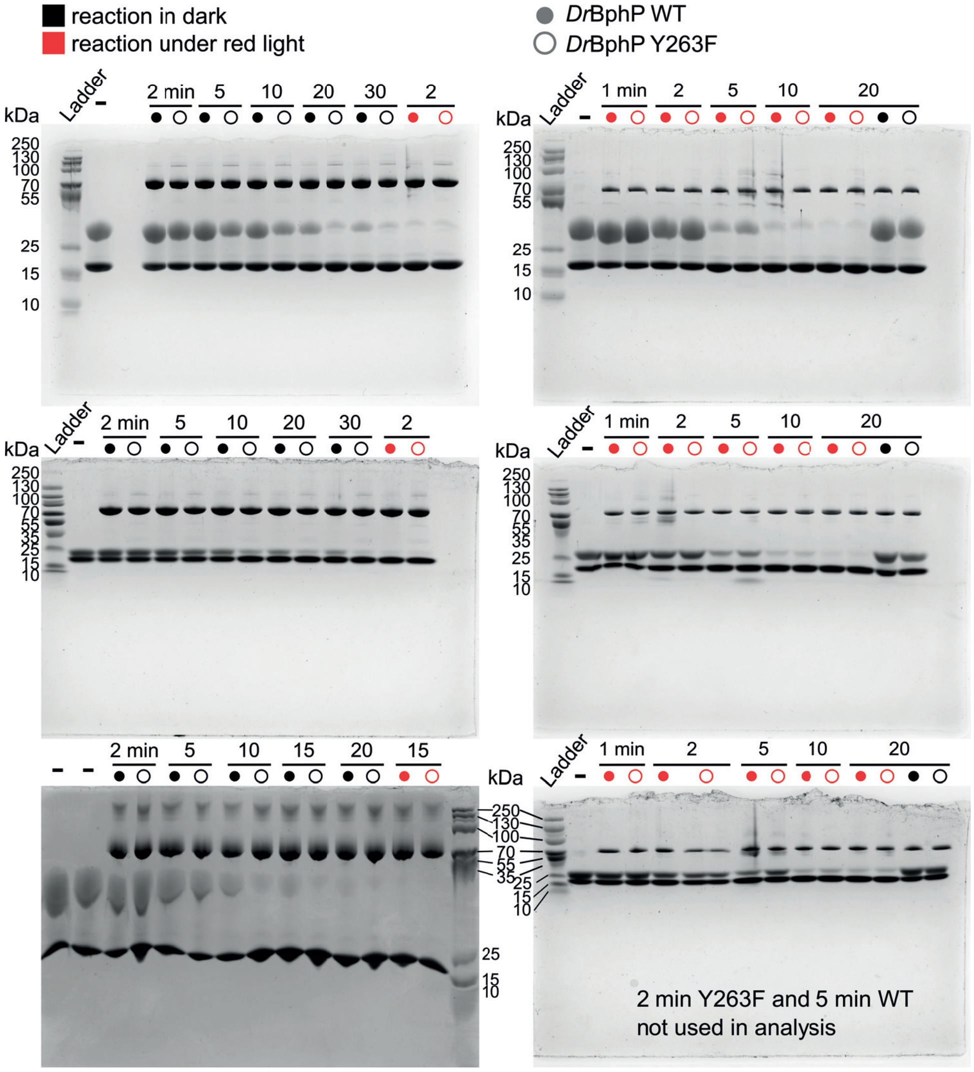

FIG. S3: Full images of PhosTag gels used in the analysis in Figures S4 and 4B. The molecular weight of *Dr*BphP response regulator (RR) is 84 kDa and 19 kDa, respectively. The phosphorylated RR migrates slightly slower than RR due to the PhosTag® in the gel, and is detected between the *Dr*BphP and RR bands.

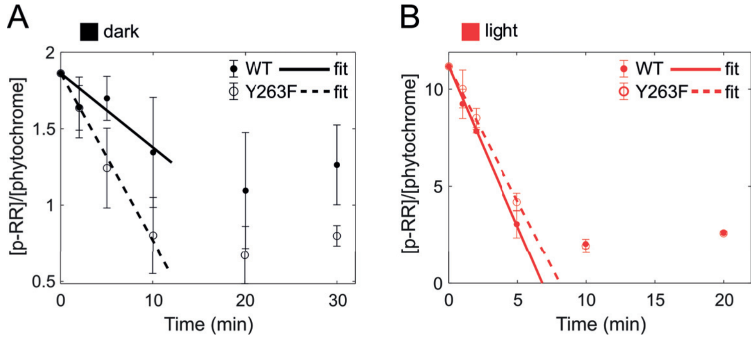

FIG. S4: The p-RR/*Dr*BphP concentration ratio in each time point plotted against the time. The ratio is calculated based on the averaged band intensities in Fig. S3, and the standard deviation is presented as error bars. The initial p-RR concentration was calculated from Fig. S2A and the correction line (in Fig. S2B) due to spontaneous p-RR breakage in time was applied. The initial velocity V_0 is was determined from the first four time points after which the reaction starts to slow down considerably due to decreasing substrate concentration and competing RR/p-RR binding to the *Dr*BphP[2]. The slope of the linear fit (lines) results as the specific activity of the construct either in dark or red light conditions, and are presented in Figure 4B.

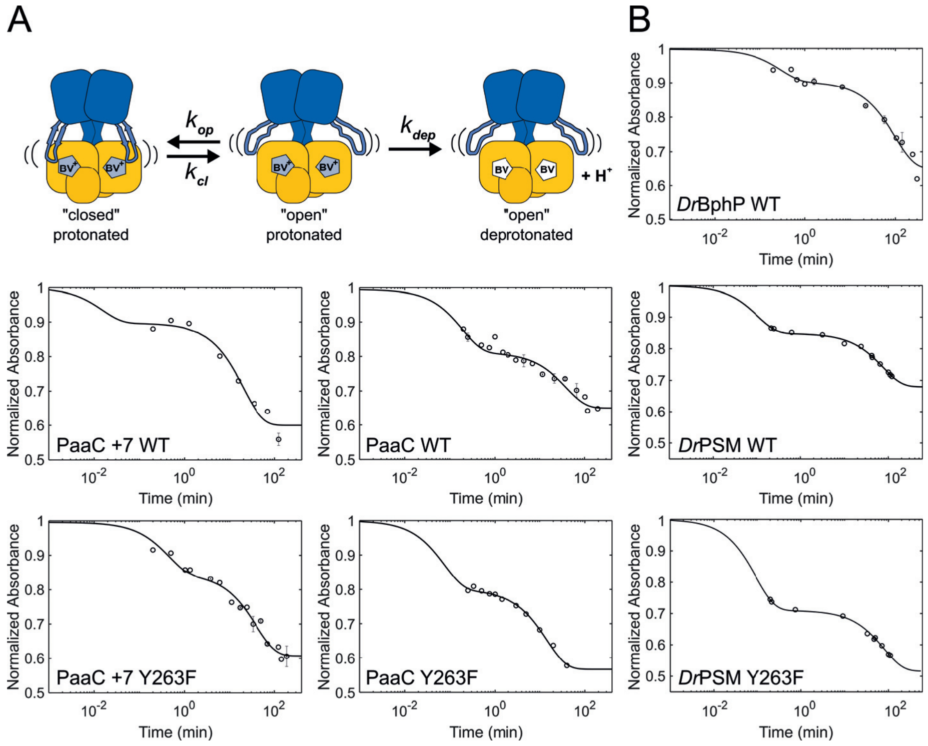

FIG. S5: A) In the *Dr*BphP systems, the solvent access to the chromophore binding pocket is gated by the tongue[3]. When folded as β-sheet, it protects the BV from the solvent ("closed" conformation). Random coil or α-helical conformations allow the solvent to access the protein interior ("open" conformation). In most bacteriophytochromes, the BV in Pr state (*ZZZssa*) is mostly in the protonated state at pH 8. When the solvent pH is rapidly increased above the BV pKa, the BV deprotonates but only once the solvent reaches the BV. The rate of deprotonation depends on the the tongue dynamics and takes place in two phases. In the fast phase (with rate k_{dep}), all the phytochromes in "open" conformation deprotonate. The slow phase is limited by the tongue fluctuations between "closed" and "open" conformations with rates k_{op} and k_{cl}. B) The deprotonation is observed as decreasing of the 700 nm absorption and can thus be followed as a function of time with UV-vis spectroscopy (dots). The amplitude of the fast phase from the total amplitude of the deprotonation is the fraction of phytochromes in "open" conformation and thus reports on the stability of the tongue. We recorded the slow phase the same way as described in[3] to scale the fast phase in Fig. 2. Measured with manual mixing (dead time of 13 s), the amplitudes of the fast phase shown here are within the error margins of the slow experiment in comparison to our stopped-flow results.

---

[*] Electronic address: `andreas.winkler@tugraz.at,janne.ihalainen@jyu.fi`

[1] Auldridge, M.E., Satyshur, K.A., Anstrom, D.M., Forest, K.T., 2012. Structure-guided Engineering Enhances a Phytochrome-based Infrared Fluorescent Protein. J. Biol. Chem. 287, 7000–7009.

[2] Multamäki, E., Nanekar, R., Morozov, D., Lievonen, T., Golonka, D., Yuan Wahlgren, W., Stucki-Buchli, B., Rossi, J., Hytönen, V.P., Westenhoff, S., Ihalainen, J.A., Möglich, A., Takala, H., 2021. Comparative analysis of two paradigm bacteriophytochromes reveals opposite functionalities in two-component signaling. Nat. Commun 12. doi:`\path{10.1038/s41467-021-24676-7}`.

[3] Rumfeldt, J.A., Kurttila, M., Takala, H., Ihalainen, J.A., 2021. The hairpin extension controls solvent access to the chromophore binding pocket in a bacterial phytochrome: a UVvis absorption spectroscopy study. Photochem. Photobiol. Sci 20, 1173–1181. doi:`\path{10.1007/s43630-021-00090-2}`.

[4] Takala, H., Lehtivuori, H., Hammarén, H., Hytönen, V.P., Ihalainen, J.A., 2014. Connection between absorption properties and conformational changes in Deinococcus radiodurans phytochrome. Biochemistry 53, 7076–7085.

[5] Wagner, J.R., Zhang, J., von Stetten, D., Günther, M., Murgida, D.H., Mroginski, M.A., Walker, J.M., Forest, K.T., Hildebrandt, P., Vierstra, R.D., 2008. Mutational analysis of Deinococcus radiodurans bacteriophytochrome reveals key amino acids necessary for the photochromicity and proton exchange cycle of phytochromes. J. Biol. Chem. 283, 12212–12226.

III

THE INTERCONNECTING HAIRPIN EXTENSION "ARM": AN ESSENTIAL ALLOSTERIC ELEMENT OF PHYTOCHROME ACTIVITY

by

Moona Kurttila, Jessica Rumfeldt, Heikki Takala, & Janne A. Ihalainen 2023

Structure 31: 1–9

https://doi.org/10.1016/j.str.2023.06.007

Structure

Article

The interconnecting hairpin extension "arm": An essential allosteric element of phytochrome activity

Graphical abstract

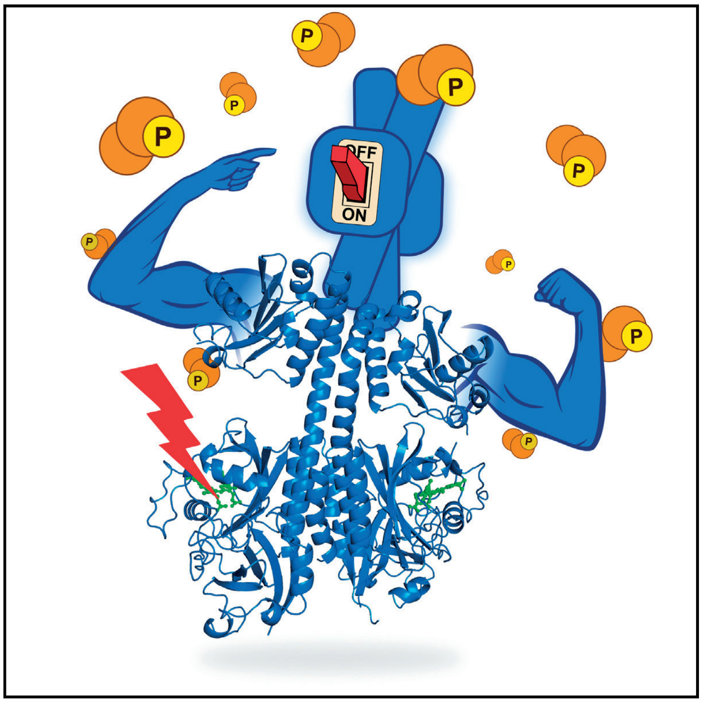

Authors

Moona Kurttila, Jessica Rumfeldt,
Heikki Takala, Janne A. Ihalainen

Correspondence

heikki.p.takala@jyu.fi (H.T.),
janne.ihalainen@jyu.fi (J.A.I.)

In brief

Kurttila et al. demonstrated that an interconnecting hairpin structure in the photosensory module of a red light photosensor phytochrome is crucial for controlling the activity of the system. For light activation, the hairpin allows signal transduction beyond the chromophore environment. In the resting state, the hairpin supports the structural stability.

Highlights

- Activity cannot be controlled by light without the hairpin extension in the sensory module
- Dark state chromophore environment is virtually unaffected upon removal of the hairpin
- Structure of a phytochrome photosensory module without the hairpin is reported
- The hairpin extension stabilizes the system, both thermally and kinetically

Kurttila et al., 2023, Structure *31*, 1–9
September 7, 2023 © 2023 The Authors. Published by Elsevier Ltd.
https://doi.org/10.1016/j.str.2023.06.007

CellPress

Please cite this article in press as: Kurttila et al., The interconnecting hairpin extension "arm": An essential allosteric element of phytochrome activity, Structure (2023), https://doi.org/10.1016/j.str.2023.06.007

Structure

CellPress
OPEN ACCESS

Article

The interconnecting hairpin extension "arm": An essential allosteric element of phytochrome activity

Moona Kurttila,[1] **Jessica Rumfeldt,**[1] **Heikki Takala,**[1,*] **and Janne A. Ihalainen**[1,2,*]
[1]University of Jyvaskyla, Nanoscience Center, Department of Biological and Environmental Science, 40014 Jyvaskyla, Finland
[2]Lead contact
*Correspondence: heikki.p.takala@jyu.fi (H.T.), janne.ihalainen@jyu.fi (J.A.I.)
https://doi.org/10.1016/j.str.2023.06.007

SUMMARY

In red-light sensing phytochromes, isomerization of the bilin chromophore triggers structural and dynamic changes across multiple domains, ultimately leading to control of the output module (OPM) activity. In between, a hairpin structure, "arm", extends from an interconnecting domain to the chromophore region. Here, by removing this protein segment in a bacteriophytochrome from *Deinococcus radiodurans* (*Dr*BphP), we show that the arm is crucial for signal transduction. Crystallographic, spectroscopic, and biochemical data indicate that this variant maintains the properties of *Dr*BphP in the resting state. Spectroscopic data also reveal that the armless systems maintain the ability to respond to light. However, there is no subsequent regulation of OPM activity without the arms. Thermal denaturation reveals that the arms stabilize the *Dr*BphP structure. Our results underline the importance of the structurally flexible interconnecting hairpin extensions and describe their central role in the allosteric coupling of phytochromes.

INTRODUCTION

All living organisms use various sensory systems to adapt to their ambient environment. Phytochromes are red-light sensory proteins in plants, bacteria, and fungi. They photoswitch between two distinguishable states: a red-light absorbing Pr state and a far-red light-absorbing Pfr state (Figure 1A). Phytochromes are known to accommodate a variety of output modules (OPM) allowing them to participate in different developmental and regulatory events.[1] The OPM in bacterial phytochromes is often a histidine kinase (HK), rendering them as sensors in two-component signaling systems. The photosensory module (PSM) of the phytochrome superfamily is conserved, consisting of the chromophore binding domain (CBD) complemented by a phytochrome-specific (PHY) domain that structurally connects the CBD and OPM. In bacterial phytochromes, absorption of red light causes isomerization of a covalently bound biliverdin (BV) chromophore.[2–5] This perturbation in the chromophore-binding pocket, the allosteric site, triggers structural and dynamic changes in the protein moiety, which ultimately leads to allosteric regulation of the OPM activity at the functional site.[6,7]

Bacterial phytochromes share a highly similar PSM organization as most plant, fungal, and cyanobacterial phytochromes, regardless of their variety in effector modules.[8] Most of these systems include a structurally flexible PHY hairpin extension, often referred to as the "tongue", but in this study referred to as an "arm" (in green in Figure 1A).[9,10] It extends from the PHY domain core to the vicinity of the chromophore, forming highly conserved interactions with the GAF (cGMP phosphodiesterase-adenylate cyclase-FhlA) domain that together with PAS (Period-ARNT-Single-minded) forms the CBD.[11,12] These interactions are found even in PAS-less phytochromes, like cyanobacterial *Synechocystis* Cph2,[11] which speaks for their high conservation within phytochrome superfamily. From its other end, the arm is connected (via a short linker region and the PHY domain core) to a long helix that in bacterial systems extends to the output HK module.[11]

The arm brings intrinsic disorder into the phytochrome system as it fluctuates between multiple conformations. In the Pr state, the arm is mainly folded as a β-sheet, and during photoconversion to Pfr, it refolds into an α-helix (Figure 1A).[7,11–15] However, it has been demonstrated that the arm can fluctuate away from its interaction site at the GAF domain even in the Pr state.[15,16] Since the discovery of the arm's light-induced refolding,[12] much attention has been drawn to its structure and role in phytochrome signal transduction.[7,15–24] The arm connects the two other structural tiers of phytochrome, the chromophore binding pocket and the OPM.[1] Although signal transduction routes via the central helix have been suggested,[22,25] no clear and coherent view of the coupling between the three tiers has been reached yet.

To elucidate the allosteric coupling in phytochromes and the role of the arm in phytochrome signaling in a direct manner, we removed the arm extension from the full-length (FL) and PSM (CBD-PHY) fragments of *Deinococcus radiodurans* bacteriophytochrome (*Dr*BphP). With the deletion, we

Please cite this article in press as: Kurttila et al., The interconnecting hairpin extension "arm": An essential allosteric element of phytochrome activity, Structure (2023), https://doi.org/10.1016/j.str.2023.06.007

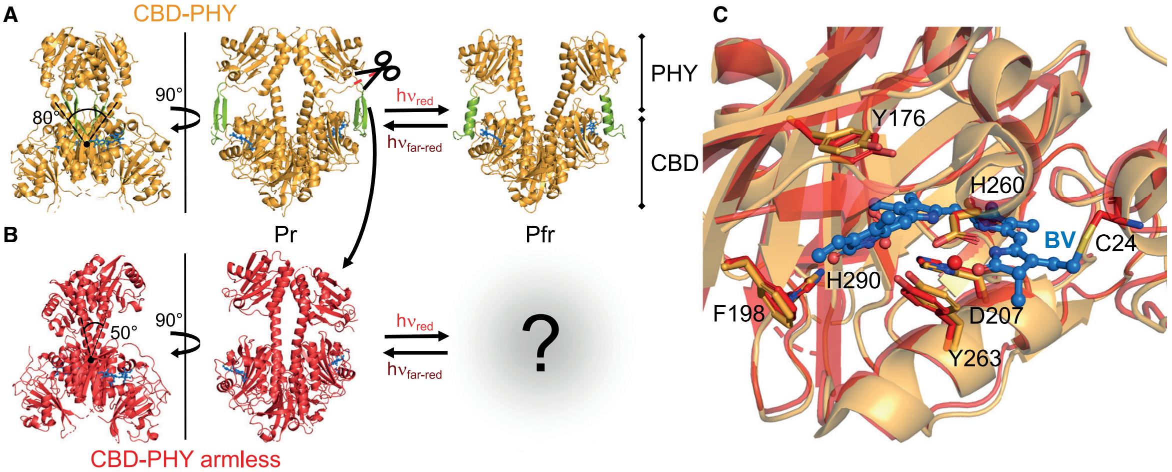

Figure 1. The dark state crystal structure of the CBD-PHY armless

(A) Dark and illuminated crystal structures of CBD-PHY. The “arm” is colored in green, and the covalently bound biliverdin (BV) is shown as blue sticks buried inside the chromophore binding domain (CBD).

(B) Dark state structure of CBD-PHY armless. The removal of the arms results in loss of the PHY domain symmetry in the dimer and change in the characteristic dimerization angle of the helical spine, visible in the 90° rotated view.

(C) Comparison of the chromophore binding pocket of CBD-PHY armless (red) and CBD-PHY (yellow) in the dark crystal structures reveals that the organization of residues in the chromophore binding pocket is highly similar. Some of the amino acids crucial for the photocycle are shown in sticks. Only the BV of CBD-PHY armless structure is shown in ball-stick presentation (blue) for clarity. PDB codes: 4O0P (CBD-PHY Pr[12]), 5C5K (CDB-PHY Pfr[14]), and 8BOR (CBD-PHY armless).

created armless phytochrome variants with disrupted allosteric tiers. By combining structural data with biochemical activity assays and spectroscopic results, we show that without the arm, the dark state structure and properties are mostly unaffected and the chromophore environment remains responsive to light, yet the information from the chromophore and CBD cannot be relayed to the OPM activity upon illumination.

RESULTS

The dark state structure of armless photosensory module

The armless variants were created by clipping out the “arm” hairpin extension (segment between R446-G478) and by replacing it with a sequence "GGGS". The CBD-PHY armless variant crystallized as a parallel dimer, like the wild-type CBD-PHY construct, and the structure could be resolved up to 2.3 Å resolution (Figures 1 and S1, Table 1).[12,14] The overall structural features resemble those of its arm-containing counterpart, except the dimer symmetry is lost without the arms as the PHY domains appear tilted. One monomer of the PHY is docked against its corresponding CBD, while the other is pulled further from its CBD. The observed PHY domain positioning can be driven by crystal packing as it results in a smaller B-factor in the docked domain (Figure S2 A). This underlines the importance of the arms in stabilizing the orientation of the PHY domains. However, the removal of the arm did not affect the overall fold of the remaining PHY domain (Figure S2B).

Further differences between the wild-type and armless dark state structures can be found from the dimerization angle of the monomers, in the 90° rotated view in Figure 1. In the wild-type, the angle between the interconnecting helices of the two monomers at the pivot point is about 80°, whereas in the armless it is only about 50°. This results in a slightly larger interface area between the two monomers in the CBD-PHY armless (Figure S2C). Despite the altered orientation, the CBD and PHY domains in both monomers have the same fold as in the wild-type. Comparison of the chromophore binding pockets of the dark state structures reveals that the organization of the residues is nearly the same (Figure 1C). Even the conserved residues Y263 and D207, which are responsible for the interaction network with the arm,[12] have configurations in the structures highly similar to wild-type.

The removal of arms results in CBD-like spectroscopic behavior

The switchability of the armless variants was confirmed with UV-vis spectroscopy (Figure 2A). The spectra reveal that both CBD-PHY armless and FL armless can be switched back and forth between the illuminated and dark states. The dark state spectra of all constructs are nearly identical, in line with the similar organization of the chromophore binding pockets (Figure 1C). The illuminated state spectra of the armless systems resemble that of CBD. The BV conformations and isomerization yields were further studied by the urea-denatured samples and their UV-vis absorption.[26] The urea-denatured Pr spectra of both armless systems reveal the BV to be in ZZZ conformation, identical to CBD-PHY and CBD (Figures S3A–S3C). The isomerization takes place in the armless systems upon illumination, but the ZZE yield is slightly lower in CBD and armless constructs than in the wild-type CBD-PHY (Figures S3D–S3F). After illumination, canonical phytochromes thermally revert back to the Pr

Please cite this article in press as: Kurttila et al., The interconnecting hairpin extension "arm": An essential allosteric element of phytochrome activity, Structure (2023), https://doi.org/10.1016/j.str.2023.06.007

Table 1. X-ray diffraction data collection and refinement statistics for the dark state (Pr) structure of CBD-PHY armless

Data Collection	
Space group	P 1 2_1 1
Cell dimensions	
a, b, c (Å)	119.63, 64.59, 131.04
α, β, γ (°)	90.00, 91.55, 90.00
Resolution (Å)	50.00–2.30 (2.36–2.30)
R_{merge}	0.152 (1.496)
$CC_{1/2}$	0.989 (0.325)
I/σ(I)	5.40 (0.94)
Completeness (%)	98.8 (99.2)
Redundancy	3.29 (3.26)
Wilson B factor	45.1
Refinement	
Resolution (Å)	45.99–2.30 (2.36–2.30)
No. of reflections	83924 (6133)
R_{work}/R_{free}	0.235/0.268 (0.366/0.393)
No. of atoms	
Protein	14041
Ligand	172
Water	426
Overall B-factor (Å^2)	53.0
Geometry	
RMSD	
Bond lengths (Å)	0.004
Bond angles (°)	0.989
Ramachandran	
Favored (%)	98.3
Allowed (%)	1.7
Outliers (%)	0
Clashscore	4.2

state with a range of rates, depending on the construct.[27] The armless constructs revert back to the Pr state in tens of minutes, much faster compared to their wild-type counterparts, which have dark reversion rates of hours (Figure S4). The armless systems have a fast monophasic reversion. The inclusion of arms results in a second slow component, with a time constant of hours (Figure S4B).

The light-induced changes in BV and protein moiety interactions were studied by recording FTIR difference spectra between the illuminated and dark states (Figures 2B and 2C). Similar to UV-vis spectroscopy, the FTIR difference signals of both CBD-PHY armless and FL armless strongly resemble those of CBD. The negative BV signals at 1736 cm^{-1} and 1712 cm^{-1}, are due to the disappearance of the A-ring and D-ring carbonyl interactions, respectively, which is a result of BV isomerization, as observed also in wild-type CBD-PHY and FL (Figure 2C).[19,28] In all systems, the H-bond network strength of the D-ring carbonyl increases from Pr to Pfr, observed as a frequency shift to lower energy. The large symmetric band at 1685 cm^{-1} observed in CBD-PHY and FL reveals the H-bond network between the C=O group of the BV and H201 and S468 sites in

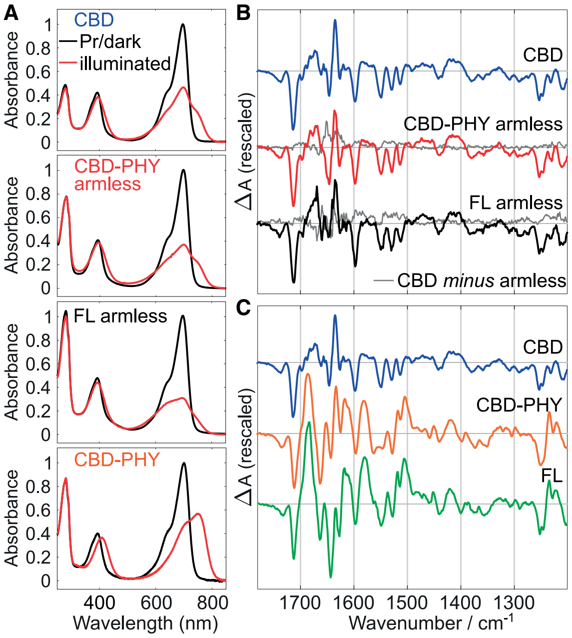

Figure 2. UV-vis and FTIR difference spectra show a CBD-like illuminated state for both armless constructs

(A) UV-vis spectra of the constructs show the difference in the biliverdin (BV) absorbance between dark (black lines) and illuminated (red lines) states.

(B) The FTIR difference spectra (Pfr *minus* Pr) of CBD-PHY armless and FL armless compared to the one of CBD. The spectral properties of both armless samples are nearly identical to CBD.

(C) In contrast, the spectral properties of wild-type CBD-PHY and FL are very different from CBD. All spectra are scaled to the BV signal at 1712 cm^{-1}.

Pfr.[28] In CBD, as well as in the armless constructs, the positive contribution of the BV C=O vibration is wider. In isotope-labeled CBD, where the shifted amide I signals do not disturb this region, the band continues up to 1620 cm^{-1} (Figure S5A). This indicates that the H-bonding strength varies on a wider scale than in arm-containing samples.[18] Comparison between isotope-labeled and non-isotope-labeled CBD indicates further signals from BV, located around 1250–1200 cm^{-1} (Figure S5A). While the peaks in this region are remarkably similar between CBD and the armless constructs, they differ from CBD-PHY and FL by having notably larger positive contributions, again suggesting differences in the illuminated state BV environment (Figure 2C).

The differences in the FTIR signals between the isotope-labeled and non-isotope-labeled CBD indicate that, in addition to the chromophore changes, illumination results in changes within the protein moiety (Figure S5A). The amide I signals (C=O stretching vibration in the peptide bond) shift typically 40–50 cm^{-1} and amide II signals (a mixed vibration of N-H bending and C-N stretching) shift about 30 cm^{-1} due to the $^{13}C^{15}N$-isotopes in the amino acids.[29,30] A negative-negative-positive peak pattern (1660 (–), 1645 (–), 1634 (+) cm^{-1}) was differentiated in CBD and isotope-labeled CBD with a 42–44 cm^{-1} shift (Figure S5A). This correlates with an increase in turns and disordered structure in Pr, and increased β-sheet

Please cite this article in press as: Kurttila et al., The interconnecting hairpin extension "arm": An essential allosteric element of phytochrome activity, Structure (2023), https://doi.org/10.1016/j.str.2023.06.007

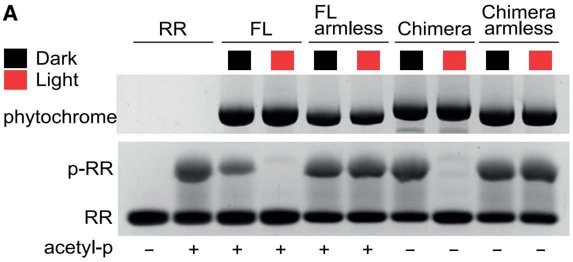

B

Activity	DrBphP (FL) Phosphatase: pRR –> RR		Chimera Kinase: RR –> pRR	
	wild-type	armless	wild-type	armless
In dark	mostly OFF	OFF	ON	ON
In light	ON	OFF	OFF	ON

Figure 3. The light control of the OPM enzymatic activity is lost upon arm removal

(A) PhosTag gel shows the amount of phosphorylated response regulator (p-RR), which is dependent on the OPM activity as well as the light conditions.

(B) Interpretation of the gel. FL construct has phosphatase activity under red light illumination, which is detected as diminished p-RR band under red light. In FL armless, the p-RR amount remains unaltered regardless of illumination. Chimera shows net kinase activity in dark, which is visible as an increase of p-RR content. Once the arm is removed in Chimera armless, its kinase activity remains unaffected by red light.

content in Pfr.[29] A similar FTIR signal pattern can also be found in the CBD-PHY and FL systems (Figure 2).[18,24] Indeed, in the Pr and Pfr state crystal structures, a slight light-induced increase in β-sheet structure is observed in the CBD region (Figure S5B).[12,14] However, direct correlation of the FTIR signals with the structural changes observed in crystallography would require site-selective isotope labeling. Naturally, the amide I region differs between CBD-PHY and FL in comparison to CBD and armless systems, indicating further protein moiety changes in the arm-containing systems. The refolding of the arm hairpin under study affects this region in both CBD-PHY and FL.[19,24] Therefore, pinpointing FTIR signals which originate from the light-induced changes in the OPM[7] is to be addressed in future studies. To conclude, no distinguishable light-induced structural changes outside the CBD are observed in the armless constructs.

Arm removal locks biochemical activity

*Dr*BphP is shown to act as a light-activated phosphatase that dephosphorylates its cognate response regulator (DrRR) under red light.[31] Here, the phosphatase activity of the FL armless was studied in the dark and under saturating red light. The light-induced and uninduced reactions were run on a PhosTag gels, which allows distinguishing phosphorylated proteins from their unphosphorylated counterparts based on their lower mobility in the gel matrix (Figure 3A). The amount of phosphorylated RR (p-RR) was not reduced when incubated with FL armless under red light, which indicates that the phosphatase activity is not switched on, unlike in the case of FL wild-type. The (in)activity remained very similar despite the light state, and therefore the FL armless activity has a close to 1-fold dynamic range describing the magnitude of change in activity between the two states.[24] Comparison to the p-RR lane alone shows that, whereas FL has a little bit of activity even in the dark state, in FL armless it is constantly inactive. Like FL armless, the apoprotein of *Dr*BphP remains inactive regardless of illumination condition (Figure S6D).

To test the possibility that the lack of light-induced activity is due to the disruption of the OPM functionality in the armless system, we analyzed a phytochrome "Chimera" variant, first introduced in Multamäki et al.[31] The Chimera consists of a PSM from *Dr*BphP, and an output HK module from *Agrobacterium tumefaciens* phytochrome Agp1. Unlike *Dr*BphP, the chimera acts as an HK that phosphorylates its cognate RR in the dark but lacks net kinase activity under red light (Figure 3B).[31,32] In the Chimera, the phosphorylation activity is observed through the appearance of a p-RR band in dark, while under red light, only a non-phosphorylated RR band is detected, indicating that the net kinase activity is turned off (Figure 3). In the Chimera armless, a p-RR band is observed in the dark as well as under red light, indicating that the protein has kinase activity in both states and therefore has lost the ability to respond to red light. Hence, the phytochrome OPM remains functional but not controllable without the arm. The full gel of the assay and repeats are shown in Figures S6A–S6C.

Interplay between the arm and OPM affects thermal stability

Circular dichroism (CD) spectroscopy was applied to study the thermal stability of our phytochrome systems. Temperature-induced denaturation was detected at two different wavelengths, at far-UV region (222 nm) and at near-UV region (281 nm), revealing changes in secondary and tertiary structures, respectively.[33] Denaturation experiments with dimeric, multidomain proteins are often complex due to protein concentration dependence of dissociation, multiple transition temperatures and increased misfolding and aggregation propensity relative to single domain proteins.[34–36] In our systems, unfolding is concomitant with irreversible aggregation and/or conformational lock, hampering a thermodynamic equilibrium analysis; the change in free energy, enthalpy, or entropy upon unfolding cannot, therefore, be determined. Instead, we used the fitted melting temperatures (T_m, Equations 1–3) as an approximation of the stability of our protein complexes in dark and illuminated states. In all studied constructs, two separate T_ms were observed: one at 41–65°C and another at 72–77°C (Figure 4). In the case of 222 nm detection, a single transition is observed in all cases. With 281 nm detection, two transitions, with decreasing and increasing signals, are observed in CBD-PHY and FL, while only one is observed in the armless systems.

To investigate the origin of the two T_ms, we also tracked the UV-vis absorbance of BV at 700 nm as a function of temperature in the dark state (Figure S7). The 700 nm signal decreased as a function of temperature due to the denaturation of the BV environment. A T_m of about 72°C was observed for both CBD and CBD-PHY (Figure S7). Further, for the CBD fragment, a T_m of over 74°C was detected at both CD detection wavelengths (Figures S8A and S8C). These observations indicate that the CBD has the highest T_m of the three subunits. Its structure is strongly stabilized by the chromophore binding, as lack of BV decreases the T_m by nearly 30°C (Figure S8). The capability to

Please cite this article in press as: Kurttila et al., The interconnecting hairpin extension "arm": An essential allosteric element of phytochrome activity, Structure (2023), https://doi.org/10.1016/j.str.2023.06.007

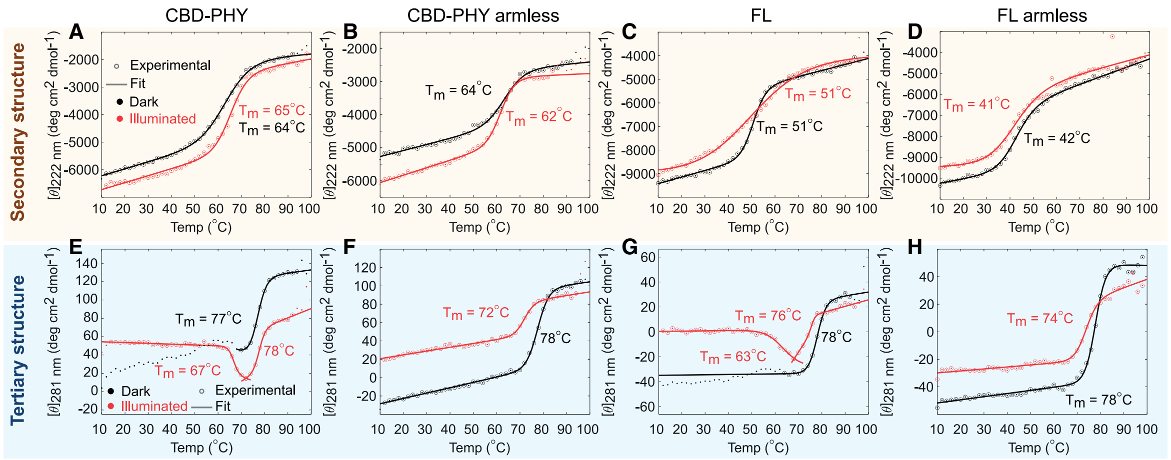

Figure 4. Thermograms of CBD-PHY, CBD-PHY armless, FL, and FL armless at 222 nm and 281 nm in dark and illuminated states

(A–D) Denaturation monitored as ellipticity at 222 nm (dots) in dark (black) and illuminated (red) states. The fits according to Equation 3 are shown as solid lines.

(E–H) Denaturation monitored as ellipticity at 281 nm in dark and illuminated states. The illuminated states of CBD-PHY and FL have two transitions, and both fits are shown. The T_m values obtained from the fits are marked next to the corresponding plots.

detect this transition with a near-UV CD signal can be rationalized from a structural point of view. The temperature-dependent signal at 281 nm mainly relates to the exposure of the aromatic amino acids in the hydrophobic pockets. In phytochromes, the most globular structure containing hydrophobic pockets is the CBD with its chromophore-binding cleft.

The lower T_ms in CBD-PHY and FL at around 64–65 and 51°C are observed at 222 nm, and are associated with denaturation of the PHY and PHY-HK modules, respectively. Confirmed by measuring the CBD-PHY melting profiles at 222 nm in three different concentrations, these transitions are not related to monomerization as a higher concentration resulted in lower T_m with a smaller change in the signal intensity (Figure S9C).[36] Rather, the observation indicates that the PHY and PHY-HK modules denature in an irreversible manner and therefore earlier at higher concentrations. The denaturation profile is also affected by the heating rate. Slower heating rate resulted in a lower T_m, due to increased time for aggregation at lower temperatures (Figure S9D).[34]

In CBD-PHY armless, the fitted T_ms tracked from secondary (64°C) and tertiary structures (78°C) are nearly identical to CBD-PHY (Figures 4B and 4F). In the dark state, the arm does not seem to affect the structural stability of the CBD-PHY construct. However, in the illuminated state, differences between the wild-type and armless constructs become apparent. In CBD-PHY, the T_ms of both PHY and CBD domains increased by 1°C (Figures 4A and 4E), whereas in CBD-PHY armless, both T_ms decreased in comparison to the dark state values (Figures 4B and 4F), which reflects decreased structural stability.

In the illuminated state of CBD-PHY, two separate transitions, decreasing and increasing signals, respectively, in the 281 nm thermogram are observed. The T_m of 67°C is observed as a decreasing CD signal, and Figure S9B reveals that the blue end of the BV Soret absorption (300–470 nm) affects this signal at the same temperature range. Especially in the illuminated state, the arm shifts the Soret band (Figure S9B), and melting of the PHY domain (including the arm) changes the BV absorption, which reflects to the 281 nm signal. This effect is also observed in FL as a T_m of 63°C (Figure 4G). This suggests that the "dip" in the signal originates from the melting of the arm with subsequent changes in the BV environment. Therefore, the decreasing signals are naturally absent in the armless variants (Figures 4F and 4H).

When comparing the denaturation of the PHY-HK units, the T_m of FL armless is notably lower than that of wild-type FL, even in the dark state (Figures 4C, 4D, 4G, and 4H). Again in the armless, the T_ms decrease in the illuminated state in comparison to the dark. In FL wild-type, the fitted T_ms in dark and illuminated states were the same, 51°C. However, in the illuminated state the shape of the denaturation curve is more shallow than others, suggesting multiple overlapping transitions. In both FL systems, the T_m of the CBD part in the dark (78°C) is nearly identical to other constructs (Figures 4G and 4H). In FL, the T_m of the CBD part decreases to 76°C in the illuminated state.

DISCUSSION

The stability and activity of multidomain protein complexes can be regulated in different ways. Subtle changes in the protein fold can lead to dramatic effects on the characteristics of large protein complexes.[7,36,37] Typically in the allostery of multidomain signaling proteins, a connecting domain transmits a signal from the regulatory site to the functional site.[37,38] In phytochromes, the PHY domain structurally and functionally links the photoactivating CBD and the biochemically active OPM. Here, we demonstrated that the arm, a dynamic hairpin structure in the PHY domain, plays a crucial role in the (de)activation of the OPM. In Pr, with the methods used here, the lack of arm did not seem to affect the chromophore binding pocket. However, two different H-bonding environments of the D-ring have been observed previously,[39,40] which in principle can result from the

Please cite this article in press as: Kurttila et al., The interconnecting hairpin extension "arm": An essential allosteric element of phytochrome activity, Structure (2023), https://doi.org/10.1016/j.str.2023.06.007

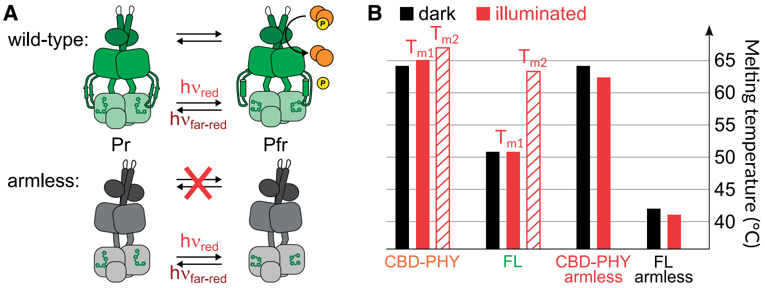

Figure 5. Phytochrome allostery

(A) Wild-type *Dr*BphP acts as a phosphatase, and its activity is switched on under red light. In the armless system, the chromophore and surrounding protein moiety remain responsive to light, as observed by FTIR and UV-vis spectroscopy, yet the activity of the OPM cannot be controlled by light.

(B) The thermal stability of CBD-PHY, FL, CBD-PHY armless, and FL armless systems represented by the T_m values of their PHY or PHY-HK unit in dark and illuminated states from Figures 4A–4D. The wild-type systems have an additional melting temperature (T_{m2}) that originates most probably from the melting of the arm and is detected as a decrease of the 281 nm signal (Figures 4E and 4G).

arm fluctuations. We showed that the arms are needed to stabilize the light-activated Pfr state of the chromophore. One suggestion is that this happens through dipole coupling between the α-helical arm and BV.[41] Further, the arm stabilizes the overall structure of the system and couples together, not only BV in the chromophore binding pocket and biochemically active OPM but also the three subunits in terms of thermal stability, making it a key element in phytochrome allostery (Figure 5).

The dynamic range of a system describes how efficiently the enzymatic activity is altered in response to a signal.[42] It depends on the magnitude of the equilibrium shift between the active and inactive conformations and therefore high dynamic range requires strong coupling of the perturbation and functional sites.[38] We have previously described 33-fold dynamic range for *Dr*BphP activity.[24] Here, we showed that the armless systems had no significant difference in activity between dark and illuminated states (close to 1-fold dynamic range), and the coupling between the light-sensing (BV) and the functional site (OPM) is completely disrupted upon arm removal. Gourinchas et al. had similar results with an armless variant of *Is*PadC (*Is*PadC $\Delta^{442-477}$SG), a bacterial phytochrome with diguanylyl cyclase activity.[22] The wild-type *Is*PadC is activated under red light illumination and has a 43-fold dynamic range. The armless variant became continuously active and had larger maximal activity than its wild-type counterpart, with 1.6-fold repression of activity upon illumination.[22] Gourinchas et al. as well as Isaksson et al. have previously concluded that the helical spine acts as a signal transduction route between BV and the OPM.[22,25] The armless variants, however, demonstrate that the helical spine on its own cannot transduce the signal and that the arms are required for allosteric control of the OPM activity (Figure 5A).

The OPM of *Dr*BphP appears very dynamic,[7] which is in accord with the thermal stability of the PHY-OPM region. The T_m of the PHY-OPM subunits in FL is over 10°C lower than the T_m of the PHY domain alone in both CBD-PHY and CBD-PHY armless (Figure 5B). In this regard, the role of the arm becomes clear in the FL systems where dimeric interactions among the OPMs take place.[7,43] Without the arm, the thermal stability of the PHY and the OPM decreases significantly (Figure 5B). Further, the FL has a multi-phasic denaturation curve of the illuminated state, not observed in other systems (Figures 4A–4D), which reflects increased dynamics in the OPM[7] that take place hand-in-hand with the refolded arm. In the wild-type systems, the melting of the arm can be observed as a separate melting temperature (T_{m2} in Figure 5B). The arm and the OPM are structurally and functionally coupled, but as the OPM and PHY domain denature hand-in-hand, also the core region of the PHY domain is closely coupled to the OPM.

Hairpin extensions and loops are known to be important allosteric mediators in multiple signaling systems.[44,45] Here, we revealed information regarding phytochrome allostery at multiple levels including atomic coordinates in the crystal structure, changes in intramolecular interactions probed by FTIR, changes in control of biochemical activity, and in thermal stability using temperature and illumination dependent CD spectroscopy. Our study indicates the role of the arm in phytochromes is particularly important for the light-activated state formation, stabilization, and regulation of phosphatase and kinase activity. In the resting state, the arm does not seem to affect the chromophore pocket organization. Despite its dynamic nature, the arm plays a role in maintaining overall structural stability and domain arrangement.[46] Upon illumination, the chromophore and CBD can switch to the light-activated state without the arm, but only the arm allows the signal transduction all the way to the OPM. The arm is therefore crucial for the allosteric coupling of the sensory and effector modules.

STAR★METHODS

Detailed methods are provided in the online version of this paper and include the following:

- KEY RESOURCES TABLE
- RESOURCE AVAILABILITY
  - ○ Lead contact
  - ○ Materials availability
  - ○ Data and code availability
- EXPERIMENTAL MODEL AND STUDY PARTICIPANT DETAILS
- METHOD DETAILS
  - ○ Cloning and DNA material
  - ○ Protein expression and purification
  - ○ Crystallography
  - ○ Protein phosphorylation by acetyl phosphate and PhosTag detection
  - ○ Spectroscopic measurements
  - ○ UV-vis absorption spectroscopy
  - ○ FTIR spectroscopy
  - ○ CD spectroscopy
- QUANTIFICATION AND STATISTICAL ANALYSIS

- ○ Crystallographic data analysis
- ○ Spectroscopic data analysis

SUPPLEMENTAL INFORMATION

Supplemental information can be found online at https://doi.org/10.1016/j.str.2023.06.007.

ACKNOWLEDGMENTS

We thank Elina Multamäki for help with the PhosTag experiments and Sami Mäkelä, Marjo Haapakoski, and Ilkka Minkkinen for temperature stability experiments performed with UV-vis spectrophotometry. We acknowledge the European Synchrotron Radiation Facility for provision of synchrotron radiation facilities and we would like to thank Dr. Gordon Leonard for assistance in using beamline ID23-1. The research was supported by the Academy of Finland (grants 332742 for J.A.I. and 330678 for H.T.).

AUTHOR CONTRIBUTIONS

M.K., H.T., and J.A.I. designed research; M.K., J.R., and H.T. performed research and analyzed data; and M.K. and J.A.I. wrote the paper with input from all other authors.

DECLARATION OF INTERESTS

The authors declare no competing interests.

INCLUSION AND DIVERSITY

We support inclusive, diverse, and equitable conduct of research.

Received: March 23, 2023
Revised: May 23, 2023
Accepted: June 6, 2023
Published: June 30, 2023

REFERENCES

1. Takala, H., Edlund, P., Ihalainen, J.A., and Westenhoff, S. (2020). Tips and turns of bacteriophytochrome photoactivation. Photochem. Photobiol. Sci. *19*, 1488–1510. https://doi.org/10.1039/D0PP00117A.
2. Kneip, C., Hildebrandt, P., Schlamann, W., Braslavsky, S.E., Mark, F., and Schaffner, K. (1999). Protonation state and structural changes of the tetrapyrrole chromophore during the Pr → Pfr phototransformation of phytochrome: a resonance raman spectroscopic study. Biochemistry *38*, 15185–15192. pMID: 10563801. https://doi.org/10.1021/bi990688w.
3. Mroginski, M.A., Murgida, D.H., von Stetten, D., Kneip, C., Mark, F., and Hildebrandt, P. (2004). Determination of the Chromophore Structures in the Photoinduced Reaction Cycle of Phytochrome. J. Am. Chem. Soc. *126*, 16734–16735. https://doi.org/10.1021/ja043959l.
4. van Thor, J.J., Mackeen, M., Kuprov, I., Dwek, R.A., and Wormald, M.R. (2006). Chromophore Structure in the Photocycle of the Cyanobacterial Phytochrome Cph1. Biophys. J. *91*, 1811–1822. https://doi.org/10.1529/biophysj.106.084335.
5. Burgie, E.S., Wang, T., Bussell, A.N., Walker, J.M., Li, H., and Vierstra, R.D. (2014). Crystallographic and electron microscopic analyses of a bacterial phytochrome reveal local and global rearrangements during photoconversion. J. Biol. Chem. *289*, 24573–24587. https://doi.org/10.1074/jbc.M114.571661.
6. Nussinov, R., and Tsai, C.-J. (2013). Allostery in Disease and in Drug Discovery. Cell *153*, 293–305. https://doi.org/10.1016/j.cell.2013.03.034.
7. Wahlgren, W.Y., Claesson, E., Tuure, I., Trillo-Muyo, S., Bódizs, S., Ihalainen, J.A., Takala, H., and Westenhoff, S. (2022). Structural mechanism of signal transduction in a phytochrome histidine kinase. Nat. Commun. *13*, 7673. https://doi.org/10.1038/s41467-022-34893-3.
8. Rockwell, N.C., and Lagarias, J.C. (2020). Phytochrome evolution in 3D: deletion, duplication, and diversification. New Phytol. *225*, 2283–2300. https://doi.org/10.1111/nph.16240.
9. Essen, L.-O., Mailliet, J., and Hughes, J. (2008). The structure of a complete phytochrome sensory module in the Pr ground state. Proc. Natl. Acad. Sci. USA *105*, 14709–14714. https://doi.org/10.1073/pnas.0806477105.
10. Yang, X., Kuk, J., and Moffat, K. (2008). Crystal structure of *Pseudomonas aeruginosa* bacteriophytochrome: Photoconversion and signal transduction. Proc. Natl. Acad. Sci. USA *105*, 14715–14720. https://doi.org/10.1073/pnas.0806718105.
11. Anders, K., Daminelli-Widany, G., Mroginski, M.A., von Stetten, D., and Essen, L.-O. (2013). Structure of the Cyanobacterial Phytochrome 2 Photosensor Implies a Tryptophan Switch for Phytochrome Signaling. J. Biol. Chem. *288*, 35714–35725. https://doi.org/10.1074/jbc.M113.510461.
12. Takala, H., Björling, A., Berntsson, O., Lehtivuori, H., Niebling, S., Hoernke, M., Kosheleva, I., Henning, R., Menzel, A., Ihalainen, J.A., and Westenhoff, S. (2014). Signal amplification and transduction in phytochrome photosensors. Nature *509*, 245–248. https://doi.org/10.1038/nature13310.
13. Yang, X., Stojković, E.A., Ozarowski, W.B., Kuk, J., Davydova, E., and Moffat, K. (2015). Light Signaling Mechanism of Two Tandem Bacteriophytochromes. Structure *23*, 1179–1189. https://doi.org/10.1016/j.str.2015.04.022.
14. Burgie, E.S., Zhang, J., and Vierstra, R.D. (2016). Crystal structure of *Deinococcus* phytochrome in the photoactivated state reveals a cascade of structural rearrangements during photoconversion. Structure *24*, 448–457. https://doi.org/10.1016/j.str.2016.01.001.
15. Gustavsson, E., Isaksson, L., Persson, C., Mayzel, M., Brath, U., Vrhovac, L., Ihalainen, J.A., Karlsson, B.G., Orekhov, V., and Westenhoff, S. (2020). Modulation of Structural Heterogeneity Controls Phytochrome Photoswitching. Biophys. J. *118*, 415–421. https://doi.org/10.1016/j.bpj.2019.11.025.
16. Rumfeldt, J.A., Kurttila, M., Takala, H., and Ihalainen, J.A. (2021). The hairpin extension controls solvent access to chromophore binding pocket in bacterial phytochrome – a UV-Vis absorption spectroscopy study. Photochem. Photobiol. Sci. *20*, 117–1181. https://doi.org/10.1007/s43630-021-00090-2.
17. Otero, L.H., Klinke, S., Rinaldi, J., Velázquez-Escobar, F., Mroginski, M.A., Fernández López, M., Malamud, F., Vojnov, A.A., Hildebrandt, P., Goldbaum, F.A., and Bonomi, H.R. (2016). Structure of the Full-Length Bacteriophytochrome from the Plant Pathogen *Xanthomonas campestris* Provides Clues to its Long-Range Signaling Mechanism. J. Mol. Biol. *428*, 3702–3720. https://doi.org/10.1016/j.jmb.2016.04.012.
18. Takala, H., Lehtivuori, H.K., Berntsson, O., Hughes, A., Nanekar, R., Niebling, S., Panman, M., Henry, L., Menzel, A., Westenhoff, S., and Ihalainen, J.A. (2018). On the (un)coupling of the chromophore, tongue interactions, and overall conformation in a bacterial phytochrome. J. Biol. Chem. *293*, 8161–8172. https://doi.org/10.1074/jbc.RA118.001794.
19. Stojković, E.A., Toh, K.C., Alexandre, M.T.A., Baclayon, M., Moffat, K., and Kennis, J.T.M. (2014). FTIR Spectroscopy Revealing Light-Dependent Refolding of the Conserved Tongue Region of Bacteriophytochrome. J. Phys. Chem. Lett. *15*, 2512–2515. https://doi.org/10.1021/jz501189t.
20. Björling, A., Berntsson, O., Lehtivuori, H., Takala, H., Hughes, A.J., Panman, M., Hoernke, M., Niebling, S., Henry, L., Henning, R., et al. (2016). Structural photoactivation of a full-length bacterial phytochrome. Sci. Adv. *2*, e1600920. https://doi.org/10.1126/sciadv.1600920.
21. Anders, K., Gutt, A., Gärtner, W., and Essen, L.-O. (2014). Phototransformation of the red light sensor cyanobacterial phytochrome 2 from *Synechocystis* species depends on its tongue motifs. J. Biol. Chem. *289*, 25590–25600. https://doi.org/10.1074/jbc.m114.562082.

Please cite this article in press as: Kurttila et al., The interconnecting hairpin extension "arm": An essential allosteric element of phytochrome activity, Structure (2023), https://doi.org/10.1016/j.str.2023.06.007

22. Gourinchas, G., Etzl, S., Göbl, C., Vide, U., Madl, T., and Winkler, A. (2017). Long-range allosteric signaling in red light-regulated diguanylyl cyclases. Sci. Adv. *3*, e1602498. https://doi.org/10.1126/sciadv.1602498.

23. Gourinchas, G., Heintz, U., and Winkler, A. (2018). Asymmetric activation mechanism of a homodimeric red light-regulated photoreceptor. Elife *7*, e34815. https://doi.org/10.7554/eLife.34815.

24. Kurttila, M., Etzl, S., Rumfeldt, J., Takala, H., Galler, N., Winkler, A., and Ihalainen, J.A. (2022). The structural effect between the output module and chromophore-binding domain is a two-way street via the hairpin extension. Photochem. Photobiol. Sci. *21*, 1881–1894. https://doi.org/10.1007/s43630-022-00265-5, ISSN 1474-9092.

25. Isaksson, L., Gustavsson, E., Persson, C., Brath, U., Vrhovac, L., Karlsson, G., Orekhov, V., and Westenhoff, S. (2021). Signaling Mechanism of Phytochromes in Solution. Structure *29*, 151–160.e3. https://doi.org/10.1016/j.str.2020.08.009.

26. Lehtivuori, H., Rumfeldt, J., Mustalahti, S., Kurkinen, S., and Takala, H. (2022). Conserved histidine and tyrosine determine spectral responses through the water network in *Deinococcus radiodurans* phytochrome. Photochem. Photobiol. Sci. *21*, 1975–1989. https://doi.org/10.1007/S43630-022-00272-6/TABLES/3, ISSN 14749092.

27. Takala, H., Lehtivuori, H., Hammarén, H., Hytönen, V.P., and Ihalainen, J.A. (2014). Connection between absorption properties and conformational changes in *Deinococcus radiodurans* phytochrome. Biochemistry *53*, 7076–7085. https://doi.org/10.1021/bi501180s.

28. Ihalainen, J.A., Gustavsson, E., Schroeder, L., Donnini, S., Lehtivuori, H., Isaksson, L., Thöing, C., Modi, V., Berntsson, O., Stucki-Buchli, B., et al. (2018). Chromophore-protein interplay during the phytochrome photocycle revealed by step-scan FTIR spectroscopy. J. Am. Chem. Soc. *140*, 12396–12404. https://doi.org/10.1021/jacs.8b04659.

29. Barth, A. (2007). Infrared spectroscopy of proteins. Biochim. Biophys. Acta *1767*, 1073–1101. https://doi.org/10.1016/j.bbabio.2007.06.004.

30. Brielle, E.S., and Arkin, I.T. (2021). Isotope-Edited Amide II Mode: A New Label for Site-Specific Vibrational Spectroscopy. J. Phys. Chem. Lett. *12*, 6634–6638. pMID: 34254809. https://doi.org/10.1021/acs.jpclett.1c01073.

31. Multamäki, E., Nanekar, R., Morozov, D., Lievonen, T., Golonka, D., Wahlgren, W.Y., Stucki-Buchli, B., Rossi, J., Hytönen, V.P., Westenhoff, S., et al. (2021). Comparative analysis of two paradigm bacteriophytochromes reveals opposite functionalities in two-component signaling. Nat. Commun. *12*, 4394. https://doi.org/10.1038/s41467-021-24676-7.

32. Lamparter, T., Michael, N., Mittmann, F., and Esteban, B. (2002). Phytochrome from *Agrobacterium tumefaciens* has unusual spectral properties and reveals an N-terminal chromophore attachment site. Proc. Natl. Acad. Sci. USA *99*, 11628–11633. https://doi.org/10.1073/pnas.152263999.

33. Greenfield, N.J. (2006). Using circular dichroism collected as a function of temperature to determine the thermodynamics of protein unfolding and binding interactions. Nat. Protoc. *1*, 2527–2535. https://doi.org/10.1038/nprot.2006.204.

34. Vermeer, A.W., and Norde, W. (2000). The Thermal Stability of Immunoglobulin: Unfolding and Aggregation of a Multi-Domain Protein. Biophys. J. *78*, 394–404. https://doi.org/10.1016/S0006-3495(00)76602-1.

35. Rumfeldt, J.A.O., Stathopulos, P.B., Chakrabarrty, A., Lepock, J.R., and Meiering, E.M. (2006). Mechanism and Thermodynamics of Guanidinium Chloride-induced Denaturation of ALS-associated Mutant Cu,Zn Superoxide Dismutases. J. Mol. Biol. *355*, 106–123. https://doi.org/10.1016/j.jmb.2005.10.042.

36. Doyle, C.M., Rumfeldt, J.A., Broom, H.R., Broom, A., Stathopulos, P.B., Vassall, K.A., Almey, J.J., and Meiering, E.M. (2013). Energetics of oligomeric protein folding and association. Arch. Biochem. Biophys. *531*, 44–64. https://doi.org/10.1016/j.abb.2012.12.005.

37. Mensa, B., Polizzi, N.F., Molnar, K.S., Natale, A.M., Lemmin, T., and DeGrado, W.F. (2021). Allosteric mechanism of signal transduction in the two-component system histidine kinase PhoQ. Elife *10*, e73336. https://doi.org/10.7554/eLife.73336, ISSN 2050-084X.

38. Tsai, C.-J., and Nussinov, R. (2014). A Unified View of "How Allostery Works". PLoS Comput. Biol. *10*, 1–12. https://doi.org/10.1371/journal.pcbi.1003394.

39. Song, C., Psakis, G., Lang, C., Mailliet, J., Gärtner, W., Hughes, J., Matysik, J., and Lagarias, C.J. (2011). Two ground state isoforms and a chromophore D-ring photoflip triggering extensive intramolecular changes in a canonical phytochrome. Proc. Natl. Acad. Sci. USA *108*, 3842–3847. https://doi.org/10.1073/pnas.1013377108.

40. Chenchiliyan, M., Kübel, J., Ooi, S.A., Salvadori, G., Mennucci, B., Westenhoff, S., and Maj, M. (2023). Ground-state heterogeneity and vibrational energy redistribution in bacterial phytochrome observed with femtosecond 2D IR spectroscopy. J. Chem. Phys. *158*, 10897690. https://doi.org/10.1063/5.0135268.

41. Buhrke, D., Michael, N., and Hamm, P. (2022). Vibrational couplings between protein and cofactor in bacterial phytochrome Agp1 revealed by 2D-IR spectroscopy. Proc. Natl. Acad. Sci. USA *119*, e2206400119. https://doi.org/10.1073/PNAS.2206400119.

42. Ziegler, T., and Möglich, A. (2015). Photoreceptor engineering. Front. Mol. Biosci. *2*, 30. https://doi.org/10.3389/fmolb.2015.00030.

43. Takala, H., Björling, A., Linna, M., Westenhoff, S., and Ihalainen, J.A. (2015). Light-induced Changes in the Dimerization Interface of Bacteriophytochromes. J. Biol. Chem. *290*, 16383–16392. https://doi.org/10.1074/jbc.M115.650127.

44. Gora, A., Brezovsky, J., and Damborsky, J. (2013). Gates of Enzymes. Chem. Rev. *113*, 5871–5923. https://doi.org/10.1021/cr300384w.

45. Ho, K., and Bradshaw, N. (2021). A conserved allosteric element controls specificity and activity of functionally divergent PP2C phosphatases from *Bacillus subtilis*. J. Biol. Chem. *296*, 100518. https://doi.org/10.1016/j.jbc.2021.100518.

46. Motlagh, H.N., Wrabl, J.O., Li, J., and Hilser, V.J. (2014). The ensemble nature of al-lostery. Nature *508*, 331–339. https://doi.org/10.1038/nature13001.

47. Wagner, J.R., Brunzelle, J.S., Forest, K.T., and Vierstra, R.D. (2005). A light-sensing knot revealed by the structure of the chromophore-binding domain of phytochrome. Nature *438*, 325–331. https://doi.org/10.1038/nature04118.

48. Wagner, J.R., Zhang, J., Brunzelle, J.S., Vierstra, R.D., and Forest, K.T. (2007). High resolution structure of *Deinococcus* bacteriophytochrome yields new insights into phytochrome architecture and evolution. J. Biol. Chem. *282*, 12298–12309. https://doi.org/10.1074/jbc.M611824200.

49. Wagner, J.R., Zhang, J., von Stetten, D., Günther, M., Murgida, D.H., Mroginski, M.A., Walker, J.M., Forest, K.T., Hildebrandt, P., and Vierstra, R.D. (2008). Mutational analysis of *Deinococcus radiodurans* bacteriophytochrome reveals key amino acids necessary for the photochromicity and proton exchange cycle of phytochromes. J. Biol. Chem. *283*, 12212–12226. https://doi.org/10.1074/jbc.M709355200.

50. Kabsch, W. (1993). Automatic processing of rotation diffraction data from crystals of initially unknown symmetry and cell constants. J. Appl. Crystallogr. *26*, 795–800. https://doi.org/10.1107/S0021889893005588.

51. McCoy, A.J., Grosse-Kunstleve, R.W., Adams, P.D., Winn, M.D., Storoni, L.C., and Read, R.J. (2007). *Phaser* crystallographic software. J. Appl. Crystallogr. *40*, 658–674. https://doi.org/10.1107/S0021889807021206.

52. Emsley, P., and Cowtan, K. (2004). *Coot*: model-building tools for molecular graphics. Acta Crystallogr. D *60*, 2126–2132. https://doi.org/10.1107/S0907444904019158.

53. Murshudov, G.N., Skubák, P., Lebedev, A.A., Pannu, N.S., Steiner, R.A., Nicholls, R.A., Winn, M.D., Long, F., and Vagin, A.A. (2011). *REFMAC5* for the refinement of macromolecular crystal structures. Acta Crystallogr. D *67*, 355–367. https://doi.org/10.1107/S0907444911001314.

54. Winn, M.D., Ballard, C.C., Cowtan, K.D., Dodson, E.J., Emsley, P., Evans, P.R., Keegan, R.M., Krissinel, E.B., Leslie, A.G.W., McCoy, A., et al. (2011).

Please cite this article in press as: Kurttila et al., The interconnecting hairpin extension "arm": An essential allosteric element of phytochrome activity, Structure (2023), https://doi.org/10.1016/j.str.2023.06.007

Overview of the *CCP*4 suite and current developments. Acta Crystallogr. D *67*, 235–242. https://doi.org/10.1107/S0907444910045749.

55. Nurizzo, D., Mairs, T., Guijarro, M., Rey, V., Meyer, J., Fajardo, P., Chavanne, J., Biasci, J.-C., McSweeney, S., and Mitchell, E. (2006). The ID23-1 structural biology beamline at the ESRF. J. Synchrotron Radiat. *13*, 227–238. https://doi.org/10.1107/S0909049506004341.

56. Karplus, P.A., and Diederichs, K. (2012). Linking Crystallographic Model and Data Quality. Science *336*, 1030–1033. https://doi.org/10.1126/science.1218231.

57. Pace, C.N., and McGrath, T. (1980). Substrate stabilization of lysozyme to thermal and guanidine hydrochloride denaturation. J. Biol. Chem. *255*, 3862–3865. https://doi.org/10.1016/S0021-9258(19)85604-1.

Please cite this article in press as: Kurttila et al., The interconnecting hairpin extension "arm": An essential allosteric element of phytochrome activity, Structure (2023), https://doi.org/10.1016/j.str.2023.06.007

STAR★METHODS

KEY RESOURCES TABLE

REAGENT or RESOURCE	SOURCE	IDENTIFIER
Chemicals, peptides, and recombinant proteins		
*Dr*BphP CBD	Takala et al. (2018)[18]	N/A
*Dr*BphP CBD-PHY	Takala et al. (2018)[18]	N/A
*Dr*BphP full-length	Kurttila et al. (2022)[24]	N/A
*Dr*BphP AtHK Chimera	Multamäki et al. (2021)[31]	N/A
Response regulator of *Dr*BphP (DrRR)	Multamäki et al. (2021)[31]	N/A
D-glucose (u^{13} C6, 99%)	Cambridge Isotope Laboratories	Cat# CLM-1396-PK
Ammonium Chloride (^{15}N, 99%)	Cambridge Isotope Laboratories	Cat# NLM-467-PK
Polyethylene glycol 3350	Sigma	Cat# 88776-250G-F
D-(+)-glucose anhydrous	MP Biomedicals LLC	Cat# 194672
D-(−)-fructose	Sigma	Cat# F3510-1006
Ammonium acetate	Merck	Cat# 1.01116
Sodium citrate	Sigma-Alrdich	Cat# 51804-500G
Ethylene glycol	Sigma-Alrdich	Cat# 324558-100ML
Critical commercial assays		
QuickChange Lightning Multi Site-Directed Mutagenesis Kit	Agilent Technologies	Cat# 210513
Zn^{2+}-Phos-tag® SDS-PAGE assay	Fujifilm Wako Chemicals Europe GmbH	Ref# AAL-107S1
Deposited data		
Crystal structure of armless *Dr*BphP in Pr state	This paper	PDB code: 8BOR
Crystal structure of *Dr*BphP in Pr state	Takala et al. (2014)[12]	PDB code: 4O0P
Crystal structure of *Dr*BphP in Pfr state	Burgie et al. (2016)[14]	PBD code 5C5K
Experimental models: Organisms/strains		
E. coli BL21(DE3)	Thermo Scientific	Cat# EC0114
E. coli DH5α	Invitroge	Cat# 18265017
Oligonucleotides		
Armless mutants: 5′- TGG CTG CGG CCC GAA CTG CGG GGA GGA GGA TCC GGC TAC GCC GAG CCC TG -3′	This paper	N/A
Recombinant DNA		
pET21b(+) with *Dr*BphP CBD	Wagner et al. (2005)[47]	N/A
pET21b(+) with *Dr*BphP CBD-PHY	Wagner et al. (2007)[48]	N/A
pET21b(+) with *Dr*BphP	Wagner et al. (2007, 2008)[48,49]	N/A
pET21b(+) with *Dr*BphP AtHK Chimera	Multamäki et al. (2021)[31]	N/A
Software and algorithms		
MATLAB (R2022b)	MathWorks	https://se.mathworks.com/products/MATLAB.html
PyMOL Molecular Graphics System (version 2.0)	Schrödinger, LLC	https://pymol.org/2/
XDS program package (version Feb 5, 2021)	Kabsch (1993)[50]	https://www.esrf.fr/UsersAndScience/Experiments/MX/Software/PXSOFT/XDS/XDS_html_doc
Phaser (version 2.8.3.)	McCoy et al. (2007)[51]	https://www.phaser.cimr.cam.ac.uk/index.php/Phaser_Crystallographic_Software
Coot (version 0.9.6)	Emsley and Cowtan (2004)[52]	https://www2.mrc-lmb.cam.ac.uk/personal/pemsley/coot/
REFMAC5 (version 5.8.0352)	Murshudov et al. (2011)[53]	https://www2.mrc-lmb.cam.ac.uk/groups/murshudov/content/refmac/refmac.html
CCP4 interface (version 8.0.005)	Winn et al. (2011)[54]	https://www.ccp4.ac.uk

Please cite this article in press as: Kurttila et al., The interconnecting hairpin extension "arm": An essential allosteric element of phytochrome activity, Structure (2023), https://doi.org/10.1016/j.str.2023.06.007

RESOURCE AVAILABILITY

Lead contact

Further information and requests for resources and reagents should be directed to and will be fulfilled by the Lead Contact, Janne Ihalainen (janne.ihalainen@jyu.fi).

Materials availability

This study did not generate new unique reagents.

Data and code availability

- The crystal structure of CBD-PHY armless is available in Protein DataBank (PDB ID: 8BOR). Any additional information required to reanalyze the data reported in this paper is available from the lead contact upon request
- This paper does not report original code.

EXPERIMENTAL MODEL AND STUDY PARTICIPANT DETAILS

The recombinant proteins used in this study were expressed in a pET21b(+) vector in *E. coli* BL21(DE3) cells as outlined in method details.

METHOD DETAILS

Cloning and DNA material

The pET21b(+) expression plasmids coding for wild-type *D. radiodurans* phytochrome fragments (CBD, CBD-PHY, full-length) were kindly provided by the laboratories of Prof. R. D. Vierstra and Prof. K. T. Forest.[5,48,47] The Chimera construct has the photosensory module of *Dr*BphP and the effector domain of phytochrome 1 from *Agrobacterium fabrum* (Agp1) as described in Multamäki et al. together with DrRR.[31] The 'arm' hairpin extension was clipped out by replacing segment between R446–G478 by a sequence "GGGS" with QuickChange Lightning Multi Site-Directed Mutagenesis Kit (Agilent Technologies) and confirmed by sequencing. The following primer, nonmatching sequence in italics, was used to mutate out the arm: 5' - TGG CTG CGG CCC GAA CTG CGG *GGA GGA GGA TCC* GGC TAC GCC GAG CCC TG - 3'.

Protein expression and purification

The protein constructs described above, with a C-terminal $(His)_6$-tag, were expressed in *Escherichia coli* BL21(DE3) at +28°C as described previously.[28] After lysis and ultracentrifugation, the purification was carried out with affinity chromatography followed by overnight incubation with 10x excess of biliverdin, and size-exclusion chromatography, where the samples were eluted with buffer (30 mM Tris pH 8.0), as described in Ihalainen et al.[28]

Crystallography

Crystals of the CBD-PHY armless were grown by hanging-drop vapor diffusion in dark at room temperature, after mixing 10 mg/mL protein at 1:1 ratio with reservoir solution (12% polyethylene glycol 3350, 200 mM ammonium acetate, 5% fructose, 5% glucose, and 100 mM sodium citrate pH 5.6). Crystal handling was conducted under green safe light. Once the first small flake-like crystals appeared within 3 weeks, they were used for seeding. There, the seed crystals were centrifuged, washed twice with a 1:1 mixture of the reservoir solution and buffer (30 mM Tris pH 8), and set to grow in 3 μL droplets in a fresh 1:1 mixture of reservoir solution and 10 mg/mL protein. After a month of crystal growth, the crystals were soaked with reservoir solution supplemented with 18% ethylene glycol, and flash-frozen.

Protein phosphorylation by acetyl phosphate and PhosTag detection

The PhosTag activity assay was adapted from Multamäki et al.[31] and performed as previously described.[24] The full-length (FL) and FL armless variants of *Dr*BphP were introduced with pre-phosphorylated response regulator from *D. radiodurans* (*p-Dr*RR). For this, *Dr*RR was phosphorylated at +37°C for 2.8 mg/mL of RR in the presence of 200 mM acetyl phosphate. Chimera and Chimera armless constructs were introduced with non-phosphorylated *Dr*RR. In the reaction, concentration of all phytochromes and *Dr*RR was 0.3 mg/mL. During a 5-min incubation at +25°C, the samples were pre-illuminated with saturating red LED (660 nm, 5 min, on average 13 mW/cm^2) or far-red laser (780 nm, Thorlabs, 20 s, 80 mW/cm^2) to reach the maximum Pr- or Pfr-state population, respectively. Once the (de)phosphorylation reactions were initiated with 1 mM ATP, the samples were incubated either under red light (as above) or in darkness at 25°C. After 10 min, the reactions were stopped with 5x SDS loading buffer. The mobility shift of phosphorylated RR (p-RR) proteins was detected using Zn^{2+}-PhosTag® SDS-PAGE assay (Wako Chemicals).

Please cite this article in press as: Kurttila et al., The interconnecting hairpin extension "arm": An essential allosteric element of phytochrome activity, Structure (2023), https://doi.org/10.1016/j.str.2023.06.007

Spectroscopic measurements

All measurements were performed in darkness and in ambient conditions (room temperature) unless otherwise stated. The samples were illuminated with 780 nm laser (ThorLabs) or 660 nm LED to drive them to either Pr or Pfr state, respectively.

UV-vis absorption spectroscopy

The steady-state UV-vis spectra were measured with a Cary 8454 UV/vis spectrometer (Agilent Technologies) in 10 mm Quartz cuvette right after saturating light conditions. After the background subtraction, the spectra were offset corrected at 850 nm and normalized to the 700 nm absorption in Pr state.

FTIR spectroscopy

The steady-state FTIR spectroscopy was performed using a Nicolet Magna IR-760 FTIR spectrometer with XT-KBr beam splitter, Ever-Glo IR source and MCT-detector. The measurements were conducted using 100 scans in the spectral range of 400–4000 cm^{-1} with a resolution of 2 cm^{-1}. Sample preparation and light-induced difference spectroscopy were performed as described in Takala et al.[18]

CD spectroscopy

The CD spectra were measured with Jasco J-715 CD spectrophotometer. The dark and illuminated spectra of the constructs were measured in 0.5 mm circular Quartz cuvette at 190–250 nm at 3–4 μM, and 250–800 nm at 0.27 mM sample concentration. For the illuminated spectra of CBD and the armless constructs, the spectra were measured in 300 nm wide sections, due to fast dark reversion of the systems (Figure S4). The samples were re-driven to the illuminated state between measurements, and four measurements per region were averaged.

The thermograms measured at 222 nm were concentration and heating rate dependent due to aggregation (Figures S9C and S9D). Therefore, the melting temperatures were determined in 10 mm cuvettes to allow lower concentration, but resulting in saturated spectra at wavelengths below 210 nm due to prominent $\Delta\epsilon$ of the Tris buffer. All measurements in far-UV region (210–250 nm) were performed in about 0.4 μM and in the near-UV-vis region (250–800 nm) in 8 μM concentration, unless otherwise stated. The 10-mm cuvettes also allowed the usage of Jasco PTC-348WI temperature control system with magnetic stirrer in the bottom during the temperature denaturation experiments. The $\Delta\epsilon$ at singular wavelength was recorded with 2°C intervals and the temperature was increased with 1°C/min heating rate. In the illuminated experiments, the sample was illuminated for 30 s between data points with a red LED mounted on the lid to prevent dark reversion.

QUANTIFICATION AND STATISTICAL ANALYSIS

Crystallographic data analysis

Diffraction data were collected at beamline ID23-1 of the European Synchrotron Radiation Facility (ESRF), Grenoble in 100 K with an X-ray wavelength of 1.07 Å,[55] and processed using the XDS program package version Feb 5, 2021.[50] The data were cut at 2.30 Å resolution, which corresponds to a correlation coefficient ($CC_{1/2}$) value of 0.325.[56] The CBD-PHY armless crystals belonged to space group $P\,1\,2_1\,1$ with four monomers in an asymmetric unit. The initial phases were solved with molecular replacement by using Phaser version 2.8.3.[51] The structure was further built and refined with Coot 0.9.6[52] and REFMAC5 version 5.8.0352,[53] and 0.01 matrix weight was applied for final refinement steps. The final structure had R_{work}/R_{free} values of 0.235/0.268. The electron density map for the figures was calculated from the final structure factor files with FFT of the CCP4 interface (version 8.0.005),[54] and the structure figures were created with the PyMOL Molecular Graphics System version 2.0 (Schrödinger, LLC). The crystal data collection and processing statistics are summarized in Table 1.

Spectroscopic data analysis

All spectroscopic data were analyzed and fitted, if need be, with Matlab version R2021b (The MathWorks, Inc).

The set of FTIR difference spectra (Pfr *minus* Pr and vice versa) were averaged together, offset corrected in the spectral range of 1981–1999 cm^{-1} and normalized to the negative D-ring C=O stretch signal at 1712 cm^{-1}.[28]

The temperature dependent data was used to determine melting temperatures. Decreasing T_m due to higher concentration, and vice versa, disclose that the T_ms do not result from monomerization of our homodimeric systems, and therefore the melting curves were fitted to unimolecular two-state model adapted from Greenfield[33] to determine the melting temperature T_m for the constructs:

$$K_{eq} = e^{\frac{\Delta H_{T_m} \cdot \frac{T}{T_m} - 1}{RT}}, \quad \text{(Equation 1)}$$

where K_{eq} is the equilibrium constant, R is the gas constant, and ΔH_{T_m} is essentially the slope at the T_m. The fraction of unfolded protein can be also expressed as follows

$$F_u = \frac{K_{eq}}{K_{eq}+1}, \quad \text{(Equation 2)}$$

Please cite this article in press as: Kurttila et al., The interconnecting hairpin extension "arm": An essential allosteric element of phytochrome activity, Structure (2023), https://doi.org/10.1016/j.str.2023.06.007

where F_u is the fraction of unfolded protein. Finally, Equation 2 is combined with linear corrections to subtract contributions from linearly increasing or decreasing ellipticity.[57] If needed, the slope was fixed to a most frequent value determined in other cases.

$$f(T) = -F_u(T(S_f - S_u) - B_u + B_f) + (S_f \cdot T + B_f). \tag{Equation 3}$$

Structure, Volume *31*

Supplemental Information

The interconnecting hairpin extension "arm": An essential allosteric element of phytochrome activity

Moona Kurttila, Jessica Rumfeldt, Heikki Takala, and Janne A. Ihalainen

Supplemental Information for
The interconnecting hairpin extension "arm": an essential allosteric element of phytochrome activity

Moona Kurttila[a], Jessica Rumfeldt[a], Heikki Takala[a,1], Janne A. Ihalainen[a,1,*]

[a] *University of Jyväskylä, Nanoscience Center, Department of Biological and Environmental Science, 40014, Jyväskylä, Finland*

Supplementary methods

Methods S1. In vivo production of isotope-labeled CBD, related to STAR Methods

Uniformly $^{13}C^{15}N$-labeled CBD apoprotein was expressed as described in the main paper, with the following modifications: Expression cultures were grown in a standard M9 minimal media with 150 μg/mL ampicillin. u-$^{13}C_6$ glucose and $^{15}NH^4Cl$ (Cambridge Isotope Laboratories) were used as carbon and nitrogen sources, respectively. Cultures were incubated at 37°C and 220 rpm until they reached OD_{600} of 0.7-0.8 and were then induced with 1mM IPTG. Temperature was decreased to 28°C and cultures were incubated for 22h, after which the cells were harvested by centrifugation. The purification was conducted as described for other constructs in the main paper STAR Methods section.

Methods S2. UV-vis absorption spectroscopy, related to STAR Methods

The Cary 8454 UV/vis spectrometer (Agilent Technologies) was used for the urea denaturation and dark reversion experiments. Saturating 660 nm LED illumination was used to drive the samples to maximal Pfr population, and 780 nm laser (ThorLabs) was used for populating the Pr state. For the chemical denaturation experiments with urea, the samples driven either to Pr or illuminated (Pfr) state were diluted with 10 M urea at pH 3.0, resulting in final urea concentration of 8.0 M, as described in Lehtivuori et al.[1]

For the dark reversion experiment, the phytochromes were first switched between the Pr and Pfr states with 775 nm and 660 nm LEDs, respectively, and then driven into the maximum population of the Pfr state. The data acquisition was started immediately after illumination by measuring spectra from 0.5 min to 6 h with logarithmically increasing time steps. The A750/A700 ratio was normalized to the ratio of the illuminated spectra and fitted to two-component exponential function:

$$\frac{A_{750}}{A_{700}}(t) = A_1 e^{-t/\tau_1} + A_2 e^{-t/\tau_2}. \tag{1}$$

In CBD and both armless systems, one component was sufficient to fit the dark reversion. The A_{750}/A_{700} ratio in the last time point was used as a baseline.

The temperature dependent measurements were carried out with Lambda 850 UV/VIS Spectrometer (Perkin Elmer) in a 10 mm Quartz cuvette. The temperature was controlled with PTP-1 Peltier System (Perkin Elmer) and monitored with a thermometer. Spectra were collected from 850 nm to 250 nm, with 2 nm resolution and scanning speed of 480.23 nm/min. Spectra were collected in five-degree temperature intervals from 20°C to 85°C. The data was fitted with Eq. 1-3, shown in the main paper STAR Methods.

---

[*] Lead Contact: janne.ihalainen@jyu.fi

[1] Correspondance: heikki.p.takala@jyu.fi and janne.ihalainen@jyu.fi

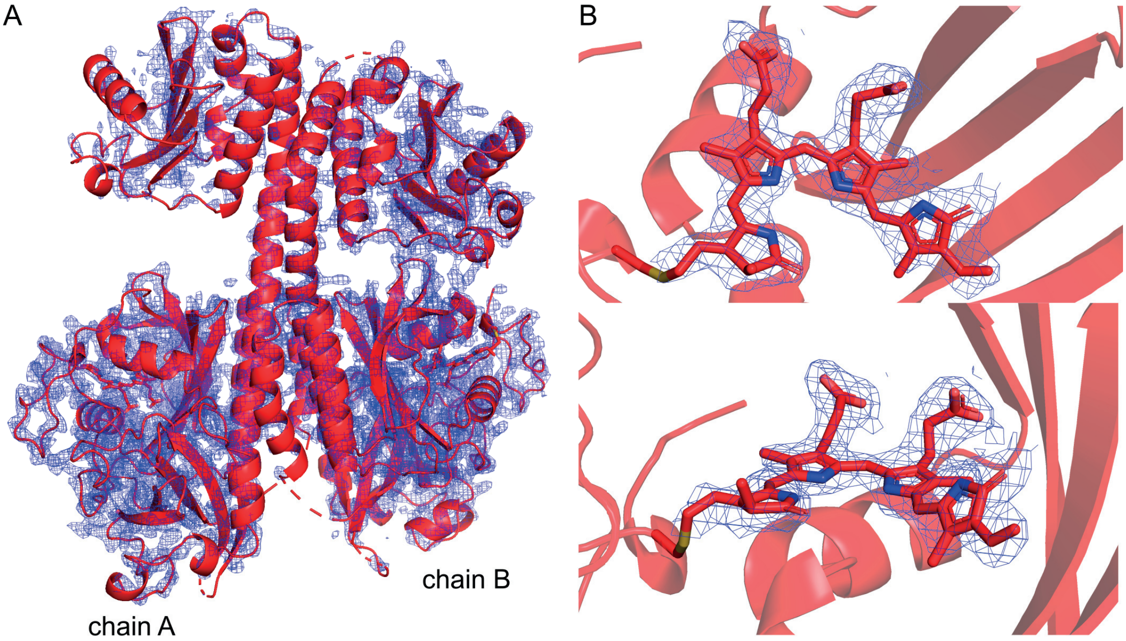

Figure S1: The electron density map of crystal structure of CBD-PHY armless, related to Figure 1. A) Protein dimer (chains A and B) shown as cartoon representation (red) with electron density map plotted (in blue mesh). B-C) Biliverdin of chain B shown as stick model with the electron density map from two different orientations. Cys24 with its covalent bond with the chromophore is shown as sticks and the chromophore environment is shown as cartoon representation. The ($2F_o$-F_c) electron density maps of all panels are shown at 1.0 σ. Figures were created with the PyMOL Molecular Graphics System (Schrödinger, LLC).

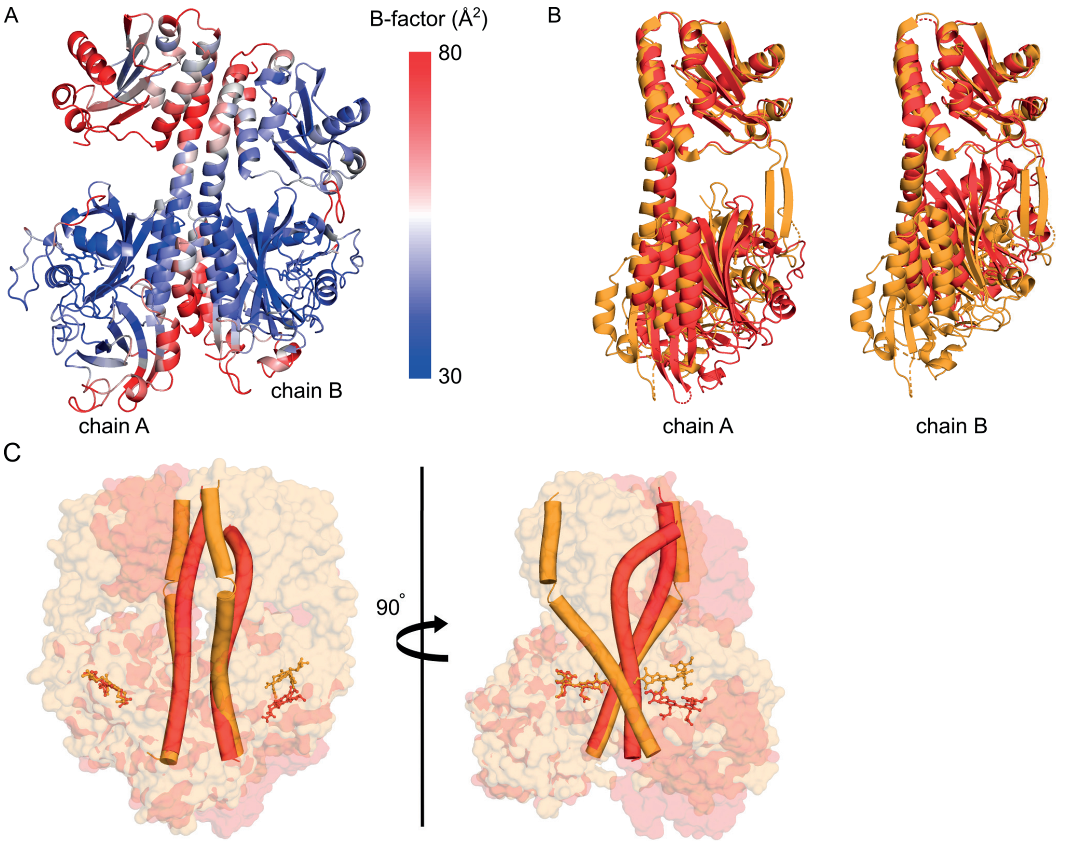

Figure S2: The B-factor and the orientation of the CBD-PHY armless protomers, related to Figure 1. A) The cartoon representation of CBD-PHY armless dimer (chains A and B) colored according to the B-factor of the amino acids. The blue-white-red spectrum is scaled to 30-80 Å^2. The biliverdin chormophore is shown as sticks. B) The PHY domain alignments of armless chain A and chain B (red, PDB: 8BOR) with their wild type counterparts (orange, PDB: 4O0P). For clarity, only one chain (A or B) is shown at one time, also highlighting the relative orientations of CBD and PHY domains within each protomer. C) Structural alignment of armless (red) and wild-type (orange) dimers in respect to CBD of chain A. Structures are shown as transparent surfaces, and the central helices are shown as cylinders. The front and 90°-rotated views reveal the altered dimer symmetry in the armless variant. BVs are shown as ball-and-stick presentation to demonstate the relative positions of CBDs. The CBDs dimerize in a different angle and orientation in CBD-PHY armless. The smaller angle in armless brings the CBDs of the dimer closer to each other. Figure was created with the PyMOL Molecular Graphics System (Schrödinger, LLC).

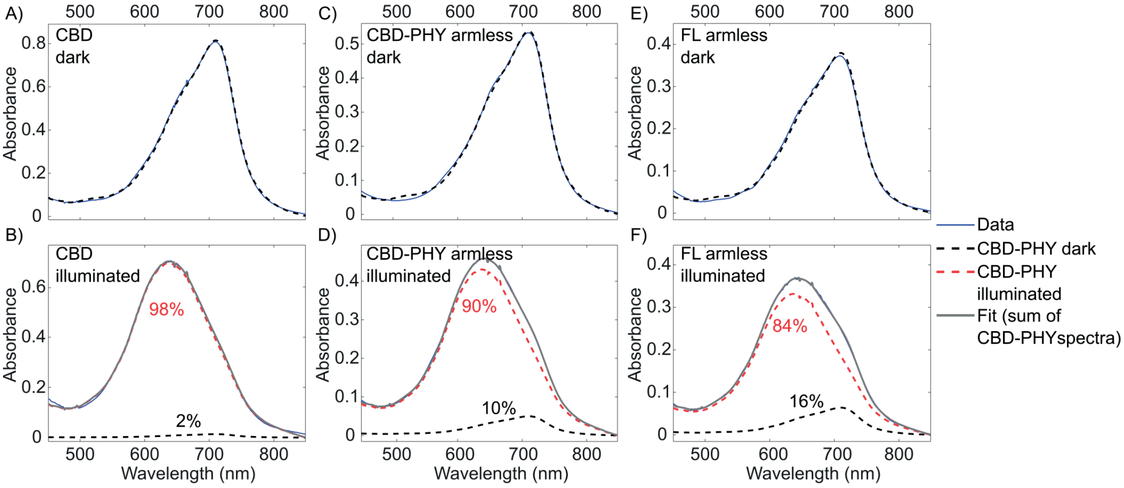

Figure S3: Chromophore UV-vis spectra, related to Figure 2A. The UV-vis spectra of variants in A-C) dark and D-F) illuminated states after urea denaturation at pH 3.0. Before the urea denaturation, the samples were driven either to dark or illuminated state. The spectra of CBD, CBD-PHY armless and FL armless are fitted to the urea-denatured spectra of CBD-PHY, as done in.[1] The dark spectra fully agree with CBD-PHY but the illuminated spectra require also a second component from the dark spectrum. The contribution of the CBD-PHY spectra in the fit is presented in the figure.

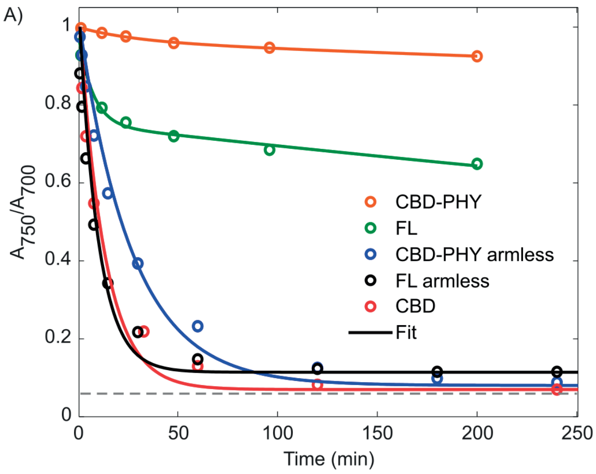

B) $f(t) = Amp_1 * e^{(-t\,/\,\tau_1)} + Amp_2 * e^{(-t\,/\,\tau_2)}$

	Amp_1	τ_1 (min)	Amp_2	τ_2 (min)	RMSE
CBD-PHY	4 %	30	96 %	5000	0.0015
FL	24 %	7	76 %	1300	0.0148
CBD-PHY armless	100 %	26	-	-	0.0261
FL armless	100 %	10	-	-	0.0304
CBD	100 %	13	-	-	0.0429

Figure S4: The CBD-like nature of the chromophore in armless variants is revealed by dark reversion, related to Figure 2. A) The dark reversion from illuminated to dark state presented as a decrease in A_{750}/A_{700} absorbance ratio. Data are shown as open circles and the fits as solid lines. The dashed grey line is marked to the A_{750}/A_{700} ratio in Pr spectrum. B) The data were fitted according to the indicated function. CBD-PHY and FL required two components, but the fast decay of CBD and both armless systems were fitted with one component. The coefficients of the fits are presented in the table. The dark reversion is fast in CBD as well as in both armless systems.

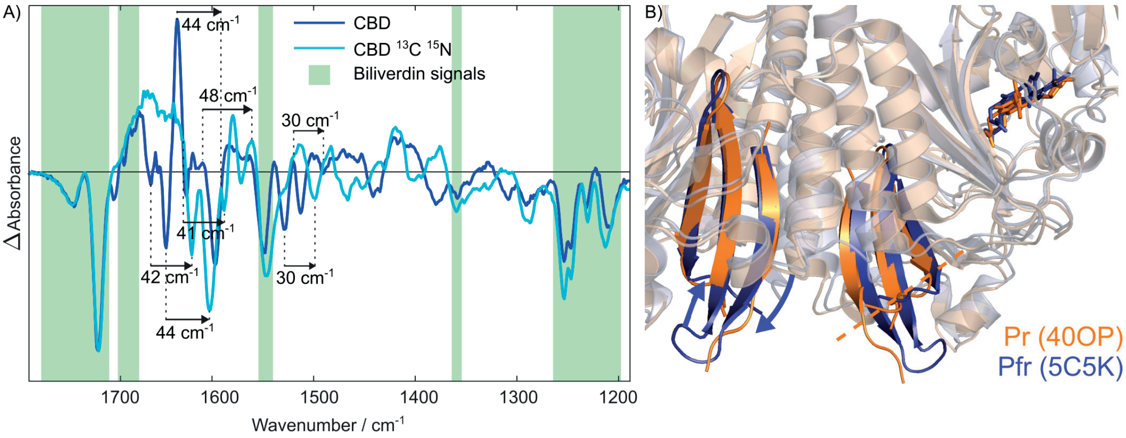

Figure S5: Vibrations of CBD, related to Figure 2B. A) FTIR difference spectra of CBD and ^{13}C^{15}N-labeled CBD. The overlapping signal, most probably arising from the biliverdin chromophore, is highlighted with green background. The shifts of some amide I and amide II signals are marked with arrows. The amide I signals shift 41-48 cm^{-1} wavenumbers, and amide II signals about 30 cm^{-1} due to the isotope labeling of both carbons and nitrogens.[2] B) Overlay or CBD-PHY Pr (orange) and Pfr (blue) structures CBD region, BV is shown in sticks. The β-sheet formed by residues 97-131 is shown in darker hue, and the differences between the length of the β-sheet is illustrated with arrows and dashed line. All three strands of the sheet become longer in the Pfr state.

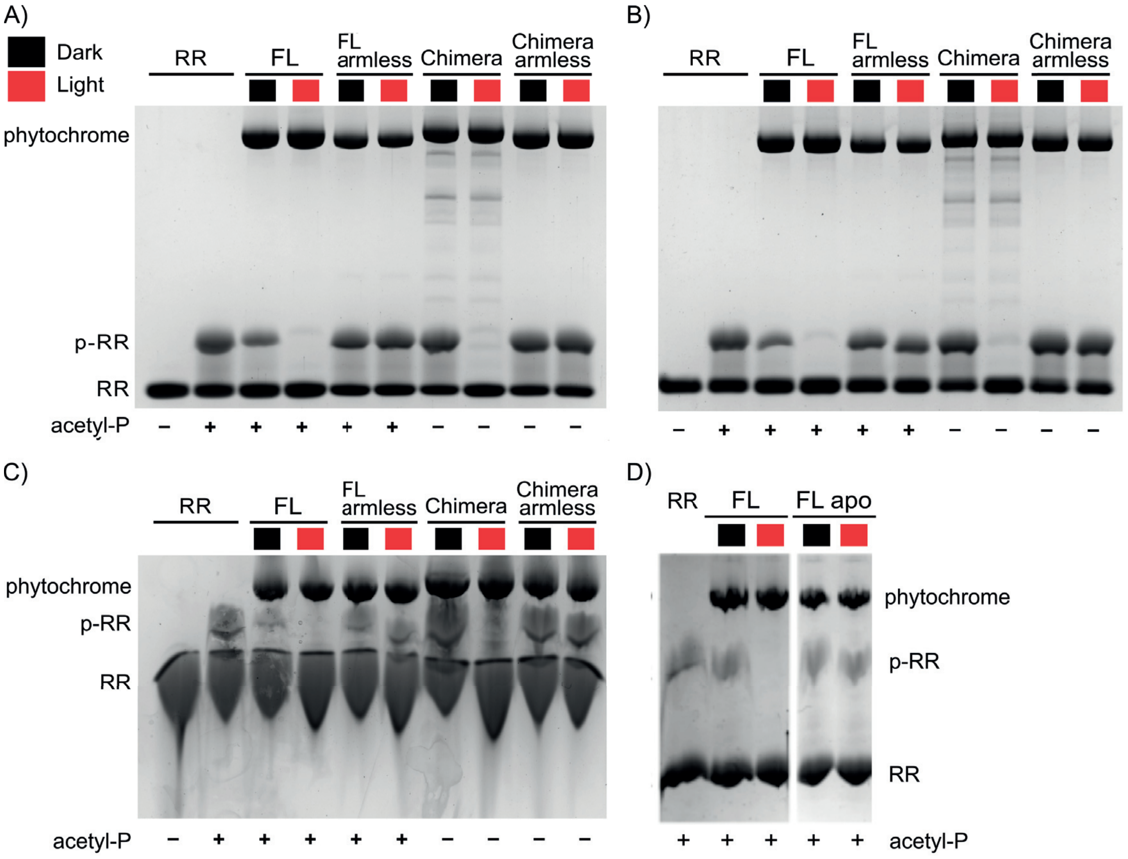

Figure S6: PhosTag gels, related to Figure 3. A) Repetition of the PhosTag activity assay (Fig. 3). The gel reproduced the result that FL armless and Chimera armless cannot be switched on and off, respectively, with red light. B) Full gel of the one shown in Figure 3. C) PhosTag activity assay of FL apo (*Dr*BphP without biliverdin).

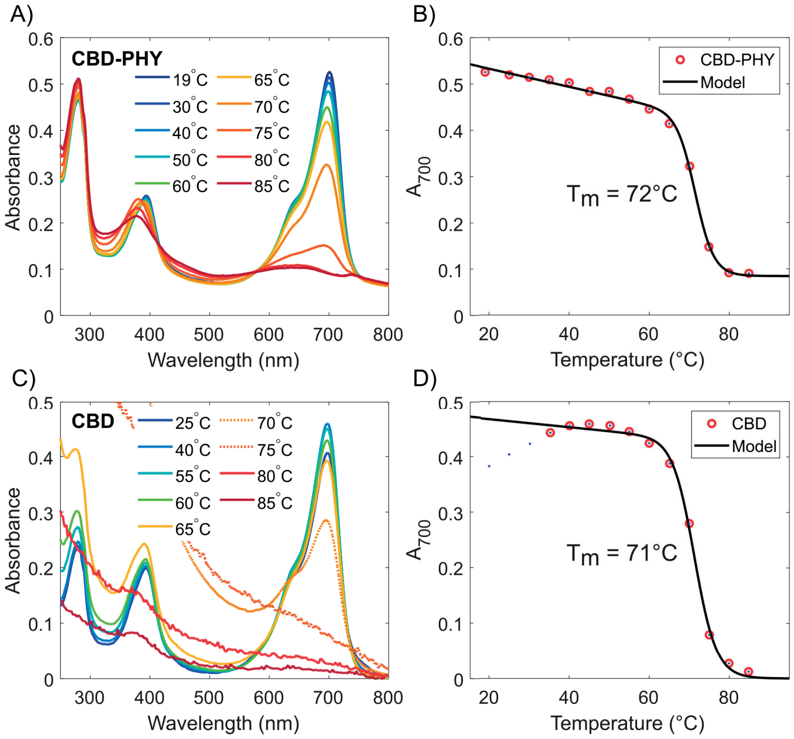

Figure S7: Temperature-dependent UV-vis spectra of CBD-PHY and CBD in dark, related to Figure 4. A) The spectra and B) melting curve at 700 nm of CBD-PHY and C) the spectra and D) the melting curve at 700 nm of CBD. For clarity, only the spectra of selected data points in B and D are shown in A and C, respectively. The data (dots) were fitted to a unimolecular two-state model according to Eq. 1-3. Data included in the fits is shown with red circles. The T_ms acquired from the fits are represented in B and D. The 700-nm absorption originates from BV, and the decrease in A_{700} results from changes in the BV environment due to denaturation of the protein moieties. CBD starts to strongly aggregate at temperatures over 65°C, which results in strong scattering of the spectra. In the spectra at 70°C and 75 °C (dotted) only the 700 nm peak is shown for clarity.

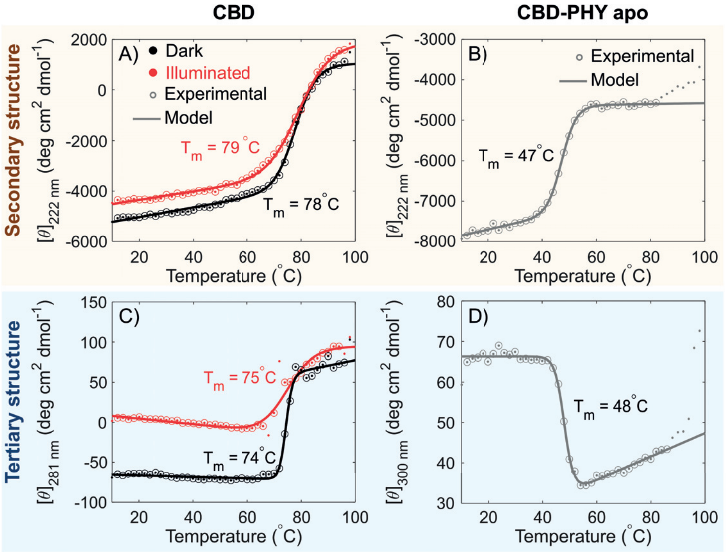

Figure S8: Melting curves of CBD and CBD-PHY apoprotein, related to Figure 4. A-B) Melting of CBD and CBD-PHY apoprotein (apo) secondary structure monitored at 222 nm. Melting of CBD was measured in dark (black) and illuminated (red) states. The fits according to Eq. 1-3 are shown as solid lines, and melting temperatures defined from the fits are marked with respective colors. C-D) Melting of CBD and CBD-PHY apo tertiary structures monitored at 281 nm and 300 nm, respectively. All data points are shown in dots, and those used for the fitting in circles.

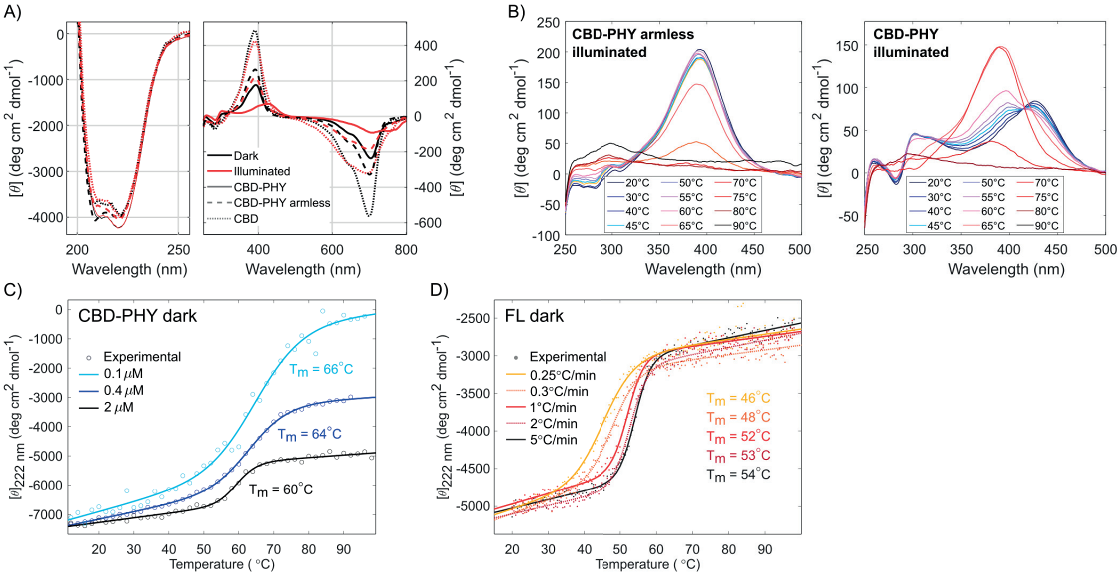

Figure S9: CD properties of CBD-PHY, CBD-PHY armless and FL, A & B, related to Figure 4, C & D related to STAR Methods. A) Full CD spectra of the constructs in dark (black) and illuminated (red) states. The 190-250 nm spectra and >250 nm spectra have been measured separately. B) CD spectra of CBD-PHY armless and CBD-PHY at 250-500 nm in the illuminated state at different temperatures. The two constructs have a different melting profile. At room temperature, CBD-PHY has a maximum at 425 nm, which shifts to 390 nm at 60-65°C before completely melting. CBD-PHY armless has maximum only at 390 nm. C) Denaturation of CBD-PHY in dark at three different concentrations reveals the concentration dependence of the melting temperature. Lower concentration also leads to a larger amplitude of the melting curve. The experimental data is fitted to Eq. 1-3 (solid line). D) Denaturation of FL in dark at different rates reveals the rate dependence of the melting temperature. The faster the heating rate, the higher the T$_m$. C-D related to

References

1. Lehtivuori, H., Rumfeldt, J., Mustalahti, S., Kurkinen, S., and Takala, H. (2022), Conserved histidine and tyrosine determine spectral responses through the water network in *Deinococcus radiodurans* phytochrome. Photochemical and Photobiological Sciences 21, 1975–1989, doi:10.1007/S43630-022-00272-6/TABLES/3, ISSN 14749092.
2. Brielle, E. S. and Arkin, I. T. (2021), Isotope-Edited Amide II Mode: A New Label for Site-Specific Vibrational Spectroscopy. The Journal of Physical Chemistry Letters 12, 6634–6638, doi:10.1021/acs.jpclett.1c01073, pMID: 34254809.

IV

SITE-BY-SITE TRACKING OF SIGNAL TRANSDUCTION IN AN AZIDOPHENYLALANINE-LABELED BACTERIOPHYTOCHROME WITH STEP-SCAN FTIR SPECTROSCOPY

by

Moona Kurttila, Brigitte Stucki-Buchli, Jessica Rumfeldt, Lea Schroeder, Heikki Häkkänen, Alli Liukkonen, Heikki Takala, Tilman Kottke & Janne A. Ihalainen 2020

Physical Chemistry Chemical Physics 23: 5615–5628

https://doi.org/10.1039/d0cp06553f

PCCP

ROYAL SOCIETY OF CHEMISTRY

PAPER

View Article Online
View Journal | View Issue

Check for updates

Cite this: *Phys. Chem. Chem. Phys.*, 2021, **23**, 5615

Site-by-site tracking of signal transduction in an azidophenylalanine-labeled bacteriophytochrome with step-scan FTIR spectroscopy†

Moona Kurttila,[a] Brigitte Stucki-Buchli,[a] Jessica Rumfeldt,[a] Lea Schroeder,[b] Heikki Häkkänen,[a] Alli Liukkonen,[a] Heikki Takala,[a] Tilman Kottke*[b] and Janne A. Ihalainen*[a]

Signal propagation in photosensory proteins is a complex and multidimensional event. Unraveling such mechanisms site-specifically in real time is an eligible but a challenging goal. Here, we elucidate the site-specific events in a red-light sensing phytochrome using the unnatural amino acid azidophenylalanine, vibrationally distinguishable from all other protein signals. In canonical phytochromes, signal transduction starts with isomerization of an excited bilin chromophore, initiating a multitude of processes in the photosensory unit of the protein, which eventually control the biochemical activity of the output domain, nanometers away from the chromophore. By implementing the label in prime protein locations and running two-color step-scan FTIR spectroscopy on the *Deinococcus radiodurans* bacteriophytochrome, we track the signal propagation at three specific sites in the photosensory unit. We show that a structurally switchable hairpin extension, a so-called tongue region, responds to the photoconversion already in microseconds and finalizes its structural changes concomitant with the chromophore, in milliseconds. In contrast, kinetics from the other two label positions indicate that the site-specific changes deviate from the chromophore actions, even though the labels locate in the chromophore vicinity. Several other sites for labeling resulted in impaired photoswitching, low structural stability, or no changes in the difference spectrum, which provides additional information on the inner dynamics of the photosensory unit. Our work enlightens the multidimensionality of the structural changes of proteins under action. The study also shows that the signaling mechanism of phytochromes is accessible in a time-resolved and site-specific approach by azido probes and demonstrates challenges in using these labels.

Received 18th December 2020,
Accepted 21st February 2021

DOI: 10.1039/d0cp06553f

rsc.li/pccp

1 Introduction

A family of photoreceptors called phytochromes mediate red and far-red light responses in plants, bacteria, algae, and fungi. These proteins undergo photoinduced structural changes which lead to biochemical signaling cascades that regulate the growth and development according to the ambient conditions.[1–3] Phytochromes cycle between two metastable states, the red light-absorbing Pr state and the far-red light-absorbing Pfr state. In canonical phytochromes, the photoconversion from the Pr state to the Pfr state is triggered by the isomerization of the covalently bound bilin chromophore, which leads to structural reorganization of the photosensory unit that eventually controls the activity of the output domain (Fig. 1A). The photoconversion proceeds from Pr to Pfr *via* at least two intermediate states, Lumi-R and Meta-R, respectively,[4,5] and the protein returns to the Pr state by far-red light excitation (Fig. 1B). Alternatively, canonical phytochromes thermally revert back to the Pr state in the dark within minutes to hours.[1]

The conserved N-terminal photosensory module (PSM) of bacterial phytochromes consists of three domains, PAS (Period/Arnt/Single-minded), GAF (cGMP phosphodiesterase/adenylate cyclase/FhlA) and PHY (phytochrome-specific) (Fig. 1A). The PHY domain is followed by a C-terminal output domain which in bacteriophytochromes is often a histidine kinase (HK). PAS and GAF together bind a biliverdin IXα (BV) as a chromophore. The four-ring (A–D) BV is covalently bound to the PAS domain *via* a thioether linkage between the A-ring and a cysteine residue.[6] The non-covalent interactions with the GAF residues and a so-called pyrrole water further position the BV.[6,7] The photo excitation of the BV chromophore causes isomerization of

---

[a] *University of Jyväskylä, Nanoscience Center, Department of Biological and Environmental Science, 40014 Jyväskylä, Finland. E-mail: janne.ihalainen@jyu.fi*

[b] *Physical and Biophysical Chemistry, Department of Chemistry, Bielefeld University, Universitätsstr. 25, 33615 Bielefeld, Germany. E-mail: tilman.kottke@uni-bielefeld.de*

† Electronic supplementary information (ESI) available. See DOI: 10.1039/d0cp06553f

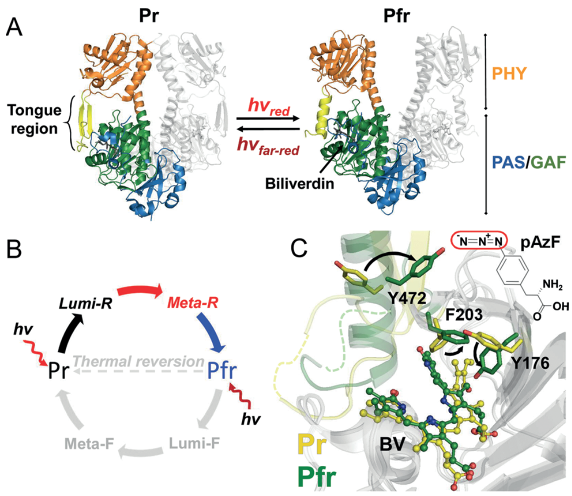

Fig. 1 Structure and photocycle of *Dr*BphP$_{PSM}$. (A) Phytochromes interconvert between red light-absorbing Pr and far-red light-absorbing Pfr states (PDB codes 4O0P and 5C5K, respectively). The different domains of the photosensory module are indicated with different colors. The tongue region is indicated in yellow. (B) The photocycle of canonical phytochromes has at least two spectrally distinguishable intermediate states, Lumi-R and Meta-R. (C) The unnatural amino acid *p*-azidophenylalanine (pAzF), incorporated into a protein, contains an azide group (red circle) of which the vibrational frequency is distinct from all other modes of protein and chromophore (biliverdin, BV, ball-and-stick). The three pAzF-exchanged side chains are shown with sticks in Pr (yellow) and in Pfr (green).

the double bond between carbons 15 and 16,[8,9] which is observed as a rotation of the D-ring. This isomerization, in turn, changes the interactions between the chromophore and the residues in the BV binding pocket.[10] Although located in separate domains, BV is linked to a hairpin extension, a so-called tongue region, *via* an aspartic acid and a tyrosine, both located in the GAF domain.[7,11] Most probably mediated by these interactions, the tongue region restructures from β-sheet to α-helix during the photoconversion (Fig. 1A).[11] Eventually, these events lead to structural changes in the whole protein, and the reorganization of the output domains ultimately controls the chemical activity of the receptor.

Time-resolved structural information is necessary to follow the signal propagation processes in photosensory proteins. This increases our understanding of the functional properties of proteins, in general. In the field of phytochromes, studies using techniques such as X-ray crystallography[6,7,11] and nuclear magnetic resonance (NMR) spectroscopy[12,13] have successfully shed light on the structural changes observed in the PSM between Pr and Pfr states without time-resolved information, however. With X-ray scattering[4,11] only large-scale structural information has been obtained with time scales of the whole photocycle. Using IR spectroscopy, both the response of the bilin chromophore and the response of the protein can be followed in solution on all time scales of the photocycle. However, a molecule with N atoms has $3N - 6$ vibrational modes and accordingly the assignment of absorption bands to single functional groups becomes extremely challenging for a large molecule such as phytochrome. Some vibrational modes in the IR difference spectra of phytochromes have been assigned to functional groups of the chromophore or protein using techniques such as isotope exchange,[14,15] chemical modification of the chromophore,[14] mutagenesis,[16] truncation[17] and computations.[8,18] Still, challenges in assignments remain such as the overlap with other modes and frequency shifts by slight conformational changes of the protein and the chromophore. An intriguing solution for this dilemma is an azido IR-probe with distinguishable vibrational properties. The introduction of vibrational labels into the protein offers a possibility to gain site-specific resolution for structural and chemical changes of proteins.[19–24]

Azido probes have been successfully employed to study proteins previously,[25–31] for example rhodopsin activation,[19,32] protein dynamics and interaction[33] and ligand binding.[20,34] They can be introduced into proteins by the unnatural amino acid *p*-azidophenylalanine (pAzF) through protein expression using the amber codon suppression technology.[26,35,36] Together, this technology and the small size of pAzF enable placing the label at surface-exposed and buried positions of the protein. pAzF carries an azido group whose asymmetric N_3 stretch vibration absorbs at around 2100 cm^{-1}, in a distinct region from all other protein modes.[37] Its high extinction coefficient of about 610 M^{-1} cm^{-1} makes it superior to many other vibrational probes such as popular cyano probes (with $\varepsilon = 120\text{–}220$ M^{-1} cm^{-1}).[22,38–40] Most importantly, pAzF is sensitive to changes in its electrostatic environment, especially to the H-bonding strength.[38–41] Therefore, the structural changes of the protein and chromophore are reflected as changes in the spectral position and shape of the pAzF signal as detected by FTIR spectroscopy.

Previously, pAzF has provided information in the ultrafast time scale on structural changes in two BLUF domains[30] and in the tens of milliseconds to seconds time scale on channelrhodopsin pore hydration with rapid-scan FTIR.[31] Here, we resolve structural changes in the protein microenvironment in the micro- to millisecond time scale, desirable as well for other photoreceptors, to our knowledge for the first time with this label. We introduce pAzF in various positions (Fig. S1, ESI†) of a bacterial phytochrome photosensory module from *Deinococcus radiodurans*, hereafter *Dr*BphP$_{PSM}$, to detect local structural changes in the protein with a site-by-site approach in a time-resolved manner using two-color step-scan FTIR spectroscopy.[5,42] As a result, we address how and when the microenvironment changes in these sites during the photocycle. Furthermore, we report on the effect of the strong dipole present in the azidophenylalanine on the kinetics of the photocycle, which provides information about the active role of these sites for the signal propagation in the protein.

2 Materials and methods

2.1 Protein expression and purification of the unlabeled *Dr*BphP$_{PSM}$ monomer

We chose to introduce the pAzF to the monomeric form of *Dr*BphP$_{PSM}$ to simplify the protein purification procedure.

This monomeric *Dr*BphP$_{PSM}$ contains the mutations F145S, L311E and L314E, which are located at the dimer interface and prevent dimerization.[43,44] The unlabeled, (His)$_6$-tagged and monomeric *Dr*BphP$_{PSM}$ was expressed in *Escherichia coli* BL21(DE3) as described previously.[44] Purification was performed as described in Ihalainen *et al.*[5]

2.2 Production of pAzF-labeled *Dr*BphP$_{PSM}$ monomers

The amber codon suppression technology[26] was used to introduce the unnatural amino acid pAzF into the phytochrome. We replaced the original amino acid encoding codon with the amber codon (TAG) using the QuikChange Lightning Multi Site-Directed Mutagenesis kit (Agilent Technologies) in nine positions, Y176, F203, R228, S257, Y263, Y307, F372, F469, and Y472, each in a separate pET21b(+) plasmid (Novagen).[44]

The plasmid with the TAG-mutated gene encoding monomeric *Dr*BphP$_{PSM}$ was co-transformed with pEVOL-pAzF[36] (Addgene plasmid # 31186) into *E. coli* BL21(DE3). The cells were grown in LB medium supplemented with 150 μg mL^{-1} ampicillin and 25 μg mL^{-1} chloramphenicol. 0.02% arabinose and 600 μg mL^{-1} H-4-Azido-Phe-OH (Bachem) was added when the OD$_{600}$ reached 0.2. The expression of the phytochrome was induced with 1 mM IPTG at an OD$_{600}$ of 0.8. The incubator was covered to protect reactive pAzF[35] from light. Further purification steps were carried out by using dim light or green light to protect both, pAzF and BV.

The cells were resuspended in 20 mM Tris, 50 mM NaCl, pH 8 and lysed with an EmulsiFlex-C3 homogenizer (Avestin). pAzF is a potentially reactive amino acid, therefore the incubation time of the protein in the cell lysate was kept as short as possible. The apoprotein was purified using Ni^{2+}-affinity chromatography (HisTrap FF crude, GE Healthcare) in a 20 mM Tris buffer, pH 8, 50 mM NaCl and eluted with an imidazole gradient. By the affinity chromatography, the protein containing a C-terminal (His)$_6$-tag was separated from truncated protein in which the amber codon was interpreted as a stop codon.

The apoprotein was supplemented with biliverdin chromophore (Frontier Scientific). A 10× molar excess of BV hydrochloride (Frontier Scientific), dissolved in a small amount of dimethyl sulfoxide, was added to the purified protein. The mixture was incubated at 4 °C overnight. The protein with BV bound was then purified by size-exclusion chromatography (HiLoad 26/600 Superdex 200 prep grade, GE Healthcare) in 30 mM Tris, pH 8.

The purified protein was concentrated with Amicon Ultra concentration tubes with a 10 kDa cutoff (Merck-Millipore) to about 25–30 mg mL^{-1}, flash frozen in liquid nitrogen and stored at −80 °C.

2.3 Steady-state FTIR spectroscopy

The steady-state FTIR spectroscopy of the labeled and unlabeled samples was performed using a Nicolet Magna IR-760 FTIR spectrometer with XT-KBr beam splitter and Ever-Glo IR source. The measurements were conducted using 100 scans in the spectral range of 400–3500 cm^{-1} with a resolution of 2 cm^{-1}. Sample preparation and light-induced difference spectroscopy were performed as described in Takala *et al.*[45]

Absorption spectra were measured in buffered D$_2$O at pD 8.0. Concentrated HCl in H$_2$O was used to adjust the pH of 30 mM Tris in D$_2$O to pH* 7.6 corresponding to pD 8.0. The buffer of the protein was exchanged using Zeba Spin desalting columns with a 7 kDa MWCO (Thermo Scientific). In buffered D$_2$O, the protein was switched between Pr and Pfr by illumination using 660 nm and 775 nm LEDs, respectively, in 5 min intervals for 1 hour to enhance the H/D exchange in both states.[5] After switching, the buffer was exchanged for a second time, concentrated to about 2–3 mM with Vivaspin 500 10 kDa centrifugal concentrators (Sartorius) and filtered with Amicon 0.22 μm centrifugal filters (Merck-Millipore). The path length was set to 50 μm by using a Teflon spacer. The combination of high concentration and high path length resulted in saturated amide I and II bands, but those were disregarded as the focus was on the signal in the label region.

2.4 Time-resolved step-scan FTIR spectroscopy

Two-color step-scan FTIR spectroscopy with a time resolution of 2.5 μs was performed on an IFS 66v spectrometer (Bruker) as described in Ihalainen *et al.*[5] The detection window was extended to 2256 cm^{-1} to include the label region by placing an LP-4500 filter (Spectrogon) and CaF$_2$ windows in front of the detector.[24] 316 discrete mirror positions were stepped and undersampling was applied for FT. The resulting spectral resolution was 8 cm^{-1}. To increase the signal in the label region, the path length was adjusted to achieve an $A_{1650} > 1.1$, while keeping the protein concentration the same as in the steady-state experiments to ensure a sufficient hydration of the sample. The resulting high water absorption in the amide I region caused a saturation in the region of 1610 to 1670 cm^{-1}, which was therefore left out in the global analysis of the difference spectra. 15 experiments on F203pAzF, 8 experiments on Y176pAzF and 11 experiments on Y472pAzF were averaged with 8 coadditions each, while exchanging the sample after less than 8000 excitations. All experiments were performed at 20 °C.

2.5 Steady-state UV-vis spectroscopy

The steady-state UV-vis difference spectra were measured with a Cary 8454 UV-vis spectrometer (Aligent Technologies) using 1.5 mL plastic, semi-micro cuvettes (Brandtech Scientific) with 10 mm path length and 500 μL sample. The sample was diluted to about 0.3 mg mL^{-1}. The initial spectrum was recorded on a sample kept in the dark, then the sample was switched multiple times between Pr and Pfr using 661 nm and 775 nm LEDs, while spectra were measured in between the switching. The illumination times were set to reach full photoconversion.

2.6 Flash photolysis

The sample with absorbance of 0.7–0.8 at 700 nm in a 1 mm cuvette was first illuminated with a 751 nm cw laser (1 s, 500 mW, Leading-Tech Laser) to produce the Pr-state. Flash photolysis was started with a 660 nm laser pulse from a tunable diode-pumped laser system (3 ns, 1.6 mJ cm^{-2}, NT230, Ekspla). The spectrum after the flash was measured using a fiber optic halogen illuminator (7010, Cambridge Technology), a spectrograph

(SpectraPro 150, Acton Research) and an intensified CCD camera (ICCD, InstaSpec V, Oriel) with time control by a delay generator (DG535, Stanford Research Systems). A long pass filter >680 nm was used in the detection. The time window of illumination with probe light was synchronized to detection by using fast shutters (Vincent Associates) to obtain the same number of photons for each time point. After each flash, the sample was switched back to the Pr state by a 751 nm laser pulse (30 ms, 6.6 mJ cm^{-2}), ensuring full conversion to Pr. Delay times were set in the region of 10 μs–50 ms with a gate time of either 10 μs or 1 ms. Each time point was recorded 20 times at a 4 Hz repetition rate. Background spectra after applying only the 751 nm pulse were measured before and after the flash photolysis cycle and then averaged. To compensate for signal instabilities, the data was acquired with either increasing or decreasing delay times. In addition, all transmission spectra were normalized to the isosbestic point of the photoconversion as determined by steady-state UV-vis spectroscopy.

2.7 Data analysis

Analysis of the steady-state FTIR spectra was performed using Matlab version R2018b (The MathWorks, Inc). The set of difference spectra (Pfr *minus* Pr and *vice versa*) were averaged and offset corrected in the spectral range of 1981–1999 cm^{-1}. Since the signal of the pAzF azide label was detected by difference spectroscopy, all the unchanged contributions were lost. To reconstruct the shape and position of the bands in Pr and Pfr, the signal at 2060–2180 cm^{-1} was fitted with the required number of Gaussian bands[40,41,46,47] using the interactive peak fitter (ipf.m, version 13, available in https://terpconnect.umd.edu/~toh/spectrum/InteractivePeakFitter.htm) with flat baseline correction.

The global analyses of time-resolved FTIR and flash photolysis data were performed with Glotaran 1.5.1.[48] Ihalainen *et al.*[5] showed that the global analysis of time-resolved FTIR spectra of *Dr*BphP$_{PSM}$ leads to SADS of two intermediate states, Lumi-R and Meta-R, and the photoproduct Pfr. Accordingly, a sequential model was applied here. The spectral region of water absorption (1610–1670 cm^{-1}) in the FTIR spectra of pAzF mutants was ignored in order not to dominate the global analyses.

The time-resolved FTIR spectra of the wild type were scaled to those of Y472pAzF and F203pAzF using the negative 1562 cm^{-1} band maximum of the Pfr spectra. For Y176pAzF, this scaling procedure did not yield satisfactory results. Instead, spectra of the wild type were scaled to the negative 1712 cm^{-1} and positive 1685 cm^{-1} bands of Pfr in Y176pAzF. The steady-state spectra were scaled using the same factors.

3 Results

We successfully introduced the pAzF vibrational probe in three prime positions, Y472, F203, and Y176, in the phytochrome photosensory module *Dr*BphP$_{PSM}$ (Fig. 1C). Important for our experimental settings, we find by UV-vis absorption spectroscopy that despite the effect of the azido group, the photo-stationary states (Pr and Pfr) of these samples are stable and can be interconverted repetitively (Fig. S1 and S2, ESI†).

Y472pAzF reports particularly on the tongue region whereas Y176pAzF and F203pAzF provide information on the role of the hydrophobic pocket around the chromophore mainly formed by F203. Furthermore, Y176 contributes to the hydrophobic pocket, but in Pfr the OH-group of tyrosine participates in a chromophore-stabilizing H-bond.[7,11]

On top of analyzing the pAzF signal of the three mutants, we also compare the photocycle of the pAzF mutants to the wild type, WT *Dr*BphP$_{PSM}$. FTIR spectroscopy captures the structural changes in both the protein moiety and the BV chromophore in the fingerprint region (1200–1765 cm^{-1}), whereas UV-vis spectroscopy reveals the changes in the BV only. At steady-state, the difference spectra show structural changes from Pr to Pfr. The time-resolved experiments reveal the differences in structure of the intermediates to that of Pr. By means of global analysis of the time-resolved data, we compare the time constants as well as spectral properties of the intermediates during the photocycle. The direct comparison of time-resolved FTIR and UV-vis data reveals whether structural rearrangements in the protein proceed even after the chromophore has finalized its conversion.

We have chosen the monomeric form of the *Dr*BphP$_{PSM}$[44] to simplify the purification process by avoiding the separation of fully expressed homodimers from heterodimers with a truncated half because of the stop codon applied in the amber codon suppression technology (see Materials and methods). Monomeric *Dr*BphP$_{PSM}$ undergoes the same photocycle as the dimer with similar FTIR as well as transient IR difference spectra and moreover provides clearer and more homogenous data than the dimer.[5]

As the phytochrome photoconversion between the Pr and Pfr state is such a complex process, additional sites would be desirable to label and investigate. Therefore, in addition to the positions mentioned above, we incorporated the probe at six other positions (Fig. S1, ESI†). However, the probe at these positions either perturbed structural and photoswitching properties or did not lead to any or only minor changes in the steady-state FTIR difference signal in the azido region (Table S1, ESI†). The UV-vis spectra (Fig. S2 and S3, ESI†) and the steady-state FTIR difference spectra (Fig. S4, ESI†) of the mutants are described in the Supplementary information including, where possible, difference spectra of the pAzF region (Fig. S5, ESI†).

3.1 Y472pAzF reports on the structural changes in the tongue

Y472 is located in the so-called tongue region of the PHY domain (Fig. 1C). In Pr, the tongue has been suggested to form a β-sheet, but to convert to an α-helix upon photoconversion to Pfr (Fig. 1A).[11] As the structure of the tongue changes, the relative position and thus the microenvironment of the label at Y472 is also expected to change. The crystal structures of the photoactive states suggest that the side chain of Y472 is solvent exposed in Pr, but the α-helical conformation of the tongue turns it towards the protein in Pfr (Fig. 1C).[7,11]

The microenvironment in Pr and Pfr is revealed by the pAzF vibrational frequency in the steady-state FTIR difference spectrum (Fig. 2A). Of note, the difference spectrum, *i.e.* Pfr *minus* Pr, allows a better resolution of the label signal than the absolute IR absorption spectrum (Fig. S6, ESI†). In the difference spectrum, the negative signal represents the disappearance of absorption from the initial Pr state and the positive signal represents the induced additional absorption of the Pfr state. Therefore, an appearance of the azido signal in the FTIR difference spectrum at around 2100 cm^{-1} reports about a change in the local electronic environment of the label and a change of the H-bonding strength between the label and its environment.

The pAzF signal in solution consists of an asymmetric azide stretch that is accompanied by two Fermi resonance bands resulting from anharmonic vibrational coupling between the asymmetric azide stretch and combination modes of the symmetric azide stretch and phenyl modes.[47] To reveal the position of the contributing bands, the difference signal of Y472pAzF is fitted using a sufficient number of Gaussians (Fig. 2A).[40,46,47] We assume that the frequency of the asymmetric azide stretch stays in the limits of 2110–2130 cm^{-1}, according to the studies of Zhang *et al.*[47] and Maj *et al.*[40] Within these limits, an upshift in frequency indicates a larger H-bond strength.[38,40,41,47] Bands outside of these limits we identify as Fermi resonance bands. We consider it unlikely but cannot exclude the possibility that the main band and the Fermi resonance bands originate from two different protein conformations.

The steady-state FTIR difference spectrum of Y472pAzF reveals that the microenvironment of the probe at this position changes upon photoconversion. The azido vibration of Y472pAzF redshifts from 2125 cm^{-1} in Pr to 2114 cm^{-1} in Pfr with additional Fermi resonance bands (at 2141 cm^{-1} and 2105 cm^{-1}) (Fig. 2A). The signals point to a strong H-bonding environment in Pr, and to a non- or weakly H-bonding environment in Pfr.[38,40,41,47] Observations in the crystal structures support the information acquired from the FTIR spectrum, as an H_2O of the solvent might be the H-bonding partner of Y472pAzF in Pr, and its rotation from solvent exposure towards the protein moiety in Pfr then causes a loss of this strong H-bond network.

The small relative intensity of the azido peak compared to the fingerprint region is rationalized by recording the absolute absorption spectra of Y472pAzF in D_2O (Fig. S6A, ESI†). We find that the label signals in Pr and Pfr are almost completely overlapping and therefore compensate each other in intensity. This significant broadening of the bands might be caused by the dynamic nature of the refolding tongue in which the label in Y472pAzF is located in both Pr and Pfr states.[49,50]

By means of time-resolved step-scan FTIR spectroscopy, we demonstrate in which time scales the observed changes between Pr and Pfr arise at the different labeled locations. In the step-scan experiments, we selected the time window

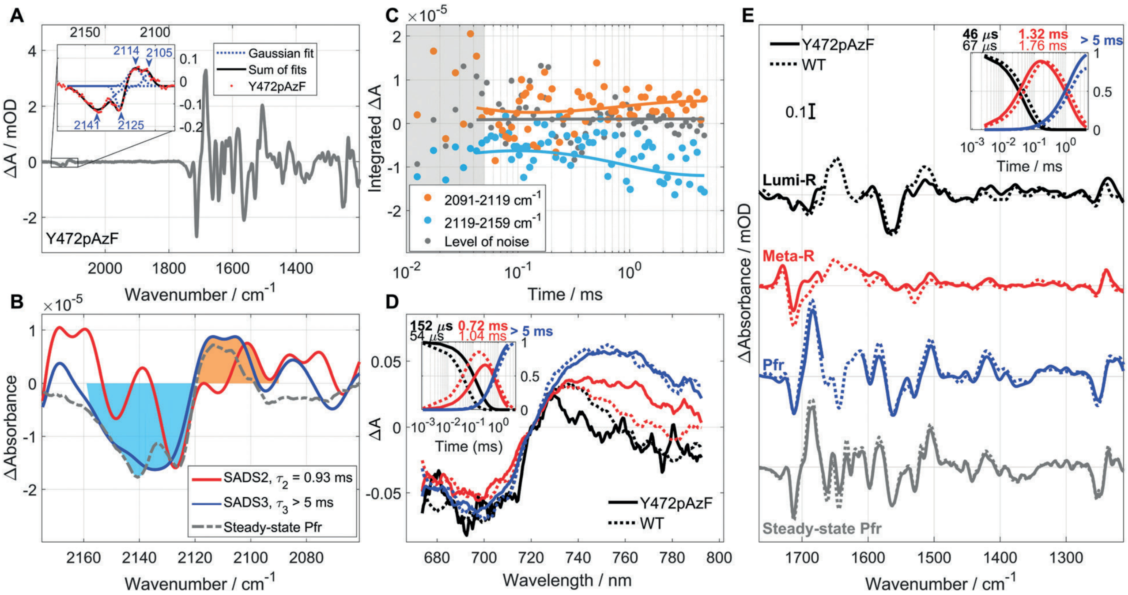

Fig. 2 Spectroscopic analysis of the Y472pAzF mutant of *Dr*BphP$_{PSM}$. (A) The steady-state FTIR difference spectrum of the labeled sample. The signal of the label is fitted with four Gaussian bands (the inset), the maxima are indicated. (B) The global analysis of the time-resolved FTIR signal in the label region reveals three components. However, only two SADS are presented due to the large noise at early times (τ_1 = 35 µs, see Fig. S7A, ESI†). The steady-state spectrum scaling is the same as in (E). (C) Kinetics of the integrated spectral signal of the label (dots) with their fit (solid lines). The time constants are indicated in (B). The grey dots indicate the noise level of the experiment (Fig. S7A, ESI†) and the grey background the time frame with high noise level. (D) SADS from the global analysis of the flash photolysis (vis to far-red detection) for Y472pAzF (bold) and WT (dotted) with their time constants. (E) Global analysis of the step-scan FTIR data in the fingerprint region for Y472pAzF *vs.* WT. The step-scan data at 1610–1670 cm^{-1} of the mutant is discarded due to dominating water absorption. The insets in (D) and (E) show the concentration fractions of the three different components in the analyses.

from 2.5 μs to 4.7 ms to capture both the early and late steps of the photocycle.[51]

We evaluate separately the events in the label region (Fig. 2B and C) and the photocycle of the pAzF-labeled mutants by global analysis[52,53] of time-resolved FTIR spectroscopy (Fig. 2B and E) and flash photolysis in the visible region (Fig. 2D). To reveal the changes in the photocycle caused by the label or removal of the native residue, we compare the spectral fingerprint and associated kinetics to the unlabeled WT.

The global analysis in the region of 2060–2175 cm^{-1} shows that the label signal in Y472pAzF evolves in three components (SADS, species associates difference spectra), *i.e.*, the site is responding to the activity in all three phases of the photocycle (Fig. 2B). Although the Lumi-R spectrum (τ = 35 μs) is dominated by a rather large noise level (Fig. S7A, ESI†), the early changes are clearly revealed by integrating the data of the label signal from 2091 to 2119 cm^{-1} and 2119 to 2159 cm^{-1}; these regions are indicated in Fig. 2B in orange and blue, respectively. The integrated data is plotted in Fig. 2C in comparison to the noise level, as a result we excluded the earliest data points from the analysis. The change in absorbance of the label appears already at 40 μs. The integrated amplitude of both positive and negative signals at 40 μs is only about half of the integrated signal intensity in Pfr, but clearly above the noise level. This finding indicates that the label environment undergoes structural changes already in the early microsecond time scale.

In the Meta-R spectrum, four bands (two negative and two positive) similar to the bands in the final photoproduct are observed, but with different amplitude ratios (Fig. 2B). Moreover, the integrated difference signals continue to grow with the time constant of 0.93 ms (Fig. 2C). This analysis reveals that the evolution of the structural changes in the tongue towards the final Pfr environment is complex, because the label experiences environments different from Pr and Pfr during the conversion process. The final SADS assigned to the Pfr state matches the steady-state Pfr spectrum (Fig. 2B), which means that the label settles to its final Pfr environment within the time frame of the experiment (4.7 ms). Accordingly, the final restructuring of the tongue occurs during the final step of the photocycle from Meta-R to Pfr, in agreement with previous analysis of the amide I and II signals in WT.[5]

The photoconversion of the labeled phytochromes is followed by flash photolysis, which shows the changes in the chromophore absorption (Fig. 2D). For comparison, the recorded step-scan FTIR spectra in the fingerprint region (below 1765 cm^{-1}) reveal the changes in chromophore and protein vibrations during the photocycle (Fig. 2E). In the global analysis, both data (flash photolysis and step-scan FTIR) are fitted with three components, leading to spectra of Lumi-R, Meta-R, and Pfr states, respectively. The three SADS of the step-scan experiment are confirmed by extracting raw data averaged according to the species concentrations in time (Fig. S8, ESI†).

The changes in the chromophore and the protein moiety proceed with similar kinetics as the spectral signatures of the label environment of Y472pAzF. The time constant of the label Lumi-R (35 μs) is very close to that of the fingerprint region (Fig. 2E). The time constant of the label for Meta-R lies in between the time constants observed in the flash photolysis and in the FTIR fingerprint region (numeric values indicated in Fig. 2B, D and E). We note that slight differences are expected as the chromophore, protein and label report different information on the photoconversion process.[45]

In comparison with the WT, the photocycle of Y472pAzF proceeds highly similarly with regards to spectral features as well as kinetics (Fig. 2E). The first intermediate Lumi-R is observed with matching spectral characteristics and a time constant comparable to the WT. The Meta-R state decays slightly faster than in WT and shows characteristic features, *e.g.*, the positive peak at 1730 cm^{-1}. Finally, the labeled phytochrome reaches, like the WT, a Pfr spectrum that strongly resembles the steady-state spectrum, considering that the spectral resolution of the time-resolved experiments was 8 cm^{-1} as compared to 2 cm^{-1} in the steady-state spectra.

The global analysis of the flash photolysis reveals slight differences in kinetics between the mutant and the WT (Fig. 2D). In Y472pAzF, the Lumi-R state decays slower than in WT and on the other hand, the Meta-R decays a bit earlier, leading to a lower population of Meta-R in the mutant. The difference spectrum at 5 ms has the same features as the steady-state difference spectrum, meaning that the photocycle of the chromophore has been finalized by this time. In fact, in all three mutants the chromophore finishes the photocycle within 5 ms, as their latest flash photolysis spectra match the steady-state absorption difference spectra (Fig. S9 and S10, ESI†).

3.2 Y176pAzF demonstrates major hydrogen bonding change in the late phase of the photoconversion

Y176 is a buried residue, located in the chromophore binding pocket near the BV D-ring in the *Dr*BphP$_{PSM}$ (Fig. 1C). In Pr, it is part of the hydrophobic pocket stabilizing the D-ring position.[6,11] In the transition to Pfr, it moves together with F203 to a new location, where it stabilizes the Pfr state.[7,45,54]

The steady-state FTIR difference spectrum of Y176pAzF shows that the azido vibrations blueshift from 2112 cm^{-1} in Pr to 2125 cm^{-1} in Pfr with an additional Fermi resonance band at 2136 cm^{-1} (Fig. 3A and Fig. S6B, ESI†). Further, a slight negative feature can be discerned at 2071 cm^{-1} in Pr, arising due to different peak widths possibly because of Fermi resonances. The intensity of the difference signal is larger in the case of Y176pAzF than for Y472pAzF, which is caused by a larger shift of the peak maximum between Pr and Pfr (Fig. S6B, ESI†).

Based on the observed frequencies (2112 cm^{-1} in Pr, 2125 cm^{-1} in Pfr), the azido group in Y176pAzF has mainly a non- or weakly H-bonding environment in the Pr state but a strong H-bond in the Pfr state.[19,39,47] The interpretation of the environments is supported by the same frequencies as in the case of Y472pAzF (Fig. 2A). However, as the side chain of Y176 is not solvent-exposed, the strong H-bonding partner of the label (or the native tyrosine) needs to locate inside the protein. Therefore, candidates for the H-bonding partner(s) are the chromophore, another residue, or intramolecular water, of which

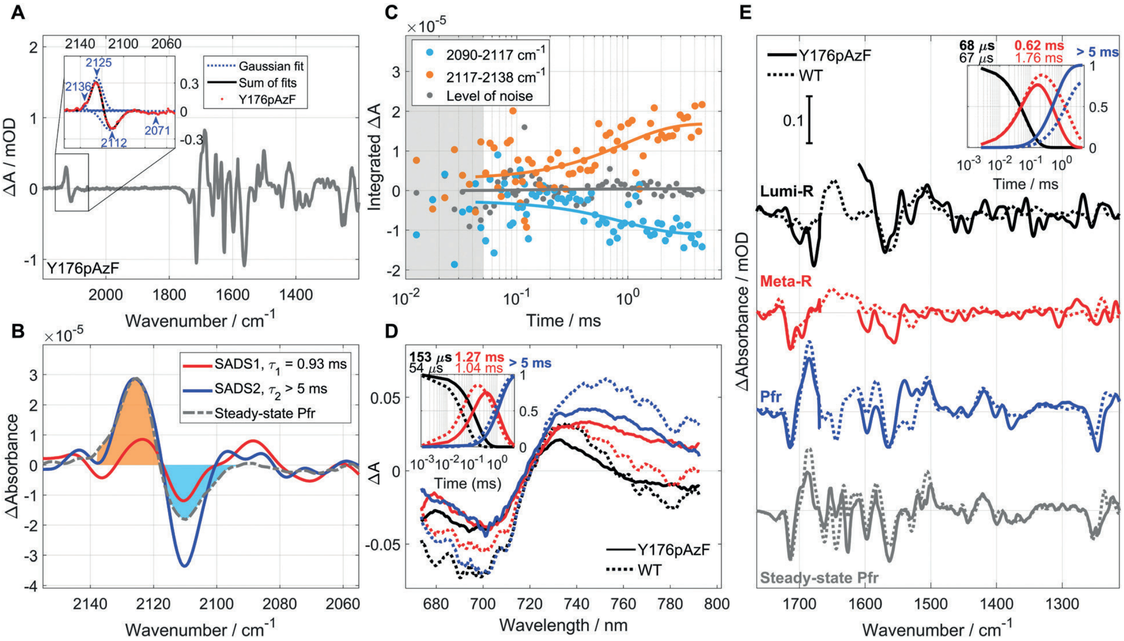

Fig. 3 Spectroscopic analysis of the Y176pAzF mutant of *Dr*BphP$_{PSM}$. (A) A prominent label signal in the Y176pAzF steady-state FTIR difference spectrum is fitted with four Gaussian bands (the inset), the maxima positions are labeled. (B) The global analysis of the pAzF signal reveals two SADS. The scaling of the steady-state spectrum is the same as in (E). (C) Kinetics of the integrated spectral signal of the label (dots) and their multiexponential fit (line) with the time constants given in (B). The grey dots indicate the noise level (Fig. S7B, ESI†), and the grey background the time frame with high noise level. (D) The flash photolysis SADS after global analysis with the resulting time constants, Y176pAzF (bold) and WT (dotted). (E) Global analysis in the FTIR fingerprint region of Y176pAzF *vs.* WT. The data at 1610–1670 cm^{-1} is discarded due to dominating water absorption. The insets in (D) and (E) show the concentration fractions of the three different components.

the latter would most probably offer the strongest H-bonding in agreement with the azide frequency.

In the time-resolved data, the global analysis of the label region reveals only one intermediate, Meta-R, between Pr and Pfr of the label (Fig. 3B). The lifetime of the Meta-R state is 0.93 ms. We interpret this finding as a change in the microenvironment that takes place only in the transition from the Pr to the Meta-R state, and then further to the Pfr state. The SADS signals have similar lineshapes in the transition from Pr to Meta-R and from Meta-R to Pfr, which suggests that the events in the microenvironment of Y176pAzF are a step-wise process.

The shift of the label frequency starts to appear with a larger amplitude only at around 300 μs, long after the decay of the Lumi-R state (Fig. 3C). Therefore, the formation of the new H-bond between the residue and the environment is locked in the Meta-R → Pfr transition. We note that the label signal does not reach its final state during the experimental time window of 4.7 ms. In particular, the ratio of the positive and negative band of the label does not match between the step-scan and steady-state Pfr difference spectra, but shows additional positive features in the step-scan spectrum below 2100 cm^{-1} (Fig. 3B). It is thus likely that once an amino acid responsible for stabilizing the Pfr state is modified, the final equilibration takes longer than the time window of our experiment. In contrast, the results from flash photolysis indicate that the Pr to Pfr conversion of BV is already completed within 5 ms (Fig. S9, ESI†), which indicates that a late relaxation process takes place close to the label that does not affect the BV.

The global analyses of the Y176pAzF fingerprint region from the time-resolved FTIR experiments and of the visible region from flash photolysis reveal that the photocycle of the mutant proceeds *via* two intermediates, Lumi-R and Meta-R (Fig. 3D and E). As observed by time-resolved FTIR, the Lumi-R state in Y176pAzF and WT and decays with identical time constants (Fig. 3E). In the visible, the Lumi-R and Meta-R intermediates of the Y176pAzF decay slower than in the WT (Fig. 3D). Accordingly, the label appears to slow down the Lumi-R decay from the perspective of the chromophore, in a similar way as in Y472pAzF. In contrast, the time-resolved FTIR shows an almost three times shorter lifetime for Meta-R of the mutant than that of the WT (Fig. 3E).

The spectral character along the photocycle clearly deviates between Y176pAzF and WT (Fig. 3D and E). The flash photolysis and steady-state UV-vis spectra of Y176pAzF reveal that the mutant converts between Pr and Pfr, but as the spectra differ from those of the WT, the label alters the environment of BV in the binding pocket (Fig. S3, ESI†). Focusing on the FTIR features, notable differences are detected already in the Lumi-R intermediate. The negative 1714 cm^{-1} band in WT, assigned to the BV D-ring carbonyl vibration,[14] is visible only as a shoulder in the Lumi-R spectrum of the mutant. A negative/positive pattern at 1699(−)/1689(+) cm^{-1}, which indicates a shift of an absorption band, locates in the mutant at higher frequencies than in the WT (1689(−)/1678(+) cm^{-1}).

The Y176pAzF Lumi-R spectrum shows much larger negative bands at 1699 and 1678 cm^{-1} than in the case of the WT, which shows only a small negative signal at 1672 cm^{-1}. This feature indicates stronger changes in the water and/or protein signals compared to the WT. The negative sign implies that labeling of the Y176 changes not only the Pfr, but also the Pr structure of the protein. These prominent signals might be characterized more closely by ultrafast experiments on the Lumi-R state of Y176pAzF, which are to be performed in the future. Of note, the prominent amide II contribution of Lumi-R at 1564(−) cm^{-1} in the WT is preserved in the mutant, which reflects comparable secondary structural changes in this phase of the photocycle.

In the Meta-R spectrum, the mutant shows the characteristic but smaller positive 1730 cm^{-1} signal and the negative signal at 1712 cm^{-1}, which form the difference band assigned to the BV D-ring carbonyl group that lost the H-bond of the Pr state and has not yet formed the interactions present in the Pfr state.[5] A notable change to the WT spectrum is the presence of an amide II mode indicating secondary structural changes in the 1550 cm^{-1} region, as in the case of the WT, this region is silent in the Meta-R state.[5] At 4.7 ms, the Pfr spectrum of Y176pAzF does not yet correspond to that of the steady-state Pfr as the ratio of the D-ring carbonyl signals (1712(−)/1685(+) cm^{-1}) notably changes and the 1540 (+) cm^{-1} band at 4.7 ms is missing in the steady-state Pfr. These changes underline that the protein still undergoes changes after the experimental time window, which is in agreement with the label region of the Pfr spectra (Fig. 3B). In contrast, flash photolysis demonstrates that the chromophore completes the photocycle within 5 ms, as the last time-resolved spectrum corresponds to the steady-state UV-vis spectrum (Fig. S9B, ESI†). Hence, some late structural changes or protein relaxation processes take place independently from the chromophore.

The labeling of Y176 causes a loss of a vibrational band at 1236(−) cm^{-1} in the Pfr difference spectrum when compared to WT (Fig. 3E). This loss is clearly observed in the double difference spectrum of Y176pAzF and WT (Fig. S11, ESI†). The 1236 cm^{-1} signal is present even after $^{13}C^{15}N$ global labeling of the protein moiety,[5] which points to BV as the major origin. To verify that the signal loss is an effect of replacing the tyrosine, we included the Y176F mutant in the analysis. For Y176pAzF and Y176F, bands were observed in the double difference of Pfr at 1236 and 1234 cm^{-1}, respectively (Fig. S11, ESI†). These findings imply that the tyrosine residue plays an important role in stabilizing the BV conformation in Pfr. For both mutants, the double difference spectrum shows a positive signal at 1506 cm^{-1} and negative signals at 1529 cm^{-1} (Y176pAzF) and 1526 cm^{-1} (Y176F) (Fig. S11, ESI†). These signals might be attributed to the missing tyrosine residue as they are near the frequencies reported for νCC of the tyrosine phenyl ring.[55,56]

A closer look at the time-resolved data reveals that the 1236 cm^{-1} signal missing in Y176pAzF is clearly visible in only the Meta-R and Pfr states of the WT, but not in Lumi-R (Fig. 3E). This finding is in line with the time scales of conformational realignment determined from the label signal of Y176pAzF (Fig. 3B and C). Like the label, the native Y176 becomes active only in the Meta-R intermediate state.

3.3 The early stage action of F203pAzF is followed by accelerated Pfr formation, diminishing Meta-R

F203 is located close to the D-ring of the BV and is part of the hydrophobic pocket that stabilizes the position of the D-ring in the Pr state (Fig. 1C). According to the crystal structures obtained from *Dr*BphP$_{\mathrm{PSM}}$,[7,11] the residue is however not fully buried inside the chromophore binding domain. The phenylalanine side chain is exposed to the structurally flexible tongue region in Pr, but expected to turn away from the tongue in Pfr.[7]

In F203pAzF, the azide vibrational frequency redshifts from 2122 cm^{-1} in Pr to 2106 cm^{-1} with an additional weaker contribution at 2153 cm^{-1} in Pfr (Fig. 4A). The frequencies were confirmed with lower resolution absorbance spectra that showed similar frequencies (Fig. S6C, ESI†). As neither of the two peaks in Pfr fit to the reported pAzF frequencies,[40] it is assumed that the original Pfr signal has split symmetrically into the two observed signals because of a resonance with combinations and overtones of modes with lower frequency. For example, the νCC vibration of AzF has a frequency of 1036 cm^{-1} (according to quantum chemical calculations), so that the overtone would be slightly below 2072 cm^{-1} and could couple with the azido vibration in Pfr, if close to this frequency. In a simplified approach to reconstruct the original azido frequency, the midpoint of the observed frequencies of 2106 and 2153 cm^{-1} would be at 2129 cm^{-1}. Accordingly, such a reconstructed frequency might point to a strongly H-bonding environment in Pfr, whereas the detected signal at 2122 cm^{-1} in Pr results from a weaker/non H-bonding environment.[40]

In the global analysis of the time-resolved data, the label signal of F203pAzF needs three components (Fig. 4B). The first intermediate decays with a time constant of 35 μs and is interpreted as a Lumi-R state spectrum as discussed below in the context of the FTIR fingerprint region and the flash photolysis. The second intermediate has a time constant of 1.2 ms. In addition, the global analysis reveals that the label signal goes through an intermediate (SADS3) that has a different lineshape than the final signal in Pfr, which indicates that the label undergoes multiple processes during the photocycle rather than a single event as for Y176pAzF (Fig. 3B).

The integrated signals are followed based on the limits of the Pfr label signal (Fig. 4C). At 40 μs, the label frequency has already shifted, observed as increased integral absorption difference of both positive and negative signals. The amplitude of the signals increases up to 1 ms and then stays constant, which implies that the label senses a conformational change. However, after 4.7 ms, the amplitude at 2106 cm^{-1} increases further and the prominent signal at 2153 cm^{-1} should fully decay to match the steady-state difference spectrum. Accordingly, the label has not reached its final microenvironment within the time frame of the experiment.

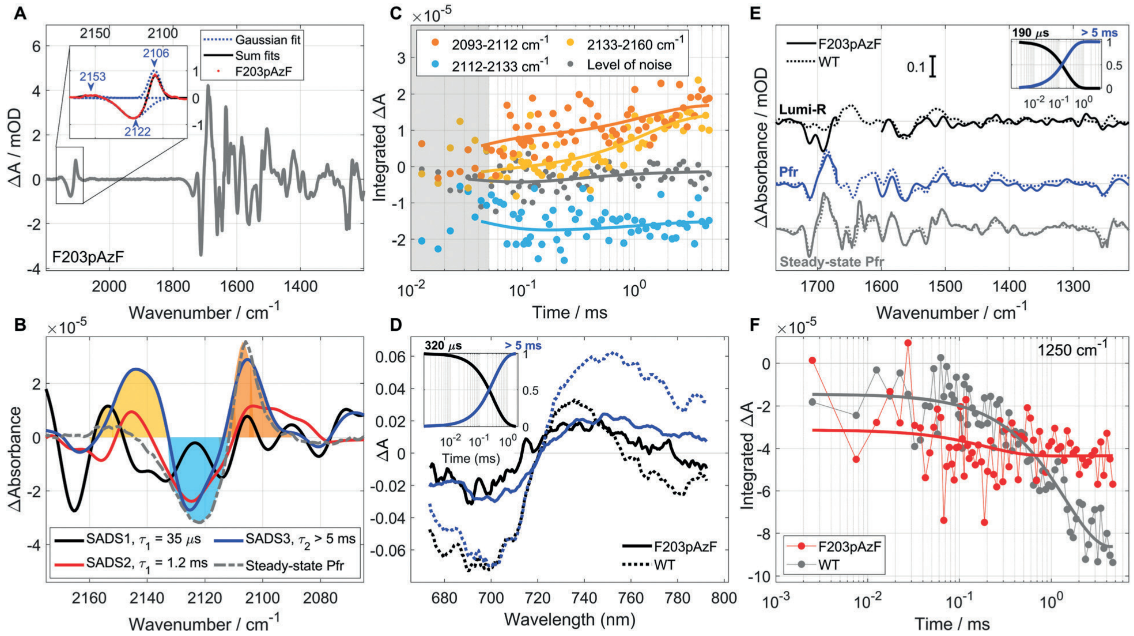

Fig. 4 Spectroscopic analysis of the F203pAzF mutant of *Dr*BphP$_{PSM}$. (A) The steady-state FTIR difference spectrum of F203pAzF shows a prominent label signal, which is fitted with three Gaussian bands and the positions of the maxima are labeled (the inset). (B) The global analysis of the label region reveals three SADS. The steady-state spectrum is scaled as in (E). (C) Kinetics of the integrated spectral signal of the label (dots) and the multiexponential fit (lines) with the time constants given in (B). The grey dots represent the noise level (Fig. S7C, ESI†) and the grey background the time frame with high noise level. (D) SADS from the global analysis of the flash photolysis for F203pAzF (bold) and WT (dotted). (E) Global analysis of step-scan FTIR data of the mutant *vs.* WT. The data at 1610–1670 cm^{-1} is discarded due to dominating water absorption. The insets in (D) and (E) show the concentration fractions of the three different components. (F) The kinetics of the 1250 cm^{-1} signal from BV (integrated at 1245–1255 cm^{-1}) of F203pAzF *vs.* WT.

The global analysis of the label revealed three SADS with very similar time constants to the WT photocycle (Fig. 4B). However, the global analysis of the F203pAzF time-resolved data of the fingerprint region reveals that the mutant skips the Meta-R intermediate, because all data can be fitted by only two components instead of three. The FTIR fingerprint region and flash photolysis reveal very similar time constants for the first intermediate with 190 μs and 320 μs, respectively (Fig. 4D and E). In the Supplementary information an alternative fit with three components is demonstrated, of which the second intermediate lacks the characteristics of Meta-R but resembles a superposition of Lumi-R and Pfr spectra (Fig. S12, ESI†). This interpretation is underlined by the kinetics of the 1250 cm^{-1} signal, which originates mainly from the BV, according to ^{13}C^{15}N labeling of the protein moiety.[5] In F203pAzF, the signal is finalized early, whereas in WT the rise starts only after hundreds of microseconds and is finalized within a few milliseconds (Fig. 4F).

Labeling of F203 leads to changes in the Lumi-R spectrum at around 1695 cm^{-1} and 1670 cm^{-1} similar to those introduced by Y176 labeling (Fig. 4E). In F203pAzF, the negative band is located at 1691 cm^{-1} and the positive at 1672 cm^{-1}. The amplitude is much stronger than in the case of WT. The large negative contribution in this region even further decreases the D-ring carbonyl signal at 1712(−) cm^{-1}. The most plausible explanation for the 1691 cm^{-1} negative signal is an H_2O molecule, either in the interior of the protein or at the protein surface, which displaces due to switching to the Lumi-R-state.

In the Pfr state, the F203pAzF mutant shows a similar steady-state FTIR difference spectrum to WT. However, the step-scan Pfr spectrum of F203pAzF differs slightly from the steady-state spectra as the A- and D-ring signals between 1680–1730 cm^{-1} reveal different amplitude ratios. In contrast, the visible absorption spectrum from flash photolysis after 5 ms resembles the final Pfr spectrum (Fig. S9, ESI†). Therefore, we interpret that the interactions chromophore are finalized to a Pfr orientation but additional changes take place after 5 ms in the label environment, similarly to the Y176pAzF mutant.

3.4 The effects of the azido group on the photocycle

The pAzF label at each studied site provides us local information on the signal propagation during the photocycle. However, the replacement of the native residues with the labeled amino acid with a strong dipole in the azido group can affect the photocycle. This effect then enlightens the role of the native residues in the photocycle. We focus on the kinetic traces at 1712(−) cm^{-1} and 1730(+) cm^{-1}, which report on the BV D-ring carbonyl signals (Fig. 5A–C), as well as on the traces at 1508(+) cm^{-1} and 1564(−) cm^{-1} to follow the secondary structural changes in the amide II region (Fig. 5D–F). The negative 1712 cm^{-1} signal evolves as the BV D-ring carbonyl moves from its H-bonding

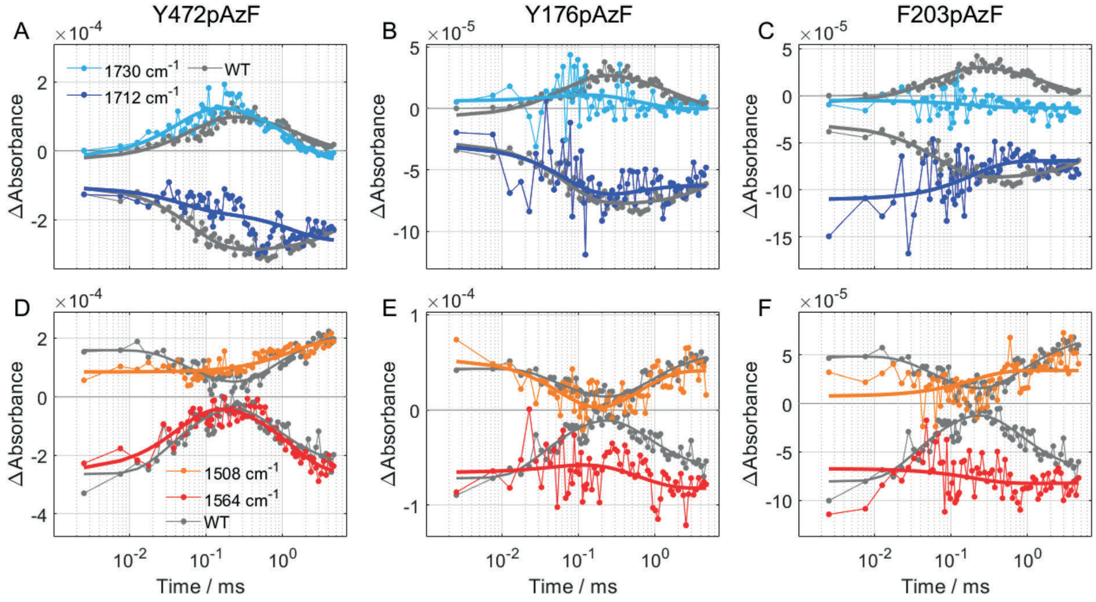

Fig. 5 Comparison of the pAzF mutants and WT signals in the BV and amide II regions. (A–C) The kinetic traces of the 1730 cm^{-1} (light blue) and 1712 cm^{-1} (blue) signals visualize the changes in the environment of the BV D-ring carbonyl in comparison to the WT (grey). (D–F) The kinetic traces of the amide II signals at 1508 cm^{-1} (orange) and 1564 cm^{-1} (red) of the mutants are compared those of the WT (grey). Fits are shown with solid lines. The time constants are given in Fig. 2–4E.

network in the Pr state *via* Lumi-R and Meta-R to that of Pfr. In Meta-R, the signal at 1730 cm^{-1} rises as characteristics of a D-ring carbonyl without H-bonding partners.[5]

In Y472pAzF, the D-ring carbonyl traces resemble those of the WT (Fig. 5A). The 1730 cm^{-1} signal rises slightly earlier than in WT in agreement with a faster Lumi-R decay in step-scan and flash photolysis. The 1712 cm^{-1} signal shows a uniform decrease in the final amplitude of the WT without the decrease and rise related to the Meta-R state. This difference is possibly due to the weaker signal at 1712 cm^{-1} in the Meta-R spectrum. Also the amide II traces are very similar in Y472pAzF and WT (Fig. 5D). The traces reveal that secondary structural changes take place already in the early phase of the photocycle but are finalized during the Meta-R to Pfr transition. This feature was also reported by the label at Y472pAzF (Fig. 2B). The photocycle of Y472pAzF follows very well the characteristics of the WT (Fig. 2D and E), which implies that either the hydroxyl group of the tyrosine is not crucial for the photocycle, or that the azido group of the label acts in a similar way to the tyrosine in its native position.

The traces of Y176pAzF follow the characteristics of the WT traces (Fig. 5B and E). The most notable difference is the lower amplitude of the 1730 cm^{-1} signal, which is explained by the lower Meta-R concentration in the mutant (Fig. 3D and E). Furthermore, the 1564 cm^{-1} trace does not decay towards Meta-R in Y176pAzF as in WT. A closer look at the amide II range of the Meta-R spectrum (Fig. 3E) reveals that the Meta-R intermediate in Y176pAzF already has characteristics of Pfr. Although Y176pAzF mostly follows the photocycle of WT, the data demonstrate that the native tyrosine stabilizes the Meta-R state of the protein because the insertion of the label suppresses the Meta-R features.

Contrary to the other mutants, the replacement of F203 with pAzF causes more notable changes in the photocycle. The 1730 cm^{-1} trace does not reveal any significant positive contribution in F203pAzF (Fig. 5C) in agreement with the fact that the global analysis does not show a recognizable Meta-R intermediate (Fig. 4E and Fig. S12, ESI†). The 1564 cm^{-1} trace behaves similarly for F203pAzF as for Y176pAzF, in which the Meta-R is suppressed (Fig. 5E and F). However, the biggest difference compared to the WT is observed in the 1712 cm^{-1} trace that in F203pAzF already has a high intensity during the first microseconds of the photocycle and then decays towards Pfr. This finding indicates that by addition of the azide moiety, the Lumi-R conformation of the chromophore is different than in WT. Furthermore, the F203 residue seems to act like a gatekeeper that forces the protein to the Meta-R intermediate. The large dipole moment of the azide group might guide the residue to a different position than in WT, which prevents F203 from fulfilling its role in the photocycle. We would like to stress that F203pAzF finally forms a photostable Pfr state, which, however, is slightly different from the WT Pfr both in terms of the steady-state UV-vis and FTIR difference spectra (Fig. S2 and S4, ESI†).

4 Discussion

4.1 Insights from the labels into the mechanism of phytochromes

Phytochromes undergo a complex photoconversion from Pr to Pfr state upon red light excitation. In the beginning of the photocycle, the chromophore binding pocket is the hotspot of action as the whole process is triggered by the isomerization of the BV D-ring. Here, photoinduced changes in three different positions, Y472 in the tongue and Y176 and F203 near the isomerizing BV D-ring, were followed by replacing the residues with the sensitive IR-probe pAzF. We were able to record the changes in the local environment of these labels in a time-resolved manner and thus deduce the time span of action of each residue during the photocycle. The response at the three positions to the photoconversion of BV is summarized in Fig. 6A, in which the coloring of the circles highlights changes during the lifetime of the two intermediates Lumi-R and Meta-R, the photoproduct Pfr and events taking place after the experimental time window of 5 ms.

We note that according to flash photolysis, the three mutants finalize the photocycle within 5 ms, detected as a vis-to-far-red signal from the chromophore. Nevertheless, both of the labels in the chromophore binding pocket report on changes taking place over tens of milliseconds (Fig. 3B and 4B). Many other (bacterio)phytochromes such as Cph1 and Agp1[57,58] show a more complex photocycle with a split Meta-R state (Meta-Ra and Meta-Rc), of which the lifetime of the Meta-Rc state is even hundreds of milliseconds. The associated proton release-uptake event has not been reported for *Dr*BphP and therefore, the lifetime of the photocycle is only in the order of few to tens of milliseconds.[4] Still, large-scale changes of the *Dr*BphP$_{PSM}$ protein occur in the time-range of tens of milliseconds as detected by X-ray scattering.[4] The late signals from the labels underline the multi-dimensional nature of the photocycle: the photoconversion processes on different levels (tiers) of the protein are only partially coupled.[45,59] Thus, the Pr or Pfr state can be reached in the chromophore even though in other sections the protein is still in the non-equilibrium state.

Y472pAzF allowed us to follow the reorganization of the tongue. We show that the tongue is in action already in the early phase (Fig. 2) and that the response continues until the end of the photocycle. Importantly, the changes in the tongue end at the same time as the chromophore finishes its photocycle underlining the tight connection of the tongue to the chromophore. The photocycle of the Y472pAzF mutant appears to be very similar to that of the WT (Fig. 2D, E, Fig. S4 and S2, ESI†). Moreover, the label signal (Fig. 6B) propagates in a similar manner as the secondary structural changes during the photocycle (Fig. 5D), which further underlines the labels effectiveness in reporting the events in the refolding tongue.

The label Y176pAzF revealed that the residue forms a strong H-bond in the Pfr state (Fig. 3A and B). The observed frequency for Y176pAzF is the same as for the solvent-exposed Y472pAzF. However, Y176 is buried and not in direct contact with solvent waters. Instead, upon photoconversion it turns away from the hydrophobic pocket in Pr towards the BV C-ring propionate (Fig. 1C). As the propionate cannot form an H-bond with pAzF and based on the observed frequencies, we propose that the H-bonding partner is an intramolecular water positioned between Y176 and the C-ring propionate. This, however, remains to be validated in future studies. The residue becomes active only in the late phase of the photocycle (Fig. 3B and C) as reflected in both the label and the tyrosine signals. Therefore, Y176 most probably has a preparative role in the photocycle within the chromophore binding pocket, and the H-bond remains as a part of the network stabilizing the Pfr conformation, possibly *via* the propionate.

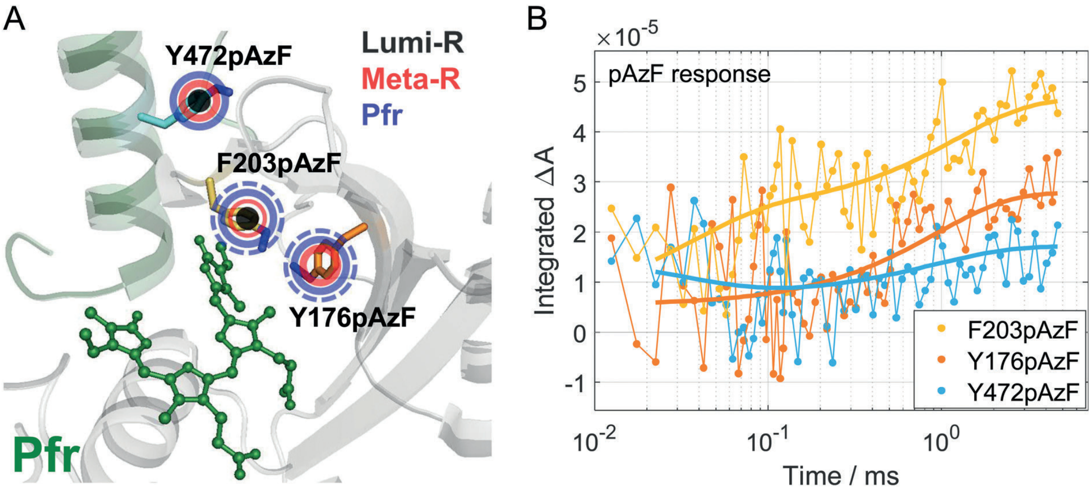

Fig. 6 The contribution of the pAzF labeled positions to the photoconversion of the *Dr*BphP$_{PSM}$ *via* its intermediate states. (A) The phases in the photocycle with label responses at respective sites are highlighted with colored circles. At positions Y472 and F203, the label responds during the first tens of microseconds of the photoconversion (Lumi-R, black). At Y176, the label responds later in the slower phase (Meta-R, red). In F203pAzF, the Meta-R state is observable in the label but not in the chromophore, therefore a thin red line. In Y176pAzF and F203pAzF, further changes for Pfr equilibration take place after 5 ms (blue dashed ring). (B) The integrated (from 2100 to 2160 cm^{-1}) label signal is shown together with fits (solid lines). The time constants are presented in Fig. 2–4C.

F203 is a hydrophobic residue unable to form H-bonds to the side chain and thus differs from pAzF. F203 offers a hydrophobic pocket for the D-ring during the photocycle. The time-resolved IR spectra of the fingerprint region underline the differences between the native residue and pAzF. The importance of phenylalanine in this position for the formation of the Meta-R intermediate becomes apparent, as the label in this position disables the formation of the conventional Meta-R state (Fig. 4E and Fig. S12, ESI†). As an explanation for this finding we offer the following. In Pfr, the positive signal at 1685 cm^{-1} originates from the interaction between the BV D-ring carbonyl and H201.[5] In Meta-R of the WT, the BV D-ring is already in its Pfr orientation, but H201 has not yet flipped to form the interaction because F203 is hindering its movement. As a result, the lack of an H-bond to the D-ring carbonyl causes the upshift to 1730 cm^{-1} in Meta-R.[5,45] As the azido group is added to F203, the natively hydrophobic residue gains polarity and hence, F203pAzF does not hinder the H201 movement in the transition towards Pfr. In conclusion, the pAzF label at F203 suppresses an intermediate in the formation of the new protein-chromophore interactions of Pfr, which explains why the global analyses of both flash photolysis and time-resolved FTIR data reveal only two components for the photocycle.

4.2 Time-resolved spectroscopy using IR probes

FTIR difference spectroscopy has the benefit of yielding information on the global protein mechanism in solution using the fingerprint region while at the same time using the signal around 2100 cm^{-1} to report on site-specific changes in the label environment.[24] Azidophenylalanine is superior to other probes due to its high extinction coefficient. Moreover, the shifts of the pAzF freqency reliably report on the H-bonding strength to the label.[41] However, two other aspects of the interpretation of the pAzF signal are challenging. First, the azide vibrations respond to the (a)polarity of the environment inconsistently and with very minor shifts.[40] Solvatochromic models of the azidophenyl vibrations have been built,[38,41] but rather underline the complexity of its influence on the vibrational frequency, and work better for nitrile probes.[60–62] Secondly, the pAzF signal is accompanied by Fermi resonance bands, which complicate the lineshape and thus the interpretation of the pAzF signal.[41,47] This complication is exemplified by the interpretation of the Pfr signal of the F203pAzF mutant (Fig. 4B). Lipkin *et al.*[63] managed to considerably reduce the Fermi resonances by isotope labeling of the middle and terminal nitrogen of the azido group. Zhang *et al.*[47] proposed instead to modulate the Fermi resonances by changing the azide position from *para* to *meta*. In contrast, the Fermi resonance bands of azido probes might be utilized to yield further information. In cyano probes, the underlying coupling constant of the Fermi resonances is an indicator of the H-bonding status of the CN-group.[64] Probably, the H-bonding status of the azido probe effects the Fermi resonance bands as well. Our findings might motivate further studies on the understanding of the Fermi resonances of azide signals in different environments, as it has been progressed for many other vibrational modes,[65] to utilize the full potential of the azido probes.

The azide vibrational frequency is tuned by the H-bonding strength of the microenvironment,[40,41] which allows for the detection of structural and conformational changes. Here, we mainly concentrate on residues that have a phenyl ring in the side chain and act as key residues in the photocycle. For example, F203pAzF indicates the importance of the native residue while providing site-specific information on the photoconversion process. However, other residues are also accessible, as demonstrated successfully for R228pAzF (Fig. S5A, ESI†). Therefore, in future trials the selection of positions should be extended to sites expected to be close to the action but without a key role in the photoconversion, as demonstrated by the Hamm group.[29] As the pAzF label has proven itself as a successful tool for the investigation of site-specific changes in a time-resolved manner, the label will be applied to the dimeric interface as well as to output domain to study the time scales of signal transduction.

To conclude, by utilizing the vibrational probe pAzF inserted into a phytochrome we obtained the site-selective signal propagation by means of both steady-state and time-resolved IR spectroscopy in the micro- to millisecond time scale. To some extent a concerted signal propagation between the protein and the chromophore is observed, in particular in the tightly linked tongue region. In contrast, other sites nearby the chromophore show individual time scales (dimensions), as reflected in extended equilibration times with respect to those of the chromophore, or in a lack of particular intermediate states. Our results demonstrate that pAzF is a reliable probe for time-resolved IR spectroscopy, and this approach opens a door to study protein movements in real time at ambient conditions and in solution.

Conflicts of interest

There are no conflicts to declare.

Acknowledgements

We thank Peter Hamm and Olga Bozovic for important discussions regarding IR labels, Valentyna Kuznetsova for the help with the data-analysis program, and Rahul Nanekar for preliminary FTIR experiments. The original plasmids for this work were a kind gift of Richard Vierstra and Katrina Forest (pET21b) and Peter Schultz (pEVOL-pAzF). We thank Prof. Thomas O'Haver for the script of the interactive peak fitter. The work of BS-B has been supported by a grant from the Swiss National Science Foundation (P2ZHP2_164991). JAI acknowledges the Academy of Finland (296135 and 332742) and the Jane and Aatos Erkko foundation. HT acknowledges the Academy of Finland (285461 and 330678). LS acknowledges a fellowship of the Studienstiftung des Deutschen Volkes. TK acknowledges a Heisenberg fellowship of the Deutsche Forschungsgemeinschaft (KO3580/4-2).

Notes and references

1 N. C. Rockwell, Y.-S. Su and J. C. Lagarias, *Annu. Rev. Plant Biol.*, 2006, **57**, 837–858.

2 E. S. Burgie, T. Wang, A. N. Bussell, J. M. Walker, H. Li and R. D. Vierstra, *J. Biol. Chem.*, 2014, **289**, 24573–24587.

3 R. A. Sharrock, *Genome Biol.*, 2008, **9**, 230.

4 A. Björling, O. Berntsson, H. Lehtivuori, H. Takala, A. J. Hughes, M. Panman, M. Hoernke, S. Niebling, L. Henry, R. Henning, I. Kosheleva, V. Chukharev, N. V. Tkachenko, A. Menzel, G. Newby, D. Khakhulin, M. Wulff, J. A. Ihalainen and S. Westenhoff, *Sci. Adv.*, 2016, **2**, e1600920.

5 J. A. Ihalainen, E. Gustavsson, L. Schroeder, S. Donnini, H. Lehtivuori, L. Isaksson, C. Thöing, V. Modi, O. Berntsson, B. Stucki-Buchli, A. Liukkonen, H. Häkkänen, E. Kalenius, S. Westenhoff and T. Kottke, *J. Am. Chem. Soc.*, 2018, **140**, 12396–12404.

6 J. R. Wagner, J. S. Brunzelle, K. T. Forest and R. D. Vierstra, *Nature*, 2005, **438**, 325–331.

7 E. S. Burgie, J. Zhang and R. D. Vierstra, *Structure*, 2016, **24**, 448–457.

8 J. J. van Thor, K. L. Ronayne and M. Towrie, *J. Am. Chem. Soc.*, 2007, **129**, 126–132.

9 Y. Yang, M. Linke, T. Von Haimberger, J. Hahn, R. Matute, L. González, P. Schmieder and K. Heyne, *J. Am. Chem. Soc.*, 2012, **134**, 1408–1411.

10 E. Claesson, W. Y. Wahlgren, H. Takala, S. Pandey, L. Castillon, V. Kuznetsova, L. Henry, M. Panman, M. Carrillo, J. Kübel, R. Nanekar, L. Isaksson, A. Nimmrich, A. Cellini, D. Morozov, M. Maj, M. Kurttila, R. Bosman, E. Nango, R. Tanaka, T. Tanaka, L. Fangjia, S. Iwata, S. Owada, K. Moffat, G. Groenhof, E. A. Stojković, J. A. Ihalainen, M. Schmidt and S. Westenhoff, *eLife*, 2020, **9**, e53514.

11 H. Takala, A. Björling, O. Berntsson, H. Lehtivuori, S. Niebling, M. Hoernke, I. Kosheleva, R. Henning, A. Menzel, J. A. Ihalainen and S. Westenhoff, *Nature*, 2014, **509**, 245–248.

12 C. Song, G. Psakis, C. Lang, J. Mailliet, W. Gärtner, J. Hughes, J. Matysik and C. J. Lagarias, *Proc. Natl. Acad. Sci. U. S. A.*, 2011, **108**, 3842–3847.

13 C. Song, T. Rohmer, M. Tiersch, J. Zaanen, J. Hughes and J. Matysik, *Photochem. Photobiol.*, 2013, **89**, 259–273.

14 H. Foerstendorf, C. Benda, W. Gärtner, M. Storf, H. Scheer and F. Siebert, *Biochemistry*, 2001, **40**, 14952–14959.

15 J. J. Van Thor, N. Fisher and P. R. Rich, *J. Phys. Chem. B*, 2005, **109**, 20597–20604.

16 N. Lenngren, P. Edlund, H. Takala, B. Stucki-Buchli, J. Rumfeldt, I. Peshev, H. Häkkänen, S. Westenhoff and J. A. Ihalainen, *Phys. Chem. Chem. Phys.*, 2018, **20**, 18216–18225.

17 H. Takala, S. Niebling, O. Berntsson, A. Björling, H. Lehtivuori, H. Häkkänen, M. Panman, E. Gustavsson, M. Hoernke, G. Newby, F. Zontone, M. Wulff, A. Menzel, J. A. Ihalainen and S. Westenhoff, *Struct. Dyn.*, 2016, **3**, 12.

18 A. Takiden, F. Velazquez-Escobar, J. Dragelj, A. L. Woelke, E.-W. Knapp, P. Piwowarski, F. Bart, P. Hildebrandt and M. A. Mroginski, *Photochem. Photobiol.*, 2017, **93**, 713–723.

19 S. Ye, T. Huber, R. Vogel and T. P. Sakmar, *Nat. Chem. Biol.*, 2009, **5**, 397–399.

20 A. Creon, I. Josts, S. Niebling, N. Huse and H. Tidow, *Struct. Dyn.*, 2018, **5**, 12.

21 K. L. Koziol, P. J. M. Johnson, B. Stucki-Buchli, S. A. Waldauer and P. Hamm, *Curr. Opin. Struct. Biol.*, 2015, **34**, 1–6.

22 J. Ma, I. M. Pazos, W. Zhang, R. M. Culik and F. Gai, *Annu. Rev. Phys. Chem.*, 2015, **66**, 357–377.

23 H. Kim and M. Cho, *Chem. Rev.*, 2013, **113**, 5817–5847.

24 L. Blankenburg, L. Schroeder, F. Habenstein, B. Błasiak, T. Kottke and J. Bredenbeck, *Phys. Chem. Chem. Phys.*, 2019, **21**, 6622–6634.

25 K.-I. Oh, J.-H. Lee, C. Joo, H. Han and M. Cho, *J. Phys. Chem.*, 2008, **112**, 10352–10357.

26 C. C. Liu and P. G. Schultz, *Annu. Rev. Biochem.*, 2010, **79**, 413–444.

27 H. Taskent-Sezgin, J. Chung, P. S. Banerjee, S. Nagarajan, R. B. Dyer, I. Carrico and D. P. Raleigh, *Angew. Chem., Int. Ed.*, 2010, **49**, 7473–7475.

28 C. G. Bazewicz, M. T. Liskov, K. J. Hines and S. H. Brewer, *J. Phys. Chem. B*, 2013, **117**, 8987–8993.

29 B. Stucki-Buchli, P. J. M. Johnson, O. Bozovic, C. Zanobini, K. L. Koziol, P. Hamm, A. Gulzar, S. Wolf, S. Buchenberg and G. Stock, *J. Phys. Chem. A*, 2017, **121**, 9435–9445.

30 C. R. Hall, J. Tolentino Collado, J. N. Iuliano, A. A. Gil, K. Adamczyk, A. Lukacs, G. M. Greetham, I. Sazanovich, P. J. Tonge and S. R. Meech, *J. Phys. Chem. B*, 2019, **123**, 9592–9597.

31 B. S. Krause, J. C. D. Kaufmann, J. Kuhne, J. Vierock, T. Huber, T. P. Sakmar, K. Gerwert, F. J. Bartl and P. Hegemann, *Biochemistry*, 2015, **58**, 1275–1286.

32 S. Ye, E. Zaitseva, G. Caltabiano, G. F. X. Schertler, T. P. Sakmar, X. Deupi and R. Vogel, *Nature*, 2010, **464**, 1386–1389.

33 M. C. Thielges, J. Y. Axup, D. Wong, H. S. Lee, J. K. Chung, P. G. Schultz and M. D. Fayr, *J. Phys. Chem. B*, 2011, **115**, 11294–11304.

34 C. Zanobini, O. Bozovic, B. Jankovic, K. L. Koziol, P. J. M. Johnson, P. Hamm, A. Gulzar, S. Wolf and G. Stock, *J. Phys. Chem. B*, 2018, **122**, 10118–10125.

35 J. W. Chin, S. W. Santoro, A. B. Martin, D. S. King, L. Wang and P. G. Schultz, *J. Am. Chem. Soc.*, 2002, **124**, 9026–9027.

36 T. S. Young, I. Ahmad, J. A. Yin and P. G. Schultz, *J. Mol. Biol.*, 2010, **395**, 361–374.

37 R. Adhikary, J. Zimmermann and F. E. Romesberg, *Chem. Rev.*, 2017, **117**, 1927–1969.

38 J. H. Choi, K. I. Oh and M. Cho, *J. Chem. Phys.*, 2008, **129**, 174512.

39 X. S. Gai, B. A. Coutifaris, S. H. Brewer and E. E. Fenlon, *Phys. Chem. Chem. Phys.*, 2011, **13**, 5926–5930.

40 M. Maj, C. Ahn, B. Błasiak, K. Kwak, H. Han and M. Cho, *J. Phys. Chem. B*, 2016, **120**, 10167–10180.

41 M. P. Wolfshorndl, R. Baskin, I. Dhawan and C. H. Londergan, *J. Phys. Chem. B*, 2012, **116**, 1172–1179.

42 W. Uhmann, A. Becker, C. Taran and F. Siebert, *Appl. Spectrosc.*, 1991, **45**, 390–397.

43 M. E. Auldridge, K. A. Satyshur, D. M. Anstrom and K. T. Forest, *J. Biol. Chem.*, 2012, **287**, 7000–7009.

44 H. Takala, A. Björling, M. Linna, S. Westenhoff and J. A. Ihalainen, *J. Biol. Chem.*, 2015, **290**, 16383–16392.

45 H. Takala, H. K. Lehtivuori, O. Berntsson, A. Hughes, R. Nanekar, S. Niebling, M. Panman, L. Henry, A. Menzel, S. Westenhoff and J. A. Ihalainen, *J. Biol. Chem.*, 2018, **293**, 8161–8172.

46 M. M. Waegele, R. M. Culik and F. Gai, *J. Phys. Chem. Lett.*, 2011, **2**, 2598–2609.

47 J. Zhang, L. Wang, J. Zhang, J. Zhu, X. Pan, Z. Cui, J. Wang, W. Fang and Y. Li, *J. Phys. Chem. B*, 2018, **122**, 8122–8133.

48 J. J. Snellenburg, S. P. Laptenok, R. Seger, K. M. Mullen and I. H. M. van Stokkum, *J. Stat. Softw.*, 2012, **49**, 1–22.

49 E. Gustavsson, L. Isaksson, C. Persson, M. Mayzel, U. Brath, L. Vrhovac, J. A. Ihalainen, G. Karlsson, V. Orekhov and S. Westenhoff, *Biophys. J.*, 2020, **118**, 415–421.

50 Q.-Z. Xu, L. Goett-Zink, W. Gärtner, K.-H. Zhao and T. Kottke, *Biochemistry*, 2020, **59**, 2047–2054.

51 J. Kübel, M. Chenchiliyan, S. A. Ooi, E. Gustavsson, L. Isaksson, V. Kuznetsova, J. A. Ihalainen, S. Westenhoff and M. Maj, *Phys. Chem. Chem. Phys.*, 2020, **22**, 9195–9203.

52 I. H. van Stokkum, D. S. Larsen and R. van Grondelle, *Biochim. Biophys. Acta, Bioenerg.*, 2004, **1657**, 82–104.

53 T. Kottke, V. A. Lórenz-Fonfría and J. Heberle, *J. Phys. Chem. B*, 2017, **121**, 335–350.

54 J. R. Wagner, J. Zhang, D. von Stetten, M. Günther, D. H. Murgida, M. A. Mroginski, J. M. Walker, K. T. Forest, P. Hildebrandt and R. D. Vierstra, *J. Biol. Chem.*, 2008, **283**, 12212–12226.

55 A. Barth, *Biochim. Biophys. Acta, Bioenerg.*, 2007, **1767**, 1073–1101.

56 R. Takahashi, K. Okajima, H. Suzuki, H. Nakamura, M. Ikeuchi and T. Noguchi, *Biochemistry*, 2007, **46**, 6459–6467.

57 J. J. Van Thor, B. Borucki, W. Crielaard, H. Otto, T. Lamparter, J. Hughes, K. J. Hellingwerf and M. P. Heyn, *Biochemistry*, 2001, **40**, 11460–11471.

58 B. Borucki, D. Von Stetten, S. Seibeck, T. Lamparter, N. Michael, M. A. Mroginski, H. Otto, D. H. Murgida, M. P. Heyn and P. Hildebrandt, *J. Biol. Chem.*, 2005, **280**, 34358–34364.

59 H. Takala, P. Edlund, S. Ihalainen and J. A. Westenhoff, *Photochem. Photobiol. Sci.*, 2020, **19**, 1488–1510.

60 S. Bagchi, S. D. Fried and S. G. Boxer, *J. Am. Chem. Soc.*, 2012, **134**, 10373–10376.

61 L. J. G. W. van Wilderen, D. Kern-Michle, H. Müller-Werkmeister and J. Bredenbeck, *Phys. Chem. Chem. Phys.*, 2014, **16**, 19643–19653.

62 W. Zhang, B. N. Markiewicz, R. S. Doerkse, A. B. Smith and F. Gai, *Phys. Chem. Chem. Phys.*, 2016, **18**, 7027–7034.

63 J. S. Lipkin, R. Song, E. E. Fenlon and S. H. Brewer, *J. Phys. Chem. Lett.*, 2011, **2**, 1672–1676.

64 J. M. Rodgers, R. M. Abaskharon, B. Ding, J. Chen, W. Zhang and F. Gai, *Phys. Chem. Chem. Phys.*, 2017, **19**, 16144–16150.

65 S. D. Fried and S. G. Boxer, *Acc. Chem. Res.*, 2015, **48**, 998–1006.

Electronic Supplementary Material (ESI) for Physical Chemistry Chemical Physics.
This journal is © the Owner Societies 2021

Supporting information for Site-by-site tracking of signal transduction in an azidophenyalanine-labeled bacteriophytochrome with step-scan FTIR spectroscopy

Moona Kurttila,† Brigitte Stucki-Buchli,† Jessica Rumfeldt,† Lea Schroeder,‡ Heikki Häkkänen,† Alli Liukkonen,† Heikki Takala,† Tilman Kottke,*,‡ and Janne A. Ihalainen*,†

†University of Jyväskylä, Nanoscience Center, Department of Biological and Environmental Science, 40014 Jyväskylä, Finland
‡Physical and Biophysical Chemistry, Department of Chemistry, Bielefeld University, Universitätsstr. 25, 33615 Bielefeld, Germany

E-mail: tilman.kottke@uni-bielefeld.de; janne.ihalainen@jyu.fi

The hunger games - nine label positions

On top of the three mutants, Y472pAzF, Y176pAzF, and F203pAzF, we labeled six addi- tional structurally interesting positions, shown in Figure S1, with pAzF. Y263 is located in the BV binding pocket and has been shown to be important for the photoconversion process, especially regarding the BV-tongue interactions.[1,2] F469 was selected as a second position in the tongue with Y472. R228 and S257 are located in the so-called knot of the phytochrome; a region of PAS domain goes through a loop in the GAF domain forming a knot structure that has been suggested to be, on some level, important for the photoactivation process.[3] Y307 is located in the dimeric interface of the phytochrome. Even though we used the monomeric form of the protein, we wanted to see if the Y307 goes through structural changes induced by the monomer. F372 is located in the PHY domain, away from the tongue region, where no local changes in the structure are expected. The idea was to see the effect of the unnatural amino acid on the protein in presumably non-functional region.

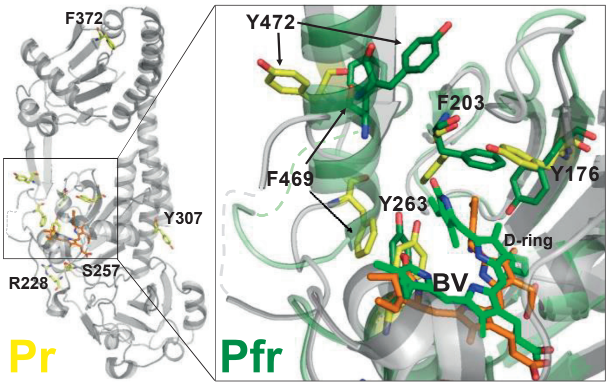

Figure S1: The nine selected label positions in the *Dr*BphP PSM Nine residues from different locations of the phytochrome PSM were selected for labeling. R228 and S257 are located in the GAF-domain part that forms a knot with the PAS domain, Y307 is located in the dimerization interface, and Y372 in the PHY domain. Residues, in which the position changes drastically according to the crystal structure, are shown in Pr and Pfr conformation in the inset. Y176, F203 and Y263 locate in the BV binding pocket close to the isomerizing D-ring, and F469 and Y472 in the 'tongue' that changes its secondary structure during the photoconversion.

All nine mutants were expressed successfully, and the yield of the purified protein varied from 1.1 to 40.6 mg per 500 mL expression between the mutants (Table S1). We evaluated the functionality and stability of the mutants by UV-vis and FTIR spectroscopy. Last, the signal of the label was analyzed from the mutants in which it was detected and signal-to-noise ratio was sufficient for the analysis. The aim was to find suitable mutants for the step-scan experiment, and the results of the most successful mutants are introduced in the main text. However, we also want to share the results from the journey as they reveal something about the inner dynamics of the phytochrome.

Table S1: All nine mutants and how far their usage and analysis could be taken.

Mutant	Yield (mg)*	UV-vis analysis	FTIR analysis	Label signal shifts	Potential for step-scan FTIR
Y372pAzF	1.1	no			
F469pAzF	7.4	yes	no		
S257pAzF	4.9	yes	no		
Y307pAzF	40.6	yes	yes	no	
Y263pAzF	20.0	yes	yes	yes***	no
R228pAzF	12.7	yes	yes	yes	no
Y472pAzF	14.3	yes	yes	yes	yes
Y176pAzF	10.6	yes	yes	yes	yes
F203pAzF	32.0**	yes	yes	yes	yes

* From 500 mL protein expression

** Calculated from 2000 ml expression

*** Amplitude of the label signal was too low/noisy for further analysis

The yield of Y372pAzF was significantly smaller than in other mutants (Table S1), and the SDS-PAGE gel (not shown) revealed that most of the protein aggregated during the purification process. In conclusion, the label drastically disturbed the folding stability of the protein in this position. Further analysis of the crystal structure showed us that the residue is surrounded by hydrophobic residues, and the introduction of the charged pAzF inhibited the formation of the crucial interactions. Further, as shown by R228pAzF, the labeled residue to be replaced does not necessarily need to have native phenyl ring.

The functionality of the labeled *Dr*BphP$_{PSM}$, i.e. their ability to photoconvert reversibly between Pr and Pfr, was assessed by measuring the UV-vis absorption spectra of the dark and illuminated photoproducts. Here, especially the comparison of the measured Q-bands to the unlabeled *Dr*BphP$_{PSM}$,[4,5] was used to estimate the proper functioning of the constructs. A700/A280 ratio was used to estimate the amount of Pr (i.e. bound BV in a correct proto- nation form) compared to the protein.[2] A750/A700 ratio was used to estimate the relative amount of Pfr in the red illuminated spectra, although the used methods do not allow deter- mination of the actual Pfr ratio. Further, the protein structural states can occur in similar amounts compared to the unlabeled protein even though the absorption spectrum does not indicate a “prototypical” Pfr state. This is because the absorption properties of the BV in Pfr state also depend on its surroundings.[6]

The labeled constructs Y472pAzF, R228pAzF, Y307pAzF and F203pAzF functioned in a similar way to the unlabeled *Dr*BphP (not shown) (Fig S2). They have the Pr and Pfr states with maxima positions at about 700 and 750 nm, respectively and similar A700/A280 ratio in the dark state, i.e. >1, except for Y472pAzF and F203pAzF with 0.99 and 0.95, respectively, which can also result from short light exposure as the A700/A280 ratio is very sensitive to light conditions.[4] Their relative amount of Pfr in the light spectra (A750/A700 ratio), were the same, 1.22-1.25, reported to *Dr*BphP PSM by Takala *et al.*,[4] except for 0.93 in F203pAzF.

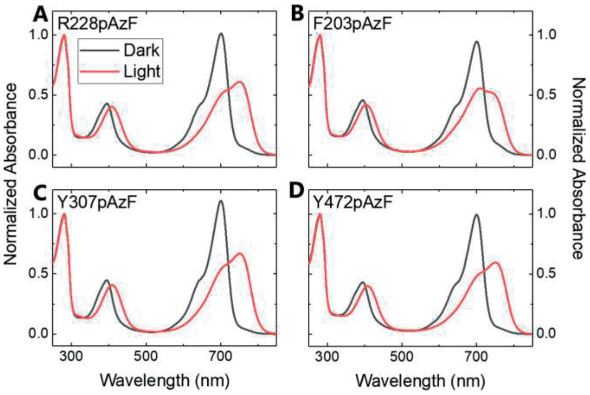

Figure S2: UV-vis absorption spectra of pAzF mutants resembling WT spectrum. Here are shown the UV-vis spectra of four mutants in dark (Pr spectrum, in black) and after red light (660 nm) illumination (in red). A) R228pAzF, B) F203pAzF, C) Y302pAzF, and D) Y472pAzF. All shown spectra resemble the WT spectra,[7] and Y307pAzF the best as it has the A_{700}/A_{280} ratio of 1.1.

In Y176pAzF, Y263pAzF, S257pAzF, and F469pAzF, the label disturbed the photoconversion of the protein (Fig. S3). The Pfr maxima positions are blueshifted from 750 nm, and the A750/A700 ratios are below 1. In the positions close to the BV, Y176 and Y263, the label or absence of the original residue inhibited the full conversion to Pfr, which was observed as the large ratio of Pr in the red illuminated spectra. The two states are however clearly distinguishable and determined Pfr maxima are at 737 and 746 nm in Y176pAzF and Y263pAzF, respectively. The relative Pfr amount was smaller than reported for the unlabeled construct, in Y176pAzF and Y263pAzF only about half of the reported values (Table 3). In Y263pAzF the A700/A280 ratio was 0.92 and in Y176pAzF 0.7.

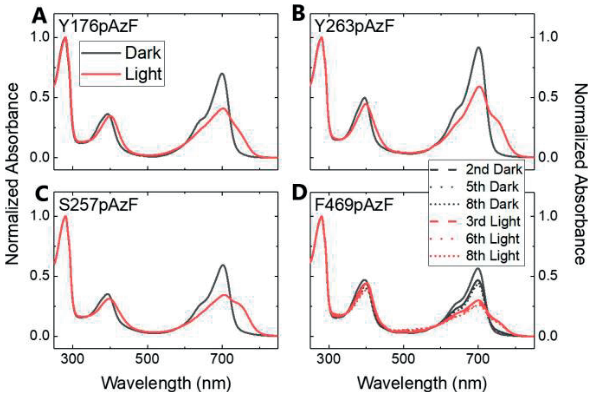

Figure S3: UV-vis absorption spectra of pAzF mutants of *Dr*BphP$_{PSM}$ differing from the WT. The UV-vis spectra in the dark (Pr) and after red light illumination are shown of A) Y176pAzF, B) Y263pAzF, C) S257pAzF, and D) F469pAzF. The spectra differ from the WT[7] as the A700/A280 ratio of Pr is substantially below 1 and the band maxima in the spectra of the red light illuminated samples are close to 700 nm instead of 750 nm.
D) The spectra of the F469pAzF mutant after the switching cycles.

In the mutants S257pAzF and F469pAzF the label severely compromised the photoconversion. The S257pAzF showed similar features to Y263pAzF and Y176pAzF but the A700/A280 ratio appeared low, only 0.59 (Fig. S3). In the mutant F469pAzF, the initial Q-band of the dark and illuminated were relatively low. Furthermore, F469pAzF revealed unstable photoconversion; the absorption of the Q-band decreased gradually after every switch, not observed in any other mutant. Reasons for this can only be speculated, but possibly the label at F469 impeded the crucial interactions between neighbouring S468 and the PAS-GAF in Pfr[8] and/or disturbed the refolding of the tongue as in Pr it locates in the beta-sheet turn, and in Pr, in the helix pointing towards the solution.[8,9] The stable switch- ing is crucial in the steady-state FTIR, where the protein is continuously switched, and the spectra in the same state were summed up and thus their similarity is necessary. Due to low

Pr yield and unstable photoswitching, the mutants S257pAzF and F469pAzF were excluded from the following sections.

The changes in the vibrations of the chromophore and protein region, here referred to as the fingerprint region, report about the structural changes caused by the label as well as miss- ing of the original residue. Therefore here, we compare the fingerprint region of the labeled constructs to the fingerprint region of the unlabeled construct, WT. To visualize the differ- ences between the mutants and WT, in Figure S4 we have calculated the double-difference spectra, i.e. the WT difference spectrum *minus* the mutant difference spectrum. The dif- ference spectra are normalized at the 1712 cm^{-1} peak to simplify the spectral comparison of mutated and WT spectra as well as the amplitude of difference in the double-difference spectra between the mutants.

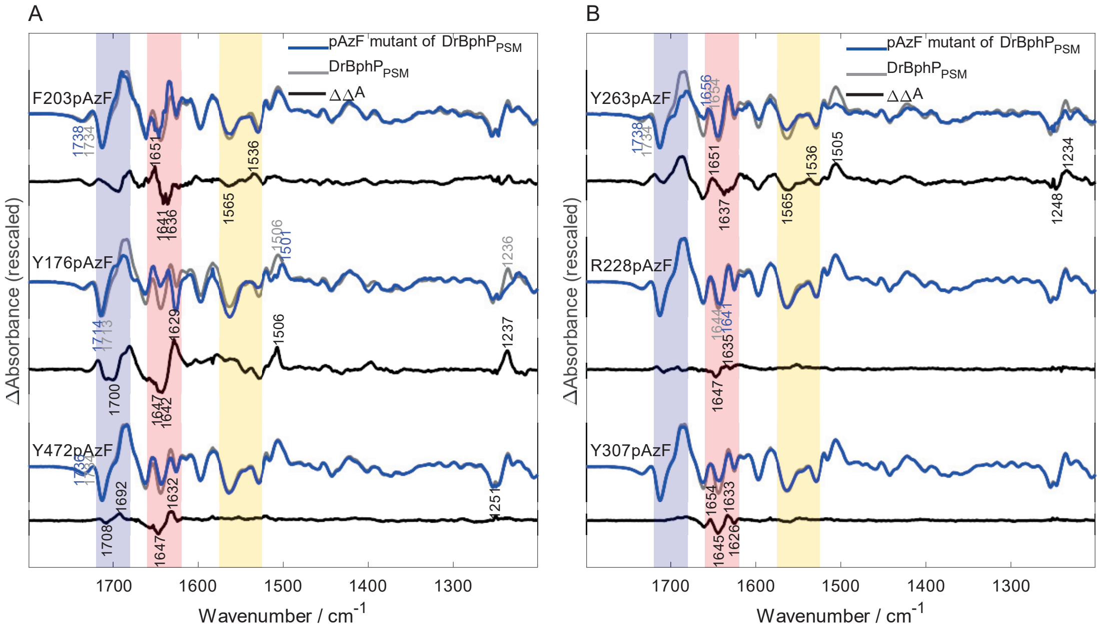

Figure S4: The FTIR difference spectra of pAzF mutants of *Dr*BphP$_{PSM}$ in con- trast to WT A) The F203pAzF, Y176pAzF, and Y472pAzF mutants. B) The Y263pAzF, R228pAzF, and Y307pAzF mutants. The spectra have been scaled to size at the 1712 cm^{-1} signal. The shifted peaks of the difference spectra have been labeled with blue (mutant) and grey (WT). The main features in the double-difference spectra are labeled. The region of BV D-ring vibrations are highlighted with blue panel and amide I and amide II regions are highlighted with red and yellow panels, respectively.

As the peaks of the fingerprint region are rather challenging to interpret, we focus here on two specific regions. First, we observe the changes in the BV C=O stretches of A-ring (1730 cm^{-1}, in Pr) and D-ring (1712 cm^{-1} in Pr, 1685 cm^{-1} in Pfr, blue panel in Figure S4).[1,5,10,11] Secondly, we observe the changes in the amide I region (1620-1660 cm^{-1}, pink panel in Figures SS4) that originate mainly from the C=O strech in the polypeptide back- bone, and thus report about the secondary structural changes in the protein; β-sheet induced vibrational band locates at 1641-1623 cm^{-1} and α-helix at 1657-1648 cm^{-1}.[12] The amide II vibrations (1570-1530 cm^{-1}, yellow panel in Figure S4) originate mainly the backbone NH bending coupled with the CN stretching, and they do not report straightforwardly about the secondary structural changes that still also affect the amide II vibrations.[12]

Changes in the chromophore A- and D-ring carbonyl vibrations were observed when the label was inserted close to BV (Fig. S4), which was also indicated by the UV-vis results (Fig. S3). The A-ring stretching vibrations upshifted from 1734 cm^{-1} with 4 cm^{-1} in F203pAzF and Y263pAzF, and with 2 cm^{-1} wavenumbers in Y176pAzF. In Y263pAzF, the A-ring vibrations were significantly decreased compared to the unlabeled construct. Shifts in D-ring carbonyl vibrations were not observed, but rather variation in the peak shapes and intensities. In Y176pAzF and Y263pAzF, the positive region of the D-ring carbonyl vibrations (1686 cm^{-1} peak) were decreased compared to the unlabeled construct. Ihalainen *et al.*[11] have shown by means of isotope labeling that also protein vibrations locate around 1695-1700 cm^{-1} in Pfr, although the peak mainly arises from the D-ring C=O. In Y176pAzF and F203pAzF the 1700 cm^{-1} was increased and in Y263pAzF decreased. In conclusion, the label near the BV can slightly disturb the conformation of the BV binding pocket, but does not prevent the photoswitching.

Stojkovic et al.,[13] Takala et al.[5] and Ihalainen et al.,[11] have confirmed a positive signal in α-helix region in Pfr and a signal in the β-sheet region in Pr due to secondary structural transition in the PHY domain during Pr to Pfr conversion. Thus, in the double difference spectra (Fig. S4), an upshift of the positive signal (i.e. positive peak in α-helix frequencies) indicates that the converting content is larger in the unlabeled construct, and a downshift of the positive peak (i.e. positive peak in β-sheet frequencies) indicates larger content in the labeled construct.

In F203pAzF and Y263pAzF double difference spectra, upshift of the positive signal was detected in the amide I region with peak patterns 1650(+)/1640-1634(-) and 1651(+)/1637(-) cm^{-1}, respectively (Fig. S4), and the change indicates smaller amount of beta-sheet con- verting to alpha-helix from Pr to Pfr than in the unlabeled DrBphP$_{PSM}$. Downshift of the positive signal was observed in the mutants Y176pAzF, Y472pAzF and R228pAzF with peaks at 1647-1642(-)/1629(+), 1647(-)/1632(+) and 1647(-)/1635(+) cm^{-1}, respectively (Fig. S4). In R228pAzF the amplitude of the observed change was the smallest. In mutants, which had the same kind of change, the observed wavenumbers corresponded well to each other.

The amide II band does not report about the secondary structural changes as straightfor- wardly as amide I, although they should affect this region as well.[12] In the amide I region, an upshift of the positive signal was detected in F203pAzF and Y263pAzF, and a downshift in Y176pAzF and Y472pAzF. Similar features were observed in the amide II band between the similarly behaving mutants; in F203pAzF and Y263pAzF the spectral direction is increasing between 1560-1536 cm^{-1}, and in Y176pAzF, where a downshift was observed, the direction is opposite compared to the two previously mentioned (Fig. S4). In Y472pAzF, the intensity of the change in the amide I band was smaller compared to Y176pAzF, and such a trend in the amide II region is not observed (Fig. S4). The tongue region fluctuates between β-sheet and random coil in Pr.[14] Here, the changes in the amide II and especially amide I regions imply that in Y176pAzF and Y472pAzF the label stabilizes the β-sheet conformation, and in F203pAzF and Y263pAzF destabilizes the β-sheet conformation.

Additionally, the fingerprint region of the spectra was selectively observed. The three tyrosine mutants had especially interesting features in their double difference spectra. The similar positive peaks at 1506, 1505 and 1519 cm^{-1} as well as at 1237, 1234 and 1251

cm^{-1}, in Y176pAzF, Y263pAzF, and Y472pAzF, respectively (Fig. S4), indicate that these vibrations are missing in Pfr from the labeled constructs, as tyrosine CC and CO/COH vibration, respectively, have been shown to occur in these regions.[12]

The change in the label environment was recorded in R228pAzF and Y263pAzF by steady-state FTIR (Fig. S5), on top of Y472pAzF, Y176pAzF and F203pAzF, analyzed in the main paper. In Y307pAzF, no label signal was observed in the difference spectrum meaning that change observable by change in the azide frequency does not take place in that position. In Y263pAzF, the label signal is so weak and has such a low signal-to-noise ratio that the maximum positions in Pr and Pfr cannot be determined. In R228pAzF the amplitude of the signal is also small compared to the chromophore and protein signals, but it could be fitted into two Gaussian functions. In Pr, the pAzF frequency is at 2123 cm^{-1}, and 2136 cm^{-1} in Pfr. The residue R228 locates in the GAF domain, on the surface of the protein under constant solvent exposure, according to the crystal structures (Fig. S1).[8,9] The amplitude of the signal and the observed frequencies propose rather a change in the peak shape than shifting of the main frequency that would lay between the two observed frequency, thus indicating expected strongly H-bonding environment, i.e. the solvent waters. Creon et al.[15] suggest that the increased broadening of the peak would be due to increased protein fluctuations. Therefore, the small change sensed by the label could report about a dynamic environment and/or different solvent shell between the two conformations at R228.

The pAzF label is detected around 2100 cm^{-1}, in distinct region from the protein and chromophore vibrations (below 1730 cm^{-1}), which is shown in Figure S6.

Figure S7 shows the amplitude of the noise compared to the amplitude of the pAzF signal in the step-scan data. As shown in Figure S7A, the amplitude of noise is the same as the amplitude of the label signal in the first species of Y472pAzF global analysis, due to small ratio of the label signal compared to the signals of the fingerprint region (Fig. 2A). In Y176pAzF and F203pAzF, the label is in action later, and the ratio of the label signal and signals of the fingerprint region is higher, and therefore the signal-to-noise ratio is better

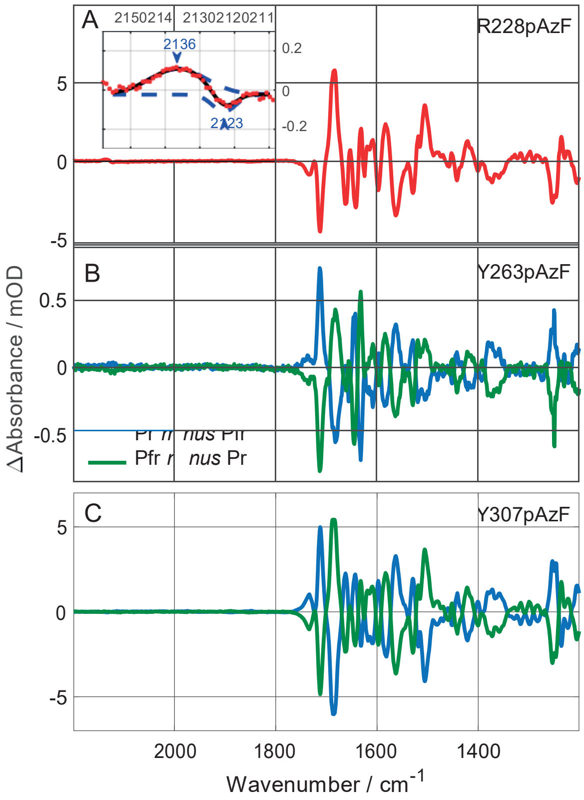

Figure S5: Tracking the label signal from the switchable pAzF mutants of DrBphP$_{PSM}$ A) In the inset of R228pAzF is shows the label signal fitted with two Gaussian bands, maximum positions labeled. The label shifts from 2123 cm^{-1} in Pr to 2136 cm^{-1} in Pfr. B) From Y263pAzF are shown both difference spectra to better demonstrate the low signal of the label that, due to low signal to noise ratio, cannot be properly interpreted. C) In Y307pAzF, there is no detectable label signal meaning that changes detectable with pAzF label do not occur in this position between Pr and Pfr.

than in Y472pAzF (Fig. S7 B-C).

Figure S8 shows that the SADS of the global analysis (Fig. 2-4E) can be extracted from the raw step-scan data based on the time scales acquired from the concentration fractions with 65 % cutoff.

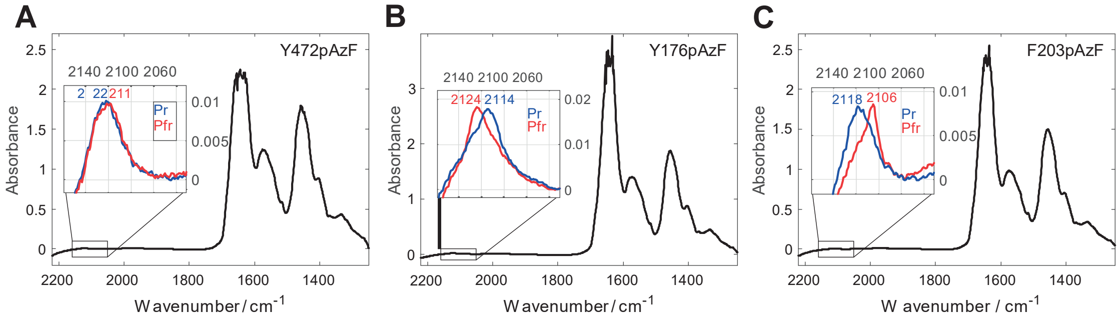

Figure S6: FTIR absorption spectra of *Dr*BphP$_{PSM}$ including the label region. The spectra of A) Y472pAzF, B) Y176pAzF, and C) F203pAzF were recorded at a high concentration of about 2 mM in buffered D_2O using a 50 μm spacer resulting in a detectable azido peak but a saturated amide I region. The separately recorded buffer spectrum was subtracted manually. The inset highlights the azido signal recorded in dark (blue) and after 661 nm red light illumination (red). About ten spectra were averaged. The positions of the maxima of the azido signals are given. An additional peak at 2153 cm^{-1} is missing in the absorption spectrum of F203pAzF because of the decreasing baseline resulting from D_2O absorption.

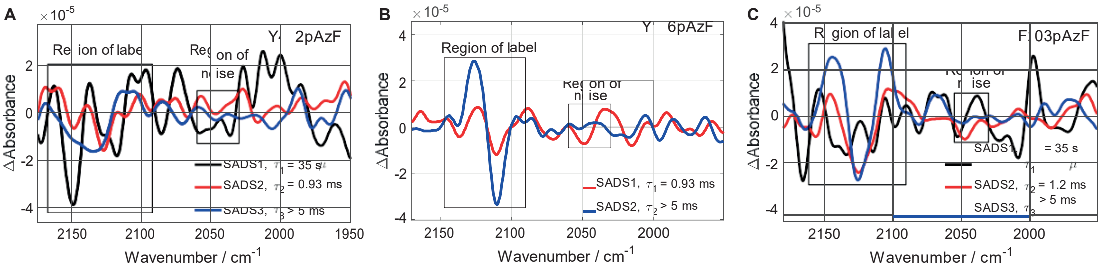

Figure S7: The window of noise in the global analysis. The amplitude of noise com- pared to the amplitude of the label signal in the time scales acquired from the global analysis.
A) The label region and the noise window of Y472pAzF shown in Fig. 2C. The first SADS of Y472pAzF has as large amplitude of noise as the amplitude of the label in Meta-R (SADS2) and Pfr (SADS3). However, the data needed the three components. Therefore the SADS1 of Y472pAzF is shown here but excluded from the result section (see Fig. 2B). B) The region of the label and noise of Y176pAzF traces of which are shown in Fig. 3C. C) The label region and the window of noise of F203pAzF traces of which are shown in Fig. 4C. In B and C the level of noise does not overrule the label region. The windows of noise is 2030-2060 cm^{-1}, which was selected as close to the label as possible but from a region definitely free of signal.

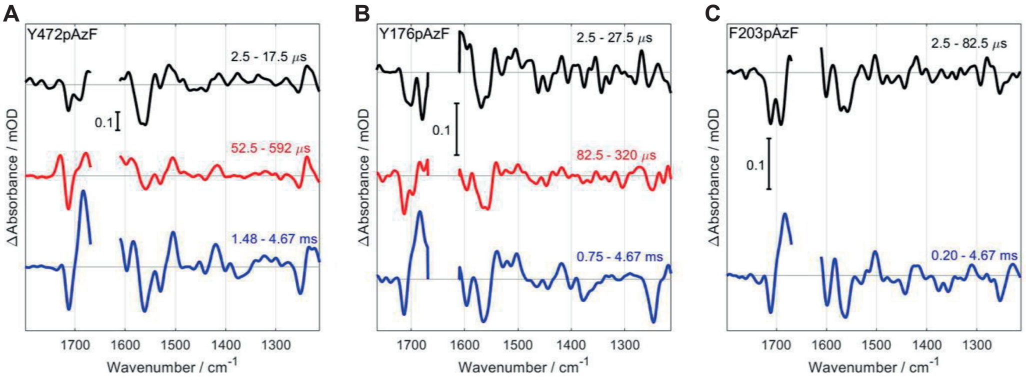

Figure S8: The raw data of time-resolved FTIR spectroscopy. The raw spectra have been integrated into three spectra that correspond the Lumi-R, Meta-R and Pfr spectra of the global analysis according to the maximal concentration fractions (cutoff 65 %). The integrated times are shown on top right of each spectrum. The region disrupted by water is cut off. A) Extracted species of Y472pAzF according to the concentration fractions in Fig. 2E. B) Extracted species of Y176pAzF according to the concentration fractions in Fig. 3E.

C) Extracted species of F203pAzF that only has two species corresponding to Lumi-R and Pfr spectra, shown with concentration fractions in Fig. 4E.

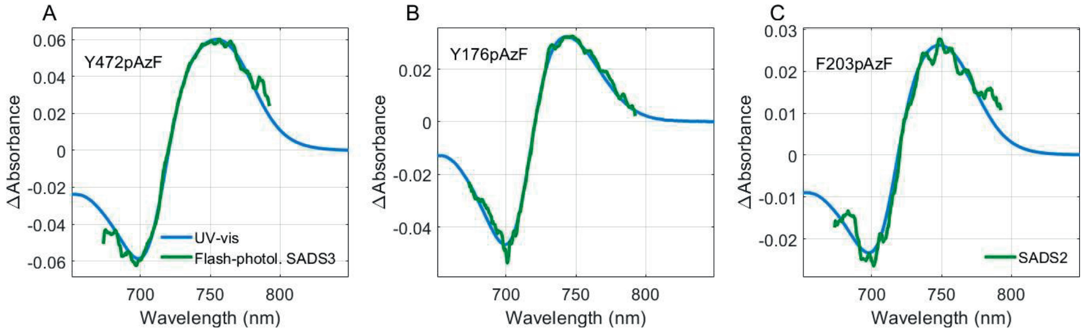

Figure S9: The last spectrum of flash photolysis are the same as in UV-vis. The last SADS spectra of the flash photolysis global analysis follow the lineshapes of UV-vis difference spectra, which tells that the chromophore completes the photocycle within 5 ms in A) Y472pAzF, B) Y176pAzF and C) F203pAzF mutants of DrBphp$_{PSM}$. The UV-vis spectra have been offset corrected and scaled according to the flash photolysis spectra.

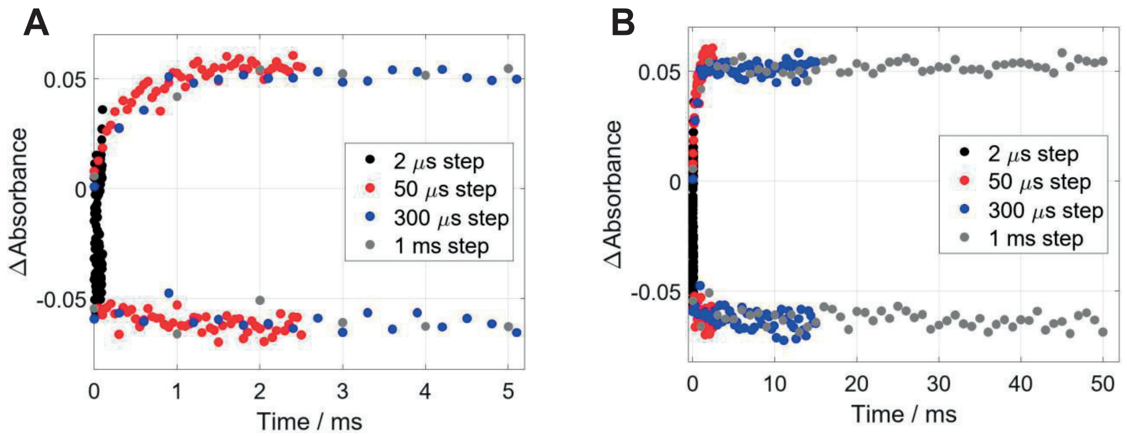

Figure S10: The phytochromes reach the equilibrium during the flash photolysis experiment. The flash photolysis data was collected with 2, 50, 300 and 1000 μs steps. A) The equilibrium is reached within 5 ms. Data until 5 ms was used in Fig. 2-4D. B) When experiment was continued until 50 ms, the equilibrium remained as in A. The example is from Y472pAzF experiment.

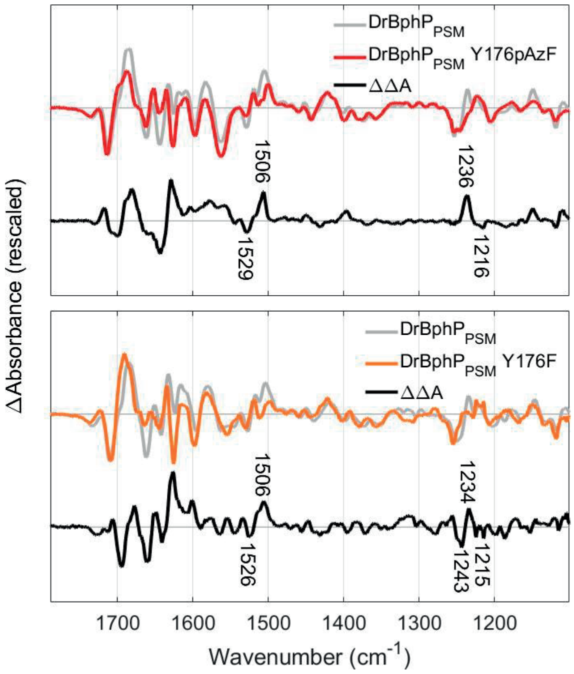

Figure S11: The mutants Y176pAzF and Y176F help to reveal the influence and contribution of Y176 to the photocycle. The tyrosine mutants Y176pAzF (monomer) and Y176F (dimer) are compared to the respective WT. The double difference spectra (WT *minus* mutant) reveal as indicated characteristic contributions originating from tyrosine and its influence on the chromophore vibrations. The spectra are scaled to the 1712 (-) cm^{-1} signal.

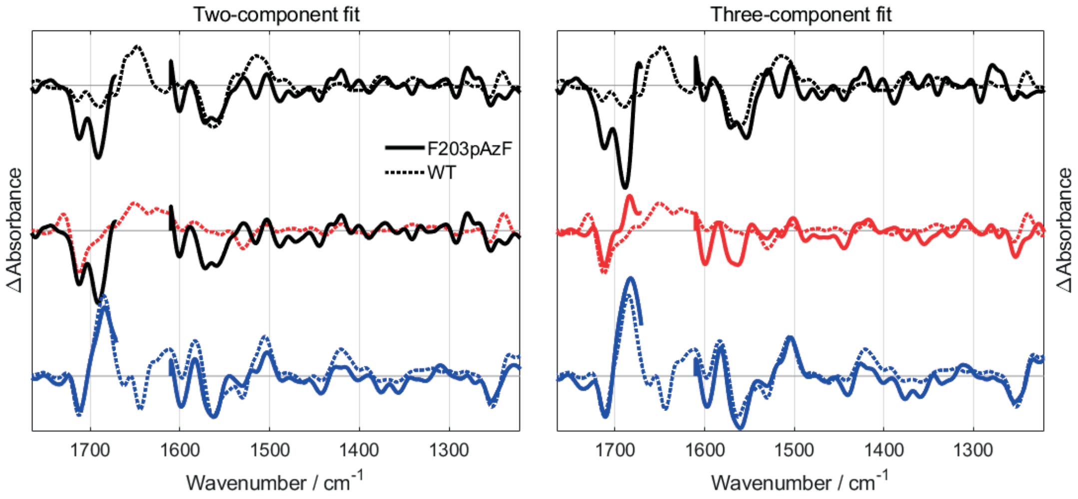

Figure S12: Global analysis of F203pAzF in the fingerprint region with a different number of components. A) The two-component fit shown in the main text. The first component (solid black line, τ_1 = 190 μs) of F203pAzF is compared with Lumi-R (τ_1 = 67 μs) and Meta-R (τ_2 = 1.76 ms) spectra of the WT. The first component more closely follows the line shape of WT Lumi-R, especially the characteristic 1564 (-) cm^{-1} peak. B) A forced three-component fit with the time-constants of WT produces a second intermediate (solid red line), which, however, does not show the Meta-R characteristics of WT Meta-R spectrum. In particular, F203pAzF lacks the 1730 (+) cm^{-1} peak. Rather, the second intermediate is a superposition of Lumi-R and Pfr states. Global analysis with three components without fixing results in two very similar time components, τ_1 = 35 μs and τ_2 = 400 μs (not shown). In conclusion, we infer that the mutant F203pAzF does not show a Meta-R state in the fingerprint region.

References

(1) Takala, H.; Lehtivuori, H. K.; Berntsson, O.; Hughes, A.; Nanekar, R.; Niebling, S.; Panman, M.; Henry, L.; Menzel, A.; Westenhoff, S.; Ihalainen, J. A. On the (un)coupling of the chromophore, tongue interactions, and overall conformation in a bacterial phytochrome. *J. Biol. Chem.* **2018**, *293*, 8161–8172.

(2) Rumfeldt, J. A.; Takala, H.; Liukkonen, A.; Ihalainen, J. A. UV-Vis Spectroscopy Re- veals a Correlation Between Y263 and BV Protonation States in Bacteriophytochromes. *Photochem. Photobiol.* **2019**, *95*, 969–979.

(3) Wagner, J. R.; Brunzelle, J. S.; Forest, K. T.; Vierstra, R. D. A light-sensing knot revealed by the structure of the chromophore-binding domain of phytochrome. *Nature* **2005**, *438*, 325–331.

(4) Takala, H.; Lehtivuori, H.; Hammarén, H.; Hytönen, V. P.; Ihalainen, J. A. Connection between absorption properties and conformational changes in Deinococcus radiodurans phytochrome. *Biochemistry* **2014**, *53*, 7076–7085.

(5) Takala, H.; Niebling, S.; Berntsson, O.; Björling, A.; Lehtivuori, H.; Häkkänen, H.; Panman, M.; Gustavsson, E.; Hoernke, M.; Newby, G.; Zontone, F.; Wulff, M.; Men- zel, A.; Ihalainen, J. A.; Westenhoff, S. Light-induced structural changes in a monomeric bacteriophytochrome. *Struct. Dyn.* **2016**, *3*, 12.

(6) Björling, A. et al. Ubiquitous Structural Signaling in Bacterial Phytochromes. *J. Phys. Chem. Lett.* **2015**, *6*, 3379–3383.

(7) Takala, H.; Björling, A.; Linna, M.; Westenhoff, S.; Ihalainen, J. A. Light-induced Changes in the Dimerization Interface of Bacteriophytochromes. *J. Biol. Chem.* **2015**, *290*, 16383–16392.

(8) Takala, H.; Björling, A.; Berntsson, O.; Lehtivuori, H.; Niebling, S.; Hoernke, M.; Kosheleva, I.; Henning, R.; Menzel, A.; Ihalainen, J. A.; Westenhoff, S. Signal amplification and transduction in phytochrome photosensors. *Nature* **2014**, *509*,245–248.

(9) Burgie, E. S.; Zhang, J.; Vierstra, R. D. Crystal structure of *Deinococcus* phytochrome in the photoactivated state reveals a cascade of structural rearrangements during photoconversion. *Structure* **2016**, *24*, 448–457.

(10) Foerstendorf, H.; Benda, C.; Gärtner, W.; Storf, M.; Scheer, H.; Siebert, F. FTIR Studies of Phytochrome Photoreactions Reveal the C=O Bands of the Chromophore: Consequences for Its Protonation States, Conformation, and Protein Interaction. *Bio- chemistry* **2001**, *40*, 14952–14959.

(11) Ihalainen, J. A.; Gustavsson, E.; Schroeder, L.; Donnini, S.; Lehtivuori, H.; Isaksson, L.; Thöing, C.; Modi, V.; Berntsson, O.; Stucki-Buchli, B.; Liukkonnen, A.; Häkkänen, H.; Kalenius, E.; Westenhoff, S.; Kottke, T. Chromophore-protein interplay during the phytochrome photocycle revealed by step-scan FTIR spectroscopy. *J. Am. Chem. Soc.* **2018**, *140*, 12396–12404.

(12) Barth, A. Infrared spectroscopy of proteins. *Biochim Biophys Acta Bioenerg.* **2007**, *1767*, 1073–1101.

(13) Stojković, E. A.; Toh, K. C.; Alexandre, M. T. A.; Baclayon, M.; Moffat, K.; Ken- nis, J. T. M. FTIR Spectroscopy Revealing Light-Dependent Refolding of the Conserved Tongue Region of Bacteriophytochrome. *J. Phys. Chem. Lett.* **2014**, *15*,2512–2515.

(14) Gustavsson, E.; Isaksson, L.; Persson, C.; Mayzel, M.; Brath, U.; Vrhovac, L.; Iha- lainen, J. A.; Karlsson, G.; Orekhov, V.; Westenhoff, S. Modulation of Structural Het- erogeneity Controls Phytochrome Photoswitching. *Biophys. J.* **2020**, *118*,415–421.

(15) Creon, A.; Josts, I.; Niebling, S.; Huse, N.; Tidow, H. Conformation-specific detection

of calmodulin binding using the unnatural amino acid p-azido-phenylalanine (AzF) as an IR-sensor. *Struct. Dyn.* **2018**, *5*, 12.